



# APPROVAL SHEET

**Title of Thesis:** PROBING THE STRUCTURE AND MORPHOLOGY OF X-RAY AND GAMMA-RAY BINARIES USING A MULTI-WAVELENGTH, MULTI-MISSION APPROACH

**Name of Candidate:** Joel B. Coley  
Doctor of Philosophy, 2015

**Thesis and Abstract Approved:** \_\_\_\_\_  
Dr. Mark Henriksen  
Department of Physics  
Chair

**Date Approved:** \_\_\_\_\_

# ABSTRACT

**Title of Dissertation:** PROBING THE STRUCTURE AND MORPHOLOGY OF  
X-RAY AND GAMMA-RAY BINARIES USING A MULTI-WAVELENGTH,  
MULTI-MISSION APPROACH

Joel Barry Coley, Doctor of Philosophy, 2015

**Dissertation directed by:** Dr. Robin Corbet  
UMBC CRESST

This thesis focuses on High-Mass X-ray Binaries (HMXBs) and their gamma-ray precursors, consisting of a compact object and an optical companion. Matter lost from the companion is accreted by the compact-object where the gravitational potential energy is converted into X-ray radiation. The predominant high-energy emissions in gamma-ray binaries are in the MeV to TeV bandpasses. Often, they are attributed to relativistic jets in microquasars or shocks from winds of the donor star and pulsar powered by rapid rotation of the neutron star.

I use multi-wavelength observations with *RXTE*, *MAXI*, *Swift*, *Suzaku*, *Fermi* and *ATCA* to provide detailed temporal and spectral information on several X-ray binaries and one gamma-ray binary, namely 1FGL J1018.6-5856.

My survey of the eclipsing HMXBs IGR J16393-4643, IGR J16418-4532, IGR J16479-4514, IGR J18027-2016 and XTE J1855-026 demonstrates that the physical parameters of both stellar components can be constrained. In IGR J16393-4643, spectral types of B0 V or B0-5 III are found to be consistent with the eclipse duration and Roche-lobe size, but the previously proposed spectral types in IGR J16418- 4532 and

IGR J16479-4514 were not. Also found to be consistent with the eclipse half-angle and Roche-lobe size were the mass donor spectral types of IGR J18027-2016 and XTE J1855-026.

4U 1210-64 was postulated to be a HMXB powered by the Be mechanism. Long-term observations show distinct high and low states and a  $6.7101 \pm 0.0005$  day modulation. A sharp dip interpreted to be an eclipse is found in the folded light curves. The eclipse half-angle is not consistent with the previously proposed spectral type B5 V, pointing to possible spectral types of B0 V or B0-5 III.

The gamma-ray binary 1FGL J1018.6-5856, discovered by the Fermi Large Area Telescope, consists of an O6 V((f)) star and suspected rapidly spinning pulsar. I exploit the  $\sim 6.5$  yr gamma-ray data to search for long-term changes in the properties of the  $16.531 \pm 0.006$  day orbital modulation. The best-fit spectral model consists of a featureless absorbed power law, evidence that 1FGL J1018.6-5856 is a non-accreting system. I find the radio amplitude modulation to decline with increasing frequency, indicating the presence of free-free absorption.

Probing the Structure and Morphology of X-ray and Gamma-ray Binaries  
Using a Multi-Wavelength, Multi-Mission Approach

by

Joel Barry Coley

Dissertation submitted to the Faculty of the Graduate School of the  
University of Maryland, Baltimore County in partial fulfillment  
of the requirements for the degree of  
Doctor of Philosophy  
2015

Advisory Committee:

Dr. Mark Henriksen, Chair  
Dr. Robin Corbet, Advisor  
Dr. Markos Georganopoulos  
Dr. James Franson  
Dr. Katja Pottschmidt  
Dr. Koji Mukai

© Copyright by  
Joel Barry Coley  
2015

*I first want to dedicate this Dissertation to my LORD and Savior Jesus Christ. I then dedicate this Dissertation to my wife, Larissa Coley, for all of her love, patience and support. Te amo por siempre. This is dedicated to my mother Rosemary Coley, who recently departed to be with the LORD. You are my Rock, my Advocate, and my Champion. I love you forever and will always cherish your memory. To my Dad, Barry S. Coley, and brother Jordan Coley, thanks for everything. Finally, I dedicate this to my late-grandmother Ruth Coley who wanted to see this moment become a reality.*

## ACKNOWLEDGMENTS

Before I begin, I first would like to thank my LORD and Savior Jesus Christ. It is my hope that for readers of this thesis to truly appreciate the wonders of the Universe and the world we live in, and by that desire to have a living and breathing relationship with the God of the Bible. I also would like to thank the many people who have supported me over the years both emotionally and scientifically. I am indebted to all of you. To my wife Larissa, thanks for all of your support and for being patient with me as I worked diligently to make this become a reality. I thank my Mother, Rosemary Coley, who has recently departed to be with the LORD. In life and now even absent from the body, you are my Advocate, my Comforter, my Champion, my Mommy. I miss you dearly and I know you are smiling at me from Heaven. To Dad, Barry S. Coley, thank you for your interest in my work and the time you invested to vastly improve the many components of this thesis. To my brother, Jordan S. Coley, you are the best brother a guy could have. I also thank all of my Uncles, Aunts, Cousins and all of my in-laws. To my entire committee, I am indebted to everything. Working with all of you has been a rewarding experience as each of you played a key role in making this dream that I've had since I was in grade school a reality. I particularly thank both my thesis advisor, Robin Corbet, and my Committee Chair, Mark Henriksen, for their mentorship and patience. I could only hope my research will be as impactful as theirs. Speaking of my Ph.D. committee, I will be remiss not to personally thank Koji Mukai, Katja Pottschmidt, James Franson and Markos Georganopoulos. I thank my many colleagues and friends both of UMBC Physics Department and NASA Goddard, but I particularly want to thank Malachi Tatum who is truly an inspiration to me and Adriana Lima for her great friendship in good times and those that were hard. I will be remiss to not include Lynne Griffith, Jennifer Salmi, Marsha Scott, Kathy Wimpling, and Stacey Tignall. I thank Jamie Stevens and Phil Edwards for use of data from the Australia Telescope Compact Array; Hans Krimm, Timothy Kallman, Joern Wilms and Vanessa McBride for their assistance; and Arash Bodaghee for his great advice. I thank the staff and my many friends of Bridgeway Community Church for their prayers through this journey. I also thank a good friend of my family Barbara Sullivan for all that she deposited into each of us. Finally, I would like to acknowledge the financial support I received from the Center for Research and Exploration in Space Science Technology (CRESST) partnership between UMBC and NASA Goddard, the *Fermi* Guest Investigator Grant, and the NASA Astrophysical Data Analysis Program (ADAP) Grant 14-ADAP14-0167. I apologize if inadvertently I missed anyone.

# TABLE OF CONTENTS

<b>DEDICATION</b>		<b>ii</b>
<b>ACKNOWLEDGMENTS</b>		<b>iii</b>
<b>LIST OF TABLES</b>		<b>viii</b>
<b>LIST OF FIGURES</b>		<b>x</b>
<b>List of Symbols</b>		<b>xiii</b>
<b>List of Abbreviations</b>		<b>xiv</b>
<b>Chapter 1</b>	<b>INTRODUCTION</b>	<b>1</b>
1.1	Overview	1
1.2	Stars and Spectral Types	2
1.3	Compact Objects	5
1.4	Evolution of Binary Stars	10
1.5	X-ray Binaries	12
1.5.1	Accretion Geometry	13
1.5.2	Classifications of High Mass X-ray Binaries	17
1.5.3	New classes of SGXBs discovered by <i>INTErnational Gamma-Ray Astrophysics Laboratory (INTEGRAL)</i>	20
1.6	Temporal Evolution of X-ray Binaries	22
1.6.1	Neutron Star Rotation Period	23
1.6.2	Orbital Period	24
1.6.3	Corbet Diagram	25
1.6.4	Superorbital periodic and aperiodic variability	27
1.7	Spectral Properties of X-ray Binaries	29
1.7.1	Emission Mechanisms in High Mass X-ray Binaries	29
1.7.2	The Continuum Spectrum in High Mass X-ray Binaries	30
1.7.3	Spectral Modifications	31
1.8	Gamma-ray Binaries	33
1.8.1	Particle Acceleration Mechanisms in Gamma-ray Binaries	34
1.8.2	Variability in Gamma-ray Binaries	35
1.9	Thesis Organization	37

**Chapter 2      PROBING THE MASSES AND RADII OF DONOR STARS IN  
ECLIPSING X-RAY BINARIES WITH THE SWIFT BURST  
ALERT TELESCOPE . . . . . 40**

2.1 Overview . . . . . 40

2.2 Introduction . . . . . 41

2.3 Data Analysis and Modelling . . . . . 44

    2.3.1 Swift BAT . . . . . 44

    2.3.2 Eclipse Modeling . . . . . 45

2.4 Five Eclipsing HMXBs . . . . . 54

    2.4.1 IGR J16393-4643 (=AX J16390.4-4642) . . . . . 54

    2.4.2 IGR J16418-4532 . . . . . 58

    2.4.3 IGR J16479-4514 . . . . . 61

    2.4.4 IGR J18027-2016 (=SAX J1802.7-2017) . . . . . 64

    2.4.5 XTE J1855-026 . . . . . 69

2.5 Discussion . . . . . 72

    2.5.1 What is the nature of the mass donors in each system? . . . . . 73

        2.5.1.1 IGR J16393-4643 . . . . . 73

        2.5.1.2 IGR J16418-4532 . . . . . 73

        2.5.1.3 IGR J16479-4514 . . . . . 77

        2.5.1.4 IGR J18027-2016 . . . . . 80

        2.5.1.5 XTE J1855-026 . . . . . 81

    2.5.2 What is the nature of the non-zero eclipse flux in IGR J16393-4643? 82

    2.5.3 What mechanism is responsible for asymmetries in the eclipse  
        profile? . . . . . 84

2.6 Conclusion . . . . . 87

**Chapter 3      PROBING THE MYSTERIES OF THE X-RAY BINARY 4U  
1210-64 WITH ASM, PCA, MAXI, BAT AND SUZAKU . . . . 98**

3.1 Overview . . . . . 98

3.2 Introduction . . . . . 99

3.3 Observations and Data Analysis . . . . . 102

    3.3.1 RXTE . . . . . 102

        3.3.1.1 ASM . . . . . 102

        3.3.1.2 PCA . . . . . 102

    3.3.2 MAXI . . . . . 103

    3.3.3 Swift . . . . . 104

    3.3.4 Suzaku . . . . . 105

        3.3.4.1 XIS data . . . . . 105

        3.3.4.2 HXD data . . . . . 106

3.4 Results . . . . . 107

    3.4.1 Long Term Temporal Analysis . . . . . 107

        3.4.1.1 ASM Temporal Analysis . . . . . 107

        3.4.1.2 MAXI Temporal Analysis . . . . . 109

3.4.1.3	BAT Temporal Analysis . . . . .	110
3.4.2	Eclipse Profile . . . . .	111
3.4.3	Short Term Temporal Analysis . . . . .	112
3.4.3.1	Suzaku . . . . .	113
3.4.3.2	PCA . . . . .	115
3.4.4	Spectral Analysis . . . . .	119
3.4.4.1	Suzaku Spectral Analysis . . . . .	120
3.4.4.2	PCA Spectral Analysis . . . . .	124
3.5	Discussion . . . . .	127
3.5.1	Constraints on the Mass-Donor . . . . .	128
3.5.1.1	Eclipse Half-Angle Constraints . . . . .	128
3.5.1.2	Does the Proposed Mass Donor Spectral Type Agree with the Optical Spectrum Reported in Masetti et al. (2009)? . . . . .	130
3.5.1.3	Is 4U 1210-64 an Intermediate-Mass X-ray Binary? . . . . .	133
3.5.2	What is the Nature of the Compact Object? . . . . .	134
3.5.3	What is the physical process responsible for the low state ob- served in the ASM data? . . . . .	136
3.5.4	What is the origin of the variability in the high-state? . . . . .	138
3.5.5	Emission Lines . . . . .	140
3.5.5.1	Fe K $\alpha$ Emission . . . . .	140
3.5.5.2	The presence of S XVI in 4U 1210-64 . . . . .	143
3.6	Conclusion . . . . .	143

**Chapter 4      A MULTI-WAVELENGTH STUDY OF THE GAMMA-RAY  
BINARY 1FGL J1018.6-5856 . . . . . 150**

4.1	Overview . . . . .	150
4.2	Introduction . . . . .	151
4.3	Observations and Data Analysis . . . . .	154
4.3.1	Fermi LAT . . . . .	154
4.3.2	Swift XRT . . . . .	155
4.3.3	ATCA . . . . .	157
4.4	Results . . . . .	157
4.4.1	Temporal Analysis . . . . .	157
4.4.1.1	<i>Fermi</i> LAT Analysis . . . . .	157
4.4.1.2	<i>Swift</i> XRT Analysis . . . . .	159
4.4.1.3	ATCA Analysis . . . . .	160
4.4.2	Spectral Analysis . . . . .	161
4.4.2.1	<i>Fermi</i> LAT Analysis . . . . .	161
4.4.2.2	<i>Swift</i> XRT Analysis . . . . .	166
4.4.2.3	ATCA Radio Analysis . . . . .	167
4.5	Discussion . . . . .	173
4.5.1	What is the nature of the gamma-ray orbital modulation? . . . . .	173

4.5.2	What is the nature of the frequency dependent modulation in the <i>ATCA</i> data? . . . . .	174
4.5.3	What is the Nature of the Compact Object? . . . . .	175
4.5.4	Comparison and Contrast with LS 5039 and LS I +61° 303 . . . . .	176
4.6	Conclusion . . . . .	178
<b>Chapter 5</b>	<b>CONCLUSION . . . . .</b>	<b>181</b>
5.1	Overview . . . . .	181
5.2	Results on the Systems in this Work . . . . .	182
5.2.1	Probing the Masses and Radii of Donor Stars in Eclipsing X-ray Binaries . . . . .	182
5.2.2	4U 1210-64 . . . . .	183
5.2.3	1FGL J1018.6-5856 . . . . .	185
5.3	Gamma-Ray Binaries . . . . .	186
5.4	Outlook . . . . .	186
<b>Appendix A</b>	<b>INSTRUMENTATION . . . . .</b>	<b>189</b>
A.1	Overview . . . . .	189
A.2	Detector Physics . . . . .	190
A.2.1	Proportional Counters . . . . .	190
A.2.2	Scintillation Detectors . . . . .	193
A.2.3	CCD Detectors . . . . .	195
A.3	Past Observatories . . . . .	198
A.3.1	Rossi X-ray Timing Explorer (RXTE) . . . . .	198
A.3.1.1	All-Sky Monitor (ASM) . . . . .	198
A.3.1.2	Proportional Counter Array (PCA) . . . . .	200
A.3.2	<i>Suzaku</i> . . . . .	202
A.3.2.1	X-ray Imaging Spectrometer (XIS) . . . . .	202
A.3.2.2	Hard X-ray Detector (HXD) . . . . .	204
A.4	Current Observatories . . . . .	206
A.4.1	Monitor of All X-ray Image (MAXI) . . . . .	206
A.4.2	<i>Swift</i> . . . . .	208
A.4.2.1	Burst Alert Telescope (BAT) . . . . .	208
A.4.2.2	X-ray Telescope (XRT) . . . . .	210
A.4.3	<i>Fermi</i> . . . . .	212
A.4.4	<i>Australia Telescope Compact Array (ATCA)</i> . . . . .	215
<b>Appendix B</b>	<b>DATA ANALYSIS TECHNIQUES . . . . .</b>	<b>216</b>
B.1	Power Spectra Techniques . . . . .	216
B.1.1	Semi-Weighted Power Spectra . . . . .	217
B.1.2	Exposure-Weighted Power-Spectra . . . . .	218
B.2	Probability Based Aperture Photometry . . . . .	218

## LIST OF TABLES

2.1	Eclipse Model Parameters, Assuming a Symmetric Eclipse Profile . . . . .	48
2.2	Eclipse Model Parameters, Assuming an Asymmetric Eclipse Profile . . . . .	49
2.3	Eclipse Model Parameters With Historic Values . . . . .	50
2.4	Mid-eclipse Time Measurements for $O - C$ Analysis . . . . .	91
2.5	Historic Mid-eclipse Time Measurements for IGR J18027-2016 and XTE J1855-026 . . . . .	92
2.6	Physical Parameters for Previously Proposed Mass Donors for IGR J16393-4643 . . . . .	92
2.7	Physical Parameters for Previously Proposed Mass Donors for IGR J16418-4532 . . . . .	93
2.8	Physical Parameters for Previously Proposed Mass Donors for IGR J16479-4514 . . . . .	93
2.9	System Parameters for IGR J18027-2016 . . . . .	94
2.10	System Parameters for XTE J1855-026 . . . . .	95
2.11	Possible Parameters of Candidate Donor Stars for IGR J16418-4532 . . . . .	96
2.12	Possible Parameters of Candidate Donor Stars for IGR J16479-4514 . . . . .	97
3.1	Best-fit Parameters for 4U 1210-64 States . . . . .	109
3.2	4U 1210-64 Eclipse Model Parameters . . . . .	114
3.3	Suzaku Spectral Parameters . . . . .	146
3.4	Spectral Parameters of 4U 1210-64 from the <i>Suzaku</i> Observation . . . . .	147
3.5	Spectral Parameters of 4U 1210-64 from the PCA Observations . . . . .	148
3.6	Physical Parameters for Candidate Mass Donors in 4U 1210-64 . . . . .	149
4.1	1FGL J1018.6-5856 Gamma-ray Spectral Parameters Using Likelihood Analysis . . . . .	163
4.2	1FGL J1018.6-5856 Gamma-ray Spectral Parameters Using Likelihood Analysis . . . . .	164
4.3	X-ray Spectral Parameters from <i>Swift</i> XRT Survey . . . . .	168

4.4 Spectral Parameters from the *ATCA* Radio Survey . . . . . 171

## LIST OF FIGURES

1.1	Typical Curves for Hadronic and Strange Quark Matter Equations of State	10
1.2	Roche-lobe Overflow . . . . .	12
1.3	Classification of X-ray Binaries . . . . .	14
1.4	Accretion Geometries . . . . .	16
1.5	Be stars in Isolation vs. Those in XRBs . . . . .	20
1.6	Circumstellar Disc of Be Star Viewed Pole-on . . . . .	21
1.7	Column Density in Obscured Supergiant X-ray Binaries . . . . .	22
1.8	Eclipse Geometry . . . . .	25
1.9	Corbet’s $P_{orb}/P_{spin}$ diagram . . . . .	26
2.1	Observed–Calculated Eclipse Time Residuals For Symmetric Step-and-Ramp Function . . . . .	51
2.2	Observed–Calculated Eclipse Time Residuals For Asymmetric Step-and-Ramp Function . . . . .	52
2.3	Observed–Calculated Eclipse Time Residuals Combined With Historic Values . . . . .	53
2.4	IGR J16393-4643 Folded Light Curve . . . . .	55
2.5	IGR J16393-4643 Eclipse Half-Angle . . . . .	57
2.6	IGR J16393-4643 Mass-Radius Plot . . . . .	58
2.7	IGR J16418-4532 Folded Light Curve . . . . .	60
2.8	IGR J16418-4532 Eclipse Half-Angle . . . . .	61
2.9	IGR J16418-4532 Mass-Radius Plot . . . . .	62
2.10	IGR J16479-4514 Folded Light Curve . . . . .	63
2.11	IGR J16479-4514 Eclipse Half-Angle . . . . .	64
2.12	IGR J16479-4514 Mass-Radius Plot . . . . .	65
2.13	IGR J18027-2016 Folded Light Curve . . . . .	66
2.14	IGR J18027-2016 Eclipse Half-Angle . . . . .	67

2.15	IGR J18027-2016 Mass-Radius Plot . . . . .	68
2.16	XTE J1855-026 Folded Light Curve . . . . .	71
2.17	XTE J1855-026 Eclipse Half-Angle . . . . .	72
2.18	XTE J1855-026 Mass-Radius Plot . . . . .	72
2.19	IGR J16418-4532 Candidate Spectral Types . . . . .	75
2.20	IGR J16479-4514 Candidate Spectral Types . . . . .	78
2.21	Eccentricity Fits for IGR J16393-4643, IGR J16418-4532 and IGR J16479-4514 . . . . .	87
3.1	4U 1210-64 ASM, MAXI and BAT Light Curves . . . . .	108
3.2	4U 1210-64 Power Spectra . . . . .	110
3.3	4U 1210-64 Folded Lightcurves . . . . .	111
3.4	4U 1210-64 Eclipse Profile . . . . .	113
3.5	<i>Suzaku</i> Lightcurve . . . . .	115
3.6	4U 1210-64 <i>Suzaku</i> Hardness-Intensity Diagram . . . . .	116
3.7	4U 1210-64 PCA Lightcurves and Hardness Ratio . . . . .	117
3.8	4U 1210-64 PCA Color-Color Diagrams . . . . .	118
3.9	4U 1210-64 PCA Scargle's Power Spectrum . . . . .	119
3.10	Typical PCA Power Spectra for 4U 1210-64 . . . . .	120
3.11	4U 1210-64 <i>Suzaku</i> Spectrum and Best Fit Model . . . . .	122
3.12	<i>Suzaku</i> Spectra of 4U 1210-64 Illustrating the S XVI and Fe K $\alpha$ Emission Regions . . . . .	123
3.13	Fluxes of Fe K $\alpha$ Lines in 4U 1210-64 vs. Unabsorbed Continuum Flux . . . . .	124
3.14	Typical PCA Spectrum of 4U 1210-64 . . . . .	125
3.15	Spectral Parameters of the PCA spectra vs. continuum flux . . . . .	126
3.16	Mass-Radius Space Diagram of 4U 1210-64 Showing Allowed Spectral Types . . . . .	130
3.17	Predicted Eclipse Half Angle in 4U 1210-64 vs. Stars with Indicated Spectral Types . . . . .	131

3.18	ASM and MAXI Folded Hardness Ratios of 4U 1210-64 . . . . .	140
4.1	1FGL J1018.6-5856 <i>Fermi</i> LAT light curve produced using a likelihood analysis . . . . .	158
4.2	Power Spectra of 1FGL J1018.6-5856 produced by <i>Fermi</i> LAT . . . . .	158
4.3	<i>Fermi</i> LAT Aperture Photometry light curve . . . . .	159
4.4	1FGL J1018.6-5856 <i>Swift</i> XRT X-ray Power Spectrum . . . . .	160
4.5	1FGL J1018.6-5856 <i>Swift</i> XRT X-ray folded light curve . . . . .	160
4.6	1FGL J1018.6-5856 ATCA radio folded light curve . . . . .	161
4.7	1FGL J1018.6-5856 <i>Fermi</i> Likelihood Light Curve . . . . .	162
4.8	Folded <i>Fermi</i> LAT lightcurve produced using a likelihood analysis . . . . .	165
4.9	<i>Swift</i> XRT Spectrum at Phase 0 . . . . .	167
4.10	Absorption-corrected <i>Swift</i> X-ray flux of 1FGL J1018.6-5856 . . . . .	169
4.11	Correlation of Spectral Parameters with Continuum Flux . . . . .	169
4.12	ATCA Radio Spectra Folded on the Orbital Period . . . . .	170
4.13	Spectral Parameters Folded on Orbital Period . . . . .	172
4.14	ATCA Spectral Index Correlation with Flux . . . . .	172
4.15	LS I +61° 303 <i>Fermi</i> LAT light curve produced using a likelihood analysis	178
A.1	ASM Overview . . . . .	199
A.2	Cross-section of one PCA detector . . . . .	201
A.3	Cross section of the XIS sensor . . . . .	203
A.4	MAXI Instrument Overview . . . . .	207
A.5	<i>Swift</i> BAT Instrument Overview . . . . .	209
A.6	<i>Swift</i> XRT Instrument Overview . . . . .	212
A.7	Energy resolution of the <i>Swift</i> XRT CCD-22 above 500 eV . . . . .	212
A.8	<i>Fermi</i> LAT schematic . . . . .	214
A.9	Five of six ATCA dishes . . . . .	215

## List of Symbols

$A_\lambda$	extinction at given wavelength
$a$	semi-major axis
$\beta$	ratio between donor star radius to Roche-lobe radius
$C_{\text{ing}}$	count rate before ingress
$C_{\text{ecl}}$	count rate during eclipse
$C_{\text{eg}}$	count rate after egress
$e$	eccentricity
$f(M)$	mass function
$\Gamma$	photon index
$i$	inclination angle
$K_{\text{O}}$	donor star radial velocity semi-amplitude
$K_{\text{X}}$	neutron star radial velocity semi-amplitude
$m_\lambda$	apparent magnitude at given wavelength
$M_\lambda$	absolute magnitude at given wavelength
$M_\odot$	solar mass
$\dot{M}$	mass accretion rate
$N_{\text{H}}$	column density
$O - C$	observed-minus-calculated
$\dot{P}$	orbital period derivative
$P_{\text{orb}}$	orbital period
$p$	probability
$q$	mass ratio between stellar components
$R_\odot$	solar radius
$r$	correlation coefficient
$\Theta_e$	Eclipse Half-Angle

## List of Abbreviations

2MASS	Two Micron All Sky Survey
ASCA	<i>Advanced Satellite for Cosmology and Astrophysics</i>
ATCA	<i>Australia Telescope Compact Array</i>
ATNF	Australia Telescope National Facility
ASM	All-Sky Monitor ( <i>RXTE</i> )
BAT	Burst Alert Telescope ( <i>Swift</i> )
<i>BeppoSAX</i>	Beppo Satellite per Astronomia a raggi X
BeXB	Be X-ray Binary
BHC	Black Hole Candidate
BMJD	Barycenter Modified Julian Date
CCD	Charge-Coupled Device
CTI	Charge Transfer Inefficiency
CTIO	Cerro Tololo Interamerican Observatory
CV	Cataclysmic Variable
CXB	Cosmic X-ray Background
DFT	Discrete Fourier Transform
EDS	Experiment Data System
EoS	Equation of State
EQW	Equivalent Width
<i>ESO VLT</i>	<i>European Southern Observatory Very Large Telescope</i>
eV	electron volt
<i>EXOSAT</i>	<i>European X-ray Observatory Satellite</i>
FAP	False-Alarm Probability
FOV	Field-of-View
GeV	Giga electron volt
GHz	Gigahertz
GLIMPSE	Galactic Legacy Infrared Mid-Plane Survey
GSC	Gas Slit Camera ( <i>MAXI</i> )
GSO	Gadolinium Silicate Crystal ( <i>Suzaku</i> )
GTI	Good-Time Interval
<i>H.E.S.S.</i>	<i>High Energy Stereoscopic System</i>
HMXB	High-Mass X-ray Binary
HR	Hardness Ratio
HXD	Hard X-ray Detector ( <i>Suzaku</i> )
IBIS	Imager on-Board the INTEGRAL Satellite
INT	Isaac Newton Telescope
<i>INTEGRAL</i>	<i>International Gamma-Ray Astrophysics Laboratory</i>
IRF	Instrument Response Functions
<i>ISS</i>	<i>International Space Station</i>
Jy	Jansky
keV	kilo electron volt
kpc	kilo parsec

## List of Abbreviations cont.

LAT	Large Area Telescope ( <i>Fermi</i> )
LMXB	Low-Mass X-ray Binary
LT	Liverpool Telescope
lt-s	light seconds
MAXI	Monitor of All-sky X-ray Image
MeV	Mega electron volt
MJD	Modified Julian Date
mJy	milli Jansky
NS-HMXB	Neutron Star High-Mass X-ray Binary
NTT	New Technology Telescope
<i>NuSTAR</i>	Nuclear Spectroscopic Telescope Array
NXB	Non X-ray Background
PCA	Proportional Counter Array ( <i>RXTE</i> )
PCU	Proportional Counter Unit
PHA	Pulse Height Amplitude
PIN	Positive Intrinsic Negative
PSF	point-spread function
PSPC	Position-Sensitive Proportional Counter
<i>RXTE</i>	<i>Rossi X-ray Timing Explorer</i>
SED	Spectral Energy Distribution
SFXT	Supergiant Fast X-ray Transient
SGXB	Supergiant X-ray Binary
TeV	Tera electron volt
UV	ultraviolet
UVOT	Ultraviolet/Optical Telescope ( <i>Swift</i> )
WFC	Wide Field Camera ( <i>BeppoSAX</i> )
WHT	William Herschel Telescope
XIS	X-ray Imaging Spectrometer ( <i>Suzaku</i> )
<i>XMM-Newton</i>	<i>X-ray Multi-Mirror Mission</i>
XRB	X-ray Binary
XRT	X-ray Telescope ( <i>Swift</i> )

## Chapter 1

# INTRODUCTION

### 1.1 Overview

People throughout the centuries have looked into the night sky and wondered what they saw. Apart from the moon, the night sky to the unaided eye is dominated by various star types, which captures the imaginations of children, adults, and as well as the amateur astronomer, and are expressed in words from nursery rhymes to poetry. Ancient civilizations named constellations based on numerous patterns that resembled things seen in nature. These included but were not limited to bears (Ursa Major and Minor) whose tails form the Big Dipper and Little Dipper, respectively; dogs such as Canis Major, which hosts the brightest star to the unaided eye, Sirius; and bulls (the Taurus constellation), a prominent constellation in the winter sky. One of history's oldest documents, the Bible, also speaks of the stars and in the book of Isaiah (~653 B.C.) it was recorded that the stars were all created and given a name by God. In the age of exploration, sailors used the stars as navigation beacons in order to determine their latitude and longitude as their ships traversed the vast seas of our Earth. Not only have we gazed into the sky and were mystified by the nature of stars but throughout the ages, we have also wondered about

the lifetimes of stars and if they have birthdates and deathdates like us. This was articulated shortly after the turn of the second Millennium, when the Chinese noted the sudden appearance of a star in Taurus (Carroll & Ostlie, 2006). It turned out not to be a random event in the evolutionary history of the star, but a violent explosion where a supergiant star expels much of its mass as a supernova. Today, only the core of the progenitor star remains as a rapidly rotating neutron star surrounded by a beautiful pulsar wind nebula and a supernova remnant that modern astronomers refer to as the Crab Nebula (Reifenstein et al., 1969).

The main topic of this thesis is the study of binary systems where high-energy emission in the X-ray and gamma-ray bandpasses is observed. The remainder of this chapter is structured in the following order: the components of X-ray and gamma-ray binary systems are introduced in Sections 1.2 and 1.3 and the evolution of binary systems is presented in Section 1.4. Sections 1.5 and 1.6 focus on the physical mechanisms responsible for the X-ray emission, Section 1.7 presents the particle acceleration mechanisms in gamma-ray binaries, and Sections 1.8 and 1.9 describe the temporal and spectral evolution of these systems. The organization of the thesis is outlined in Section 1.10.

## **1.2 Stars and Spectral Types**

The birth of a star takes place in a region of gas and dust, which collapses under its own gravity to the point where the process of nuclear fusion can begin. The energy released in its core, which is dense and hot enough where H nuclei fuse into He nuclei, provides the necessary pressure to halt further gravitational collapse and places the star

in hydrostatic equilibrium (González-Galán, 2015). Due to nuclear fusion of hydrogen, the stage where the outward thermal pressure is in balance with the gravitational force is called the main-sequence. It can last for millions to trillions of years depending on the stellar mass. For example, the lifetime of massive stars in the main-sequence phase is significantly shorter than those that are less massive due to the larger temperatures, initial luminosities and energy generation in their cores (Carroll & Ostlie, 2006).

Stars have different colors to the unaided eye on an evening of star gazing. This is a direct consequence that stellar spectra can be approximated by black-body radiation, which can be expressed in terms of the relationship between the color of a star and its temperature (Carroll & Ostlie, 2006). The color of a star, which is referred to as its wavelength peak emission, is inversely proportional by its temperature and can be quantified using Wien's Displacement Law (see Equation 1.1).

$$(1.1) \quad \lambda_{\max} = \frac{2.898 \text{ mmK}}{T}$$

This assumes that the star emits as a perfect blackbody and therefore its corresponding temperature is a description of the energy output (Carroll & Ostlie, 2006; Karttunen et al., 2007). Peaking in the blue and violet regions of the visible part of the electromagnetic spectrum, the temperatures of stars with masses  $M \sim 6\text{--}28 M_{\odot}$  are between 15,000–35,000 K, which is much greater than that of stars with masses comparable to the Sun. Less massive stars such as the Sun and cool red-dwarfs on the other hand have temperatures of  $\sim 5500$  K and  $\sim 3000$  K, respectively. These properties are sorted by the Harvard Spectral Classification where massive blue stars are labeled as O and B, respectively; cooler white and yellow stars are referred to as A, F and G; and still cooler stars are K

and M, which peak in the orange and red. In recent decades, astronomers found objects referred to as brown dwarfs adding the types L and T to the Harvard Spectral Classification. These objects lack the necessary temperatures in their cores to ignite nuclear fusion and the surface temperatures in many of these objects is  $\sim 750$  K (Kirkpatrick, 2005).

The physical property that drives the evolution of a star on and past the main-sequence is its mass. The energy in main-sequence O and B stars is generated via the carbon-nitrogen-oxygen (CNO) cycle, which is the dominant means of nuclear fusion in stars where the temperature of the core exceeds  $1.7 \times 10^6$  K (Schuler et al., 2009). When the hydrogen in the core is exhausted, the energy generation in the core and hence the thermal pressure that kept the star in hydrostatic equilibrium during the main-sequence ceases. This results in a slow collapse of the stellar core where He nuclear fusion can begin. At this point, helium nuclei fuse into carbon nuclei supplying a new mechanism that halts further gravitational collapse and once again places the star into hydrostatic equilibrium. Different nuclear reactions occur at ever faster rates and in the case where the star has a sufficient mass can eventually lead to the formation of Fe. Due to its negative binding energy, nuclear fusion is unable to exothermally progress beyond Fe and instead results in a supernova. Depending on the mass of the core, the compact object left behind is either a neutron star or black hole. These will be detailed in Section 1.3.

The gravitational potential at the surface of stars, surface gravity, is used to form another classification scheme referred to as the Yerkes Spectral Classification (Karttunen et al., 2007). In this scheme defining the stellar luminosity class, supergiants have the lowest surface gravity and are designated with Ia, Iab or Ib. Giant stars and main-sequence stars form the III and V luminosity classes, respectively.

### 1.3 Compact Objects

White dwarfs, neutron stars and stellar mass black holes are collectively referred to as compact objects and represent the endpoint in the evolutionary history of normal stars<sup>1</sup>. These are the remnants of stars that once radiated in the optical and/or ultraviolet part of the electromagnetic spectrum and are a direct result of gravitational collapse. Apart from black holes that collapse into a region smaller than the Schwarzschild radius where not even light can escape the immense gravitational potential (see equation 1.2), compact objects are degenerate stars that are in hydrostatic equilibrium between gravity and the degeneracy pressure due to fermions, particles with half-integer spins such as electrons and neutrons.

$$(1.2) \quad r_s = \frac{2GM}{c^2}$$

Degeneracy pressure is a direct consequence of the Pauli exclusion principle from quantum mechanics, which states that no two fermions can simultaneously occupy the same quantum state (Griffiths, 1995). While the end of the life of a star like the Sun will be relatively quiet as the core becomes a white dwarf approximately the size of the Earth, stars with masses in excess of  $\sim 8M_\odot$  explode as Type II supernovae (Woosley & Janka, 2005). The stellar core becomes the only remaining intact part of the star as the majority of its mass is expelled in a supernova, forming supernova remnants such as the Crab Nebula. Depending on the mass of the remaining core, what is left is either a neutron star supported by neutron degeneracy pressure or a black hole. While black holes and white dwarfs are fascinating objects in their own right, the majority of the binary systems

---

<sup>1</sup>Here, I refer to stars where nuclear fusion occurs.

discussed in this thesis are known or suspected to host X-ray pulsars. These are neutron stars powered by matter accretion from a donor star.

The study of compact objects commenced in the early 20th century with the discovery and subsequent study of white dwarfs (Adams, 1914; Hertzsprung, 1915). While the nature of white dwarf stars at first appeared elusive<sup>2</sup>, these stars were found to be supported by the hydrostatic equilibrium between electron degeneracy pressure and gravity (Fowler, 1926, Dirac, 1926). Correctly asserting electrons at high densities to be relativistic, Chandrasekhar (1931) calculated the maximum stable mass of a degenerate gas of relativistic electrons to be  $\sim 1.4 M_{\odot}$ . This is now referred to as the Chandrasekhar limit for white dwarfs.

With the discovery of the neutron in 1932 (Chadwick, 1932), theorists postulated the existence of more massive compact objects composed of a degenerate gas of neutrons (Baade & Zwicky, 1934). These objects referred to as neutron stars are compact objects that are supported by the hydrostatic equilibrium between neutron degeneracy pressure and gravity. The first calculations of their internal structure were reported in Oppenheimer & Volkoff (1939), where mass limit calculations similar to the white dwarf Chandrasekhar limit were made. While theorists calculated the internal structure and supernovae as the formation site of neutron stars, the first pulsar was not observationally discovered until 1968 (Hewish et al., 1968).

Today, nearly 2000 neutron stars are known and can be either isolated in space or part of a binary stellar system (Manchester et al., 2005). The subclasses of isolated

---

<sup>2</sup>E.g. The first white dwarf was initially found to be an A-type star with low luminosity; Adams (1914).

neutron stars include radio pulsars<sup>3</sup>, Soft Gamma-ray Repeaters (SGRs), and Anomalous X-ray Pulsars. Due to their rapid rotation and extreme magnetic fields, which are on the order of  $10^{12}$ – $10^{15}$  G (Manchester et al., 2005; Haensel et al., 2007), radio pulsars are powered by the rotational kinetic energy of the neutron star (Pacini, 1967). This is observed in a broad spectrum that covers nearly all wavelengths on the electromagnetic spectrum. It should be noted that the pulsed emission observed in AXP and SGRs is on the order of  $10^{41}$  erg s<sup>-1</sup> (Kouveliotou et al., 1998), which is too luminous to entirely be powered by the spin-down energy of the pulsar (Manchester et al., 2005). AXP and SGRs are also characterized by a long rotation period and rapid spin down rate. This implies that the magnetic field is in excess of  $10^{14}$  G (Manchester et al., 2005). The resulting X-ray emission is attributed to magnetic field relaxation. In the case that the magnetic and rotational axes are misaligned, this radiation sweeps along the line-of-sight and can be observed as radio pulsations. It should be noted that some pulsars powered by the neutron star rotational kinetic energy were discovered in the X-ray and gamma-ray bandpasses, and might not show radio pulsations (e.g. Geminga, SNR N157B; Halpern & Holt, 1992; Marshall et al., 1998). This electromagnetic radiation produces a torque, which effectively causes the neutron star to lose rotational kinetic energy over time and can be quantified by the neutron star characteristic age,  $\tau_c$  (Manchester et al., 2005; Gaensler & Slane, 2006).

---

<sup>3</sup>These are to be distinguished from accretion-powered pulsars seen in X-ray binaries.

This is dependent on both the spin period and derivative of the spin period of the neutron star (see equation 1.3).

$$(1.3) \quad \tau_c = \frac{P_{\text{pulse}}}{2\dot{P}_{\text{pulse}}}$$

As a whole, neutron stars are exotic objects where matter behaves in ways that are impossible to replicate in the laboratory setting and are studied to test the laws of fundamental physics in the presence of extreme thermal environments as well as gravitational and electromagnetic potentials. The mass and radius of neutron stars are typically  $\sim 1.4 M_{\odot}$ <sup>4</sup> and 10–15 km, resulting in a density on the order of  $10^{15} \text{ g cm}^{-3}$  (Lattimer & Prakash, 2004). This is approximately an order of magnitude larger than that of atomic nuclei. Since matter in a neutron star is crushed to supra-nuclear densities, its Equation of State (see Equation 1.1), the relationship between mass and radius, is unknown and there are currently over 100 models to predict its behavior (Mason et al., 2011; Lattimer, 2012). This is dependent on the number of bosons, which do not contribute to neutron degeneracy pressure, and the number of bosons is directly proportional to the maximum mass of the neutron star. In the case of a large fraction of bosons formed in the interior of a neutron star, neutron star masses can approach masses up to  $\sim 3 M_{\odot}$  (i.e. near the limit originally predicted by Oppenheimer & Volkoff, 1939).

At present, the internal structure of a neutron star is poorly understood and can only be described using theories such as, but by no means limited to, General Relativity, Quantum Chromodynamics, super-fluidity. Based on a review presented by Haensel et al. (2007), neutron stars could consist of a thin atmosphere, a crust and a core. The

---

<sup>4</sup>The Chandrasekhar limit for white dwarfs.

atmosphere consists of a thin plasma, only a few millimeters thick, which emits thermal radiation. This has been exploited to probe properties of the neutron star such as its gravitational and electromagnetic potentials, effective temperature, and chemical composition (Zavlin & Pavlov, 2002). Studying the thermal radiation emitted from the atmosphere also can reveal properties such as the mass and radius of neutron stars, which can be studied to disentangle the poorly constrained neutron star Equation of State. The crust of the neutron star is separated into two layers, where the outermost layer is a solid envelope about 200–500 m thick primarily consisting of  $^{56}\text{Fe}$  (Haensel et al., 2007). In the outer crust, electron degeneracy pressure is dominant where the density is  $\sim 4 \times 10^{11} \text{ g cm}^{-3}$ . However, at the bottom of the outer crust these electrons undergo inverse  $\beta$ -decay with protons to form a free neutron liquid (e.g. Lattimer & Prakash, 2004; Lattimer, 2012, and references therein). The inner crust is postulated to be  $\sim 1$  km thick and thought to be composed of free neutrons, neutron-rich nuclei and electrons. Its density exceeds those that can be studied in terrestrial laboratories and the matter could possibly be in a super-fluid state (Haensel et al., 2007). The core is also separated into an outer core and inner core. Consisting of a degenerate neutron plasma with protons, electrons and possibly muons, the density in the outer core can approach twice that of heavy atomic nuclei (Haensel et al., 2007). Densities in the inner core are on the order of a magnitude larger than heavy atomic nuclei. While the structure of the inner core is far beyond a tested theoretical description, it is possible that the inner core could be composed of quark matter (Haensel et al., 2007).

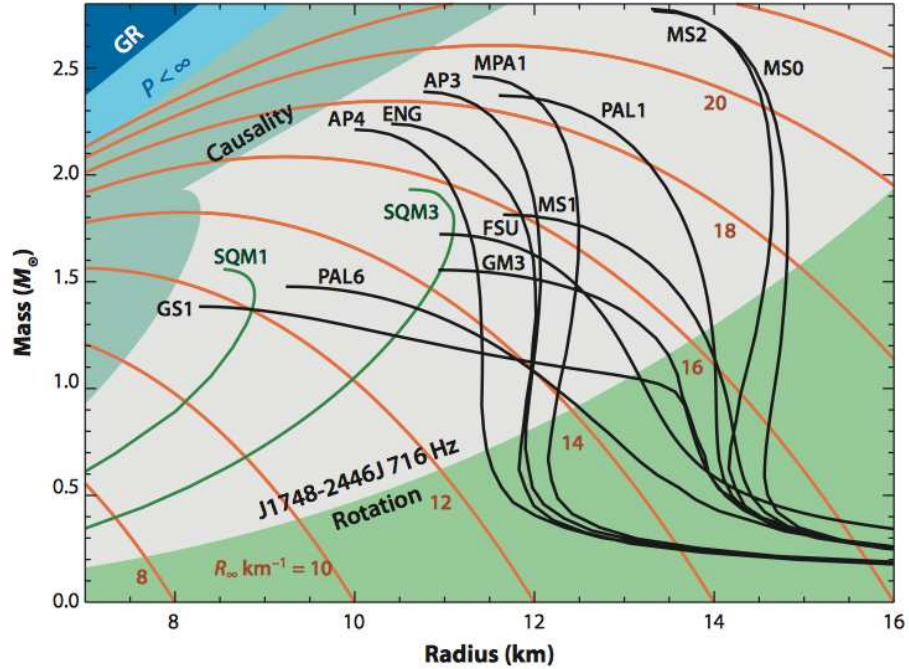


FIG. 1.1. Typical curves for hadronic and strange quark matter equations of state in Mass-Radius space. The regions that are excluded due to general relativity, finite pressure and causality are indicated (Lattimer, 2012).

#### 1.4 Evolution of Binary Stars

Many stars in the observable Universe reside in binary systems. These are defined as two stars orbiting their common center of mass. It is currently estimated that anywhere from one-third of stars in the Milky Way to 70% of stars are binary stars (Lada, 2006; Li & Han, 2008). The evolution of these stellar systems is dependent on the orbital separation and the gravitational interaction between the stellar components. In wide-binaries the components evolve separately. In close-binaries there is a small orbital separation where the components gravitationally influence the outer atmosphere, leading to interactions between the components in the form of tidal forces and mass accretion. As a whole, the study of binary stellar systems is important to the field of astrophysics where the masses of the components can be accurately calculated resulting in indirect methods to probe

their radii and density. Eclipsing binaries in particular are important because the radii of the components, the orbital inclination angle and masses can accurately be determined, which further reduces the uncertainties.

The interaction between the components in a binary system can significantly complicate the evolutionary history of these paired stars. This is attributed to the Roche potential (see Figure 1.2), which is described as the superposition between the gravitational potentials of the stars and that due to the centrifugal force between the two stars. These forces cancel out at the *Lagrangian* points of equilibrium,  $L_1-L_5$ , where  $L_1$  is the region where the equipotential lines touch between the two stars (Paczynski, 1971). The critical gravitational equipotential line that surrounds a star is referred to as the Roche lobe. This is important to the mass transfer process referred to as Roche-lobe overflow where material at  $L_1$  of one star in a binary system with an outward angular momentum can be captured by the gravitational potential of the other (see Figure 1.2). One way to classify binary stars is dependent on whether one or both stars fill their respective Roche lobes (Paczynski, 1971). A contact binary is when both stars fill their respective Roche lobes, a semi-detached system is when only one of the stars fill its Roche lobe and a detached binary is when neither star fills its respective Roche lobe.

The binary nature of the system in many cases is disrupted when one of the components explodes as a supernova, as was found in Brandt & Podsiadlowski (1995). They note that it is possible that the less massive star can evolve off the main-sequence prior to the more massive star, which is a consequence of Roche-lobe overflow. This is called the Algol paradox, named after the famous Algol binary, and it can directly influence the lifetime of the binary components. In a bound system that consists of a neutron star and mass

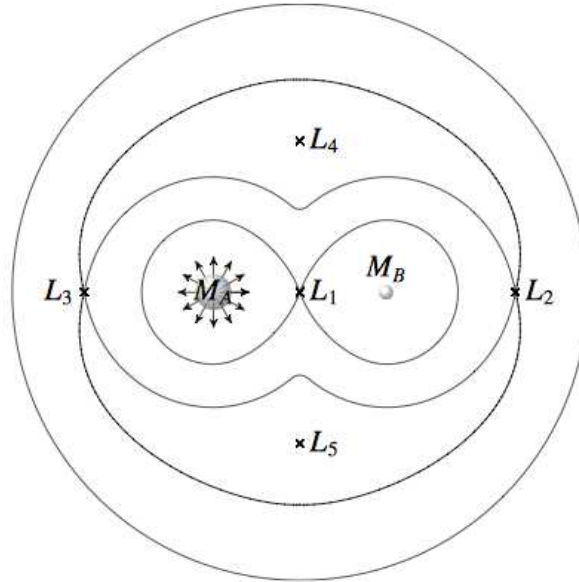


FIG. 1.2. The Roche potential on the orbital plane showing the location of the Lagrangian points for a mass ratio  $q = 1$  (Figure 2, de Val-Borro et al., 2009).

donor, the energy released during the supernova strongly affects the orbital parameters of the system such as the eccentricity and a natal kick velocity (Brandt & Podsiadlowski, 1995).

### 1.5 X-ray Binaries

At the point in the evolutionary history of close binary systems when the primary component – initially the most massive – becomes a compact object (neutron star or black hole), very powerful emissions in the X-ray bandpass can occur. These systems called X-ray binaries (XRBs) were first discovered in 1962 by Giacconi et al. (1962) and are among the brightest sources in the X-ray extrasolar sky. This is due to the extreme gravitational field of the compact object, which accretes matter from the companion star – called a mass donor – in a number of different processes. The accreted matter in an X-ray binary that hosts a neutron star has a free-fall velocity that approaches  $\sim 0.7 c$ . This then impacts the

solid surface of the neutron star where its potential energy stored in the gravitational field is converted into thermal energy and where the temperature exceeds  $10^7$  K (Shklovskii, 1967; Makishima, 2010). Using the canonical neutron star mass defined by the white dwarf Chandrasekhar limit and a radius of 10 km, it can be estimated that a mass loss rate of  $\sim 10^{-8} M_{\odot} \text{ yr}^{-1}$  can power an X-ray source of  $10^{36}$ – $10^{37} \text{ erg s}^{-1}$  (Seward & Charles, 1995).

Depending on the mass of the donor star, XRBs are divided into two groups: High-Mass X-ray Binaries (HMXBs) and Low-Mass X-ray Binaries (LMXBs, see Figure 1.3). The donor star in LMXBs is a late-type star typically  $1 M_{\odot}$  or less. In such systems, the primary mechanism for mass transfer is almost always Roche-lobe overflow. Symbiotic X-ray binaries form a second class of LMXBs, which consists of just eight known members (see Kuranov & Postnov, 2015, for review). These consist of neutron stars that accrete from the winds of M-type giant stars, where the neutron star rotation periods were found to be the longest so far<sup>5</sup> (e.g. 3A 1954+319, Corbet et al., 2008). High-mass X-ray binaries (HMXBs), on the other hand, host massive OB counterparts where mass loss occurs via Roche-lobe overflow or direct accretion of the stellar wind (e.g. Bondi-Hoyle accretion; Bondi & Hoyle, 1944). As of 2011, there were  $\sim 300$  Galactic X-ray binaries in which nearly 38% of the total are HMXBs (Chaty, 2011).

### 1.5.1 Accretion Geometry

X-ray binaries have a significant impact on high-energy astronomy. They offer the opportunity to investigate the coupled evolutionary history between the mass donor and

---

<sup>5</sup>The longest spin period in a neutron star is 5.3 hr.

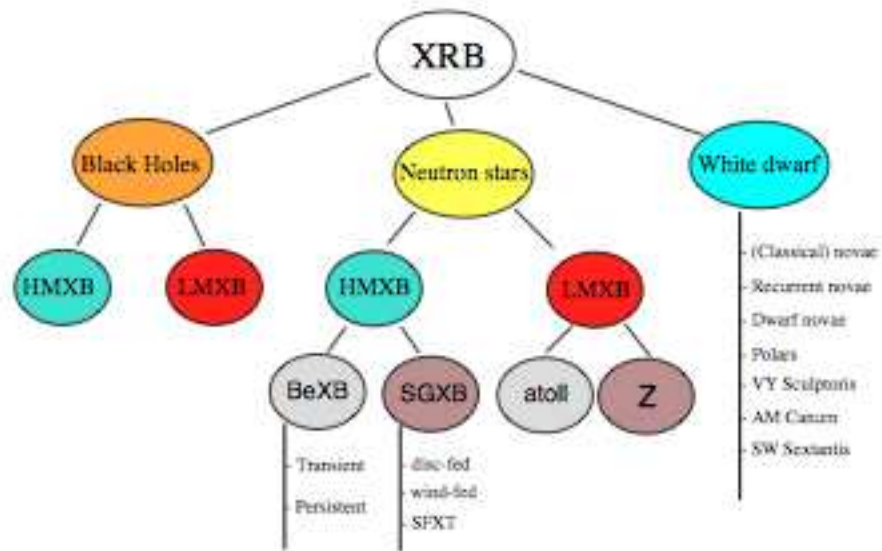


FIG. 1.3. Classification of X-ray binaries (Reig, 2011).

compact object at a key phase in their lifetime. Interactions such as tidal effects and mass accretion drive changes in the stellar components that can be monitored over time. While tidal effects in short period systems lead to the orbital circularization of the components, the consequences of mass transfer can be studied by the X-ray radiation observed in these systems. Eclipsing XRBs provide opportunities for us to constrain the mass and radius of the donor star. The mass of the compact object and therefore the neutron star Equation of State can be constrained, when measurements from a pulse-timing analysis and radial velocity measurements are available.

A fundamental astrophysical property in accreting sources when the forces of gravitation and that due to radiation pressure are at equilibrium is known as the Eddington

luminosity (see Equation 1.4; Frank et al., 1992; Seward & Charles, 1995; Becker et al., 2012).

$$(1.4) \quad L_{\text{edd}} = \frac{4\pi GMm_p c}{\sigma_T}$$

The radiative pressure is a consequence of the scattering of electromagnetic radiation off matter, where photons interact with the electrons via Thomson scattering (e.g. Frank et al., 1992). The gravitational force primarily interacts with protons, which are  $\sim 1836$  times more massive than electrons. It should be mentioned that for this relation to hold, the accretion process is assumed to be spherically symmetric (Becker et al., 2012). Due to the extreme ionized nature of the accreted material and highly magnetized nature of neutron stars, where the Eddington luminosity is found to be  $\sim 10^{38} \text{ erg s}^{-1}$ , the above mentioned regime only naively describes the accretion process in X-ray binaries. The extreme magnetic field must be taken into account (see Section 1.3). The Alfvén radius is defined as the distance from the center of the neutron star to where the kinetic energy density of accreted material is equal to the energy density stored in the magnetic field (Becker et al., 2012). At distances closer to the neutron star, or about  $\sim R_{\text{ns}}$ , the dominant force on the accreted material is the magnetic force, which forces it to follow the trajectory of the magnetic field lines (Arons & Lea, 1980; Becker et al., 2012). This forms accretion columns above the magnetic poles (see Figure 1.4). While many threading mechanisms have been proposed, the most efficient mechanism that couples the inflowing material with the magnetic field is the Kelvin-Helmholtz instability (Arons & Lea, 1980; White et al., 1983). The exact geometry of these columns is poorly understood, but theorists postulated that it could take the form of either a filled cylinder, a hollow cylinder, several

layers or multiple cylinders (see e.g. Meszaros, 1984). The hot spots that form when the accreted material impacts the solid surface of the neutron star may be on the order of 1 km (Becker & Wolff, 2005).

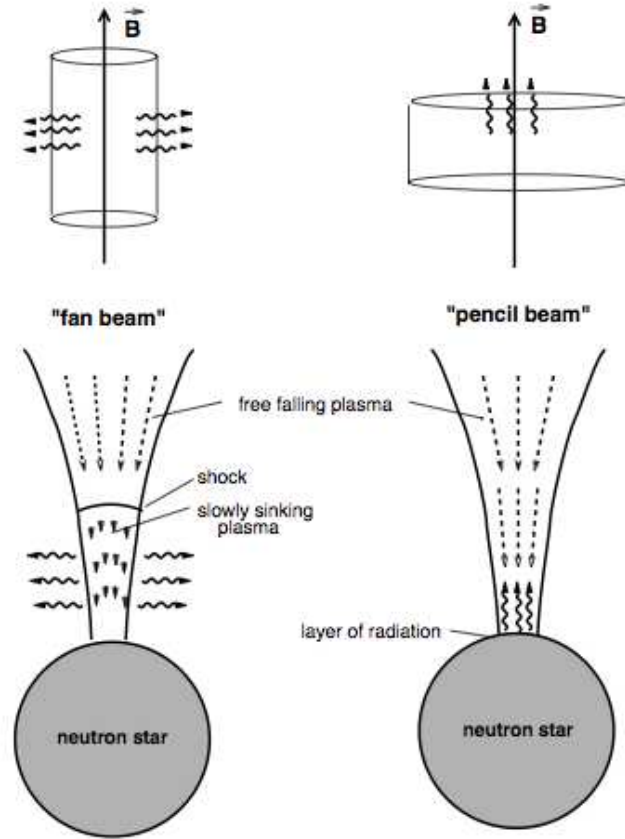


FIG. 1.4. Diagrams of the fan (left) and pencil (beam) geometries resulting from material accreting onto the magnetic polar cap of a neutron star (Schönherr et al., 2007).

Inside the accretion columns and resulting hot spots, the modified Eddington luminosity may be reduced up to a factor of  $\sim 200$  (Becker & Wolff, 2005; Becker et al., 2012). This is a direct consequence of both scaling down the Eddington luminosity to the ratio of the surface area of the neutron star to that of the accretion column, and modifying the Thomson scattering cross-section to that for photons parallel to the magnetic field (Basko & Sunyaev, 1976; Arons et al., 1987; Becker et al., 2012). It is postulated that this

modified Eddington luminosity is not a hard limit, as opposed to that seen in a spherically symmetric regime, and can be exceeded locally. Depending on the luminosity regime, a possible shock front can form in the accretion column that can prevent X-ray photons that propagate parallel to the magnetic field from escaping (Becker & Wolff, 2005; Schönherr et al., 2007). These X-ray photons may instead escape from the walls of the accretion column and are called fan beam radiation (see Figure 1.4). At luminosities lower than the critical luminosity, which is on the order of  $\sim 10^{35}\text{--}10^{37}$  erg s<sup>-1</sup>, the X-ray radiation is postulated to be emitted from the top of the accretion column and is called pencil beam radiation (Nelson et al., 1993; Becker et al., 2012). A mixture of pencil and fan beam radiation is seen near the critical luminosity (see Figure 1.4, Schönherr et al., 2007).

### 1.5.2 Classifications of High Mass X-ray Binaries

The physical characteristics of an X-ray binary depend on the nature of the stellar remnant and the configuration of the components of the system. Since the mid-1970s, HMXBs have been split into two individual classes: Be X-ray binaries (BeXBs) and supergiant X-ray binaries (SGXBs). The donor star in a BeXB is a rapidly rotating non-supergiant B-type star, where accretion mostly occurs when the compact object passes through the circumstellar decretion disc around the B star. In SGXBs, the compact object is in a short ( $\sim 1\text{--}40$  day) orbit around an OB-supergiant where the accretion mechanism is either via the powerful stellar wind and/or Roche-lobe overflow. While the eccentricity in most SGXBs with short orbital periods is near zero, some SGXBs host compact objects in highly eccentric orbits (e.g. GX 301-2, Islam & Paul, 2014). In wind-accretors, the X-ray luminosity is on the order of  $10^{35}\text{--}10^{36}$  erg s<sup>-1</sup>. However, a much higher luminosity is

found in systems where the donor fills its Roche lobe,  $\sim 10^{38}$  erg s $^{-1}$  (Kaper et al., 2004).

I first discuss the mass transfer process in wind-fed systems, where the compact object accretes material from the strong radiatively driven and highly supersonic wind of the OB-supergiant (e.g. Bondi-Hoyle-Littleton processes; Bondi & Hoyle, 1944). In their review, Castor et al. (1975) predict that OB stars lose approximately  $10^{-6} M_{\odot}$  a year due to radiation driven winds. The mass expelled from the OB star gains momentum due to the absorption and scattering of surrounding photons in the environment near the OB star, forming a highly energetic wind with a terminal velocity that can approach up to 2000 km s $^{-1}$  (Reig, 2011). X-ray emission in classical SGXBs is typically persistent where the total luminosity of the system is on the order of  $10^{35}$ – $10^{36}$  erg s $^{-1}$ . I note that short-term periodic variations due to wind inhomogeneities have been observed (Chaty, 2011). The neutron star rotation period in wind-fed SGXBs is typically long, on the order of hundreds to thousands of seconds. One particular SGXB, 2S 0114+65, hosts a neutron star with a spin period  $\sim 10^4$  s (Farrell et al., 2008).

I also discuss the accretion process in disk-fed systems, where the Roche lobe of the donor star is overfilled (e.g. Cen X-3, SMC X-1, LMC X-4; Reig, 2011). Due to the large angular momentum, the accreted material forms an accretion disc around the compact object transferring significant mass and momentum. This results in much higher X-ray luminosity,  $\sim 10^{38}$  erg s $^{-1}$ , which can approach the Eddington luminosity of some compact objects (Kaper et al., 2004). Wind accretion may also affect the dynamics of many SGXBs where mass transfer takes place via Roche-lobe overflow (e.g. Cen X-3; Day & Stevens, 1993).

Another accretion process is transitional Roche-lobe overflow, which is seen in

SGXBs where the donor star nearly fills the Roche lobe (e.g. Cygnus X-1, IGR J16479-4514; Hanke et al., 2009; Sidoli et al., 2013, and references therein). In this regime, tidal interactions at the inner Lagrangian point substantially focuses the stellar wind into a weak accretion stream (Blondin & Owen, 1997; Sidoli et al., 2012). The mass accreted onto the compact object is a superposition of the spherical wind and the focused wind, resulting in a significant increase in both the accretion rate and X-ray variability (Sidoli et al., 2012).

Finally, I discuss the mass transfer mechanism that is seen in BeXBs, which is commonly referred to as the Be mechanism. BeXBs are transient systems where the compact object is in a wide, typically eccentric, orbit ( $P_{\text{orb}} \gtrsim 10$  days) around a rapidly rotating non-supergiant B-type star or Be-star (see Section 1.2). In their reviews, Negueruela (1998) and Chaty (2011) found the narrow band of allowed spectral types in BeXBs contrasts with that seen in isolated Be stars, where the spectral type of isolated Be stars can extend to B9e (see Figure 1.5). This is possibly attributed to the natal “kick” velocity and angular momentum loss during the formation of the compact object where low mass stars are ejected from the binary system. The primary star rotates near the breakup speed where the rotational kinetic energy is large enough to form a circumstellar “decretion” disc (see Figures 1.6 and 1.7). The decretion disc, composed of a low-velocity, high-density stellar wind, can be studied in multiple wavelengths—each giving a different part of the story. Optical and near-infrared spectra show that  $H\alpha$  emission lines and a continuum characterized by free-free or free-bound emission describe the physical properties of the “decretion disc” (Chaty, 2011). While  $H\alpha$  lines are the most dominant emission lines seen in Be-stars, He and Fe emission lines can be observed as well (Reig, 2011). The width of the

H $\alpha$  line is correlated with the size of the disc, which is shown to form and disappear with time. The time-scale for the development and dissipation of a circumstellar disc is typically on the order of 3–7 years (Reig et al., 2010).

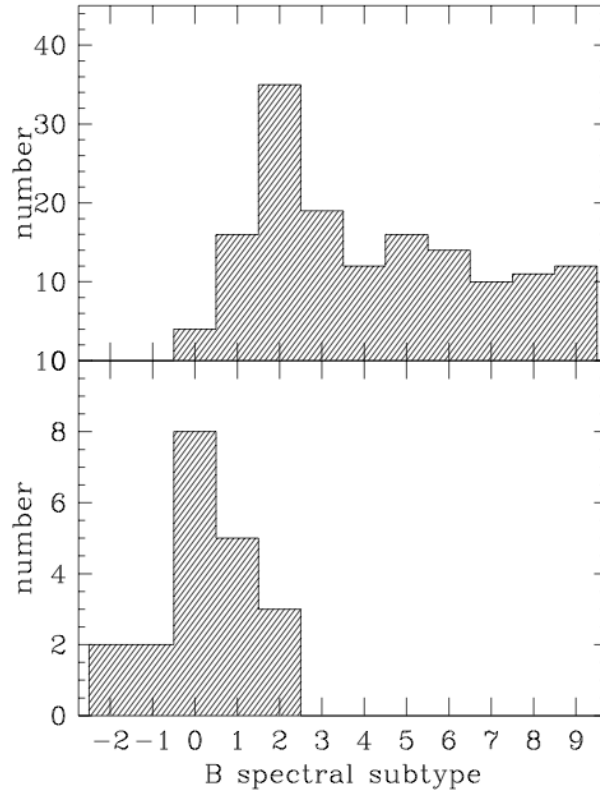


FIG. 1.5. This figure compares the spectral distribution between Be stars in isolation (top) and Be stars in Be/X-ray binary systems (bottom). It can be shown that Be stars in X-ray binary systems follow a different trend compared to similar stars isolated from any nearby neighbors (Negueruela, 1998).

### 1.5.3 New classes of SGXBs discovered by *INTErnational Gamma-Ray Astrophysics Laboratory (INTEGRAL)*

Prior to the launch of *INTErnational Gamma-Ray Astrophysics Laboratory (INTEGRAL)* in 2002, SGXBs were identified as a rather rare subgroup of HMXBs. In fact, only five out of 130 HMXBs were classified as SGXBs in the catalog reported in Liu et al.

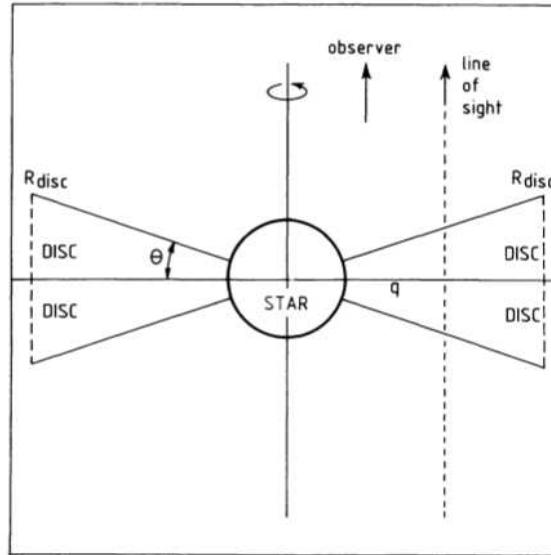


FIG. 1.6. The disc geometry viewed pole-on of a Be star (Waters et al. 1987)

(2000). In this catalog,  $\sim 50$  were reported as BeXBs. This was due to an observational bias where the emission in SGXBs is persistent compared to BeXBs, which are usually transient (Reig, 2011). Classical SGXBs are typically persistent systems where detection requires an improvement of the sensitivity of X-ray detectors, compared to BeXBs where detection is additionally related to their transient nature.

*INTEGRAL*, sensitive to X-rays in the 17–100 keV band (Bird et al., 2010), provides an excellent way to study highly absorbed SGXBs. This sensitivity to higher energy X-rays allows *INTEGRAL* to peer through the absorption, resulting in the detection of new X-ray sources. In their review, Bird et al. (2010) reported a total of 723 sources detected by *INTEGRAL* where 185 sources are XRBs. Out of the new population of XRBs, two new subclasses of SGXBs were discovered: obscured persistent SGXBs where  $N_{\text{H}}$  is on the order of  $10^{23}$  atoms  $\text{cm}^{-2}$  and Supergiant Fast X-ray Transients (SFXTs), characterized by fast and transient outbursts. For more information, see Kuulkers (2005) and Chaty (2013) for reviews.

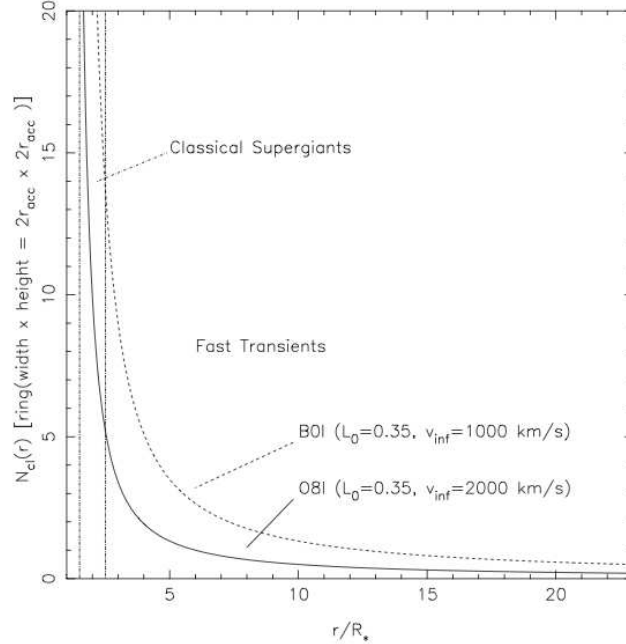


FIG. 1.7. The disc geometry viewed pole-on of a Be star (Waters et al. 1987)

## 1.6 Temporal Evolution of X-ray Binaries

The variability of X-ray binaries is seen on different timescales, giving different pieces of a larger picture. In the case that the compact object is a highly magnetized neutron star, X-ray pulsations can be seen at the neutron star rotation period. Variability can also be seen at the orbital and superorbital periods of many X-ray binaries due to a variety of different binary processes. Additionally, long-term variability allows the study of changes in the physical and geometric properties of HMXBs on long timescales. I discuss the physical mechanisms responsible for the variability seen at different timescales below.

### 1.6.1 Neutron Star Rotation Period

Many HMXBs host a highly magnetized neutron star where modulation is often seen at the rotation period. This is a consequence due to the misalignment of the rotation and magnetic field axes of the neutron star, which results in a periodic variation of X-ray flux for a given line of sight. The shape of the pulse profile, which is the light curve folded on the neutron star rotation period, is directly affected by the accretion geometry (see Section 1.5.1 for description). Therefore, the study of pulse profiles and their evolution can be exploited to probe the amount of angular momentum that is accreted onto the surface of the neutron star and converted into spin-up and spin-down torques (see e.g. Fürst, 2011, and references therein).

In the simplest geometry when the luminosity is far below the critical value, which is described by the pencil-beam emission when only one magnetic pole is visible, the pulse profile appears to be quasi-sinusoidal with one-peak per orbital phase (Nelson et al., 1993; Becker et al., 2012). The fraction of the pulsed emission in comparison to the total flux determines the flux of the trough. More common, however, is a pulse profile that consists of two peaks where the X-ray emission from the accretion columns over both poles can be studied (White et al., 1983). A proper theoretical treatment involves the consideration of gravitational light bending, halos and asymmetries in the magnetic field (Kraus et al., 1995, 2003). Since the study of pulse profiles and their evolution is beyond the scope of this thesis, I refer the reader to Kraus et al. (1995, 2003) for a proper treatment.

Finally, I note that no pulsation period is found in some HMXBs that are highly

likely to host neutron stars. The physical mechanisms and geometries that have been proposed to describe the absence of a pulsation period include the following: co-alignment of the magnetic and spin axes of the neutron star (e.g. Bodaghee et al., 2010), the accretion beam points in our direction and the presence of a weak magnetic field. These are discussed in Section 4.5.3 in application to my study of 4U 1210-64.

### **1.6.2 Orbital Period**

HMXBs typically show modulations on the orbital period of the binary. Variability on orbital periods is attributed to a large variety of binary properties including eclipses and eccentric orbits.

Of the hundreds of X-ray binaries found so far (Chaty, 2011, 2013), the orbital inclination is sufficiently large for the mass donor to occult the compact object along our line of sight in only a handful of systems. This phenomenon results in X-ray eclipses, where several physical and geometric properties of the system can be constrained. These properties include the mass and radius of the donor star, the mass of the compact object, and the accretion mechanism itself. The study of these properties is made possible through the exploitation of the eclipse duration, which is dependent on the radius of the mass donor, inclination angle of the system and the orbital separation of the components (see Figure 1.8). Additionally, eclipse measurements can also be exploited as timing markers to determine the orbital period changes of HMXBs where effects such as tidal interactions and rapid mass transfer can be studied (e.g. van der Klis & Bonnet-Bidaud, 1984; Levine et al., 2000). In their recent survey on ten eclipsing HMXBs, Falanga et al. (2015) note that such measurements can also be used to probe the apsidal motion in eccentric systems

such as Vela X-1 and 4U 1538-522.

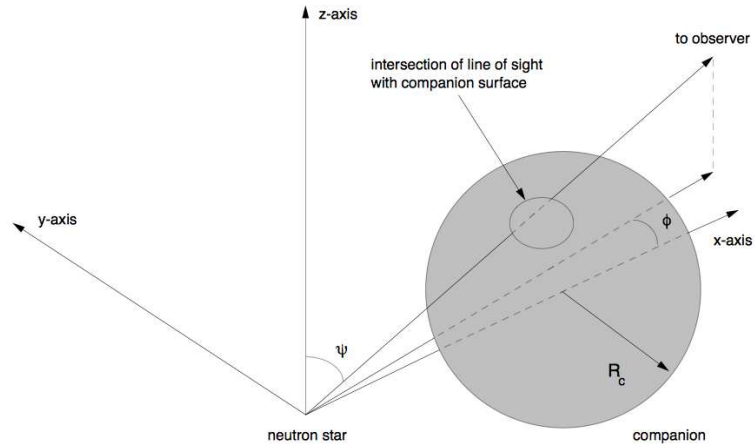


FIG. 1.8. This is a depiction of the eclipse geometry where the neutron star is at the origin and donor star is some distance,  $R$ , away. The eclipse duration depends on the orbital separation between the compact object and mass donor, radius of the donor, inclination of the orbit (Chakrabarty, 1996).

I also discuss orbital modulation due to eccentric orbits, which is an effect primarily seen in BeXBs. In a BeXB, the primary mode of mass transfer is referred to as “Type I” outbursts when the compact object passes through the circumstellar decretion disc of the mass donor during periastron. While BeXBs spend the majority of time in low X-ray luminosity states, the X-ray luminosity during periastron is on the order of  $10^{36}$ – $10^{37}$  erg  $s^{-1}$  (Reig, 2011; Chaty, 2011).

### 1.6.3 Corbet Diagram

The interaction between the rotating neutron star and the accreted matter can be expressed in terms of the Corbet diagram (see Figure 1.9), which illustrates the relationship between the orbital period and neutron star spin periods of HMXBs (Corbet, 1984, 1986). The different types of accretion mechanisms populate different regions on the Corbet di-

agram where correlations or anti-correlations between the orbital period and neutron star rotation period are seen. Disk-fed SGXBs, the neutron star rotation period is on the order of  $\sim 1\text{--}10$  s, which shows an anti-correlation with the orbital period, typically  $\sim 1\text{--}3$  d (Corbet, 1986). This can be attributed to the large intrinsic angular momentum present in the accretion disk, which must be conserved when the accreted matter impacts the surface of the neutron star. Angular momentum is transferred to the spin rate of the neutron star. There are currently three confirmed SGXBs that persistently accrete via Roche-lobe overflow. No correlation or anti-correlation is seen in the relationship between the spin period and orbital period in wind-fed SGXBs. This could be attributed to an insufficient amount of angular momentum is presented in the stellar wind. BeXBs show a correlation between the neutron star rotation period and orbital period of the binary (Corbet, 1984). Since the amount of accreted matter depends on orbital period, this could be attributed to the spin-equilibrium of the neutron star (Corbet, 1986).

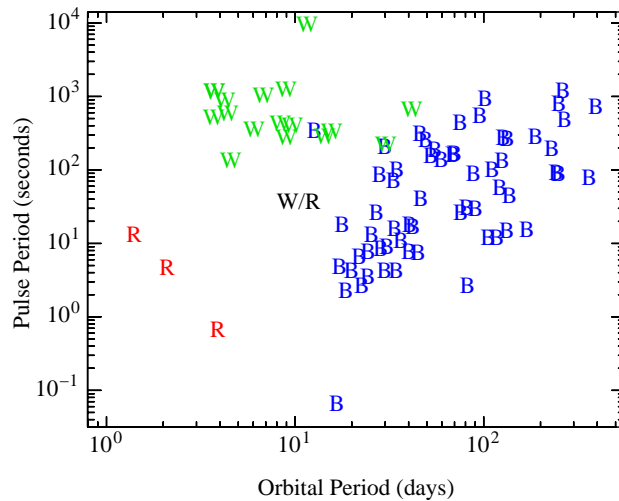


FIG. 1.9. The  $P_{orb}/P_{spin}$  diagram (Corbet's diagram) comparing the orbital period of HMXB with their classification (Corbet, 1986).

#### 1.6.4 Superorbital periodic and aperiodic variability

Modulation on timescales longer than the orbital period is seen in X-ray binaries of a variety of subtypes. First revealed in the 1970s, superorbital variability was first found in systems where the donor star overfills the Roche lobe (e.g. Her X-1, Petterson, 1977). The timescale for such long-term variations is on the order of tens of days to several years in the case of BeXBs, where changes in physical and geometric binary properties can be probed over long timescales (Rajoelimanana et al., 2011; Corbet & Krimm, 2013). The stability of superorbital periods has been found to range from steady in the cases of LMC X-4 and Her X-1, to evolving in a systematic way (e.g. SMC X-1, Clarkson et al., 2003; Trowbridge et al., 2007; Kotze & Charles, 2012) to chaotic as seen in the LMXB Cyg X-2 (Boyd & Smale, 2004). While the physical mechanisms responsible for long-term variability are poorly understood, the origin could be linked to accretion disc properties in the case of Roche-lobe overflow systems, changes in  $\dot{M}$  and/or changes in the donor star. I discuss superorbital variability and the possible mechanisms in the context of each subtype of HMXB below.

Since superorbital variability was first found in Roche-lobe overflow systems, I first discuss its origin in disk-fed SGXBs. As discussed in Section 1.5.2, the accreted material forms an accretion disc around the compact object due to a large specific angular momentum. The radiation from the central source non-uniformly illuminates the accretion disc, which in turn can induce twists and warps that obscure the compact object on timescales comparable to observed superorbital periods (Pringle, 1996; Ogilvie & Dubus, 2001). In the case that the accretion disc is optically thick, an uneven distribution of forces induces

a torque that can change the angular momentum of the disc (Ogilvie & Dubus, 2001). In addition to disc precession, the precession of the neutron star itself can also lead to superorbital periods (e.g. Her X-1; Postnov et al., 2013).

I also consider the origin of superorbital variability in BeXBs. Changes in the decretion disc, particularly its formation and dissipation, as well as the one-arm oscillation are mechanisms that could explain superorbital activity (Reig et al., 2010; Rajoelimanana et al., 2011). These properties have been explored at optical wavelengths (Rajoelimanana et al., 2011). In their study of the Small Magellanic Cloud (SMC), Rajoelimanana et al. (2011) found an apparent correlation between the orbital and superorbital periods in BeXBs as well as variations in the amplitude of the modulation. A  $\sim 1667$  d superorbital period was also found in the gamma-ray binary LS I+61° 303, which hosts a B0 Ve donor star (Li et al., 2014).

I finally discuss highly coherent superorbital variability, which was also found in at least five wind-fed SGXBs (Farrell et al., 2008; Corbet & Krimm, 2013; Drave et al., 2013b). Compared to superorbital variability seen in Roche-lobe overflow systems and BeXBs, the mechanism responsible for the long timescale modulation in wind-fed SGXBs has so far proven elusive. Corbet & Krimm (2013) show a monotonic correlation between the orbital and superorbital periods of these binaries. While superorbital variability was seen in at least five SGXBs, the long-term variability is not ubiquitous (Corbet & Krimm, 2013). Stable accretion disks are also expected to be absent in wind-fed SGXBs because of the low angular momentum of material accreted by the wind mechanism.

## 1.7 Spectral Properties of X-ray Binaries

### 1.7.1 Emission Mechanisms in High Mass X-ray Binaries

The typical continuum spectra for HMXBs that host neutron stars can be described by a power law with photon index  $\Gamma$  that is modified by a high-energy cutoff at energies 10–20 keV (White et al., 1983). X-ray photons that are emitted in the soft energy bandpass (up to 3 keV) have an origin that can be traced to blackbody radiation (Hickox et al., 2004), bremsstrahlung and/or cyclotron radiation (Becker & Wolff, 2005).

I first describe blackbody radiation that originates in neutron star hot spots, thermal mounds of accreted material that form at the surface of the neutron star. These hot spots, from which blackbody radiation is emitted (Hickox et al., 2004), have a surface area that is dependent on the X-ray luminosity, the spin period of the neutron star, and the distance between the Alfvén radius and the equator of the magnetic field (White et al., 1983; Bartlett et al., 2013). At luminosities exceeding  $10^{35}$  erg s<sup>-1</sup>, the surface area of the hot spot is inversely proportional to the square root of the X-ray luminosity. Conversely, the hot spot surface area increases with increasing luminosity when  $L_X$  is less than  $10^{35}$  erg s<sup>-1</sup>. This can be expressed as proportional to  $L_X^{2/7}$ . At energies  $\sim 1$  keV (Hickox et al., 2004), part of the X-ray photons emitted by the thermal mound propagate in a trajectory that is parallel to the magnetic field lines and contribute to the “pencil beam” geometry described in Section 1.5.1. I note that blackbody radiation can also originate at the inner radius of the accretion disc in systems primarily powered by Roche-lobe overflow. In this case, the blackbody emission could be a consequence of the reprocessing of hard X-rays (Hickox et al., 2004).

I also describe bremsstrahlung radiation that originates in the accretion column itself, which is strongly ionized. Free-free emission or bremsstrahlung<sup>6</sup> radiation is the consequence of a charge accelerating in the Coulomb field of another charge (Rybicki & Lightman, 1986). Since the bremsstrahlung produced by the collision of like charge particles in the dipole approximation is zero, it is customary to consider particles of opposite charge such as electron-ion pairs. In the context of NS-HMXBs, X-ray photons produced via bremsstrahlung originate through the interaction between the electrons and ions in the plasma (White et al., 1983; Becker & Wolff, 2005; Becker et al., 2012).

Another source of soft X-ray photons that originate in the accretion column is cyclotron radiation, which is electromagnetic radiation emitted from the interaction between a charged particle and a magnetic field. Since the Lorentz force due to the magnetic field is perpendicular to both the motion of the charged particle and the magnetic field itself, the particle is accelerated resulting in dipole emission (Rybicki & Lightman, 1986). In the context of NS-HMXBs, quantum electrodynamics is necessary to describe the motion of charged particles (Araya-Góchez & Harding, 2000).

The above mechanisms describe different sources of X-ray emission that produce X-ray photons with energies below 3 keV (Becker & Wolff, 2005, 2007). Hard X-ray photons are produced when these seed photons are upscattered to higher energies via inverse Compton scattering that leads to further broadening of the spectrum.

## **1.7.2 The Continuum Spectrum in High Mass X-ray Binaries**

The broadening in the continuum spectrum described in Section 1.7.1 can be at-

---

<sup>6</sup>Bremsstrahlung is German for braking radiation.

tributed to “bulk” and “thermal” Comptonization, which are found to be dominant in different regimes. “Bulk” Comptonization is significant when kinetic energy is converted to the photons by scatterings across the shock (Becker & Wolff, 2007). Here the continuum can be fit using a power law with a soft photon index and no high-energy cutoff. However, second order Fermi-acceleration, which manifests itself in “thermal” Comptonization, is important in bright sources where the temperature of the accretion column exceeds  $10^7$  K (Becker & Wolff, 2007). The resulting spectrum is described by a flat photon index and a high energy cutoff (Becker & Wolff, 2007).

The components of the observed X-ray spectra seen in NS-HMXBs include Comptonized blackbody radiation, Comptonized cyclotron emission and Comptonized bremsstrahlung. Among these processes, Comptonized bremsstrahlung is the dominant emission mechanism (Becker & Wolff, 2007). In BeXBs, the photon index and high-energy cutoff are found to range from 0.6–1.4 and 10–30 keV, respectively (Haberl et al., 2008; Lutovinov et al., 2005; Reig, 2011). The spectral continuum in SGXBs can be described as a power law with a hard spectral index and high-energy cutoff in the range of 10–20 keV (White et al., 1983).

### **1.7.3 Spectral Modifications**

In many XRBs, a spectral model consisting of only continuum parameters described above gives a naive and often poor interpretation of what is observed. X-ray photons interact with material both between the emitter and observer and that intrinsic to the source itself via absorption and scattering. This results in spectral modifications such as photoelectric absorption and fluorescence due to material that must be properly taken into

account to achieve a description of XRBs. Prior to the launch of *INTEGRAL*, many obscured SGXBs and SFXTs eluded detection due to their large intrinsic column densities, which are on the order of  $10^{23}$  atoms  $\text{cm}^{-2}$  (see Section 1.5.3). Additional spectral modifications arise due to the interaction between Comptonized X-ray photons and the extreme magnetic field in the accretion column.

Photoelectric absorption, where X-ray photons are absorbed by atoms, is one of the most important physical mechanisms that result in modifications to the above continuum spectrum. The energy from the photon is transferred to an electron, which results in excitation or ionization. This is dependent on the cross section of the photon, which describes the probability that it is absorbed by an atom. As a first approximation, the cross section of the photon follows an inverse-cube law with respect to its energy (Pradhan & Nahar, 2011), indicating that material is more transparent to higher-energy photons. However, it should be noted that absorption edges such as the 7.1 keV Fe  $K\alpha$  edge can result due to the ionization of electrons from lower shells.

Emission lines due to fluorescence<sup>7</sup> also allow the study of material intrinsic to X-ray binaries. A vacancy in an inner atomic shell results when an electron in the K shell absorbs a photon and the atom is subsequently ionized, resulting in an unstable state. The unstable ion decays when an electron from a higher state (e.g. L or M shells) fills the gap, which results in the emission of a photon. Similar to photoelectric absorption described above, the properties of the accreted material itself can be probed using fluorescence. In Sections 3.4.4.1 and 3.5.5.1, I present and discuss the presence of Fe  $K\alpha$ , Fe XXV  $K\alpha$  and Fe XXVI  $K\alpha$  in 4U 1210-64. In this work, I describe that the Fe XXV  $K\alpha$  and

---

<sup>7</sup>The Fe  $K\alpha$  and Fe  $K\beta$  emission lines at 6.4 keV and 7.1 keV are important to X-ray astronomy.

Fe XXVI  $K\alpha$  lines, which originate far from the compact object, could be attributed to photoionization.

Comptonized cyclotron radiation also modifies the observed continuum spectrum described in Section 1.7.2. In this context, the magnetic field influences the interaction cross section of the electrons, which results in a quantization of their kinetic energy perpendicular to the magnetic field (Rybicki & Lightman, 1986; Araya-Góchez & Harding, 2000). This quantization influences the cyclotron radiation where it is emitted when electrons undergo transitions from one level to another similar to transitions found in atomic and ionic species. These transitions are seen in absorption-like Cyclotron Resonant Scattering Resonant Features and were found in several XRBs between  $\sim 10$  keV and 100 keV (e.g. Her X-1; 4U 1907+09; Vela X-1, Staubert et al., 2014; Maitra & Paul, 2013; Wang, 2014).

## 1.8 Gamma-ray Binaries

Gamma-ray binaries are high-energy binaries where most of the radiative emission is seen in the MeV-TeV energy range. Gamma-ray emission is modulated on the orbital phase and might represent an early stage in the evolutionary lifetime of an HMXB (Meurs & van den Heuvel, 1989; Dubus, 2006). Emitting photons on the order of GeV to TeV, gamma-ray binaries are observed to be far less common than X-ray binaries. The relative paucity of known gamma-ray binaries is largely attributed to the short lifetime of a gamma-ray binary and the fact that most of the emission is observed in the GeV/TeV bandpasses, which is less accessible for study than optical or X-ray emission. Since both

accreting neutron stars and black holes peak in the X-ray part of the electromagnetic spectrum, thermal mechanisms cannot be responsible for the emission of high energy gamma rays (Carroll & Ostlie, 2006).

### **1.8.1 Particle Acceleration Mechanisms in Gamma-ray Binaries**

Gamma-ray binaries can form when the wind from a young pulsar injects relativistic particles in the surrounding environment (Takahashi et al., 2009). Non-thermal relativistic particles in the shocked pulsar wind of the binary companion acquire a large stable input of energy by the pulsar's spin-down torque (Takahashi et al., 2009). Inverse Compton scattering between the relativistic particles and the pulsar wind on stellar photons produces emission in the GeV as well as the TeV region of the gamma ray spectrum, creating a gamma ray binary (Takahashi et al., 2009).

An alternative particle acceleration mechanism that results in the production of gamma-rays is seen in microquasars (Dubus et al., 2010). At a distance of approximately 7 kpc, the microquasar Cygnus X-3 is likely to consist of a stellar mass black hole and a Wolf-Rayet companion with an orbital period of 4.8 hours (Hill et al., 2011). Since the inclination of the orbit has to be firmly characterized, the true nature of the compact object is uncertain (Zdziarski et al., 2012). The optical radial velocity semi-amplitude reveals that the compact object could be a black hole with an approximate mass of  $20 M_{\odot}$  in the case of low orbital inclinations. Large orbital inclinations, on the other hand, imply that the compact object is a neutron star with a mass near the Chandrasekhar limit (Zdziarski et al., 2012). This is further complicated due to scattering processes in the wind of the WR star (Dubus et al., 2010). The mass loss rate in a Wolf-Rayet star is on the order of

$10^{-5} M_{\odot}$  a year; in contrast to the Sun, which loses  $10^{-14} M_{\odot}$  a year (Dubus et al., 2010).

The wind velocity is on the order of  $1000 \text{ km s}^{-1}$  (Dubus et al., 2010).

### 1.8.2 Variability in Gamma-ray Binaries

Similar to XRBs, gamma-ray binaries show variability on a variety of different timescales. Radio pulsations at 47.8 ms were found in PSR B1259-63 (Aharonian et al., 2005; Johnston et al., 1994), which is powered by the pulsar-wind mechanism. Geometrical effects where the epoch of maximum flux occurs when the compact object is at superior conjunction and the orbital phase dependence of the seed photon density responsible for inverse Compton emission in an eccentric orbit are different mechanisms that could lead to orbital modulation in a gamma-ray binary. These will be further discussed in Section 4.5.1.

Gamma-ray binaries powered by the pulsar-wind mechanism are non-accreting sources and are typically described in the X-ray regime by a power law where the photon index is generally softer than that observed in accretion-powered sources (e.g. LS 5039, Takahashi et al., 2009), which transitions to a power law modified by a high-energy cutoff or broken power law in the gamma-ray bandpass. The break in the gamma-ray spectrum could be a consequence of the cooling times of synchrotron and inverse-Compton emission, which are both inversely proportional to the Lorentz factor.

I first describe synchrotron radiation that can originate in both microquasars as well as gamma-ray binaries powered by the pulsar wind mechanism. The synchrotron power emitted by a single electron is dependent on the Thomson cross section, velocity of the electrons, Lorentz boost factor and energy density stored in the magnetic field (Equation

6.7b, Rybicki & Lightman, 1986). In the context of microquasars, synchrotron emission arises in the relativistic jets, which is typically observed in the radio bandpass. However, synchrotron emission has been studied in detail in the X-ray bandpass in pulsar-wind candidates (LS I+61° 303, LS 5039, 1FGL J1018.6-5856; Esposito et al., 2007; Takahashi et al., 2009; An et al., 2015). This could be attributed to the interaction between the electrons and the magnetic field of the compact object, suspected to be a rotationally powered pulsars.

As described in Section 1.7.2 in the context of high-mass X-ray binaries, inverse Compton scattering is a significant production mechanism in the gamma-ray regime. In the Thomson scattering regime, the power emitted via inverse Compton scattering is similar to that of synchrotron radiation where the photon energy density replaces the magnetic field density (Equation 7.17, Rybicki & Lightman, 1986). Gamma-ray emission could result when UV photons collide with charged particles in the shock due to the pulsar wind and stellar wind inverse Compton scatter to GeV and TeV gamma-ray energies (Mirabel, 2012). If this is the case, the maximum gamma-ray emission would be expected to occur at superior conjunction, where the compact object is on the far side of the companion (Mirabel, 2012). It is possible that the seed density is modulated on the orbital period in eccentric systems, which could lead to spectral and temporal variations that can be monitored. In the TeV regime, it is thought that the same population of electrons that emit in the X-ray bandpass via synchrotron emission contribute to the population that interacts via inverse Compton emission. While some sort of correlation in flux or power-law index might be expected in this case, it should be noted that Klein-Nishina effects can modify the photon index in the TeV energies. I discuss this in context with 1FGL J1018.6-5856

in Section 4.5.3.

## 1.9 Thesis Organization

This thesis describes the use of long-term monitoring along with pointed observations of HMXBs and their gamma-ray precursors and shows how each provides key insights in the temporal and spectral properties of these systems.

Chapter 2 reports on long-term *Swift* BAT observations of the eclipsing wind-fed SGXBs IGR J16393-4643, IGR J16418-4532, IGR J16479-4514, IGR J18027-2016 and XTE J1855-026 for which I am the primary author (Coley et al., 2015). In this study, I constrained the physical parameters of the mass donor, refined the orbital periods and improved on the time of mid-eclipse for each XRB in this sample using eclipse measurements. The spectral types that satisfy these constraints in IGR J16393-4643 could be recognized in spectral types B0 V, and B0-5 III. In IGR J16418-4532 and IGR J16479-4514 the previously proposed mass donors were found to overfill the Roche lobe; however, spectral types O7.5 I and earlier satisfy the constraints of the eclipse half-angle and the Roche lobe. The mass donor spectral types in the “double-lined” binaries IGR J18027-2016 and XTE J1855-026 were found to be consistent with the eclipse half-angle and Roche-lobe size. The neutron star masses are also constrained in these systems.

Chapter 3 presents a detailed temporal and spectral analysis of the HMXB 4U 1210-64 using *Suzaku*, the *ISS* Monitor of All-sky X-ray Image (MAXI), the *Swift* Burst Alert Telescope (BAT) and the *Rossi X-ray Timing Explorer* Proportional Counter Array (PCA) and All Sky Monitor (ASM) for which I am the primary author (Coley et al., 2014).

It should be noted that the extraction of the PCA data was carried out by Koji Mukai (UMBC/CRESST). 4U 1210-64 is an HMXB that has been postulated to be powered by the Be mechanism and the mass donor was previously proposed to be a B5V. Using long-term ASM and MAXI observations, distinct high and low states were found, which are suggestive of a variable accretion rate. While I considered several possibilities to explain the variability seen in the state transitions, no mechanism considered in my analysis appeared to be consistent with 4U 1210-64. The ASM and MAXI data also reveal an orbital period of  $6.7101 \pm 0.0005$  d as well as a sharp dip in the folded light curve, which was interpreted as an eclipse. To determine the nature of the mass donor, the predicted eclipse half-angle was calculated as a function of inclination angle for several stellar spectral types. The eclipse half-angle was found to be inconsistent with a mass donor of spectral type B5 V; however, stars with spectral types B0 V or B0-5 III are possible. Emission lines at 2.62, 6.41, 6.7 and 6.97 keV were all clearly detected in the *Suzaku* spectra, which were interpreted as S XVI  $K\alpha$ , Fe  $K\alpha$ , Fe XXV  $K\alpha$  and Fe XXVI  $K\alpha$ , respectively. While the spectral features strongly contrast with those typically seen in BHCs and CVs, no sign of pulsations or cyclotron features that would prove the compact object is a neutron star were found.

Chapter 4 focuses on my preliminary analysis on the gamma-ray binary 1FGL J1018.6-5856 using *Fermi* Large Area Telescope (LAT), *Swift* X-ray Telescope (XRT) and the Australia Telescope Compact Array (ATCA). It should be noted that the primary extraction of the ATCA radio data was conducted by Philip Edwards and Jamie Stevens (CSIRO Astronomy and Space Science). 1FGL J1018.6-5856, the first Gamma-ray binary discovered by *Fermi* LAT, consists of a O6 V((f)) star and suspected rapidly spinning pul-

sar, which is possibly powered by the interaction between the relativistic pulsar wind and the stellar wind of the companion. A microquasar scenario where the compact object is a black hole cannot be ruled out. No long-term flux variability was found in the *Fermi* gamma-ray light curve. Quasi-sinusoidal behavior was found in the *Fermi* LAT folded light curve where I define phase zero as the epoch of maximum flux. Another peak was also found at binary orbital phase  $\sim 0.3$  in the *Swift* X-ray Telescope (XRT) and *Australia Telescope Compact Array* (ATCA) folded light curves. It should be noted that the only maximum in the radio data is the peak at orbital phase  $\sim 0.3$ .

Chapter 5 presents a discussion of the results and outlines the conclusions of each section, respectively. The direction for future research is additionally outlined in Chapter 5. The instrumentation and methods used in this study are presented in the Appendices A and B.

## Chapter 2

# PROBING THE MASSES AND RADII OF DONOR STARS IN ECLIPSING X-RAY BINARIES WITH THE SWIFT BURST ALERT TELESCOPE

### 2.1 Overview

Physical parameters of both the mass donor and compact object can be constrained in X-ray binaries with well-defined eclipses, as my survey of wind-fed supergiant X-ray binaries (SGXBs) IGR J16393-4643, IGR J16418-4532, IGR J16479-4514, IGR J18027-2016 and XTE J1855-026 reveals. Using the orbital period and Kepler's third law, I express the eclipse half-angle in terms of radius, inclination angle and the sum of the masses. Pulse-timing and radial velocity curves can give masses of both the donor and compact object as in the case of the "double-lined" binaries IGR J18027-2016 and XTE J1855-026. The eclipse half angles are  $15_{-2}^{+3}$ ,  $31.7_{-0.8}^{+0.7}$ ,  $32 \pm 2$ ,  $34 \pm 2$  and  $33.6 \pm 0.7$  degrees for IGR J16393-4643, IGR J16418-4532, IGR J16479-4514, IGR J18027-2016 and XTE 1855-026, respectively. In wind-fed systems, the condition that the primary not exceeding the Roche-lobe size provides an upper limit on system parameters. In IGR J16393-4643,

spectral types of B0 V or B0-5 III are found to be consistent with the eclipse duration and Roche lobe, but the previously proposed donor stars in IGR J16418-4532 and IGR J16479-4514 were found to be inconsistent with the Roche-lobe size. Stars with spectral types O7.5 I and earlier are possible. For IGR J18027-2016, the mass and radius of the donor star lie between  $18.6\text{--}19.4 M_{\odot}$  and  $17.4\text{--}19.5 R_{\odot}$ . I constrain the neutron star mass between  $1.37\text{--}1.43 M_{\odot}$ . I find the mass and radius of the donor star in XTE J1855-026 to lie between  $19.6\text{--}20.2 M_{\odot}$  and  $21.5\text{--}23.0 R_{\odot}$ . The neutron star mass was constrained to  $1.77\text{--}1.82 M_{\odot}$ . Eclipse profiles are asymmetric in IGR J18027-2016 and XTE J1855-026, which I attribute to accretion wakes.

## 2.2 Introduction

High-Mass X-ray Binaries (HMXBs) are relatively young systems, which consist of a compact object (neutron star or black hole) and an early-type OB star orbiting the common center of mass. First discovered in the 1970s, HMXBs are split into two individual classes—Be X-ray binaries (BeXBs) and supergiant X-ray binaries (SGXBs). BeXBs are transient systems where the compact object is in a wide, typically eccentric, orbit ( $P \gtrsim 10$  days) around a rapidly rotating non-supergiant B-type star. The primary mode of mass transfer occurs when the compact object passes through the circumstellar decretion disc of the mass donor. In SGXBs, the compact object is in a short ( $\sim 1\text{--}42$  day) orbit around an OB-supergiant where the accretion mechanism is either via the powerful stellar wind and/or Roche-lobe overflow. While the eccentricity in most SGXBs with short orbital periods is near zero, some SGXBs host compact objects in highly eccentric orbits

(e.g. GX 301-2 Islam & Paul, 2014). In wind-accretors, the X-ray luminosity is on the order of  $10^{35}$ – $10^{36}$  erg s<sup>-1</sup>. However, a much higher luminosity is found in systems where the donor fills its Roche lobe,  $\sim 10^{38}$  erg s<sup>-1</sup> (Kaper et al., 2004).

Many HMXBs host a neutron star where modulation is often seen at its rotation period. The mass of the neutron star can be constrained in eclipsing X-ray pulsars, which can lead to an improved understanding of the neutron star Equation of State (Mason et al., 2011, and references therein). Currently, the neutron star mass has been constrained in 10 XRBs where the lower limit for each object corresponds to edge-on orbital inclinations and the upper limit is calculated when the donor star just fills its Roche lobe. While over 100 Equations of State have been proposed (Kaper et al., 2006), only one model is physically correct (Mason et al., 2010, 2011).

The mass ratio between the neutron star and donor star is equal to the ratio between the semi-amplitude of the radial velocities of the donor star,  $K_O$ , and the neutron star,  $K_X$ . Throughout the paper, I use a definition of mass ratio,  $q$ , as the ratio of the compact object mass to that of the donor star mass (Joss & Rappaport, 1984). The orbital period of the binary,  $P$ , and  $K_X$  can be calculated using pulse-timing analysis (Val Baker et al., 2005, and references therein), which is analogous to measuring the Doppler shift of spectral lines in the optical and/or near-infrared (Joss & Rappaport, 1984). The projected semi-major axis can be determined from the semi-amplitude of the radial velocity of the neutron star. The semi-amplitude of the radial velocity of the donor star can be determined using optical and/or near-infrared spectroscopic information.

Eclipse measurements can also be exploited as timing markers to determine the binary orbital evolution of HMXBs. A significant orbital period derivative,  $\dot{P}_{orb}$ , was

previously found in several eclipsing HMXBs (e.g 4U 1700-377; SMC X-1; Cen X-3; LMC X-4 and OAO 1657-415, Rubin et al., 1996; Raichur & Paul, 2010; Falanga et al., 2015) and can be used to investigate the orbital evolution over long periods of time. While several contending theories to explain the orbital decay have been investigated, the most probable explanations involve tidal interaction and rapid mass transfer between the components of the binary systems (Falanga et al., 2015, and references therein).

The *Swift* Burst Alert Telescope (BAT), sensitive to X-rays in the 15–150 keV band (Barthelmy et al., 2005), provides an excellent way to study highly absorbed SGXBs. The large absorption found in these systems is problematic for instruments such as the *Rossi X-ray Timing Explorer (RXTE)* All Sky Monitor (ASM), which operated in the 1.5–12 keV band (Levine et al., 2011). The sensitivity to higher energy X-rays allows *Swift*-BAT to peer through this absorption (Corbet & Krimm, 2013, and references therein).

I present here constraints on the mass and radius of the donor star in eclipsing XRBs. The probability of an eclipse in a supergiant XRB with an orbital period less than 20 d can be expressed in terms of the orbital period, mass of the donor star, and radius of the donor star (Equation 1; Ray & Chakrabarty, 2002). The probability of an eclipse in long-period XRBs is low. Using a literature search, I determined HXMB systems where BAT observations can significantly improve the properties of the stellar components and orbital evolution of the systems using eclipsing properties. Five eclipsing XRBs were identified: IGR J16393-4643, IGR J16418-4532, IGR J16479-4514, IGR J18027-2016 and XTE J1855-026, which are all highly obscured SGXBs. I note while the masses of both the donor and compact object had previously been constrained in IGR J18027-2016, the error on the eclipse half-angle was large at  $4.5^\circ$  (Hill et al., 2005). The error

estimates concerning the radius and mass of the donor star are significantly improved in this analysis.

This chapter is structured in the following order: *Swift* BAT observations and the description of the eclipse model are presented in Section 2.2; Section 2.3 focuses on individual sources that are known to be eclipsing. Section 2.4 presents a discussion of the results and the conclusions are outlined in Section 2.5. If not stated otherwise, the uncertainties and limits presented in this chapter are at the  $1\sigma$  confidence level.

## 2.3 Data Analysis and Modelling

### 2.3.1 Swift BAT

The BAT on board the *Swift* spacecraft is a hard X-ray telescope operating in the 15–150 keV energy band (Barthelmy et al., 2005). For more information, see Appendix A.4.2.1.

I analyzed BAT data obtained during the time period MJD 53416–56745 (2005 February 15–2014 March 29). Light curves were retrieved using the extraction of the BAT transient monitor data available on the NASA GSFC HEASARC website<sup>1</sup> (Krimm et al., 2013), which includes orbital and daily-averaged light curves. I used the orbital light curves in the 15–50 keV energy band in my analysis, which have typical exposures of  $\sim 6$  min (see Section 2.4). The short exposures, which are somewhat less than typical *Swift* pointing times ( $\sim 20$  min), can arise due to the observing plan of *Swift* itself where BAT is primarily tasked to observe gamma-ray bursts (Krimm et al., 2013).

---

<sup>1</sup><http://heasarc.gsfc.nasa.gov/docs/swift/results/transients/>

The light curves were further screened to exclude bad quality points. I only considered data where the data quality flag (“DATA\_FLAG”) was set to 0. Data flagged as “good” are sometimes suspect, where a small number of data points with very low fluxes and implausibly small uncertainties were found (Corbet & Krimm, 2013). These points are likely the result of extremely short exposure times and were removed from the light curves. I corrected the photon arrival times to the solar system barycenter. I used the scripts made available on the Ohio State Astronomy webpage<sup>2</sup> In this paper, the barycenter-corrected times are referred to as Barycenter Modified Julian Date (BMJD).

I initially derived the orbital period for each XRB in this sample using Discrete Fourier Transforms (DFTs) of the light curves to search for periodicities in the data. I weighted the contribution of each data point to the power spectrum by its uncertainty, using the “semi-weighting” technique (Corbet et al., 2007a; Corbet & Krimm, 2013), where the error bars on each data point and the excess variability of the light curve are taken into account (see Appendix B.1.1 for additional information). I derived uncertainties on the orbital periods using the expression given in Horne & Baliunas (1986).

### **2.3.2 Eclipse Modeling**

I initially modeled the eclipses using a symmetric “step and ramp” function (see Table 2.1) where the intensities are assumed to remain constant before ingress, during eclipse and after egress and follow a linear trend during the ingress and egress transitions, which reveal the stellar wind structure of the mass donor (see Section 2.5.3). The count rates before ingress, during eclipse and after egress were each considered to be free

---

<sup>2</sup><http://astroutils.astronomy.ohio-state.edu/time/>.

parameters and were fit as follows:  $C_{\text{ing}}$  was fit from binary phase  $\phi = -0.2$  to the start of ingress,  $C_{\text{ecl}}$  was fit during eclipse and  $C_{\text{eg}}$  was fit from the end of egress to phase  $\phi = 0.2$  (see Equation 2.1). While I find the eclipse profiles of IGR J16393-4643, IGR J16418-4532 and IGR J16479-4514 to be symmetric within errors, the profiles show some asymmetry in the cases of IGR J18027-2016 and XTE J1855-026. I note that a symmetric “step and ramp” function could lead to systematic errors and I therefore fit the eclipse profiles using an asymmetric “step and ramp” function (see Equation 2.1 and Table 2.2). The parameters in this model are as follows: the phases corresponding to the start of ingress and start of egress,  $\phi_{\text{ing}}$  and  $\phi_{\text{egr}}$ , the duration of ingress,  $\Delta\phi_{\text{ing}}$ , the duration of egress,  $\Delta\phi_{\text{eg}}$ , the pre-ingress count rate,  $C_{\text{ing}}$ , the post-egress count rate,  $C_{\text{eg}}$ , and the count rate during eclipse,  $C_{\text{ecl}}$ . The eclipse duration and mid-eclipse phase are calculated using Equations 2.2 and 2.3, respectively.

$$(2.1) \quad C = \begin{cases} C_{\text{ing}}, & -0.2 \leq \phi \leq \phi_{\text{ing}} \\ \left(\frac{C_{\text{ecl}} - C_{\text{ing}}}{\Delta\phi_{\text{ing}}}\right)(\phi - \phi_{\text{ing}}) + C_{\text{ing}}, & \phi_{\text{ing}} \leq \phi \leq \phi_{\text{ing}} + \Delta\phi_{\text{ing}} \\ C_{\text{ecl}}, & \phi_{\text{ing}} + \Delta\phi_{\text{ing}} \leq \phi \leq \phi_{\text{egr}} \\ \left(\frac{C_{\text{egr}} - C_{\text{ecl}}}{\Delta\phi_{\text{eg}}}\right)(\phi - \phi_{\text{egr}}) + C_{\text{ecl}}, & \phi_{\text{egr}} \leq \phi \leq \phi_{\text{egr}} + \Delta\phi_{\text{eg}} \\ C_{\text{eg}}, & \phi_{\text{egr}} + \Delta\phi_{\text{eg}} \leq \phi \leq 0.2 \end{cases}$$

$$(2.2) \quad \Delta\phi_{\text{ecl}} = \phi_{\text{egr}} - (\phi_{\text{ing}} + \Delta\phi_{\text{ing}})$$

$$(2.3) \quad \phi_{\text{mid}} = \frac{1}{2}(\phi_{\text{egr}} + (\phi_{\text{ing}} + \Delta\phi_{\text{ing}}))$$

The eclipse duration, time of mid-eclipse, and eclipse half-angle ( $\Theta_e = \Delta\phi_{\text{ecl}} \times 180^\circ$ ) from fitting the BAT folded light curves for each source are reported in Tables 2.1– 2.3. For each source, I initially used an ephemeris based on my determination of the orbital period from the DFT and time of mid-eclipse. Using an ‘observed minus calculated’  $O - C$  analysis (see Figures 2.1–2.3), I refined the orbital periods and improved on the time of mid-eclipse for each XRB in the sample. I note that no eclipses are visible in the unfolded light curves and it is necessary to observe multiple cycles of folded light curves in order for eclipses to be seen. I divide the light curves into five equal time intervals ( $\sim 670$  days), with the exception of IGR J16393-4643 (see Section 2.4.1), and calculate the mid-eclipse epoch for each interval (see Table 2.4) In the cases of IGR J18027-2016 and XTE J1855-026, I combine the derived mid-eclipse times with those reported in the literature (Falanga et al., 2015, and references therein). I note that while mid-eclipse times were previously derived for both IGR J16393-4643 and IGR J16479-4514 (see Table 2.5), these were not used since no error estimate was reported (Islam et al., 2015; Bozzo et al., 2009). I then fit the mid-eclipse times using the orbital change function (see Equation 2.4) where  $n$  is the number of binary orbits given to the nearest integer,  $P_{\text{orb}}$  is the orbital period in days,  $\dot{P}_{\text{orb}}$  is the period derivative at  $T_0$ , and the error on the linear term is the orbital period error. In all five cases, I improve the error estimate on the orbital period by nearly an order of magnitude (see Section 2.4). I do not find a significant  $\dot{P}_{\text{orb}}$  for any source (see Tables 2.1– 2.3).

$$(2.4) \quad T_n = T_0 + nP_{\text{orb}} + \frac{1}{2}n^2P_{\text{orb}}\dot{P}_{\text{orb}}$$

X-ray binaries that are eclipsing have an eclipse duration that is only dependent on the radius of the mass donor, inclination angle of the system and the orbital separation

Model Parameter	IGR J16393-4643	IGR J16418-4532	IGR J16479-4514	IGR J18027-2016	XTE J1855-026
$\phi_{\text{ing}}$	$-0.079^{+0.006}_{-0.014}$	$-0.107 \pm 0.002$	$-0.114^{+0.003}_{-0.004}$	$-0.150^{+0.005}_{-0.003}$	$-0.131^{+0.001}_{-0.002}$
$\Delta\phi$	$0.040^{+0.009}_{-0.008}$	$0.019^{+0.002}_{-0.003}$	$0.029^{+0.003}_{-0.004}$	$0.053^{+0.004}_{-0.003}$	$0.038 \pm 0.002$
$C^a$	$1.27 \pm 0.04$	$1.18 \pm 0.05$	$1.05 \pm 0.06$	$1.59 \pm 0.06$	$2.64 \pm 0.06$
$\phi_{\text{egr}}$	$0.048^{+0.004}_{-0.005}$	$0.088^{+0.002}_{-0.001}$	$0.092^{+0.003}_{-0.004}$	$0.098^{+0.002}_{-0.004}$	$0.094 \pm 0.002$
$C_{\text{ecl}}^a$	$0.71 \pm 0.06$	$0.00 \pm 0.05$	$0.03 \pm 0.05$	$0.17 \pm 0.04$	$-0.04 \pm 0.05$
$\Delta\phi_{\text{ecl}}$	$0.09^{+0.01}_{-0.02}$	$0.175 \pm 0.003$	$0.177^{+0.005}_{-0.007}$	$0.196^{+0.007}_{-0.005}$	$0.187 \pm 0.003$
$P_{\text{orb}}^b$	$4.23794 \pm 0.00007$	$3.73880 \pm 0.00002$	$3.31965 \pm 0.00006$	$4.56999 \pm 0.00005$	$6.07410 \pm 0.00004$
$\dot{P}_{\text{orb}}^c$	$-5 \pm 4$	$0.7 \pm 1.0$	$3 \pm 2$	$-2 \pm 2$	$0.5 \pm 1.0$
$T_{\text{mid}}^d$	$55074.99^{+0.02}_{-0.04}$	$55087.714 \pm 0.006$	$55081.571^{+0.009}_{-0.012}$	$55083.79^{+0.02}_{-0.01}$	$55079.055^{+0.010}_{-0.009}$
$\Theta_e^e$	$16^{+2}_{-3}$	$31.5 \pm 0.6$	$31.9^{+0.9}_{-1.3}$	$35 \pm 1$	$33.6^{+0.6}_{-0.5}$
$\chi^2_{\nu}$ (dof)	$1.13(77)$	$0.84(77)$	$1.03(77)$	$0.93(77)$	$1.23(77)$

Table 2.1. Eclipse Model Parameters, Assuming a Symmetric Eclipse Profile

<sup>a</sup> Units are  $10^{-3}$  counts  $\text{cm}^{-2}$   $\text{s}^{-1}$ .

<sup>b</sup> Refined orbital periods using an  $O - C$  analysis. Units are days.

<sup>c</sup> The orbital period derivative at the 90% confidence interval found using an  $O - C$  analysis. Units are  $10^{-7}$   $\text{d}^{-1}$ .

<sup>d</sup> Units are Barycentered Modified Julian Day (BMJD). Phase 0 is defined as eclipse center.

<sup>e</sup> Units are degrees.

Model Parameter	IGR J16393-4643	IGR J16418-4532	IGR J16479-4514	IGR J18027-2016	XTE J1855-026
$\phi_{\text{ing}}$	$-0.092^{+0.008}_{-0.005}$	$-0.108 \pm 0.002$	$-0.118 \pm 0.003$	$-0.160 \pm 0.005$	$-0.136 \pm 0.002$
$\Delta\phi_{\text{ing}}$	$0.06 \pm 0.01$	$0.020 \pm 0.003$	$0.024 \pm 0.008$	$0.08 \pm 0.01$	$0.042 \pm 0.003$
$\Delta\phi_{\text{eg}}$	$0.039 \pm 0.006$	$0.014^{+0.003}_{-0.004}$	$0.026^{+0.007}_{-0.003}$	$0.018^{+0.005}_{-0.004}$	$0.038 \pm 0.003$
$C_{\text{ing}}^a$	$1.28 \pm 0.06$	$1.07^{+0.07}_{-0.06}$	$1.01 \pm 0.08$	$1.43 \pm 0.08$	$2.44 \pm 0.08$
$C_{\text{eg}}^a$	$1.26 \pm 0.06$	$1.22 \pm 0.07$	$1.04 \pm 0.08$	$1.67 \pm 0.08$	$2.79^{+0.09}_{-0.08}$
$\phi_{\text{egr}}$	$0.049^{+0.004}_{-0.006}$	$0.089 \pm 0.002$	$0.086 \pm 0.003$	$0.112 \pm 0.002$	$0.092^{+0.001}_{-0.002}$
$C_{\text{ecl}}^a$	$0.69 \pm 0.06$	$0.00 \pm 0.05$	$0.05 \pm 0.05$	$0.14 \pm 0.05$	$-0.05 \pm 0.05$
$\Delta\phi_{\text{ecl}}$	$0.09^{+0.02}_{-0.01}$	$0.176 \pm 0.004$	$0.180 \pm 0.009$	$0.19 \pm 0.01$	$0.186 \pm 0.004$
$P_{\text{orb}}^b$	$4.23810 \pm 0.00007$	$3.73881 \pm 0.00002$	$3.31961 \pm 0.00004$	$4.56988 \pm 0.00006$	$6.07413 \pm 0.00004$
$\dot{P}_{\text{orb}}^c$	$-6 \pm 4$	$0.2 \pm 0.8$	$3 \pm 2$	$-3 \pm 4$	$0.5 \pm 1.9$
$T_{\text{mid}}^d$	$55074.99 \pm 0.03$	$55087.721^{+0.007}_{-0.008}$	$55081.57 \pm 0.02$	$55083.88 \pm 0.03$	$55079.07 \pm 0.01$
$\Theta_e^e$	$15^{+3}_{-2}$	$31.7^{+0.7}_{-0.8}$	$32 \pm 2$	$34^{+3}_{-2}$	$33.6 \pm 0.7$
$\chi^2_{\nu}$ (dof)	$1.18(80)$	$0.97(80)$	$1.08(80)$	$1.01(80)$	$1.03(80)$

Table 2.2. Eclipse Model Parameters, Assuming an Asymmetric Eclipse Profile

<sup>a</sup> Units are  $10^{-3}$  counts  $\text{cm}^{-2} \text{s}^{-1}$ .

<sup>b</sup> Refined orbital periods using an  $O - C$  analysis. Units are days.

<sup>c</sup> The orbital period derivative at the 90% confidence interval found using an  $O - C$  analysis. Units are  $10^{-7} \text{d} \text{d}^{-1}$ .

<sup>d</sup> Units are Barycentered Modified Julian Day (BMJD). Phase 0 is defined as eclipse center.

<sup>e</sup> Units are degrees.

Model Parameter	IGR J18027-2016 <sup>a,c</sup>	IGR J18027-2016 <sup>a,d</sup>	XTE J1855-026 <sup>b,c</sup>	XTE J1855-026 <sup>b,d</sup>
$\phi_{\text{ing}}$	$-0.147^{+0.004}_{-0.005}$	$-0.167^{+0.005}_{-0.004}$	$-0.131^{+0.001}_{-0.002}$	$-0.136 \pm 0.002$
$\Delta\phi_{\text{ing}}$	$0.053^{+0.005}_{-0.007}$	$0.082 \pm 0.009$	$0.038 \pm 0.002$	$0.040 \pm 0.003$
$\Delta\phi_{\text{eg}}$	$0.053^{+0.005}_{-0.007}$	$0.027^{+0.004}_{-0.006}$	$0.038 \pm 0.002$	$0.037 \pm 0.003$
$C_{\text{ing}}^e$	$1.59 \pm 0.05$	$1.25 \pm 0.08$	$2.64 \pm 0.06$	$2.45 \pm 0.08$
$C_{\text{eg}}^e$	$1.59 \pm 0.05$	$1.68 \pm 0.08$	$2.64 \pm 0.06$	$2.79^{+0.09}_{-0.08}$
$\phi_{\text{egr}}$	$0.099 \pm 0.003$	$0.102 \pm 0.002$	$0.094 \pm 0.002$	$0.092^{+0.001}_{-0.002}$
$C_{\text{ecl}}^e$	$0.17 \pm 0.04$	$0.14 \pm 0.04$	$-0.04 \pm 0.05$	$-0.03 \pm 0.05$
$\Delta\phi_{\text{ecl}}$	$0.193^{+0.007}_{-0.009}$	$0.19 \pm 0.01$	$0.187 \pm 0.003$	$0.187 \pm 0.004$
$P_{\text{orb}}^f$	$4.56982 \pm 0.00003$	$4.56993 \pm 0.00003$	$6.07412 \pm 0.00003$	$6.07414 \pm 0.00003$
$\dot{P}_{\text{orb}}^g$	$0.8 \pm 0.9$	$0.2 \pm 1.1$	$-0.1 \pm 0.5$	$0.0 \pm 0.5$
$T_{\text{mid}}^h$	$55083.78 \pm 0.01$	$55083.82 \pm 0.01$	$55079.056 \pm 0.009$	$55079.07 \pm 0.01$
$\Theta_e^i$	$35 \pm 1$	$34 \pm 2$	$33.6^{+0.5}_{-0.6}$	$33.7 \pm 0.7$
$\chi^2_{\nu}$ (dof)	$1.20(77)$	$0.93(80)$	$1.02(77)$	$1.05(80)$

Table 2.3. Eclipse Model Parameters With Historic Values

<sup>a</sup> Includes the mid-eclipse times derived in Hill et al. (2005), Jain et al. (2009b) and Falanga et al. (2015).

<sup>b</sup> Includes the mid-eclipse times derived in Corbet & Mukai (2002) and Falanga et al. (2015).

<sup>c</sup> Assuming a Symmetric Eclipse Profile.

<sup>d</sup> Assuming an Asymmetric Eclipse Profile.

<sup>e</sup> Units are  $10^{-3}$  counts  $\text{cm}^{-2} \text{s}^{-1}$ .

<sup>f</sup> Refined orbital periods using an  $O - C$  analysis. Units are days.

<sup>g</sup> The orbital period derivative at the 90% confidence interval found using an  $O - C$  analysis. Units are  $10^{-7} \text{d d}^{-1}$ .

<sup>h</sup> Units are BMJD. Phase 0 is defined as eclipse center.

<sup>i</sup> Units are degrees.

of the components provided that the orbit is circular ( $e = 0$ ). Using the observed orbital period and Kepler's third law, the duration can be written in terms of the sum of the donor star and compact object masses, which stipulates that the eclipse half-angle,  $\Theta_e$ , can now be expressed in terms of the radius, inclination and masses of the components. In one set of calculations, I assume a  $1.4 M_{\odot}$  compact object which may be appropriate for an accreting neutron star (Chandrasekhar, 1931). The region allowed by the measured eclipse half-angle for each binary in Mass-Radius space is shown in Section 2.4. The inclination

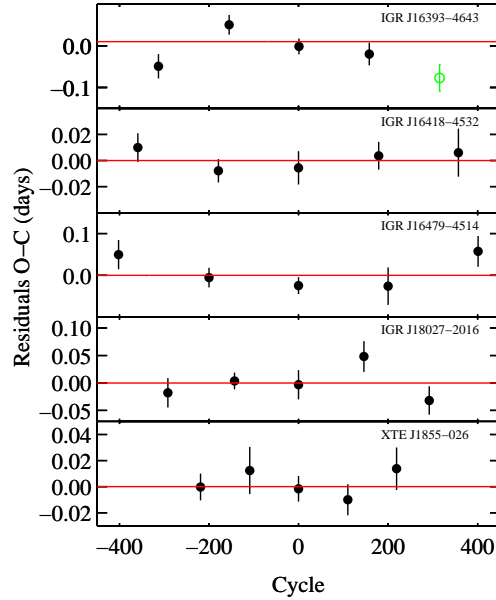


FIG. 2.1. The observed minus calculated ( $O - C$ ) eclipse time residuals for IGR J16393-4643 (top), IGR J16418-4532 (second panel), IGR J16479-4514 (middle), IGR J18027-2016 (fourth panel) and XTE J1855-026 (bottom) fit using a symmetric step-and-ramp function. I subtract the best linear polynomial fit for each source and correct the orbital periods accordingly. For IGR J16393-4643 (top) I only use the first four points to obtain a good fit (see Section 2.4.1).

is constrained between edge-on orbits (left boundary of the dark shaded region) and close to face-on orbits (the right boundary of the light shaded region). I can attach additional constraints assuming that the mass donor underfills the Roche lobe (right boundary of the dark shaded region), which is dependent on the mass ratio of the system and the orbital separation. To calculate the eclipse half-angle and the Roche-lobe radius, I used Equation 7 in Joss & Rappaport (1984), also used by Rubin et al. (1996), and Equation 2 in Eggleton (1983), respectively. Further constraints on the parameters of the donor star are imposed with pulse-timing techniques (dashed red lines in Figures 2.15 and 2.18). For the systems where pulse-timing results were not available, I additionally calculated the minimum inclination angle of the system,  $i_{\min}$ , that is consistent with the measured eclipse

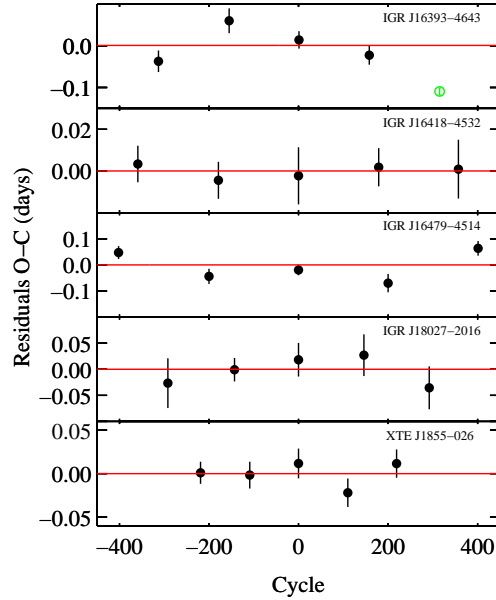


FIG. 2.2. The observed minus calculated ( $O - C$ ) eclipse time residuals for IGR J16393-4643 (top), IGR J16418-4532 (second panel), IGR J16479-4514 (middle), IGR J18027-2016 (fourth panel) and XTE J1855-026 (bottom) fit using an asymmetric step-and-ramp function. I subtract the best linear polynomial fit for each source and correct the orbital periods accordingly. For IGR J16393-4643 (top) I only use the first four points to obtain a good fit (see Section 2.4.1).

half-angle (see Table 2.1).

When the semi-amplitude of the radial velocities of both the compact object and the mass donor are known (e.g. IGR J18027-2016, XTE J1855-026), the mass ratio between the compact object and mass donor can be calculated (Equation 6, Joss & Rappaport, 1984). This means that in addition to the radius and mass of the donor star, the mass of the compact object can be constrained. The mass of the donor star can be written in terms of the semi-amplitude of the radial velocity of the compact object, orbital period, Newton's gravitational constant, inclination angle of the system and the mass ratio (Joss & Rappaport, 1984). Likewise, the compact object mass can be written in terms of the semi-amplitude of the radial velocity of the donor star, orbital period, Newton's gravitational

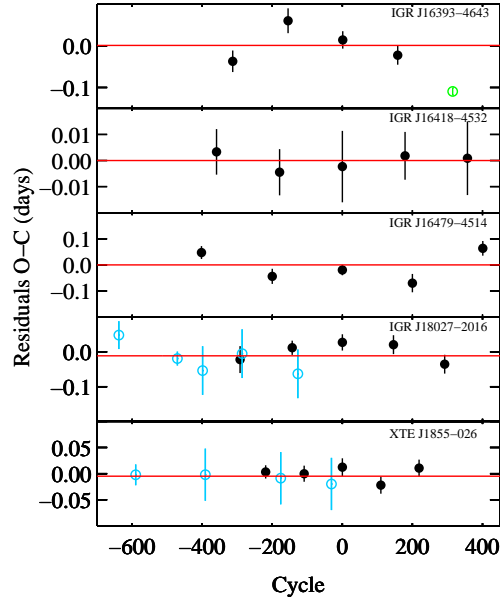


FIG. 2.3. Derived  $O - C$  eclipse time residuals for IGR J16393-4643 (top), IGR J16418-4532 (second panel), IGR J16479-4514 (middle), IGR J18027-2016 (fourth panel) and XTE J1855-026 (bottom) fit combined with those in the literature (blue points). I subtract the best linear polynomial fit for each source and correct the orbital periods accordingly. For IGR J16393-4643 (top) I only use the first four points to obtain a good fit (see Section 2.4.1).

constant, inclination angle of the system and the mass ratio (Joss & Rappaport, 1984). To calculate the masses of both the donor star and the compact object, I used Equations 2 and 3 in Ash et al. (1999), also used by Rappaport & Joss (1983).

For consistency, I compare my derived constraints on the masses and radii of the donor stars with those expected for the previously proposed spectral types. For the systems where pulse-timing results were not available, I calculate the predicted eclipse half-angles as a function of inclination angle using the mass and radius for the derived spectral types (see Section 2.4). Generally I used results from Carroll & Ostlie (2006) for main-sequence, giant and supergiant luminosity classes. These are represented by the red, green and blue dashed lines in mass-radius space for each system (see Section 2.4). For O-type

supergiants, I also use Tables 3 and 6 in Martins et al. (2005) to compare the results (see blue dotted lines in Figures 2.6, 2.9 and 2.12). The constraints for B-type supergiants are additionally compared with Tables 3 and 6 in Lefever et al. (2007) for B-type supergiants (blue crosses in Figures 2.15 and 2.18).

## 2.4 Five Eclipsing HMXBs

### 2.4.1 IGR J16393-4643 (=AX J16390.4-4642)

IGR J16393-4643 is an HMXB first discovered and listed as AX J16390.4-4642 in the *ASCA* Faint Source Catalog (Sugizaki et al., 2001) and was later detected with *INTEGRAL* (Bodaghee et al., 2006). The average flux in the 20–40 keV band was found to be  $5.1 \times 10^{-11}$  erg cm<sup>-2</sup> s<sup>-1</sup>, and intensity variations were found to exceed a factor of 20 (Bodaghee et al., 2006). In the 2–10 keV energy band, the unabsorbed flux was found to be  $9.2 \times 10^{-11}$  erg cm<sup>-2</sup> s<sup>-1</sup> (Bodaghee et al., 2006). A proposed mass donor 2MASS J16390535-4242137 was found in the *XMM-Newton* error circle, which is thought to be an OB supergiant (Bodaghee et al., 2006). However, a precise position of the X-ray source obtained with *Chandra* shows this candidate to be positionally inconsistent with the proposed counterpart (Bodaghee et al., 2012). Using the *Spitzer* Galactic Legacy Infrared Mid-Plane Survey (GLIMPSE), Bodaghee et al. (2012) proposed that the counterpart must be a distant reddened B-type main-sequence star.

Using *INTEGRAL* and *XMM-Newton*, Bodaghee et al. (2006) found a  $912.0 \pm 0.1$  s modulation, which was interpreted as the neutron star rotation period. Islam et al. (2015) recently refined this to  $908.79 \pm 0.01$  s using *Suzaku*. A  $\sim 3.7$  day orbital period was sug-

gested using a pulse timing analysis, although orbital periods of  $\sim 50.2$  and  $\sim 8.1$  days were not completely ruled out (Thompson et al., 2006). While various possible orbital solutions and accretion mechanisms have been proposed, orbital periods of  $4.2368 \pm 0.0007$  and  $4.2371 \pm 0.0007$  days were clearly found from data from *Swift*-BAT and *RXTE* PCA, respectively (Corbet et al., 2010). This was refined to  $4.2386 \pm 0.0003$  d (Corbet & Krimm, 2013), also using BAT data. Islam et al. (2015) recently derived an orbital period of  $\sim 366150$  s (4.24 d) with BAT, which is also consistent with the result from Corbet & Krimm (2013). The position in Corbet’s diagram shows that IGR J16393-4643 is an SGXB (Corbet & Krimm, 2013). Corbet & Krimm (2013) identified the presence of a possible superorbital period of  $\sim 15$  days; although with low significance.

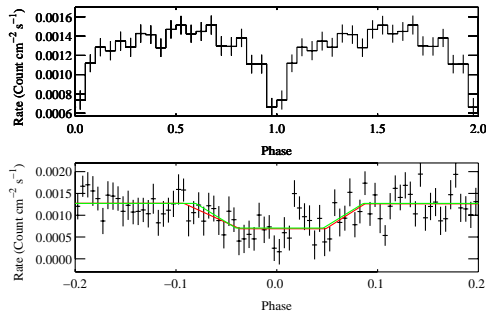


FIG. 2.4. *Swift*-BAT light curve of IGR J16393-4643 in the 15–50 keV band folded on the orbital period (top) using 20 bins.  $T_0$  is defined at BMJD 55074.99, corresponding to mid-eclipse. A detailed folded light curve with 80 bins (bottom) is fit with both a symmetric “step and ramp” function (green) and asymmetric “step and ramp” function (red), which model the eclipse. The ingress and egress start times calculated using symmetric “step and ramp” function were shifted to align with those calculated with the asymmetric “step and ramp” function.

The BAT light curves folded on the orbital period revealed a sharp dip, which was interpreted as an eclipse (Corbet & Krimm, 2013; Islam et al., 2015). With *Swift* BAT, Islam et al. (2015) constrained the eclipse half angle to be  $\sim 17^\circ$ , corresponding to a duration

of  $\sim 0.75$  d ( $\sim 65.1$  ks). Using the relationship between eclipse duration and stellar radius, along with the definition of the Roche lobe from Bowers & Deeming (1984), Islam et al. (2015) calculated the allowed range of orbital inclinations of the system. Assuming a star with spectral type O9 I (Bodaghee et al., 2012), the orbital inclination was constrained to  $39\text{--}57^\circ$  (Islam et al., 2015). A main-sequence B-type star yields orbital inclinations between  $60\text{--}77^\circ$  (Bodaghee et al., 2012; Islam et al., 2015).

I derive a  $4.2378 \pm 0.0004$  d orbital period for IGR J16393-4643 using a DFT, which is consistent with the results from Corbet & Krimm (2013). Using an  $O - C$  analysis (see Section 2.3.2), this is further refined to  $4.23810 \pm 0.00007$  d. I note that a sharp contrast in the step-and-ramp model during the time between MJD 56079–56745. Particularly, the eclipse duration is much shorter than that calculated at times prior to MJD 56079. As a result, I only use data between MJD 53416–56078 in my  $O - C$  analysis (see Figures 2.1–2.3). Using the quadratic orbital change function (see Equation 2.4), I find the orbital period derivative to be  $-5 \pm 4 \times 10^{-7}$  d d $^{-1}$ , which is consistent with zero. The duration of the observed eclipse was calculated to be  $31_{-5}^{+6}$  ks ( $0.36_{-0.06}^{+0.07}$  d), yielding an eclipse half-angle of  $15_{-3}^{+2}^\circ$  (see Table 2.1). I find these to be consistent with the result from Islam et al. (2015). The source flux does not reach 0 counts cm $^{-2}$  s $^{-1}$  in the folded light curves during eclipse (see Figure 2.4). I interpret this dip as an eclipse since the feature is persistent over many years of data. The rapid ingress and egress requires obscuration by clearly defined boundaries that are suggestive of an object such as the mass donor in the system (e.g. Coley et al., 2014, Section 3.4.2). I discuss the nature of the non-zero flux during eclipse in Section 2.5.2.

I calculate the predicted eclipse half-angle  $\Theta_e$  as a function of inclination angle

of the system (see Figure 2.5). The calculation assumes a neutron star mass of  $1.4 M_{\odot}$ , and the primary stellar masses and radii given in Table 2.6. I calculate the minimum inclination angle of the system,  $i_{\min}$ , that is consistent with the measured eclipse half-angle (see Table 2.6). I find that stars with spectral types B0 V, B0-5 III and B0 I satisfy the constraint imposed by the eclipse half-angle (see Table 2.6). I note that while a B5 III star satisfies the constraint imposed by the minimum value of the eclipse half-angle under the assumption that the neutron star is  $1.4 M_{\odot}$ , this spectral type does not satisfy the eclipse half-angle for a more massive neutron star.

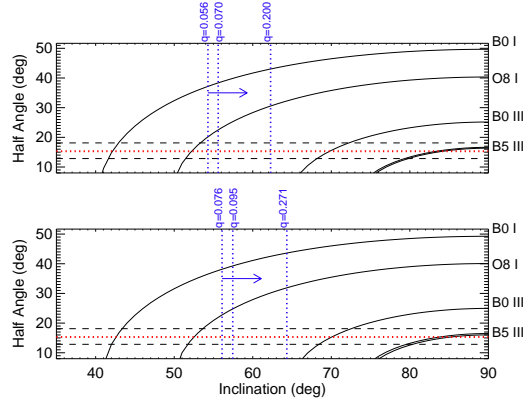


FIG. 2.5. The black curves show the predicted eclipse half angle of IGR J16393-4643 as a function of inclination angle for stars with the indicated spectral types. The red and black dashed lines indicate the eclipse half angle and estimated error as measured by *Swift* BAT. I assume a neutron star mass of  $1.4 M_{\odot}$  (top) and of mass  $1.9 M_{\odot}$  (bottom) and typical masses and radii for the assumed companion spectral type (see Table 2.6). The blue vertical dashed lines indicate the lower limit of the inclination angle. Inclinations to the left of these correspond to stars that overflow the Roche lobe.

Since the X-ray luminosity is lower than what would be expected for Roche-lobe overflow (Kaper et al., 2004), I can attach an additional constraint assuming that the mass donor underfills the Roche-lobe radius (see Figure 2.6). I note that while the derived masses and radii for the spectral type B0 I from Carroll & Ostlie (2006) satisfies the eclipse half-angle, the assumed radius would be larger than the Roche-lobe radius

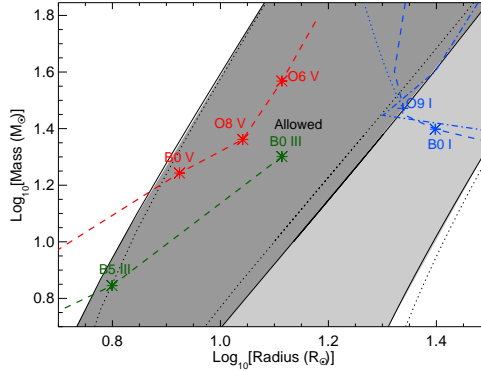


FIG. 2.6. Log-log plot of stellar mass as a function of stellar radius for IGR J16393-4643. The dark shaded region indicates the allowed spectral types that satisfy the constraints imposed by both the eclipse duration and Roche-lobe size. The light shaded region only indicates spectral types that satisfy the observed eclipse duration. Stellar masses and radii are reported in Table 2.6. The red, green and blue lines indicate interpolations for main-sequence, giant and supergiant luminosity classes, respectively. The dashed, dotted and dash-dotted lines indicate stellar masses and radii derived from Carroll & Ostlie (2006), Martins et al. (2005) and Allen (2000), respectively.

(Eggleton, 1983). Therefore, an B0 I spectral type must be excluded (see Table 2.6).

## 2.4.2 IGR J16418-4532

IGR J16418-4532 is a candidate Supergiant Fast X-ray Transient (SFXT) first discovered with the *INTEGRAL* satellite by Tomsick et al. (2004) at a flux of  $3 \times 10^{-11}$  erg  $\text{cm}^{-2} \text{s}^{-1}$  in the 20–40 keV band. The near-infrared spectral energy distribution of the most probable Two Micron All Sky Survey (2MASS) counterpart was measured with the 3.5 m New Technology Telescope (NTT) at La Silla Observatory, Rahoui et al. (2008) found a spectral type of O8.5 I. Coleiro et al. (2013) proposed a spectral type of BN0.5 Ia based on features in the near-infrared spectrum such as Br(7 – 4) and the emission and absorption of neutral helium. Using *XMM-Newton*, Walter et al. (2006) found a  $1246 \pm 100$  s modulation, which was interpreted as a neutron star rotation period. This was later refined to  $1212 \pm 6$  s (Sidoli et al., 2012), also using *XMM-Newton*. Recently, Drave

et al. (2013a) further refined the rotation period to  $1209.1 \pm 0.4$  s with *XMM-Newton*. A  $\sim 3.73$  d orbital period was found using data from the *Swift* BAT and the *RXTE* ASM instruments, where  $P_{\text{orb}}$  was reported as  $3.753 \pm 0.004$  d and  $3.7389 \pm 0.0004$  d, respectively (Corbet et al., 2006). Using an extended ASM dataset, Levine et al. (2011) found a  $3.73886 \pm 0.00028$  d period, which is consistent with the earlier result from Corbet et al. (2006). Corbet & Krimm (2013) further refined this to  $3.73886 \pm 0.00014$  d using BAT. A  $\sim 14.7$  d modulation was found using BAT and *INTEGRAL*, which was interpreted as a superorbital period (Corbet & Krimm, 2013; Drave et al., 2013b).

The ASM and BAT light curves folded on the orbital period revealed a sharp dip with near zero mean flux, which was interpreted as a total eclipse (Corbet et al., 2006). Subsequent observations of the eclipse included *Swift* X-ray Telescope (XRT) and *INTEGRAL* (Romano et al., 2012; Drave et al., 2013a). With *Swift* BAT, Romano et al. (2012) constrained the eclipse half-angle to be  $0.17 \pm 0.05$  of the orbital period, corresponding to a duration of  $0.6 \pm 0.2$  d ( $55 \pm 16$  ks). The duration of the eclipse was found to be  $\sim 0.75$  d in the archival data set from *INTEGRAL/IBIS*, covering the time period MJD 52650–55469 (Drave et al., 2013a). While the estimate in Drave et al. (2013a) is significantly larger than the constraints from Romano et al. (2012), a lower limit of  $\sim 0.583$  d was found in a combined study with *INTEGRAL/IBIS* and *XMM-Newton* (Drave et al., 2013a).

I derive a  $3.73863 \pm 0.00015$  d orbital period for IGR J16418-4532 using the fundamental peak in the power spectrum, while the first harmonic yields  $3.73882 \pm 0.00011$  d. Using an  $O - C$  analysis (see Figures 2.1–2.3), I refine this to  $3.73881 \pm 0.00002$  d. Using the quadratic orbital change function (see Equation 2.4), I find the orbital period derivative to be  $0.7 \pm 1.0 \times 10^{-7}$  d d $^{-1}$ , which is consistent with zero. Folding the light curve

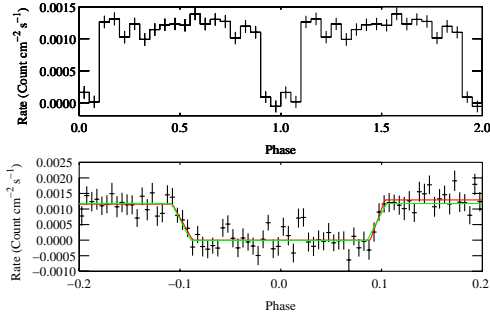


FIG. 2.7. *Swift*-BAT light curve of IGR J16418-4532 in the 15–50 keV band folded on the orbital period (top) using 20 bins. T0 is defined at BMJD 55087.721, corresponding to mid-eclipse. A detailed folded light curve with 80 bins (bottom) is fit with both a symmetric “step and ramp” function (green) and asymmetric “step and ramp” function (red), which model the eclipse. The ingress and egress start times calculated using symmetric “step and ramp” function were shifted to align with those calculated with the asymmetric “step and ramp” function.

on the refined orbital period (see Figure 2.7), I calculate the duration of the observed eclipse to be  $57 \pm 1$  ks ( $0.66 \pm 0.01$  d). This yields an eclipse half-angle of  $31.7^{+0.7}_{-0.8}^\circ$  (see Table 2.2). I note that I find the eclipse half-angle to be  $31.5 \pm 0.6^\circ$  assuming a symmetric step-and-ramp function. I find the eclipse properties to be consistent with the results from Romano et al. (2012) and Drave et al. (2013a). Under the assumption that the mass and radius of the proposed mass donor are  $31.54 M_\odot$  and  $21.41 R_\odot$  (Martins et al., 2005), the duration of the observed eclipse is consistent with the proposed mass donor, where I find the orbital inclination to be  $60\text{--}63^\circ$  for an O8.5 I spectral type (see Figures 2.8 and 2.9).

Since the X-ray luminosity is lower than what would be expected for Roche-lobe overflow (Kaper et al., 2004), I can attach an additional constraint assuming that the mass donor underfills the Roche-lobe radius (see Figure 2.9). I note that while the derived masses and radii for the spectral types from Martins et al. (2005) satisfy the eclipse half-angle, the assumed radius would be larger than the Roche-lobe radius (Eggleton, 1983).

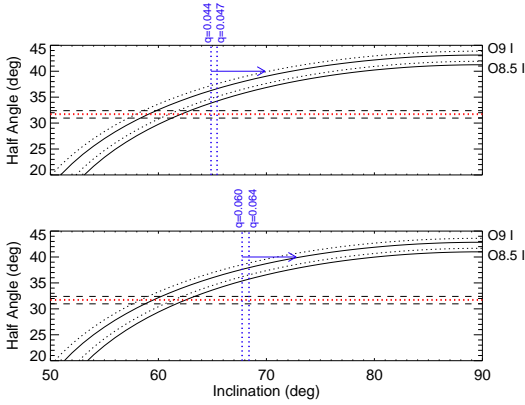


FIG. 2.8. The black curves show the predicted eclipse half angle of IGR J16418-4532 as a function of inclination angle for stars with the indicated spectral types. The red and black dashed lines indicate the eclipse half angle and estimated error as measured by *Swift* BAT. I assume a neutron star mass of  $1.4 M_{\odot}$  (top) and of mass  $1.9 M_{\odot}$  (bottom) and typical masses and radii for the assumed companion spectral type (see Table 2.7). The blue vertical dashed lines indicate the lower limit of the inclination angle. Inclinations to the left of these correspond to stars that overflow the Roche lobe.

Therefore, an O8.5 I spectral type must be excluded.

### 2.4.3 IGR J16479-4514

IGR J16479-4514 is an intermediate SFXT, which has been proposed to host either an O8.5 I (Chaty et al., 2008; Rahoui et al., 2008) or a O9.5 Iab (Nespoli et al., 2008) mass donor. First discovered by the *INTEGRAL* satellite in 2003 August (Molkov et al., 2003), the fluxes in the 18–25 keV and 25–50 keV energy bands were found to be  $\sim 12$  mCrab and  $\sim 8$  mCrab, respectively. The flux was later shown to increase by a factor of  $\sim 2$  on 2003 August 10 (Molkov et al., 2003). Using *Swift* BAT data, Jain et al. (2009a) found the presence of a  $3.319 \pm 0.001$  day modulation, which was interpreted as the orbital period. A  $3.3193 \pm 0.0005$  day modulation was independently found by Romano et al. (2009) also using BAT. Corbet & Krimm (2013) found the orbital period to be  $3.3199 \pm 0.0005$  d, which is consistent with the results from Jain et al. (2009a) and Romano et al. (2009).

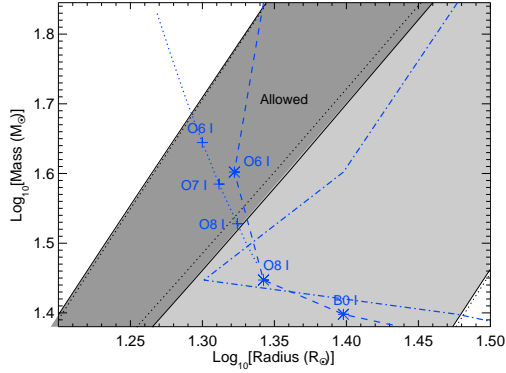


FIG. 2.9. Log-log plot of stellar mass as a function of stellar radius for IGR J16418-4532. The dark shaded region indicates the allowed spectral types that satisfy the constraints imposed by both the eclipse duration and Roche-lobe size. The light shaded region only indicates spectral types that satisfy the observed eclipse duration. Stellar masses and radii are reported in Table 2.7. The dashed, dotted and dash-dotted lines indicate stellar masses and radii derived from Carroll & Ostlie (2006), Martins et al. (2005) and Allen (2000), respectively.

The presence of a  $11.880 \pm 0.002$  d superorbital period was found by Corbet & Krimm (2013) using BAT. Drave et al. (2013b) reported a  $11.891 \pm 0.002$  d superorbital period using *INTEGRAL*, confirming the result. No pulse period has been identified.

The BAT light curves folded on the orbital period revealed a sharp dip, which was interpreted as an eclipse with a proposed duration of  $\sim 52$  ks (Jain et al., 2009a). This confirmed an earlier *XMM-Newton* observation where a decay from a higher to lower flux state was interpreted as the ingress of an eclipse (Bozzo et al., 2009). A 2012 *Suzaku* observation covered  $\sim 80$  percent of the orbital cycle of IGR J16479-4514, where temporal and spectral properties were analyzed during eclipse and out-of-eclipse (Sidoli et al., 2013). Since the ingress of the eclipse was not covered in the *Suzaku* observation, the exact duration of the eclipse could only be constrained to 46–143 ks, 0.53–1.66 d, (Sidoli et al., 2013).

Using a DFT, I derive the orbital period of IGR J16479-4514 to be  $3.31998 \pm 0.00014$  d.

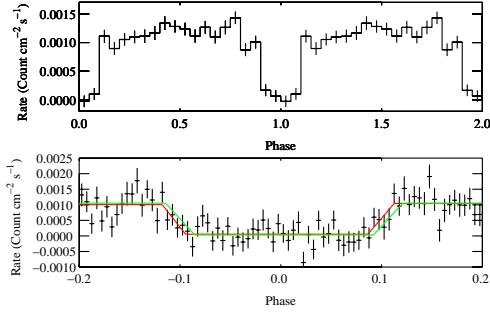


FIG. 2.10. *Swift*-BAT light curve of IGR J16479-4514 in the 15–50 keV band folded on the orbital period (top) using 20 bins.  $T_0$  is defined at BMJD 55081.57, corresponding to mid-eclipse. A detailed folded light curve with 80 bins (bottom) is fit with both a symmetric “step and ramp” function (green) and asymmetric “step and ramp” function (red), which models the eclipse. The ingress and egress start times calculated using symmetric “step and ramp” function were shifted to align with those calculated with the asymmetric “step and ramp” function. This figure was updated from (Coley et al., 2015).

I refine this to  $3.31961 \pm 0.00004$  d using an  $O - C$  analysis (see Figures 2.1–2.3) and fold the light curve on the refined orbital period to calculate the eclipse half-angle (see Figure 2.10). Using the quadratic orbital change function (see Equation 2.4), I find the orbital period derivative to be  $3 \pm 2 \times 10^{-7}$  d d $^{-1}$ , which is consistent with zero. I calculate the duration of the observed eclipse to be  $52 \pm 3$  ks ( $0.60 \pm 0.03$  d), which is consistent with results from Jain et al. (2009a). This yields an eclipse half-angle of  $31.9^{+0.9}_{-1.3}$ ° (see Table 2.1). Using values from Martins et al. (2005) for the masses and radii of the proposed spectral type of the mass donor, the duration of the observed eclipse is consistent with the proposed mass donor (see Figures 2.11), where I find the orbital inclination to be  $54\text{--}58^\circ$  or  $47\text{--}51^\circ$  for a O8.5 I or O9.5 Iab spectral type, respectively (see Table 2.8). While the previously proposed spectral types satisfy the eclipse half-angle, I note that the radius of the proposed spectral type is larger than the Roche lobe (Eggleton, 1983). Therefore, the previously proposed O8.5 I or O9.5 Iab spectral types must be excluded (see Figure 2.12).

Sidoli et al. (2013) proposed a mass donor with mass  $\sim 35 M_{\odot}$  and radius  $\sim 20 R_{\odot}$ , which could satisfy the constraints imposed by the Roche-lobe radius.

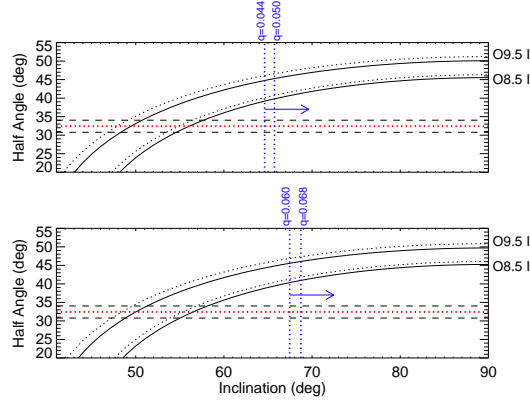


FIG. 2.11. The black curves show the predicted eclipse half angle of IGR J16479-4514 as a function of inclination angle for stars with the indicated spectral types. The red and black dashed lines indicate the eclipse half angle and estimated error as measured by *Swift* BAT. I assume a neutron star mass of  $1.4 M_{\odot}$  (top) and of mass  $1.9 M_{\odot}$  (bottom) and typical masses and radii for the assumed companion spectral type (see Table 2.8). The blue vertical dashed lines indicate the lower limit of the inclination angle. Inclinations to the left of these correspond to stars that overfill the Roche lobe.

#### 2.4.4 IGR J18027-2016 (=SAX J1802.7-2017)

IGR J18027-2016 (=SAX J1802.7-2017) is an SGXB, which has been proposed to host either a B1 Ib (Torrejón et al., 2010) or B0-B1 I (Mason et al., 2011) mass donor. First detected with *BeppoSAX* in 2001 September (Augello et al., 2003), the average flux in the 0.1–10 keV energy band was found to be  $3.6 \times 10^{-11}$  ergs  $\text{cm}^{-2} \text{s}^{-1}$ . Pulse-timing analysis suggested a  $\sim 4.6$  day orbital period (Augello et al., 2003), which was later refined to  $4.5696 \pm 0.0009$  days using *INTEGRAL* (Hill et al., 2005). Combining the mid-eclipse times derived in Augello et al. (2003) and Hill et al. (2005) with later observations with *Swift* BAT and *INTEGRAL* in an  $O-C$  analysis, the orbital period was further refined to  $4.5693 \pm 0.0004$  d (Jain et al., 2009b). Fitting a quadratic model to the derived mid-eclipse

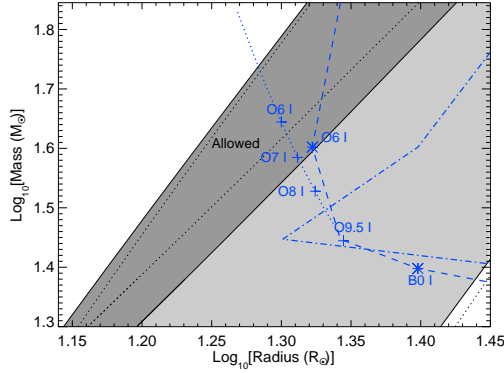


FIG. 2.12. Log-log plot of stellar masses as a function of stellar radius for IGR J16479-4514. The light shaded region indicates the allowed spectral types that satisfy the observed eclipse. The dark shaded region indicates the spectral types where both the eclipse duration and Roche-lobe radius constraints are satisfied. Stellar masses and radii are reported in Table 2.8. The dashed, dotted and dash-dotted lines indicate stellar masses and radii derived from Carroll & Ostlie (2006), Martins et al. (2005) and Allen (2000), respectively.

times, a period derivative of  $(3.9 \pm 1.2) \times 10^{-7} \text{ d d}^{-1}$  was found (Jain et al., 2009b). Using *INTEGRAL*, Falanga et al. (2015) recently refined the orbital period and period derivative to  $4.5697 \pm 0.0001 \text{ d}$  and  $(2.1 \pm 3.6) \times 10^{-7} \text{ d d}^{-1}$ , respectively. Augello et al. (2003) found the presence of a  $\sim 139.6 \text{ s}$  modulation using *BeppoSAX*, which they interpreted as the neutron star rotation period. Hill et al. (2005) found the pulse period using *XMM-Newton* to be  $139.61 \pm 0.04 \text{ s}$ , which is consistent with an earlier result from Augello et al. (2003). However, no evidence for superorbital modulation was found (Corbet & Krimm, 2013).

Augello et al. (2003) derived the epoch of the NS superior conjunction to occur during the first 50 ks of an observation where IGR J18027-2016 was undetected. Since the epoch of superior conjunction corresponds to a time where the mid-eclipse is expected to occur, Augello et al. (2003) suggested the presence of a possible eclipse with a half-duration of  $0.47 \pm 0.10 \text{ days}$ . Hill et al. (2005) and Jain et al. (2009b) later confirmed this result where the eclipse half-angle was found to be  $0.61 \pm 0.08 \text{ radians}$  ( $34.9 \pm 4.6^\circ$ ) and

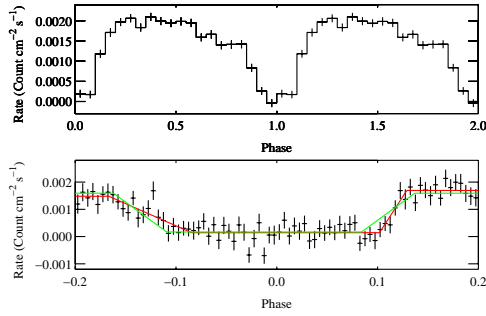


FIG. 2.13. *Swift*-BAT light curve of IGR J18027-2016 in the 15–50 keV band folded on the orbital period (top) using 20 bins. T0 is defined at BMJD  $55083.82 \pm 0.01$ , corresponding to mid-eclipse. A detailed folded light curve with 80 bins (bottom) is fit with both a symmetric “step and ramp” function (green) and asymmetric “step and ramp” function (red), which model the eclipse. The ingress and egress start times calculated using symmetric “step and ramp” function were shifted to align with those calculated with the asymmetric “step and ramp” function.

$\sim 0.604$  radians ( $\sim 34.6^\circ$ ), respectively. Falanga et al. (2015) recently refined the eclipse half-angle to  $31 \pm 2^\circ$  using *INTEGRAL*.

Pulse-timing and radial velocity curves have helped place constraints on the physical properties on both the donor star as well as the compact object. Using a pulse-timing analysis with *BeppoSAX* and *XMM-Newton*, the projected semi-major axis of the neutron star was found to be  $68 \pm 1$  lt-s (Hill et al., 2005). Assuming a  $1.4 M_\odot$  neutron star, Hill et al. (2005) constrained the mass and radius of the mass donor star to  $18.8\text{--}29.3 M_\odot$  and  $14.7\text{--}23.4 R_\odot$ , respectively. Using *Swift* BAT and *INTEGRAL*, Jain et al. (2009b) further constrained the radius of the donor star to  $16.4\text{--}24.7 R_\odot$ . The mass donor was observed between 2010 May 26 and 2010 September 8 (MJD 55342–55447) with the *European Southern Observatory Very Large Telescope (ESO VLT)*, Mason et al., (2011). The semi-amplitude of the radial velocity of the mass donor,  $K_O$ , was found to be  $23.8 \pm 3.1$  km s $^{-1}$  (Mason et al., 2011). Since the projected semi-major axis of the

neutron star can be expressed in terms of a radial velocity semi-amplitude,  $K_X$ , the ratio between the masses of the compact object and the mass donor can be calculated according to Equation 2 in Ash et al. (1999). Mason et al. (2011) found the mass ratio,  $q$ , to be  $0.07 \pm 0.01$ . Using the mass ratio and the eclipse half-angle measured in Hill et al. (2005), the mass and radius of the donor star were refined to values between  $18.6 \pm 0.8 M_\odot$  and  $16.8 \pm 1.5 R_\odot$  at edge-on inclinations to  $21.8 \pm 2.4 M_\odot$  and  $19.8 \pm 0.7 R_\odot$  where the donor star fills the Roche lobe (Mason et al., 2011). The mass of the compact object was constrained to be between  $1.36 \pm 0.21$  and  $1.58 \pm 0.27 M_\odot$  in the two limits. The large error on the estimate of the eclipse half-angle from Hill et al. (2005) contributes significantly to the uncertainties on these measurements. Using a similar analysis with *INTEGRAL*, Falanga et al. (2015) constrained the mass of the neutron star to  $1.6 \pm 0.3 M_\odot$ .

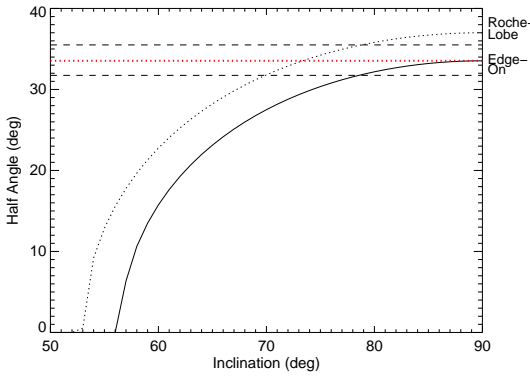


FIG. 2.14. The black curves show the predicted eclipse half angle of IGR J18027-2016 as a function of inclination angle for stars with the indicated spectral types. The red and black dashed lines indicate the eclipse half angle and estimated error as measured by *Swift* BAT.

I derive a  $4.57022 \pm 0.00013$  d orbital period for IGR J18027-2016 using a DFT, which is consistent with the results from Hill et al. (2005). Using an  $O - C$  analysis (see Figures 2.1–2.3), I refine this to  $4.56993 \pm 0.00003$  d. Using the quadratic orbital change

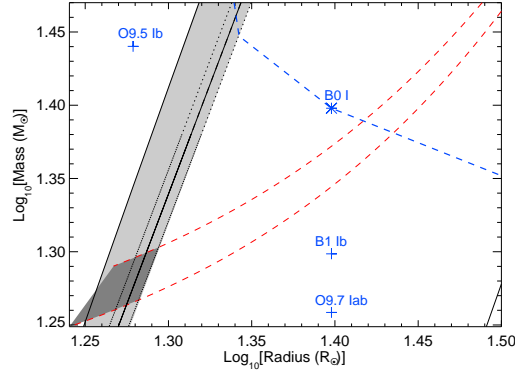


FIG. 2.15. Log-log plots of stellar masses as a function of stellar radii for IGR J18027-2016. The shaded region indicates the allowed spectral types to satisfy the observed eclipse duration and pulse-timing constraints. Stellar masses and radii are reported in Table 2.9. Stars and crosses indicate the spectral types according to Carroll & Ostlie (2006) and Lefever et al. (2007), respectively.

function (see Equation 2.4), I find the orbital period derivative to be  $0.2 \pm 1.1 \times 10^{-7} \text{ d d}^{-1}$ , which is consistent with zero. Folding the light curve on the refined orbital period (see Figure 2.13), I measure the duration of the observed eclipse to be  $74 \pm 4 \text{ ks}$  ( $0.85 \pm 0.05 \text{ d}$ ). I find the eclipse half-angle to be  $34 \pm 2^\circ$  (see Table 2.1). Since the X-ray luminosity of IGR J18027-2016 is modest, I again attach the constraint that the donor star underfills the Roche lobe (see Figures 2.14 and 2.15). This constrains the mass and radius of the donor star as well as the mass of the neutron star (see Figure 2.15). Using the eclipse half-angle and the expression for the mass donor when the mass ratio is known (Eq.4; Mason et al., 2011), I calculate the donor star mass and radius as well as mass of the compact object. I find the mass and radius of the donor star to be  $18.6 \pm 0.9 M_\odot$  and  $17.4 \pm 0.9 R_\odot$  and  $19.4 \pm 0.9 M_\odot$  and  $19.5^{+0.8}_{-0.7} R_\odot$  in the two limits (see Table 2.9). In the allowed limits, I constrain the mass of the neutron star to between  $1.37 \pm 0.19 M_\odot$  and  $1.43 \pm 0.20 M_\odot$  (see Table 2.9). While my results are in agreement with calculations in Mason et al. (2011), I note that the error estimate is only marginally improved in my analysis. The driving

factor on the error estimate of the neutron star mass is the uncertainty of  $\sim 13\%$  on the semi-amplitude of the radial velocity of the donor star as reported in Mason et al. (2011).

#### 2.4.5 XTE J1855-026

XTE J1855-026 is an SGXB discovered during *RXTE* scans along the Galactic plane (Corbet et al., 1999). Through 11 scanning observations of the Scutum arm, the 2–10 keV flux of XTE J1855-026 varied from an upper limit of 10 counts  $\text{s}^{-1}$  to  $136 \pm 15$  counts  $\text{s}^{-1}$  (Corbet et al., 1999). Using the *RXTE* Proportional Counter Array (PCA), Corbet et al. (1999) found a  $361.1 \pm 0.4$  s modulation, which was interpreted as the neutron star rotation period. Corbet & Mukai (2002) later refined the pulse period to  $360.741 \pm 0.002$  s with the PCA. An analysis using the *RXTE* All-sky Monitor (ASM) revealed the presence of a  $6.0724 \pm 0.0009$  d modulation, which is interpreted as the orbital period (Corbet & Mukai, 2002). Using an  $O - C$  analysis with *INTEGRAL*, Falanga et al. (2015) recently refined this to  $6.07415 \pm 0.00008$  d. No significant orbital period derivative was found using the quadratic orbital change function (Falanga et al., 2015). This places XTE J1855-026 in the wind-fed supergiant region of the Corbet diagram (Corbet, 1986). Corbet & Mukai (2002) constrained the eccentricity of XTE J1855-026 to  $e \leq 0.04$  using pulse-timing analysis. The projected semi-major axis of the neutron star was found to be  $82.8 \pm 0.8$  lt-s for a circular orbit and  $80.5 \pm 1.4$  lt-s for the eccentric solution (Corbet & Mukai, 2002). Using optical and near-infrared spectroscopy obtained with the William Herschel Telescope (WHT), Negueruela et al. (2008) found the mass donor to be a supergiant with spectral type B0 Iaep.

The light curves folded on the orbital period reveal a sharp dip, which was inter-

preted as an eclipse with a total phase duration of 0.198–0.262 (Corbet & Mukai, 2002). The phase duration corresponded to an eclipse half-angle  $36^\circ \leq \Theta_e \leq 47^\circ$ . The eclipse duration was found to be  $93 \pm 3$  ks ( $1.08 \pm 0.03$  d) in the archival *INTEGRAL* data set (Falanga et al., 2015), corresponding to an eclipse half-angle of  $32 \pm 1^\circ$ . This measurement is somewhat lower than the result from Corbet & Mukai (2002).

Optical radial velocity curves recently obtained with the *Isaac Newton Telescope* (*INT*), the *Liverpool Telescope* (*LT*) and the *WHT* help place additional constraints on the components of the system (González-Galán, 2015). The semi-amplitude of the radial velocity of the donor star was found to be  $26.8 \pm 8.2$  km s<sup>-1</sup>. Expressing the projected semi-major axis of the neutron star as a radial velocity semi-amplitude, González-Galán (2015) found the ratio between the masses of the components of the system to be  $0.09 \pm 0.03$  and notes that a large eccentricity of  $\sim 0.4$ – $0.5$  was found in the optical orbital solutions. This strongly contrasts with the X-ray orbital solution reported in Corbet & Mukai (2002), suggesting that caution must be taken in interpreting the optical orbital solutions. González-Galán (2015) refined the spectral type of the mass donor to a BN0.2 Ia supergiant and found the mass and radius of the donor star to be  $13_{-7}^{+19} M_\odot$  and  $27_{-10}^{+21} R_\odot$ , respectively.

I derive a  $6.07411 \pm 0.00014$  d orbital period for XTE J1855-026 using the fundamental peak in the power spectrum. Using an  $O - C$  analysis (see Figures 2.1–2.3), I refine this to  $6.07413 \pm 0.00004$  d and fold the light curve on the refined orbital period to calculate the eclipse half-angle (see Figures 2.16 and 2.17). I calculate the duration of the observed eclipse to be  $98 \pm 2$  ks ( $1.13 \pm 0.02$  d), yielding an eclipse half-angle of  $33.6 \pm 0.7$  degrees (see Table 2.10). This indicates that the derived eclipse duration is

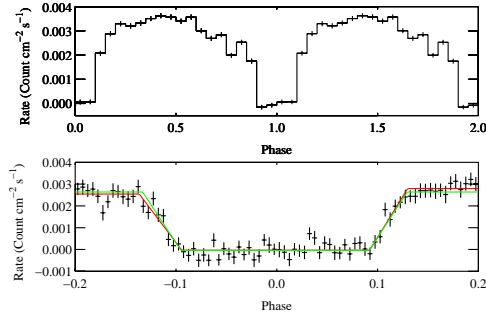


FIG. 2.16. *Swift*-BAT light curve of XTE J1855-026 in the 15–50 keV band folded on the orbital period (top) using 20 bins. T0 is defined as MJD 55079.0685, corresponding to mid-eclipse. A detailed folded light curve with 80 bins (bottom) is fit with both a symmetric “step and ramp” function (green) and asymmetric “step and ramp” function (red), which models the eclipse. The ingress and egress start times calculated using symmetric “step and ramp” function were shifted to align with those calculated with the asymmetric “step and ramp” function.

somewhat less than the result from Corbet & Mukai (2002) and is consistent with the measurement in Falanga et al. (2015). Using the quadratic orbital change function (see Equation 2.4), I find the orbital period derivative to be  $0.0 \pm 0.5 \times 10^{-7} \text{ d d}^{-1}$ , which is consistent with zero.

Since the upper limits of the stellar mass and radius are constrained by the orbital inclination where the Roche lobe is just filled, I again attach constraints on the mass and radius of the donor star as well as the mass of the compact object. I find the inclination where the donor star fills the Roche lobe to be  $76.4^\circ$ . The stellar mass and radius of the donor star are found to be  $19.6 \pm 1.1 M_\odot$  and  $21.5 \pm 0.5 R_\odot$  and  $20.2 \pm 1.2 M_\odot$  and  $23.0 \pm 0.5 R_\odot$  in the two limits (see Table 2.18). I find the mass of the neutron star to be between  $1.77 \pm 0.55 M_\odot$  and  $1.82 \pm 0.57 M_\odot$  (see Table 2.18), where the driving factor on the large error estimate is the uncertainty of  $\sim 31\%$  on the radial velocity semi-amplitude of the donor star as reported in González-Galán (2015).

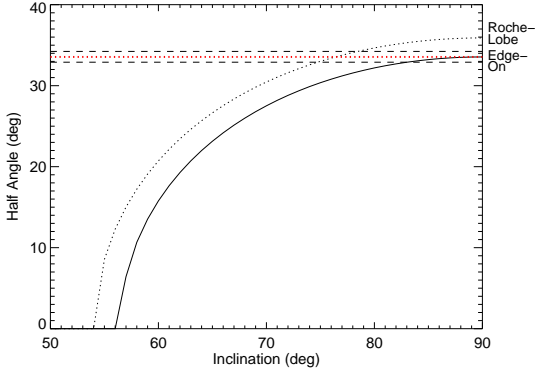


FIG. 2.17. The black curves show the predicted eclipse half angle of XTE J1855-026 as a function of inclination angle for stars with the indicated spectral types. The red and black dashed lines indicate the eclipse half angle and estimated error as measured by *Swift* BAT.

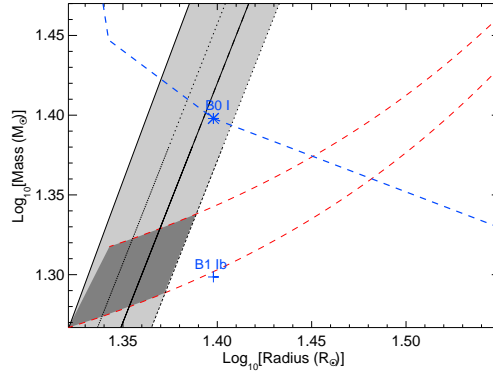


FIG. 2.18. Log-log plots of stellar masses as a function of stellar radii for XTE J1855-026. The shaded region indicates the allowed spectral types to satisfy the observed eclipse duration, pulse-timing and optical radial velocity constraints. Stellar masses and radii are reported in Table 2.10. Stars and crosses indicate the spectral types according to Carroll & Ostlie (2006) and Lefever et al. (2007), respectively.

## 2.5 Discussion

I discuss my findings for IGR J16393-4643, IGR J16418-4532, IGR J16479-4514, IGR J18027-2016 and XTE J1855-055. The radii for the previously proposed spectral types in IGR J16418-4532 and IGR J16479-4514 would significantly overfill the Roche lobe, which suggests an earlier spectral type. Below, I discuss in detail the nature of the mass donors in each system, mechanisms that could result in the residual emission observed in IGR J16393-4643 and comment on the nature of the eclipse profiles.

## 2.5.1 What is the nature of the mass donors in each system?

**2.5.1.1 IGR J16393-4643** My results show that stars with spectral type B0 V and B0-5 III satisfy the constraints imposed by the eclipse half-angle as well as the Roche lobe (see Section 2.4.1). While some supergiant stars such as a B0 I satisfy the eclipse half-angle, the required radius would be larger than the Roche lobe. I calculated the Roche-lobe radius for stars of spectral type B0 I to be  $18.5 R_{\odot}$ . This is clearly smaller than the radii reported in Carroll & Ostlie (2006) and Allen (2000), which are  $25 R_{\odot}$  and  $30 R_{\odot}$ , respectively (see Table 2.6). Since the radius for this proposed supergiant is too large to satisfy the constraint imposed by the Roche lobe, I suggest that if the donor star is a supergiant then it must be a slightly earlier spectral type.

IGR J16393-4643 was observed in the near-infrared on 2004 July 9 (MJD 53195.3) using the 3.5 m New Technology Telescope (NTT) at La Silla Observatory (Chaty et al., 2008). While Chaty et al. (2008) conclude that the spectral type of the donor star is BIV-V based on the spectral features and spectral energy distribution (SED), I note that Nespoli et al. (2008) proposed the donor star to be a K or M supergiant using the same SED. Furthermore, observations with the *Chandra* observatory show that the previously proposed counterpart is positionally inconsistent with the X-ray source (Bodaghee et al., 2012). Using the GLIMPSE survey, Bodaghee et al. (2012) proposed that the counterpart must be a distant reddened B-type star.

**2.5.1.2 IGR J16418-4532** My results show that while the derived masses and radii for the previously proposed spectral types satisfy the eclipse half-angle (see Table 2.7), the radius would be larger than the Roche-lobe size (Eggleton, 1983). An O8 I

star has a mass of  $28 M_{\odot}$  according to Carroll & Ostlie (2006) and Allen (2000). I find the maximum radius for a  $28 M_{\odot}$  star to satisfy the constraint imposed by the Roche lobe to be  $18.2 R_{\odot}$ . This is clearly smaller than the radii reported in Carroll & Ostlie (2006) and Allen (2000), which are  $22 R_{\odot}$  and  $20 R_{\odot}$ , respectively (see Table 2.7). Since the radius for each proposed spectral type is too large to satisfy the constraint imposed by the Roche lobe, it is my contention that the donor must be an earlier spectral type.

I find that spectral classes O7.5 I and earlier satisfy the constraint imposed by the Roche-lobe radius (see Table 2.11). The ratio between the radius of the donor star and that of the Roche lobe,  $\beta$ , is found to exceed 0.9, which is consistent with other HMXBs that host supergiants (Joss & Rappaport, 1984). Transitional Roche-lobe accretion has been proposed in IGR J16418-4532 where a fraction of the mass transfer is due to a focused wind (Sidoli et al., 2012). A focused wind or accretion stream requires a mass donor that nearly fills the Roche lobe. If this is the case, variations in the mass accretion rate that would be attributable to a focused wind or accretion stream would be expected (Blondin & Owen, 1997). This mechanism would lead to large variability in the X-ray intensity and could be observed in folded-light curves as well as hardness-intensity diagrams. Large intensity swings on the order of  $\sim 100$  were observed in both *Swift* and *XMM-Newton* observations of IGR J16418-4532 (Sidoli et al., 2012; Drave et al., 2013b).

Near-infrared spectral features previously led to a spectral classification of either a late O-type supergiant (Chaty et al., 2008) or BN0.5 Ia (Coleiro et al., 2013). I note the presumed radius of both spectral types overfills the Roche lobe, which shows that the proposed spectral classifications are incorrect. The spectral type of the mass donor places an additional constraint on the source distance. Under the assumption that the K-band

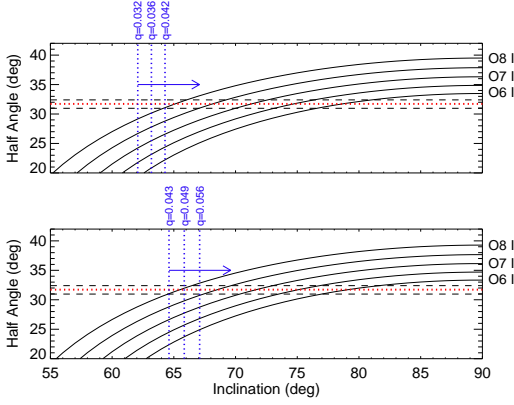


FIG. 2.19. The black curves show the predicted eclipse half angle as a function of inclination angle for stars with the candidate spectral types for IGR J16418-4532. The red and black dashed lines indicate the eclipse half angle and estimated error as measured by *Swift* BAT. I assume a neutron star mass of  $1.4 M_{\odot}$  (top) and of mass  $1.9 M_{\odot}$  (bottom) and typical masses and radii for the assumed companion spectral type (see Table 2.12). The blue vertical dashed lines indicate the lower limit of the inclination angle. Inclinations to the left of these correspond to stars that overflow the Roche lobe.

magnitude ( $m_K$ ) and extinction in the V-band ( $A_V$ ) are magnitudes 11.48 and 14.5 for an O8.5 I classification, Rahoui et al. (2008) found the distance of the source to be  $\sim 13$  kpc. Converting  $A_V$  to  $A_K$  using Table 3 in Rieke & Lebofsky (1985), I confirm the calculations for the distance of IGR J16418-4532 in Rahoui et al. (2008) using the distance modulus. The distance of IGR J16418-4532 assuming the aforementioned spectral types are reported in Table 2.11 using the values for  $M_V$  obtained from Wegner (2006) and Martins & Plez (2006). I also use the radius to distance ratio from the near-infrared spectral energy distribution (SED) measurements reported in Rahoui et al. (2008) together with my eclipse measurements to estimate the distance of IGR J16418-4532. I find the distance to be between 11.9–12.6 kpc, which is slightly smaller than that reported in Rahoui et al. (2008) for an O8 I star.

IGR J16418-4532 is a heavily absorbed SFXT where the observed  $N_H$ , measured to be between  $3.9_{-0.9}^{+1.2} \times 10^{22}$  atoms  $\text{cm}^{-2}$  and  $7 \pm 2 \times 10^{22}$  atoms  $\text{cm}^{-2}$  (Romano et al.,

2012), exceeds the values reported by the Leiden/Argentine/Bonn survey (Kalberla et al., 2005) and in the review by Dickey & Lockman (1990), which are  $1.59 \times 10^{22}$  and  $1.88 \times 10^{22}$  atoms  $\text{cm}^{-2}$ , respectively. Since the measured  $N_{\text{H}}$  was found to be in excess of the Galactic H I, determining the interstellar fraction of  $N_{\text{H}}$  is problematic and the value in Rahoui et al. (2008) for the extinction cannot be verified without the presence of systematic error.

I compare the observed value of the  $J - K$  color of  $2.39^3$  with the intrinsic  $(J - K)_0$  for the proposed mass donors (see Table 2.11). Calculating the difference between the observed  $J - K$  and the intrinsic  $(J - K)_0$ , I find the reddening values  $E(J - K)$  for each proposed spectral type for the mass donor (see Table 2.11). I calculate the reddening in the  $B - V$  band,  $E(B - V)$ , using Equation 1 in Güver & Oumlzel (2009) and the extinction in the V-band (Rahoui et al., 2008). Converting  $E(B - V)$  to  $E(J - K)$  using Table 3 in Rieke & Lebofsky (1985), I find  $E(J - K)$  to be 2.45. While this is slightly lower than what would be expected for late O supergiant spectral types (see Table 2.11), the presence of systematic error described above prevents an exact calculation.

These results show that stars with spectral type O7.5 I and earlier satisfy the constraints imposed by both the duration of the eclipse and the Roche lobe (see Figure 2.19). Since the measured  $N_{\text{H}}$  is largely in excess of interstellar values measured by Kalberla et al. (2005) and Dickey & Lockman (1990), determining what fraction of  $N_{\text{H}}$  is interstellar in origin is problematic. I find measurements such as the distance to be consistent with the distances determined by Rahoui et al. (2008). Given these measurements, spectral types near O7.5 I are reasonable. By constraining this type of star, I solved the first part

---

<sup>3</sup><http://www.iasfbo.inaf.it/~masetti/IGR/sources/16418.html>

of a three part problem. The remaining pieces include pulse-timing measurements which can be done in the X-ray and radial velocity measurements in the near-infrared.

**2.5.1.3 IGR J16479-4514** My results show that while the expected masses and radii for the previously proposed spectral types for IGR J16479-4514 satisfy the eclipse half-angle (see Table 2.8), the implied radius would be larger than the Roche-lobe radius (Eggleton, 1983). This is similar to the situation observed in IGR J16418-4532, which I describe in Section 2.5.1.2. I calculate the Roche-lobe radius for stars of spectral types O8.5 I and O9.5 Iab to be  $19.1 R_{\odot}$  and  $18.1 R_{\odot}$ , respectively (see Table 2.8). Since the radius for each proposed spectral type is too large to satisfy the constraint imposed by the Roche lobe (see Table 2.8), I suggest that the donor must be a slightly earlier spectral type.

I find that spectral classes O7 I and earlier satisfy the Roche-lobe constraint (see Table 2.12). The ratio between the radius of the donor star and that of the Roche lobe,  $\beta$ , is found to exceed 0.9, which is consistent with other HMXBs that host supergiants (Joss & Rappaport, 1984). Transitional Roche-lobe overflow has been proposed in IGR J16479-4514 (Sidoli et al., 2013), which requires a mass donor that nearly fills the Roche lobe. Sidoli et al. (2013) found phase-locked flares in their observation of IGR J16479-4514. Sidoli et al. (2013) attributes the physical mechanism responsible for these flares which are spaced 0.2 in phase as large-scale structures in the wind.

Using near-infrared spectral features, Chaty et al. (2008) previously determined the spectral classification of the donor star to be a late O-type supergiant (Chaty et al., 2008). The donor spectral type places an additional constraint on the distance of IGR J16479-

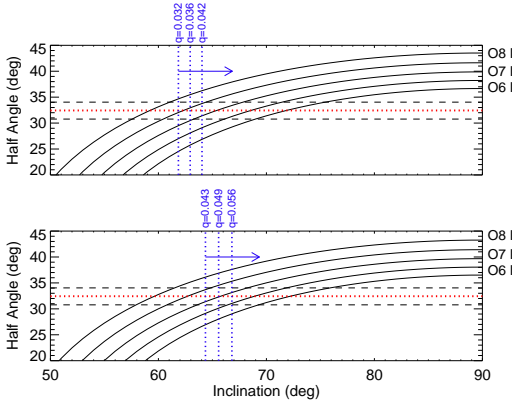


FIG. 2.20. The black curves show the predicted eclipse half angle as a function of inclination angle for stars with the candidate spectral types for IGR J16479-4514. The red and black dashed lines indicate the eclipse half angle and estimated error as measured by *Swift* BAT. I assume a neutron star mass of  $1.4 M_{\odot}$  (top) and of mass  $1.9 M_{\odot}$  (bottom) and typical masses and radii for the assumed companion spectral type (see Table 2.12). The blue vertical dashed lines indicate the lower limit of the inclination angle. Inclinations to the left of these correspond to stars that overflow the Roche lobe.

4514. The K-band magnitude ( $m_K$ ) and the extinction in the V-band ( $A_V$ ) are found to be 9.79 and 18.5 (Rahoui et al., 2008). Additionally, the  $R_*/D_*$  ratio was found to be  $1 \times 10^{-10}$  (Chaty et al., 2008). Using this information, the minimum distance of IGR J16479-4514 was found to be  $\sim 4.9$  kpc (Chaty et al., 2008). Converting  $A_V$  to  $A_K$  using Table 3 in Rieke & Lebofsky (1985), I find  $A_K$  to be 2.07 and confirm the calculation for the distance of IGR J16479-4514 using the distance modulus. The distances of IGR J16479-4514 assuming the aforementioned spectral types are reported in Table 2.12 using the values for  $M_V$  obtained from Wegner (2006) and Martins & Plez (2006). I find that the distance of stars with spectral type O7 I and earlier to be between 4.4–4.6 kpc, which are reasonably consistent with the measurements in Rahoui et al. (2008).

IGR J16479-4514 is a heavily absorbed SFXT where the  $N_H$  was measured to be  $9.5 \pm 0.3 \times 10^{22}$  atoms  $\text{cm}^{-2}$  (Sidoli et al., 2013). This is an order of magnitude larger than the Galactic H I values reported by the Leiden/Argentine/Bonn survey (Kalberla et

al., 2005) and in the review by Dickey & Lockman (1990), which are  $1.87 \times 10^{22}$  and  $2.14 \times 10^{22}$  atoms  $\text{cm}^{-2}$ , respectively. Since the measured  $N_{\text{H}}$  for both sources was found to be in excess of the Galactic H I, determining the interstellar fraction of  $N_{\text{H}}$  is difficult. Therefore, I cannot verify the value for the extinction in Rahoui et al. (2008) without the presence of systematic error.

I calculate the reddening values  $E(J - K)$  for each proposed spectral type for the mass donor (see Table 2.12) using the observed value of the  $J - K$  color of  $3.27^4$  and the intrinsic  $(J - K)_0$  for the proposed mass donors (see Table 2.12). To check for consistency with late O supergiant stars, I compare this with the reddening in the  $B - V$  band using Equation 1 in Güver & Oumlzel (2009) and the extinction in the V-band ( $A_V$ ) (Rahoui et al., 2008). Converting  $E(B - V)$  to  $E(J - K)$  using Table 3 in Rieke & Lebofsky (1985), I find the reddening in the  $E(J - K)$  band to be 3.12. While this is slightly lower than what would be expected for late O supergiant spectral types, the presence of systematic errors, described above prevents an exact calculation.

Stars with spectral type O7 I and earlier satisfy the eclipse duration and Roche-lobe constraints (see Figure 2.20). Determining the interstellar fraction of  $N_{\text{H}}$  is difficult since the measured  $N_{\text{H}}$  is greatly in excess of interstellar values. I find the distance of the proposed counterparts to be consistent with those determined by Rahoui et al. (2008). Since no pulsation period has been identified, the next step to constrain the donor star would be radial velocity measurements in the near-infrared.

---

<sup>4</sup><http://www.iasfbo.inaf.it/~masetti/IGR/sources/16479.html>

**2.5.1.4 IGR J18027-2016** My results show that the mass and radius of the donor star in IGR J18027-2016 can be constrained to be between  $18.6 \pm 0.9 M_{\odot}$  and  $17.4 \pm 0.9 R_{\odot}$  and  $19.4 \pm 0.9 M_{\odot}$  and  $19.5^{+0.8}_{-0.7} R_{\odot}$  for edge-on orbits and inclinations where the Roche lobe is completely filled, respectively. I find the inclination where the Roche lobe is filled to be  $73.3^{\circ}$ , which is consistent with the earlier results from Mason et al. (2011). Since the semi-amplitude of the radial velocities of both the donor star and compact object are known, I also find that the mass of the neutron star can be constrained. I calculate the mass of the neutron star to be between  $1.37 \pm 0.19 M_{\odot}$  and  $1.43 \pm 0.20 M_{\odot}$  for the lower and upper limits (see Section 2.4.4).

Since the radius of the donor star is constrained, I also can estimate the distance, optical and near infrared magnitudes of IGR J18027-2016. Using SED measurements, Chaty et al. (2008) calculated the radius to distance ratio to be  $4 \pm 1 \times 10^{-11}$ , where the uncertainties are at the 90% confidence interval. At the 90% confidence interval, I find the eclipse half-angle to be  $34^{+4}_{-3}$  and the radius of the donor star to be constrained to between  $17^{+2}_{-1} R_{\odot}$  and  $19 \pm 1 R_{\odot}$  in the two limits described in Section 2.4.4. Combining my results for the radius of the donor star with the radius to distance ratio (Table 6; Chaty et al., 2008), I find that the distance of IGR J18027-2016 can be constrained to  $11 \pm 2$  kpc and  $12 \pm 2$  kpc in the two limits. Using the distance modulus (e.g. Nespoli et al., 2008), the absolute magnitude of IGR J18027-2016 can be calculated. The apparent magnitude in the R-band,  $R$ , and the extinction in the V-band,  $A_V$  were found to be 16.9 and 8.5 (Masetti et al., 2008). I find the absolute magnitude in the R-band,  $M_R$  to be  $\sim -5$  at both constraints, which is what would be expected for a B-type supergiant (Martins & Plez, 2006; Wegner, 2006).

My results are consistent with the previously proposed B1 Ib (Torrejón et al., 2010) or B0-B1 I (Mason et al., 2011) spectral types in IGR J18027-2016. I constrain the mass and radius of the donor star to be between  $18.6\text{--}19.4 M_{\odot}$  and  $17.4\text{--}19.5 R_{\odot}$ . I also constrain the mass of the neutron star to be  $1.18\text{--}1.63 M_{\odot}$ , which marginally improves on the results in Mason et al. (2011), which was found to be  $1.15\text{--}1.85 M_{\odot}$ .

**2.5.1.5 XTE J1855-026** I find that the mass and radius of the donor star in XTE J1855-026 are constrained between  $19.6\pm 1.1 M_{\odot}$  and  $21.5\pm 0.5 R_{\odot}$  at edge-on orbits to  $20.2\pm 1.2 M_{\odot}$  and  $23.0\pm 0.5 R_{\odot}$  where the Roche lobe is just filled. The inclination where the Roche lobe is filled is found to be  $76.4^{\circ}$ . I find the derived masses and radii to be consistent with those reported in Carroll & Ostlie (2006) and Allen (2000) for stars with spectral type B0 I. Since the semi-amplitude of the radial velocities for both the donor star and compact object are known, I find that the mass of the neutron star can be constrained to be between  $1.77\pm 0.55 M_{\odot}$  and  $1.82\pm 0.57 M_{\odot}$  (see Section 2.4.5). I note that the large error estimates in the mass of the neutron star are likely to be attributed to substantial uncertainties in the estimate in  $K_{\circ}$  as reported in González-Galán (2015). This is likely to be attributed to emission line contamination and/or changes in the stellar wind.

Based on optical and near-infrared spectra together with the analysis reported in Verrecchia et al. (2002), the spectral type of the donor star was previously determined to be a B0 Iaep (Negueruela et al., 2008). Based on the ratio of the equivalent widths of Si IV to Si III which is a diagnostic for supergiant spectral types (Walborn, 1971), the mass donor was recently refined to a BN0.2 Ia by González-Galán (2015). Using SED measurements, Coleiro & Chaty (2013) calculated the radius and distance to be  $26.9 R_{\odot}$

and  $10.8 \pm 1.0$  kpc, which places XTE J1855-026 in the Scutum arm region. Combining the properties of the newly derived spectral type with the distance modulus, González-Galán (2015) recently calculated the nominal distance of XTE J1855-026 to be  $10_{-4}^{+7}$  kpc. Based on these results, the radius to distance ratio can be calculated to be  $5.6 \pm 0.5 \times 10^{-11}$ . Combining my results for the radius of the donor star with the calculated radius to distance ratio, I find the distance of XTE J1855-026 can be constrained to  $8.6 \pm 0.8$  kpc and  $9.2 \pm 0.9$  kpc in the two limits.

Corbet et al. (1999) measured the  $N_{\text{H}}$  in XTE J1855-026 to be  $14.7 \pm 0.6 \times 10^{22}$  atoms  $\text{cm}^{-2}$ , which exceeds the values reported by the Leiden/Argentine/Bonn survey (Kalberla et al., 2005) and in the review by Dickey & Lockman (1990). In a *Swift* XRT observation, the  $N_{\text{H}}$  was found to be  $4.1 \pm 0.5 \times 10^{22}$  atoms  $\text{cm}^{-2}$  (Romano et al., 2008). These are significantly larger than the measurements for the interstellar  $N_{\text{H}}$ , which are  $6.62 \times 10^{21}$  atoms  $\text{cm}^{-2}$  (Kalberla et al., 2005) and  $7.35 \times 10^{21}$  atoms  $\text{cm}^{-2}$  (Dickey & Lockman, 1990). Since the measured  $N_{\text{H}}$  was found to be in excess of the Galactic H I, the conversion between the interstellar  $N_{\text{H}}$  and the extinction  $A_{\text{V}}$  is problematic and the value of  $5.8 \pm 0.9$  in Coleiro & Chaty (2013) cannot be verified without the presence of systematic error.

### 2.5.2 What is the nature of the non-zero eclipse flux in IGR J16393-4643?

The source flux during eclipse in IGR J16393-4643 does not reach 0 counts  $\text{s}^{-1}$  in the folded light curves (see Figure 2.4). I find the ratio between the flux during eclipse to the flux outside eclipse to be  $54 \pm 5\%$ . This is significantly larger than what is observed in the other XRBs in this study (see Table 2.1).

I first discuss the possible scenario where we observe a partial eclipse in IGR

J16393-4643. In my model for the eclipse (see Section 2.3.2), I assume the compact object to be a point source (Joss & Rappaport, 1984). While this is a valid assumption since the radius of the compact object is much smaller than that of the donor star, this approximation does not consider the extended X-ray emission region. In this case, the constraints on the mass and radius of the donor star must take into account the size of the extended emission region. Since a significant residual flux is observed, it is likely a partial eclipse is observed.

I also consider the possibility that the residual emission observed in IGR J16393-4643 is attributed to a dust-scattering halo similar to what is observed in some other HMXBs (Cen X-3; Vela X-1; OAO 1657-415, Day & Tennant, 1991; Woo et al., 1994; Audley et al., 2006). While residual emission has been attributed to dust-scattering in some other HMXBs, the residual emission found in IGR J16393-4643 in the BAT folded light curves (15–50 keV) is seen at much higher levels (see Table 2.1). A dust-scattering halo is predominantly a soft X-ray phenomenon. While a significant fraction of the out-of-eclipse flux may be in a dust-scattering halo (Predehl & Schmitt, 1995), I expect a smaller fraction to be in the energies resolved by BAT. Therefore, it can be concluded that a dust-scattering halo cannot be the sole mechanism responsible for the residual emission seen in the folded light curves.

Finally, I discuss the possibility that Compton scattering and reprocessing in a region of dense gas could account for the residual flux in eclipse. Bodaghee et al. (2006) found that a Compton emission (`comptt` within `Xspec`) model with an electron temperature of  $4.4 \pm 0.3$  keV and optical depth of  $9 \pm 1$  provides a good fit to the average spectrum of IGR J16393-4643. Additionally, Fe  $K\alpha$  and Fe  $K\beta$  lines were found at 6.4 keV and

7.1 keV, respectively, where the ratio of the iron intensities is seen to be consistent with photoionization (Bodaghee et al., 2006; Kaastra & Mewe, 1993; Islam et al., 2015). The equivalent widths (EQW) in the *XMM-Newton* observation were found to be  $60 \pm 30$  eV and an upper limit of 120 eV, for the Fe  $K\alpha$  and Fe  $K\beta$  lines respectively (Bodaghee et al., 2006). In a recent *Suzaku* observation, the EQW of the Fe  $K\alpha$  and Fe  $K\beta$  lines were found to be  $46^{+7}_{-6}$  eV and an upper limit of 30 eV (Islam et al., 2015). While the mechanism responsible for the Fe  $K\alpha$  and Fe  $K\beta$  emission is likely to be fluorescence of cold matter, the equivalent widths point to a likely origin in a spherical distribution of dense gas (Bodaghee et al., 2006). Therefore, Compton scattering and reprocessing might be the sole contributor to the residual emission observed in the BAT folded light curves.

It is likely that a combination of the mechanisms described above account for the residual emission found in the folded light curves of IGR J16393-4643 (see Section 2.4.1). Since the count rate during eclipse is significantly larger than what is observed in most other eclipsing HMXBs, it is likely that only a small fraction comes from a dust-scattering halo.

### **2.5.3 What mechanism is responsible for asymmetries in the eclipse profile?**

The eclipse profiles show the presence of asymmetries (see Tables 2.2 and 2.3) as previously noted by Falanga et al. (2015) in the cases of IGR J18027-2016 and XTE J1855-026 and Jain et al. (2009a) in the case of IGR J16479-4514. These asymmetries seen in the ingress and egress durations are suggestive of the presence of complex structures in the wind such as accretion or photoionization wakes.

I first discuss the possible case that the asymmetry in the eclipse profiles can be

attributed to accretion wakes. In an HMXB driven entirely by a spherical wind, material is only accreted in a cylindrical region where the kinetic energy is less than the gravitational potential energy of the compact object. The radius of the accretion cylinder is the Bondi-Hoyle accretion radius (Equation 1, Feldmeier et al., 1996). Perturbed material forms an “accretion wake” that typically trails the orbit of the neutron star and results in large intrinsic column densities (Blondin et al., 1990). Prior to eclipse, the progressively increasing  $N_{\text{H}}$  partially obscures the X-ray emission resulting in longer ingress durations compared to the duration of egress. Since the accretion wake is located beyond the compact object during egress, no apparent increase in the intrinsic  $N_{\text{H}}$  is observed. The ingresses observed are somewhat larger than egress, which is consistent with the presence of an accretion wake (Blondin et al., 1990). The count rate prior to ingress is also somewhat smaller than that observed after egress, providing additional evidence for accretion wakes. Hardness ratios or measurements of  $N_{\text{H}}$  folded on the orbital period could be implemented to confirm the possibility of accretion wakes.

I also consider the possibility that photoionization wakes could explain the asymmetric eclipse profiles. The eclipse profiles of IGR J18027-2016 and XTE J1855-026 are compared to those seen in eclipsing systems where asymmetric density enhancements are observed on large spatial dimensions (e.g. Vela X-1; Feldmeier et al., 1996). In systems where the X-ray luminosity is significantly high, a switch-off of the radiative driving force could lead to a reduced wind velocity and enhanced wind density (Feldmeier et al., 1996). This enhanced X-ray scattering region trails the neutron star and results in ingress durations that are significantly larger than those observed at egress (Feldmeier et al., 1996). The eclipse profiles of IGR J18027-2016 and XTE J1855-026 differ from those expected

from a photoionization wake—the ingress duration in Vela X-1 was seen to be  $\Delta\phi = 0.11$  (Feldmeier et al., 1996).

I additionally discuss how energy dependence in the asymmetric eclipse profiles can arise. The high  $N_{\text{H}}$ , on the order of  $10^{23}$  atoms  $\text{cm}^{-2}$ , implies the presence of a strong circumstellar wind (Kuulkers, 2005), and the X-ray absorption due to this will lead to sharper ingress and egress transitions compared to that seen at lower energies. In a *Suzaku* observation of IGR J16479-4514 that covers part of the eclipse, Sidoli et al. (2013) found the egress transition to be broader in soft energies. In their review, Falanga et al. (2015) found asymmetries to be slightly enhanced at lower energies compared to higher energies. While investigating the energy dependence in the eclipse transitions is beyond the scope of the present paper, this study in obscured SGXBs will be difficult due to a reduced count rate at low energies that results from the large intrinsic absorption present in these systems (Falanga et al., 2015).

Finally, I consider the possibility that the asymmetric eclipse profiles could be attributed to a small to modest eccentricity. Since objects with relatively short orbital periods were considered, the eccentricity of the systems can be expected to be near zero (Zahn, 1977; Maccarone et al., 2014). The eccentricity in IGR J18027-2016 and XTE J1855-026 were both noted to be small to modest, where  $e$  was found to be less than 0.2 and 0.04, respectively (Augello et al., 2003; Corbet & Mukai, 2002). In the cases of IGR J16393-4643, IGR J16418-4532 and IGR J16479-4514 where no pulse-timing or radial-velocity methods are available to determine an orbital solution, I constrain the maximum allowed eccentricity to that where the radius of the donor star completely fills the Roche lobe at periastron (Goossens et al., 2013, and references therein). These were all found to

be near zero (see Figure 2.21). Since the eccentricities are found to be small to modest, the asymmetries are not expected to result in sizeable asymmetries in the eclipse profile. Additionally, apsidal advance will be apparent in the case that an eccentric orbit could lead to asymmetries in the eclipse profile. While apsidal advance would be difficult to detect in the  $\sim 9$  yr of *Swift* data, it is unlikely for asymmetries to be solely attributed to small to modest eccentricities. Furthermore, accurate measurements of apsidal advance will depend on multiple pulse-timing measurements of these systems, which are not yet available.

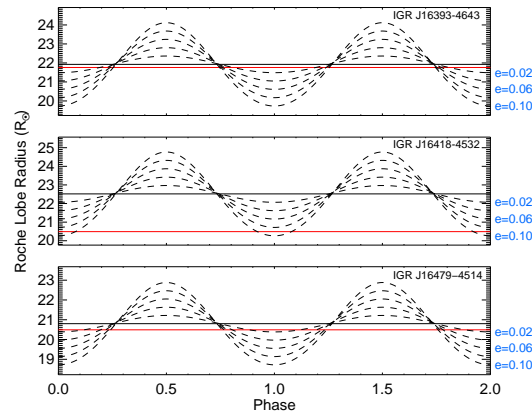


FIG. 2.21. A sample plot of the Roche-lobe radius of the donor stars in IGR J16393-4643 (top), IGR J16418-4532 (middle) and IGR J16479-4514 (bottom) vs. orbital phase for eccentricities ranging from 0.0 to 0.1 in steps of 0.02. The horizontal red line represents the radius of the donor star under the assumption that the donor is an O9 I for IGR J16393-4643 and O7 I for both IGR J16418-4532 and IGR J16479-4514 (Martins et al., 2005).

## 2.6 Conclusion

Eclipsing X-ray binaries provide an opportunity to constrain the physical parameters of the donor star as well as the compact object. To determine the eclipse half-angle in this survey, I modeled the eclipses using both symmetric and asymmetric step-and-ramp functions. The luminosity of each system is less than expected for Roche-lobe overflow

(Kaper et al., 2004), which means the constraint that the mass donor underfills the Roche lobe can be attached. Since IGR J18027-2016 and XTE J1855-026 are the only “double-lined binaries” in this sample, I calculate the parameters of the other systems assuming the neutron stars to be at the white-dwarf Chandrasekhar limit,  $1.4M_{\odot}$ . I also calculated the parameters of the other systems assuming a more massive neutron star— $1.9M_{\odot}$ .

My results show that stars with spectral type B III satisfy both constraints imposed by the eclipse duration and Roche lobe for IGR J16393-4643. Assuming the estimates for the mass and radius of a B5 III star reported in Carroll & Ostlie (2006), I find the mass and radius of the donor star to exceed  $7 M_{\odot}$  and  $6.3 R_{\odot}$ . B I stars were found to overfill the Roche lobe. The source emission in IGR J16393-4643 does not reach 0 counts  $s^{-1}$  in the folded light curves, where the fraction between the flux in eclipse to that outside eclipse was found to be  $54 \pm 5\%$  (see Tables 2.1– 2.3). Compton scattering and reprocessing in a dense region of gas could possibly account for the X-ray emission region not obscured by the donor star.

My results show that the previously proposed O8.5 I and BN0.5 Ia spectral types for the mass donor in IGR J16418-4532 must be excluded. While these spectral types satisfy the eclipse half-angle, the Roche lobe is significantly overfilled. Stars with spectral type O7.5 I or earlier are consistent with both the eclipse half-angle and the Roche lobe. In this case, I find the mass and radius of the donor star to exceed  $36.00 M_{\odot}$  and  $20.79 R_{\odot}$  assuming the estimates for the mass and radius of an O7.5 I star reported in Martins et al. (2005). I find the minimum inclination angle of the system to be  $67^{\circ}$ . The distance measurements of IGR J16418-4532 are consistent with the previously determined distance (see Table 2.11); however, determining the interstellar fraction of  $N_{\text{H}}$  was found to be

problematic. The ingress and egress durations in the folded light curves were found to be asymmetric where the ingress duration is longer than the egress duration. This is likely attributed to the presence of an accretion wake or from a focused stream as noted in Sidoli et al. (2012) and Drave et al. (2013b).

The previously proposed O8.5 Ia and O9.5 Iab spectral classifications of the mass donor in IGR J16479-4514 must be excluded because the Roche lobe is significantly overfilled. However, I found that stars with spectral type O7 I and earlier satisfy both constraints imposed by the eclipse duration and Roche lobe. Assuming the estimates for the mass and radius of an O7 I star reported in Martins et al. (2005), the mass and radius of the donor star are found to exceed  $38.44 M_{\odot}$  and  $20.49 R_{\odot}$ , respectively. I find the minimum inclination angle of the system to be  $63^{\circ}$ . The distance measurements remain unchanged from earlier measurements (see Table 2.12); however, the interstellar fraction of  $N_{\text{H}}$  remains undetermined. I find the ingress and egress durations to be symmetric within the error bars. The ratio between the radius of the donor star and Roche lobe was found to exceed 0.9, which shows the possibility of transitional Roche-lobe overflow.

The mass and radius of the donor star in IGR J18027-2016 were constrained to  $18.6 \pm 0.9 M_{\odot}$  and  $17.4 \pm 0.9 R_{\odot}$  and  $19.4 \pm 0.9 M_{\odot}$  and  $19.5^{+0.8}_{-0.7} R_{\odot}$  in the two limits. I find the inclination angle where the donor star just fills the Roche lobe size to be  $73.3^{\circ}$ . I also find the distance measurements of IGR J18027-2016 to be  $11 \pm 2$  kpc and  $12 \pm 2$  kpc in the allowed limits. In the allowed limits, I constrained the mass of the neutron star to between  $1.37 \pm 0.19 M_{\odot}$  and  $1.43 \pm 0.20 M_{\odot}$ . The folded light curve shows complicated and asymmetric ingress and egress durations, which can be explained by the presence of accretion wakes.

My results show the mass and radius of the donor star in XTE J1855-026 to be constrained to  $19.6 \pm 1.1 M_{\odot}$  and  $21.5 \pm 0.5 R_{\odot}$  at edge-on orbits to  $20.2 \pm 1.2 M_{\odot}$  and  $23.0 \pm 0.5 R_{\odot}$  where the Roche lobe size is just filled. I find the inclination angle where the donor star just fills the Roche lobe size to be 76.4 degrees. In the allowed limits, I find the distance of XTE J1855-026 can be constrained to  $8.6 \pm 0.8$  kpc and  $9.2 \pm 0.9$  kpc. I find the mass of the neutron star to be constrained between  $1.77 \pm 0.55 M_{\odot}$  and  $1.82 \pm 0.57 M_{\odot}$ . Complicated and asymmetric ingress and egress durations were seen in the folded light curve, which suggests the presence of complex structure in the wind.

To further constrain the physical parameters of the donor star and the compact object in all these systems, additional observations are required. Constraining the mass of the neutron star will help constrain the Equation-of-State. Since the pulse period has been accurately measured, for IGR J16393-4643 and IGR J16418-4532 the study would benefit from both pulse-timing analysis as well as radial-velocity curves in the near-infrared. A radial-velocity curve in the optical or near-infrared would provide additional constraints for IGR J16479-4514 where a pulse-period has yet to be identified.

Source	Orbital Cycle (N)	Mid-eclipse time <sup>a</sup> (MJD)	Mid-eclipse time <sup>b</sup> (MJD)
IGR J16393-4643	-313	53748.46±0.03	53748.44±0.03
IGR J16393-4643	-155	54418.15 <sup>+0.04</sup> <sub>-0.02</sub>	54418.14 <sup>+0.04</sup> <sub>-0.03</sub>
IGR J16393-4643	1	55079.22 <sup>+0.07</sup> <sub>-0.02</sub>	55079.22 <sup>+0.03</sup> <sub>-0.02</sub>
IGR J16393-4643	158	55744.55 <sup>+0.02</sup> <sub>-0.03</sub>	55744.54 <sup>+0.02</sup> <sub>-0.08</sub>
IGR J16393-4643	315	<sup>c</sup>	<sup>c</sup>
IGR J16418-4532	-359	53745.50±0.01	53745.491 <sup>+0.013</sup> <sub>-0.009</sub>
IGR J16418-4532	-179	54418.461 <sup>+0.009</sup> <sub>-0.010</sub>	54418.468±0.009
IGR J16418-4532	0	55087.71±0.01	55087.72±0.01
IGR J16418-4532	179	55756.963 <sup>+0.011</sup> <sub>-0.008</sub>	55756.967±0.009
IGR J16418-4532	357	56422.47±0.02	56422.47 <sup>+0.02</sup> <sub>-0.01</sub>
IGR J16479-4514	-402	53747.19 <sup>+0.02</sup> <sub>-0.03</sub>	53747.21 <sup>+0.02</sup> <sub>-0.03</sub>
IGR J16479-4514	-200	54417.63±0.02	54417.61 <sup>+0.03</sup> <sub>-0.02</sub>
IGR J16479-4514	0	55081.47 <sup>+0.03</sup> <sub>-0.02</sub>	55081.48 <sup>+0.02</sup> <sub>-0.03</sub>
IGR J16479-4514	200	55745.33 <sup>+0.03</sup> <sub>-0.04</sub>	55745.28±0.04
IGR J16479-4514	401	56412.60 <sup>+0.06</sup> <sub>-0.04</sub>	56412.59 <sup>+0.03</sup> <sub>-0.04</sub>
IGR J18027-2016	-292	53749.41 <sup>+0.05</sup> <sub>-0.03</sub>	53749.40 <sup>+0.04</sup> <sub>-0.05</sub>
IGR J18027-2016	-143	54430.32±0.02	54430.34 <sup>+0.04</sup> <sub>-0.02</sub>
IGR J18027-2016	0	55083.79 <sup>+0.02</sup> <sub>-0.03</sub>	55083.85 <sup>+0.08</sup> <sub>-0.03</sub>
IGR J18027-2016	146	55751.02±0.03	55751.06 <sup>+0.03</sup> <sub>-0.04</sub>
IGR J18027-2016	292	56418.12 <sup>+0.02</sup> <sub>-0.03</sub>	56418.20 <sup>+0.03</sup> <sub>-0.04</sub>
XTE J1855-026	-219	53748.82±0.01	53748.84±0.01
XTE J1855-026	-109	54416.99±0.02	54416.99±0.02
XTE J1855-026	0	55079.05±0.01	55079.09 <sup>+0.02</sup> <sub>-0.03</sub>
XTE J1855-026	110	55747.20±0.01	55747.21±0.02
XTE J1855-026	219	56409.30±0.02	56409.33±0.02

Table 2.4. Mid-eclipse Time Measurements For  $O - C$  Analysis

<sup>a</sup> Obtained using the symmetric step-and-ramp function.

<sup>b</sup> Obtained using the asymmetric step-and-ramp function.

<sup>c</sup> A bad fit for IGR J16393-4643 was obtained in the mid-eclipse time between MJD 56079–56745.

Source	Orbital Cycle (N)	Mid-eclipse time (MJD)	Satellite (MJD)	Reference
IGR J16393-4643	-391	53417.955	<i>Swift</i>	Islam et al. (2015)
IGR J16479-4514	-161	54547.05418	<i>Swift</i>	Bozzo et al. (2009)
IGR J18027-2016	-638	52168.22±0.12	<i>BeppoSAX</i>	Augello et al. (2003)
IGR J18027-2016	-638	52168.26±0.04	<i>BeppoSAX</i>	Hill et al. (2005)
IGR J18027-2016	-471	52931.37±0.04	<i>INTEGRAL</i>	Hill et al. (2005)
IGR J18027-2016	-399	53260.37±0.07	<i>INTEGRAL</i>	Jain et al. (2009b)
IGR J18027-2016	-286	53776.82±0.07	<i>Swift</i>	Jain et al. (2009b)
IGR J18027-2016	-267	53863.10±0.14	<i>INTEGRAL</i>	Falanga et al. (2015)
IGR J18027-2016	-127	54503.38±0.07	<i>Swift</i>	Jain et al. (2009b)
XTE J1855-026	-590	51495.25±0.02	<i>RXTE</i>	Corbet & Mukai (2002)
XTE J1855-026	-391	52704.04±0.05	<i>INTEGRAL</i>	Falanga et al. (2015)
XTE J1855-026	-176	54009.97±0.05	<i>INTEGRAL</i>	Falanga et al. (2015)
XTE J1855-026	-31	54890.68±0.05	<i>INTEGRAL</i>	Falanga et al. (2015)

Table 2.5. Historic Mid-eclipse Time Measurements For IGR J18027-2016 and XTE J1855-026

Historical mid-eclipse times for IGR J16479-4514, IGR J18027-2016 and XTE J1855-026 found using *RXTE*, *Swift* BAT and *INTEGRAL*.

Spectral Type	$M/M_{\odot}$	$q^a$	$R/R_{\odot}$	$R_L/R_{\odot}^b$	$i_{\min}^{\circ c}$
<i>B0 III</i>	20	0.070	13	18.5	68
<i>B5 III</i>	7	0.200	6.3	11.7	79
<i>B0 V</i>	17.5	0.080	8.4	17.5	79
<i>B0 I</i>	25	0.056	25 <sup>d</sup>	20.4 <sup>d</sup>	41

Table 2.6. Physical Parameters for Previously Proposed Mass Donors for IGR J16393-4643

<sup>a</sup> The mass ratio,  $q$ , is defined as  $M_x/M_c$  where  $M_x$  is the compact object and  $M_c$  is the donor star.

<sup>b</sup> The definition for the Roche lobe,  $R_L$ , as given in Eggleton (1983), assuming  $M_{NS}$  is  $1.4 M_{\odot}$ .

<sup>c</sup> The minimum inclination angle of the system that is consistent with the measured eclipse half-angle.

<sup>d</sup> A B0 I classification significantly overfills the Roche lobe and are therefore, it is excluded from my analysis.

Spectral Type	$M/M_{\odot}$	$q^a$	$R/R_{\odot}$	$R_L/R_{\odot}^b$	$i_{\min}^{\circ c}$
<i>O8.5 I</i>	31.54	0.044	21.41 <sup>c</sup>	20.71 <sup>c</sup>	61–63
<i>O8.5 I</i>	33.90	0.041	22.20 <sup>c</sup>	21.35 <sup>c</sup>	60–62
<i>O9 I</i>	29.63	0.047	21.76 <sup>c</sup>	20.17 <sup>c</sup>	58–60
<i>O9 I</i>	31.95	0.044	22.60 <sup>c</sup>	20.82 <sup>c</sup>	57–59

Table 2.7. Physical Parameters for Previously Proposed Mass Donors for IGR J16418-4532

<sup>a</sup> The mass ratio,  $q$ , is defined as  $M_x/M_c$  where  $M_x$  is the compact object and  $M_c$  is the donor star.

<sup>b</sup> The definition for the Roche lobe,  $R_L$ , as given in Eggleton (1983), assuming  $M_{\text{NS}}$  is  $1.4 M_{\odot}$ .

<sup>c</sup> The minimum inclination angle of the system that is consistent with the measured eclipse half-angle.

<sup>d</sup> A B0 I classification significantly overfills the Roche lobe and are therefore, it is excluded from my analysis.

Spectral Type	$M/M_{\odot}$	$q^a$	$R/R_{\odot}$	$R_L/R_{\odot}^b$	$i_{\min}^{\circ c}$
<i>O8.5 I</i>	31.54	0.044	21.41 <sup>c</sup>	19.13 <sup>c</sup>	55–58
<i>O8.5 I</i>	33.90	0.041	22.20 <sup>c</sup>	19.73 <sup>c</sup>	54–56
<i>O9.5 I</i>	27.83	0.050	22.11 <sup>c</sup>	18.14 <sup>c</sup>	48–51
<i>O9.5 I</i>	30.41	0.046	23.11 <sup>c</sup>	18.84 <sup>c</sup>	47–49

Table 2.8. Physical Parameters for Previously Proposed Mass Donors for IGR J16479-4514

<sup>a</sup> The mass ratio,  $q$ , is defined as  $M_x/M_c$  where  $M_x$  is the compact object and  $M_c$  is the donor star.

<sup>b</sup> The definition for the Roche lobe,  $R_L$ , as given in Eggleton (1983), assuming  $M_{\text{NS}}$  is  $1.4 M_{\odot}$ .

<sup>c</sup> The minimum inclination angle of the system that is consistent with the measured eclipse half-angle.

<sup>d</sup> A B0 I classification significantly overfills the Roche lobe and are therefore, it is excluded from my analysis.

Parameter	Value
$P_{\text{orb}}^a$	$4.56993 \pm 0.00003$ d
$P_{\text{pulse}}^b$	$139.61 \pm 0.04$ s
$a_x \sin i^b$	$68 \pm 1$ lt-s
$K_o^c$	$23.8 \pm 3.1$ km s <sup>-1</sup>
$T_{\text{mid}}$	BMJD 55083.82 $\pm$ 0.01
$f(M)^b$	$16 \pm 1 M_{\odot}$
$q^c$	$0.07 \pm 0.01$
$\Theta_e$	$34 \pm 2^{\circ}$
$M_{\text{donor}}$	$18.6 \pm 0.9 - 19.4 \pm 0.9 M_{\odot}$
$R_{\text{donor}}$	$17.4 \pm 0.9 - 19.5_{-0.7}^{+0.8} R_{\odot}$
$a$	$31.4 - 33.2 R_{\odot}$
$M_{\text{NS}}$	$1.37 \pm 0.19 - 1.43 \pm 0.20 M_{\odot}$
$i$	$73.3 - 90^{\circ}$

Table 2.9. System Parameters for IGR J18027-2016

<sup>a</sup> The orbital period is refined using an  $O - C$  analysis.

<sup>b</sup> The pulse period, projected semi-major axis and mass function are given in Hill et al. (2005).

<sup>c</sup> The semi-amplitude of the radial velocity of the mass donor and mass ratio are given in Mason et al. (2011).

Parameter	Value
$P_{\text{orb}}^a$	$6.07413 \pm 0.00004$ d
$P_{\text{pulse}}^b$	$360.741 \pm 0.002$ s
$\dot{P}_{\text{pulse}}^b$	$1.5 \pm 3.6 \text{ s s}^{-1} \times 10^{-8}$
$a_x \sin i^b$	$82.8 \pm 0.8$ lt-s
$K_o^c$	$26.8 \pm 8.2 \text{ km s}^{-1}$
$T_{\text{mid}}$	MJD $55079.07 \pm 0.01$
$f(M)^b$	$16.5 \pm 0.5 M_{\odot}$
$q^c$	$0.09 \pm 0.03$
$\Theta_e$	$33.6 \pm 0.7^{\circ}$
$M_{\text{donor}}$	$19.6 \pm 1.1 - 20.2 \pm 1.2 M_{\odot}$
$R_{\text{donor}}$	$21.5 \pm 0.5 - 23.0 \pm 0.5 R_{\odot}$
$a$	$38.9 - 39.2 R_{\odot}$
$M_{\text{NS}}$	$1.77 \pm 0.55 M_{\odot} - 1.82 \pm 0.57 M_{\odot}$
$i$	$76.4 - 90^{\circ}$

Table 2.10. System Parameters for XTE J1855-026

<sup>a</sup> The orbital period is refined using an  $O - C$  analysis.

<sup>b</sup> The pulse period, derivative of the pulse period, projected semi-major axis and mass function are given in Corbet & Mukai (2002).

<sup>c</sup> The semi-amplitude of the radial velocity of the mass donor and mass ratio are given in González-Galán (2015).

Spectral Type	$M/M_{\odot}$	$q$	$R/R_{\odot}$	$R_L/R_{\odot}^a$	$R_L/R$	$M_V$	$(J - K)_0^a$	$E(J - K)^a$	$i_{\circ}^b$	$d_{\text{odot}}^c$ (kpc)	$d_{\text{odot}}^d$ (kpc)
<i>O6 Ia</i>	44.10	0.032	19.95	23.85	0.84	-6.38	-0.21	2.60	77–81	11.9	11.9
<i>O6.5 Ia</i>	41.20	0.034	20.22	23.18	0.87	-6.38	-0.21	2.60	73–76	12.0	12.1
<i>O7 Ia</i>	38.44	0.036	20.49	22.52	0.91	-6.38	-0.21	2.60	70–73	12.0	12.3
<i>O7.5 Ia</i>	36.00	0.039	20.79	21.90	0.95	-6.38	-0.21	2.60	67–69	12.0	12.4
<i>O8 Ia</i>	33.72	0.042	21.10	21.31	0.99	-6.38	-0.21	2.60	64–66	11.9	12.6

Table 2.11. Possible Parameters of Candidate Donor Stars for IGR J16418-4532

<sup>a</sup> The value for  $(J - K)_0$  was calculated using  $(J - H)_0$  and  $(H - K)_0$  published in Martins & Plez (2006).

$E(J - K)$  is found by subtracting  $(J - K)_0$  from the observed  $J - K$

<sup>b</sup> The range of inclination angles of the system consistent with the measured eclipse half-angle.

<sup>c</sup> The distance the object is from the Sun using the distance modulus.

<sup>d</sup> The distance the object is from the Sun using the radius to distance ratio derived from spectral energy distribution. The radius to distance ratio is found to be  $3.77 \times 10^{-11}$  (Chaty et al., 2008).

Spectral Type	$M/M_{\odot}$	$q$	$R/R_{\odot}$	$R_L/R_{\odot}^a$	$R_L/R$	$M_V$	$(J - K)_0^a$	$E(J - K)^a$	$i_{\circ}^b$	$d_{\text{odot}}^c$ (kpc)	$d_{\text{odot}}^d$ (kpc)
<i>O6 Ia</i>	44.10	0.032	19.95	22.03	0.91	-6.38	-0.21	3.48	69–75	4.44	4.50
<i>O6.5 Ia</i>	41.20	0.034	20.22	21.42	0.94	-6.38	-0.21	3.48	66–71	4.46	4.56
<i>O7 Ia</i>	38.44	0.036	20.49	20.80	0.99	-6.38	-0.21	3.48	63–68	4.46	4.62
<i>O7.5 Ia</i>	36.00	0.039	20.79	20.23	1.03	-6.38	-0.21	3.48	60–64	4.48	4.69
<i>O8 Ia</i>	33.72	0.042	21.10	19.68	1.07	-6.36	-0.21	3.48	58–61	4.44	4.81

Table 2.12. Possible Parameters of Candidate Donor Stars for IGR J16479-4514

<sup>a</sup> The value for  $(J - K)_0$  was calculated using  $(J - H)_0$  and  $(H - K)_0$  published in Martins & Plez (2006).

$E(J - K)$  is found by subtracting  $(J - K)_0$  from the observed  $J - K$

<sup>b</sup> The range of inclination angles of the system consistent with the measured eclipse half-angle.

<sup>c</sup> The distance the object is from the Sun using the distance modulus.

<sup>d</sup> The distance the object is from the Sun using the radius to distance ratio derived from spectral energy distribution. The radius to distance ratio is found to be  $1 \times 10^{-10}$  (Chaty et al., 2008).

## Chapter 3

# PROBING THE MYSTERIES OF THE X-RAY BINARY

## 4U 1210-64 WITH ASM, PCA, MAXI, BAT AND

### *SUZAKU*

#### 3.1 Overview

4U 1210-64 has been postulated to be a High-Mass X-ray Binary powered by the Be mechanism. X-ray observations with *Suzaku*, the *ISS* Monitor of All-sky X-ray Image (MAXI) and the *Rossi X-ray Timing Explorer* Proportional Counter Array (PCA) and All Sky Monitor (ASM) provide detailed temporal and spectral information on this poorly understood source. Long-term ASM and MAXI observations show distinct high and low states and the presence of a  $6.7101 \pm 0.0005$  day modulation, interpreted as the orbital period. Folded light curves reveal a sharp dip, interpreted as an eclipse. To determine the nature of the mass donor, the predicted eclipse half-angle was calculated as a function of inclination angle for several stellar spectral types. The eclipse half-angle is not consistent with a mass donor of spectral type B5 V; however, stars with spectral types B0 V or B0-5 III are possible. The best-fit spectral model consists of a power law with index

$\Gamma=1.85_{-0.05}^{+0.04}$  and a high-energy cutoff at  $5.5\pm 0.2$  keV modified by an absorber that fully covers the source as well as partially covering absorption. Emission lines from S XVI  $K\alpha$ , Fe  $K\alpha$ , Fe XXV  $K\alpha$  and Fe XXVI  $K\alpha$  were observed in the *Suzaku* spectra. Out-of-eclipse, the Fe  $K\alpha$  line flux was strongly correlated with unabsorbed continuum flux, indicating that the Fe I emission is the result of fluorescence of cold dense material near the compact object. The Fe I feature is not detected during eclipse, further supporting an origin close to the compact object.

### 3.2 Introduction

4U 1210-64 is an unusual X-ray Binary (XRB) first detected by the *Uhuru* satellite in 1978 (Forman et al., 1978). Forman et al. (1978) found that 4U 1210-64 appears to be a variable source with a mean flux of  $8.9\times 10^{-11}$  erg cm $^{-2}$  s $^{-1}$  in the 2–6 keV band. Subsequent detections of 4U 1210-64 include the *Einstein* (Elvis et al., 1992) and *EXOSAT* (Reynolds et al., 1999) slew surveys at fluxes  $1.7\times 10^{-11}$  erg cm $^{-2}$  s $^{-1}$  and  $\sim 7\times 10^{-10}$  erg cm $^{-2}$  s $^{-1}$  in the 0.16–3.5 keV and 1–8 keV bands, respectively; the wide-field cameras (WFC) on board *BeppoSAX* (Verrecchia et al., 2007), *INTEGRAL/IBIS* (Ubertini et al., 2003) and the Burst Alert Telescope (BAT) on board the *Swift* observatory (Tueller et al., 2010; Cusumano et al., 2010) at fluxes  $2.57\times 10^{-10}$  erg cm $^{-2}$  s $^{-1}$ ,  $1.1\times 10^{-11}$  erg cm $^{-2}$  s $^{-1}$  and  $\sim 2\times 10^{-11}$  erg cm $^{-2}$  s $^{-1}$  in the 2–10 keV, 20–100 keV and 14–195 keV bands, respectively.

A soft X-ray counterpart at coordinates (J2000) RA=12<sup>h</sup>13<sup>m</sup>14<sup>s</sup>.7, Dec=−64°52′31″ with a position uncertainty of  $\sim 4''$  was revealed (Revnivtsev et al., 2007) in observations

conducted with the X-ray telescope (XRT, Burrows et al., 2005) on board *Swift*. Revnivtsev et al. (2007) modeled the X-ray spectrum of 4U 1210-64 using a continuum consisting of a power law with hard photon index and an emission feature at 6.7 keV with an equivalent width (EQW) of  $\sim 400$  eV. These observations resulted in a classification of 4U 1210-64 as an intermediate polar cataclysmic variable (CV, Revnivtsev et al., 2007).

Observations using the *Swift*/XRT in late 2006 and early 2008 confirmed the presence of an emission feature at 6.7 keV, thought to be Fe XXV (Masetti et al., 2010). The emission feature, observed to be prominent when the source is at intermediate flux levels, was not seen when the source entered periods of low or high flux (Masetti et al., 2010). At intermediate flux levels, the EQW of the emission line was observed to be  $\sim 1.6$  keV. This very large EQW is suggestive of a blend of Fe lines. While Revnivtsev et al. (2007) suggested that the spectral properties indicate that 4U 1210-64 is a CV, Masetti et al. (2010) proposed that the stellar remnant in the system is a neutron star based on the very large EQW and variability of the emission feature. Under the assumption of a power law continuum and a distance of  $\sim 2.8$  kpc (Masetti et al., 2009), the high state X-ray luminosity of 4U 1210-64 was found to be  $1.9 \times 10^{35}$  erg s $^{-1}$  in the 2–10 keV band (Masetti et al., 2010). This exceeds the typical luminosities observed in CVs by a factor of  $\sim 1$ –2 orders of magnitude (Barlow et al., 2006; Revnivtsev et al., 2008; Brunschweiger et al., 2009). A blackbody soft excess with a temperature of  $\sim 1.5$  keV was found in 4U 1210-64, which implies that the accretor is more compact than a white dwarf (Masetti et al., 2010). Masetti et al. (2010) concluded that the presence of the soft excess provides compelling evidence against a CV interpretation of the system.

The optical counterpart of 4U 1210-64 was observed on MJD 54529.3 using the

1.5 m Cerro Tololo Interamerican Observatory (CTIO) in Chile (Masetti et al., 2009). Based on its optical spectrum, Masetti et al. (2009) proposed that the spectral class of the mass donor is B5 V. The features observed in the optical spectrum consist of Balmer series lines in absorption and emission of neutral helium, singly ionized helium and a blend of doubly ionized nitrogen and carbon. The EQW of the  $H\alpha$  line was observed to be approximately  $2.5 \text{ \AA}$  (Masetti et al., 2009). This is less than half the expected value for a B5 V star, which suggests that emission features are present. While an early-type mass donor suggests that 4U 1210-64 is a High-Mass X-ray Binary, the presence of a B5 V main-sequence star in an HMXB would be unprecedented (Negueruela, 1998). The majority of Be X-ray binaries (BeXBs) host primaries with spectral properties that range from late O to early B type stars. This will be discussed in further detail in Section 4.

A 6.7 day orbital period was discovered using data from the *Rossi X-ray Timing Explorer* All-Sky Monitor (ASM, Corbet & Mukai, 2008). In addition, Corbet & Mukai (2008) report three main states of the system along with the possibility of an eclipse. I investigate these results in more detail in Section 3.1 using additional data from ASM, the Monitor of All-Sky X-ray Image (MAXI) on board the *International Space Station (ISS)* and Burst Alert Telescope (BAT) on board the *Swift* spacecraft.

This chapter is structured in the following order: *Suzaku*, MAXI, PCA, and ASM observations are presented in Section 3.2, Section 3.3 focuses on the results of the X-ray campaign, and Section 3.4 presents a discussion of the results. The conclusions are outlined in Section 3.5. As in Chapter 2, the uncertainties and limits presented are at the  $1\sigma$  confidence level.

### 3.3 Observations and Data Analysis

The observations outlined below consist of data collected during a two day *Suzaku* observation of 4U 1210-64 (2010 Dec. 23–25), pointed observations using the *RXTE* Proportional Counter Array (PCA) as well as long-term observations of the system using the following all-sky monitors: MAXI, ASM, and BAT.

#### 3.3.1 RXTE

**3.3.1.1 ASM** The ASM on board *RXTE* (Levine et al., 1996) consisted of three coded-aperture Scanning Shadow Cameras (SSCs), sensitive to energies in the 1.5–12 keV band. For more information, see Appendix A.3.1.1.

ASM observed 4U 1210-64 from MJD 50087 to 55924. The light curves were retrieved from the *ASM/RXTE* database<sup>1</sup> managed by MIT, which includes “dwell-by-dwell” light curves and daily averaged light curves. The light curves are divided into three energy bands: 1.5–3 keV, 3–5 keV and 5–12 keV. Over the entire energy range (1.5–12 keV), the Crab produces approximately  $75.5 \text{ counts s}^{-1}$  (Remillard & Levine, 1997; Levine et al., 1996). “Blank field” observations of regions at high Galactic latitudes indicate that a systematic uncertainty of  $\sim 0.1 \text{ counts s}^{-1}$  must be taken into account (Remillard & Levine, 1997; Levine et al., 1996). I used the “dwell-by-dwell” light curves in this analysis (see Section 3.4.1).

**3.3.1.2 PCA** Consisting of five proportional counter units (PCUs), the PCA was sensitive to X-rays in the energy band 2–60 keV. For more information, see Ap-

---

<sup>1</sup><http://xte.mit.edu/ASM.lc.html>

pendix A.3.1.2.

4U 1210-64 was observed 65 times between MJD 54804.0–54842.0. Individual observations typically lasted for 2–4 ks but were as short as 1.4 ks and as long as 45.6 ks. Dataset IDs were 93455-01 (23 observations) and 94409-01 (42 observations). The majority of the observations were performed during a single spacecraft orbit with no interruptions; longer ones spanned multiple orbits, with interruptions due to Earth occultations and/or SAA passages. Of the 5 PCUs, only PCU2 was used consistently for these observations, so only data taken with PCU2 were analyzed. The Crab produces  $\sim 2000$ – $2400$  counts  $s^{-1}$  in the PCU2 top layer<sup>2</sup>.

Each detected event was recorded in different ways by the on-board experiment data system (EDS). The analysis was done by Koji Mukai, who analyzed Standard2 mode data, producing 129-channel spectra every 16 seconds, for spectral analysis and for low-frequency timing analysis. He generated the “faint” model background<sup>3</sup>, since the source mostly stayed below  $40$  counts  $s^{-1}$  PCU<sup>-1</sup>. For high-frequency timing analysis, light curves in 10 ms bins were generated using the GoodXenon event mode data, without background subtraction. Spectral data including background subtraction were reduced and analyzed using the standard screening criteria (Jahoda et al., 2006).

### 3.3.2 MAXI

The MAXI instrument is an X-ray slit camera sensitive to energies 0.5–30 keV (Matsuoka et al., 2010). MAXI consists of two types of slit cameras, the Gas Slit Camera

---

<sup>2</sup><http://www.sternwarte.uni-erlangen.de/wilms/rxte/>

<sup>3</sup><http://heasarc.nasa.gov/docs/xte/recipes/pcabackest.html>

(GSC) and the Solid-state Slit Camera (SSC), which observe the X-ray variability of over 1000 sources over every ISS orbit of approximately 92 minutes (Matsuoka et al., 2010). Of the two cameras, I make use of the GSC data that are routinely made available by the MAXI team. The GSC is sensitive to the energy bandpass of 2–30 keV. For additional information, see Appendix A.4.1.

I analyzed MAXI data obtained between MJD 55061.5–56394.5. Light curves of energies 2–4 keV, 4–10 keV and 10–20 keV were retrieved from the data available in the MAXI RIKEN database<sup>4</sup>. The 2–4 keV and 4–10 keV light curves were subsequently co-added for comparison with the light curves produced by the ASM.

### 3.3.3 Swift

The BAT on board the *Swift* spacecraft is a hard X-ray telescope operating in the 15–150 keV energy band (Barthelmy et al., 2005). For additional information, see Appendix A.4.2.1.

I analyzed BAT data obtained during the time period MJD 55152–56141. Light curves were retrieved using the extraction of the BAT data reported in Krimm et al. (2013). These are available on the NASA GSFC HEASARC website<sup>5</sup>, which includes orbital and daily-averaged light curves. I used the orbital light curves in the 15–50 keV energy band in this analysis (see Section 3.4.1.3).

---

<sup>4</sup><http://maxi.riken.jp/top/>

<sup>5</sup><http://heasarc.gsfc.nasa.gov/docs/swift/results/transients/>

### 3.3.4 Suzaku

The *Suzaku* observation of 4U 1210-64 took place in 2010 December 23–25 (MJD 55553.16–55555.15) with an exposure time of  $\sim 80$  ks (ObsID 405045010). Data, collected using the X-ray Imaging Spectrometer (XIS) and Hard X-ray Detector (HXD) instruments, were reduced and analyzed using standard criteria as described below.

**3.3.4.1 XIS data** The *Suzaku* XIS suite consists of four X-ray imaging telescopes each fitted with a CCD, sensitive to X-rays ranging from 0.6–10 keV (Koyama et al., 2007; Mitsuda et al., 2007). For additional information, see Appendix A.3.2.1.

4U 1210-64 was observed in full window mode with a data readout of 8 s. Data collected using the XIS were reduced and screened using the HEASoft v.6.13 package and calibration files dated 2013 September 08 (XIS) and 2011 June 30 (XRT) implementing the procedures defined in the *Suzaku* ABC Guide. The data were reprocessed with the FTOOL `aepipeline` using the standard criteria to apply the newest calibration and default screening criteria. The XIS exposures in the  $3\times 3$  and  $5\times 5$  event modes were combined using `XSELECT`. Circular regions of radius  $3'9$  centered on the source and offset from the source were selected to distinguish between photons originating from the source and those originating from the background. The light curves were binned at 16 s.

Response matrices were generated using the `xisrmfgen` and `xissimarfgen` FTOOL packages. Pileup was taken into consideration in the region files, where the central pixels were shown to be affected. As a result, the inner parts of the point spread function (PSF) were removed using two overlapping rectangular shaped regions to reduce pile-up to  $\lesssim 1\%$  using the FTOOLS `aeattcor2` and `pileest`. `Aeattcor2` creates

an improved attitude file, which is then applied to the event file. The FTOOL `pileest` was then used on the improved event file, which provides a rough estimate of the degree of pile-up.

Data in the spectral file produced by `XSELECT` were further processed using the FTOOL `GRPPHA`. `GRPPHA` is designed to define the binning, quality flags and systematic errors of the spectra and used the bad quality flag to further eliminate bad data from the PHA file. Bins were grouped to ensure a minimum of 20 counts in each in the XIS spectra. The spectrum was analyzed using `XSPEC v12.7.1d`. To avoid poorly calibrated Si and Au features, only the energy ranges 0.5–1.7 keV and 2.1–9.2 keV were considered (Nowak et al., 2011). I will discuss the spectral analysis and results in Section 3.4.

**3.3.4.2 HXD data** The HXD is a non-imaging X-ray spectrometer consisting of 64 silicon PIN diodes as well as the Gadolinium silicate crystal (GSO) instruments (Mitsuda et al., 2007). My analysis only considers data collected by the PIN diodes because 4U 1210-64 is not bright enough for GSO analysis. The calibration files used in the analysis of the HXD data were dated 2010 December 6. For this specific observation, 4U 1210-64 is not easily detectable at energies exceeding  $\sim 30$  keV. As a result, the analyzed part of the spectrum is between 15–30 keV. For more information see Appendix A.3.2.2.

The HXD-PIN spectral data were extracted and reduced using the “cleaned” event files in the `hxd/event_cl` directory and the `hxdpinxbpi` FTOOL package, respectively. The FTOOL `hxdpinsbpi` automatically runs the tasks outlined as follows. Good Time Intervals were calculated using the Non X-ray Background (NXB)<sup>6</sup> data overlap-

---

<sup>6</sup>[ftp://legacy.gsfc.nasa.gov/suzaku/data/background/pinnxb\\_ver2.0\\_tuned/](ftp://legacy.gsfc.nasa.gov/suzaku/data/background/pinnxb_ver2.0_tuned/)

ping in time with the GTI of the observation. The source and NXB spectra are extracted using `hxdpinxbpi`. The rate in the NXB event file is scaled by a factor of 10 to account for Poisson errors. As a result, the exposure time of the derived background spectra and light curves must be increased by a factor of 10. Since the NXB spectrum does not include the Cosmic X-ray Background (CXB), a simulated CXB spectrum was produced using the parameters determined by Boldt (1987). The total PIN background spectrum is the sum of the NXB and simulated CXB spectra, which were added together using `addspec`. The net count rates for the NXB and CXB spectra are  $0.2336 \pm 0.0006$  and  $0.0153 \pm 0.0001$  counts  $s^{-1}$ , respectively. The source spectrum is dead time corrected by  $\sim 4\text{--}5\%$ .

## 3.4 Results

### 3.4.1 Long Term Temporal Analysis

Using data acquired from the ASM, MAXI, and BAT instruments, I produced light curves of 4U 1210-64 to investigate long-term variability of the source (see Figure 3.1). Data produced by ASM, MAXI and BAT span periods of  $\sim 16$  years,  $\sim 3.3$  years, and  $\sim 5$  years respectively.

**3.4.1.1 ASM Temporal Analysis** Three distinct states of the system, two active phases and a quiescent phase, are seen in the ASM light curve (see Figure 3.1, bottom). To parameterize the states observed in the system, the light curve was fit using an asymmetric “step-and-ramp” function (see Figure 3.1, bottom). The parameters in this model are as follows: the times corresponding to the start of the transition between the first active state

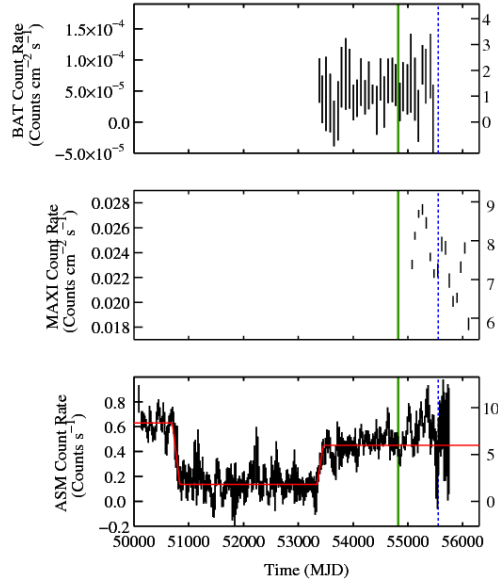


FIG. 3.1. Long term light curves of 4U 1210-64 produced by BAT in the 15–150 keV band (top), MAXI in the 2–10 keV band (middle) and ASM in the 1.5–12 keV band (bottom) show a two year time overlap between ASM and MAXI and a five year time overlap between ASM and BAT. The ASM, MAXI and BAT light curves use 21 day, 70 day and 70 day time bins, respectively. The times of the PCA and *Suzaku* observations are indicated by the green shaded region and blue dashed line, respectively. The ASM light curve (bottom) is fit with an asymmetric “step and ramp” function (see solid red line), which models the long-term behavior of the system.

to the quiescent state,  $T_1$ , the start of the transition between the quiescent state and the second active state,  $T_2$ , the transition time between state 1 and state 2,  $\Delta T_1$ , the transition time between state 2 and state 3,  $\Delta T_2$ , the count rates during both active states,  $C_{\text{act1}}$  and  $C_{\text{act2}}$ , and the count rate during the quiescent state,  $C_{\text{quies}}$ . The model parameters are reported in Table 3.1. The duration of the quiescent phase was found to be  $2506^{+36}_{-26}$  days ( $6.19^{+0.10}_{-0.07}$  yr) using the following equation:

$$(3.1) \quad \Delta T_{\text{quies}} = T_2 - (T_1 + \Delta T_1)$$

Model Parameter	ASM
$T_1$ (MJD)	$50703^{+13}_{-5}$
$\Delta T_1$ (days)	$135^{+32}_{-22}$
$T_1 + \Delta T_1$ (MJD)	$50838^{+35}_{-22}$
$C_{\text{act1}}$ (Counts s <sup>-1</sup> )	$0.63 \pm 0.02$
$C_{\text{act2}}$ (Counts s <sup>-1</sup> )	$0.45^{+0.02}_{-0.01}$
$T_2$ (MJD)	$53444^{+11}_{-13}$
$\Delta T_2$ (days)	$109^{+16}_{-21}$
$T_2 + \Delta T_2$ (MJD)	$53452^{+19}_{-25}$
$C_{\text{quies}}$ (Counts s <sup>-1</sup> )	$0.136 \pm 0.009$
$\Delta T_{\text{quies}}$ (days)	$2506^{+36}_{-26}$
$\chi^2_{\nu}$ (dof)	1.19 (222)

Table 3.1. Best-fit parameters for the states observed in 4U 1210-64.

A power spectrum was used to search for periodicities in temporal data (Scargle, 1982; Corbet & Mukai, 2008). Power spectra, produced using the MAXI and ASM light curves at a time resolution of one dwell (90 s), show the presence of a  $6.7101 \pm 0.0005$  day peak (see Figure 3.2, bottom). The false-alarm probability (FAP; Scargle, 1982) in the ASM light curve is  $\sim 10^{-9}$ . I interpret this peak as the orbital period of the system.

For this paper, I use an ephemeris based on the orbital period observed in the power spectrum (see Figure 3.3, bottom) and time of mid-eclipse:  $P = 6.7101 \pm 0.0005$  days and  $T_0 = \text{MJD } 54001.8 \pm 0.2$ . To parameterize the orbital modulation of the system, the “dwell-by-dwell” ASM lightcurves were folded using the orbital period.

**3.4.1.2 MAXI Temporal Analysis** I confirmed the orbital period using MAXI. I folded the MAXI light curve on the orbital period using the ephemeris described above (see Figure 3.3, middle), showing that the binned folded light curve strongly agrees with that produced by ASM. Compared to the ASM power spectrum, more statistical noise is

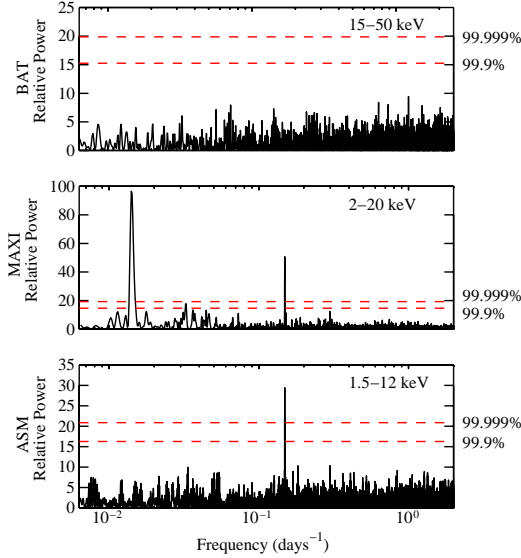


FIG. 3.2. Power spectra produced by BAT (top), MAXI (middle) and ASM (bottom) with the 99.9% and 99.999% confidence intervals shown. The BAT (top), MAXI (middle) and ASM (bottom) data are in the 15–50 keV, 2–20 keV and 1.5–12 keV bands, respectively. The  $\sim 70$  day precession period of the ISS is also seen in the MAXI power spectrum.

apparent in the power spectrum produced using MAXI data (see Figure 3.2, middle). A “blind search” for the period of the system yields a FAP of  $\lesssim 10^{-6}$ .

**3.4.1.3 BAT Temporal Analysis** The modulation interpreted as the 6.7 day orbital period was not detected in the power spectrum produced by the BAT instrument (see Figure 3.2, top). Comparisons between the BAT power spectrum and ASM power spectrum indicate that BAT does not have the sensitivity to detect the 6.7 day modulation at the level seen in ASM and MAXI respectively (see Figure 3.2, top). The modulation depth is defined as  $(Count_{\max} - Count_{\min}) / MeanCount$ .

I folded the BAT light curve on the orbital period using the ephemeris defined by the ASM (see Section 3.1.1 and Figure 3.3, top), showing that the binned folded light

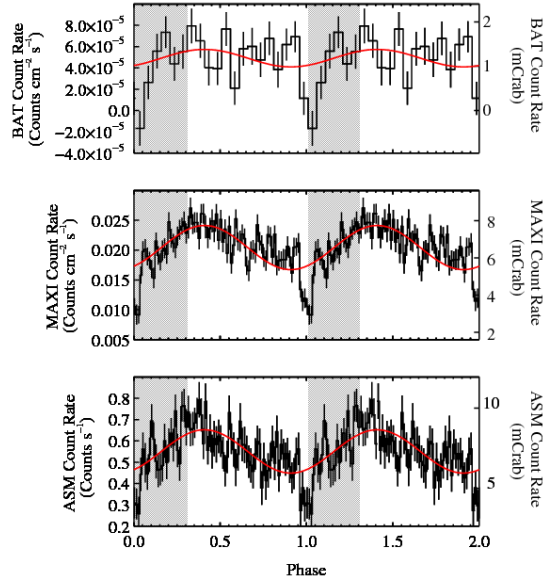


FIG. 3.3. BAT (top), MAXI (middle) and ASM (bottom) lightcurves folded on the orbital period using 20 bins (BAT) and 80 bins (ASM and MAXI). The shaded region indicates the orbital phases of the system for the duration of the *Suzaku* observation. The sharp dip in flux between phases  $\phi \sim -0.04$  and  $\phi \sim 0.03$  is interpreted as an eclipse. The solid red line is the sinusoidal fit to the folded light curves using the ephemeris defined in Section 3.1.1.

curve is consistent with that produced by ASM and MAXI with a possible indication of an eclipse centered at  $\phi = 0$ .

### 3.4.2 Eclipse Profile

The folded light curves show the presence of a sharp dip between orbital phases  $\phi \sim -0.04$  and  $\phi \sim 0.03$ , which is suggestive of an eclipse. Similar to what is found in IGR J16393-4643 (see Section 2.4.1), the source emission in 4U 1210-64 does not reach 0 counts  $s^{-1}$ . I interpret this dip as an eclipse since the feature is persistent over many years of data. The feature is seen at the same orbital phase in States 1 and 3 (see Table 3.1), which are separated by  $\gtrsim 6$  years. The rapid ingress and egress requires obscuration by

clearly defined boundaries that are suggestive of an object such as the mass donor in the system.

As described in Section 2.3.2, the eclipse was modeled using a step and ramp function (see Figure 3.4). Since the eclipse profile was found to be symmetric within the errors, I chose the model to be a symmetric step and ramp function. The symmetric nature of the model ensures that the duration of ingress and egress,  $\Delta\phi$ , as well as the count rate before ingress and after egress,  $C$ , are equal. The eclipse model parameters are reported in Table 3.2. The eclipse duration and mid-eclipse are calculated using Equations 2.2 and 2.3.

Since the Suzaku observation begins at MJD 55553.1, I express the time of mid-eclipse,  $T_{\text{mid}}$ , at an epoch closest to the Suzaku observation (see Table 3.2). The eclipse duration, time of mid-eclipse, and eclipse half-angle ( $\Delta\phi_{\text{ecl}} \times 180^\circ$ ) from fitting the ASM and MAXI folded light curves are reported in Table 3.2. The fits of both the ASM and MAXI data, which use 150 and 88 bins respectively, indicate that the mid-eclipse times and eclipse durations are in agreement at the  $1\sigma$  level. For the best-fit step-and-ramp model, I chose to express the ingress and egress start times and transition duration to the weighted average of the ASM and MAXI values (see Table 3.2). While all model parameters were free for the ASM and MAXI fits, the phases corresponding to the start of ingress as well as egress and the transition duration in the BAT fit, which uses 96 bins, were frozen to the weighted average of the ASM and MAXI values.

### 3.4.3 Short Term Temporal Analysis

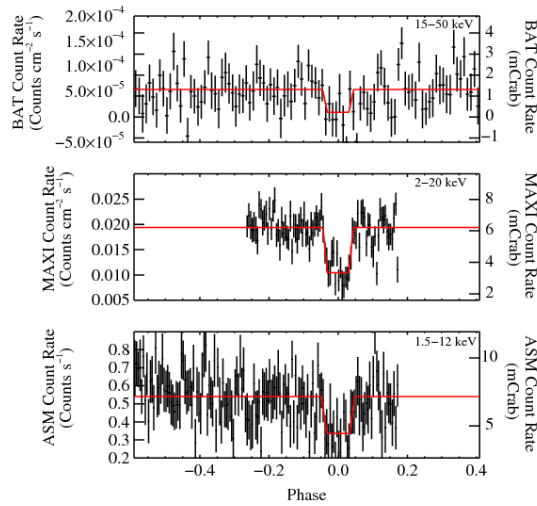


FIG. 3.4. BAT (top), MAXI (middle) and ASM (bottom) folded light curves are fit with a symmetric “step and ramp” function, which models the eclipse. The BAT (top), MAXI (middle) and ASM (bottom) data are in the 15–50 keV, 2–20 keV and 1.5–12 keV bands, respectively. The orbital phase coverage in the ASM and MAXI folded light curves were restricted to where the count rate outside of eclipse could be approximated to a constant.

**3.4.3.1 Suzaku** The two-day *Suzaku* observation in 2010 Dec. took place during the phase of transition from the minimum to the maximum of the 6.7 day modulation (see Figure 3.3). I binned the *Suzaku* light curves to a resolution of 16 s to investigate short-term variability in the system, shown in the light curve produced by the sum of the XIS-0 and XIS-3 light curves (see Figure 3.5).

The two-day *Suzaku* observation revealed large variations in flux indicative of significant variability beyond the orbital modulation. The modulation depth between the peak in the light curve and the mean count rate is on the order of 140%.

I divided the light curve into two energy bands where the soft band is defined between energies 0.5–4 keV, characterized by the count rate  $C_{\text{soft}}$ , and the hard band is

Model Parameter	ASM (1.5–12 keV)	MAXI (2–20 keV)	Combined	BAT <sup>a</sup> (15–50 keV)
$\phi_{\text{ing}}$	$-0.047^{+0.004}_{-0.003}$	$-0.044 \pm 0.002$	$-0.045 \pm 0.002$	
$\Delta\phi$	$0.014^{+0.001}_{-0.006}$	$0.013 \pm 0.002$	$0.014^{+0.001}_{-0.002}$	
$C$	$0.54 \pm 0.01^b$	$1.97 \pm 0.03^c$		$5.5 \pm 0.4^d$
$\phi_{\text{egr}}$	$0.033 \pm 0.005$	$0.031 \pm 0.002$	$0.031 \pm 0.002$	
$C_{\text{ecl}}$	$0.34^{+0.02b}_{-0.03}$	$1.11 \pm 0.07^c$		$1.0 \pm 1.4^d$
$\Delta\phi_{\text{ecl}}$	$0.066^{+0.007}_{-0.008}$	$0.062 \pm 0.004$	$0.062 \pm 0.003$	
$T_{\text{mid}}^e$	$55553.099 \pm 0.004$	$55553.098 \pm 0.002$	$55553.098 \pm 0.002$	
$\Theta_e^f$	$11.9^{+1.3}_{-1.5}$	$11.1^{+0.6}_{-0.7}$	$11.2 \pm 0.6$	
$\chi^2_{\nu}$ (dof)	$0.92(146)$	$1.21(84)$		$0.93(96)$

Table 3.2.

<sup>a</sup> The  $\phi_{\text{ing}}$ ,  $\Delta\phi$ ,  $\phi_{\text{egr}}$  parameters in the BAT fit are frozen to the weighted average of the ASM and MAXI values.

<sup>b</sup> Units are counts  $\text{s}^{-1}$ .

<sup>c</sup> Units are  $10^{-2}$  counts  $\text{cm}^{-2}$   $\text{s}^{-1}$ .

<sup>d</sup> Units are  $10^{-5}$  counts  $\text{cm}^{-2}$   $\text{s}^{-1}$ .

<sup>e</sup> Units are MJD.

<sup>f</sup> Units are degrees.

between 4–10 keV, characterized by the count rate  $C_{\text{hard}}$ . Using the definition in Equation 3.2, I produced a hardness ratio (see Figure 3.5, bottom) binned to a resolution of  $\sim 1000$  s, where a soft spectrum is indicated by negative values and a hard spectrum is indicated by positive. The hardness ratio was also plotted against the count rate in the full energy band of 0.5–10 keV to search for a correlation between the hardness ratio and source intensity (see Figure 3.6). Throughout this chapter, I use the weighted Pearson correlation coefficient,  $r$  (e.g. Bevington & Robinson, 2003). I only take the data observed out-of-eclipse into account since the phenomenology is different from the data observed during eclipse (see Table 3.3). Out-of-eclipse, I found a positive correlation between the hardness ratio and source intensity ( $r=0.69$ ,  $p \lesssim 10^{-6}$ ), which will be interpreted in Sec-

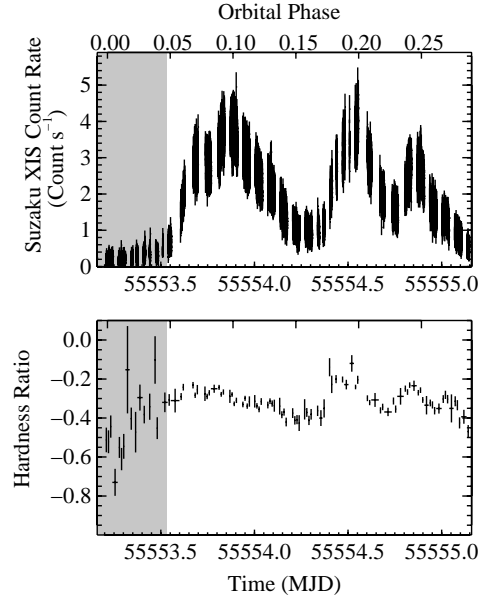


FIG. 3.5. The weighted average of the *Suzaku* XIS0 and XIS3 light curves using bin sizes of 16 s (top). The top axis indicates the orbital phase of the system. The shaded region indicates the mid-eclipse and egress end times calculated by the “step-and-ramp” function. The hardness ratio (bottom), which uses bin sizes of 1000 s, is defined as  $(C_{\text{hard}} - C_{\text{soft}})/(C_{\text{hard}} + C_{\text{soft}})$ , where the soft and hard energy bands are 0.5–4 keV and 4–10 keV, respectively.

tion 3.5.4.

$$(3.2) \quad HR = (C_{\text{hard}} - C_{\text{soft}})/(C_{\text{hard}} + C_{\text{soft}})$$

**3.4.3.2 PCA** To present an overview of the RXTE observations, the average, background-subtracted count rate of 4U 1210-64 was calculated during each spacecraft orbit and plotted against time in Figure 3.7. The PCA light curves were divided into three energy bands defined between energies 2.5–6 keV, 6–10 keV and 10–20 keV, which are characterized by count rates  $C_1$ ,  $C_2$  and  $C_3$ , respectively. Using the definition in Equation 3.2, I produced hardness ratios binned to a resolution of  $\sim 0.2$  d (see

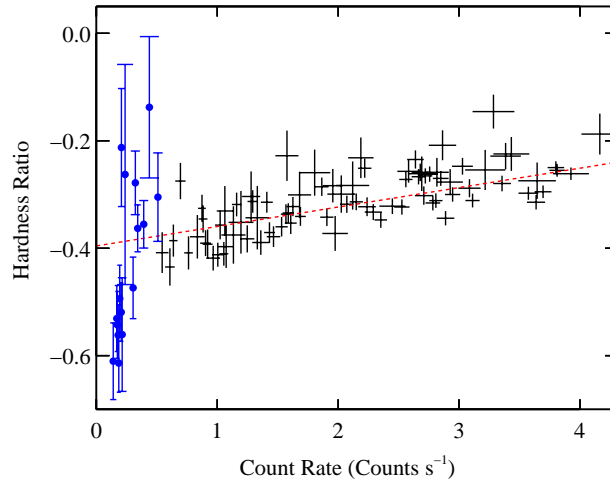


FIG. 3.6. The hardness ratio as defined in Figure 5 vs. the full energy band of 0.5–10 keV of the *Suzaku* light curve. The red dashed line indicates the best linear fit to the points outside the eclipse. The blue points indicate the data collected during eclipse.

Figure 3.7, middle and bottom). To search for correlations between the hardness ratios in each energy band, I produced a color-color diagram (see Figure 8) between the two hardness ratios to examine the correlation between them. A strong correlation was found in the color-color diagram ( $r=0.79$ ,  $p \lesssim 10^{-6}$ .)

I performed a Fourier transform of all background-subtracted *RXTE* PCA Standard2 mode data together, up to a frequency of 100 cycles per day (Scargle, 1982). The power spectrum is dominated by low frequency (see Figure 3.9), “red” noise, and the orbital period was not detected in this data set. This is likely because of a patchy orbital phase coverage.

Note that Scargle’s method is strictly correct only in judging the FAP of the highest peak mixed in with otherwise frequency-independent, “white”, noise (Scargle, 1982). This is clearly not the case here. To improve the search for a spin period, I analyzed the relationship between power and frequency in log-log space to estimate and remove

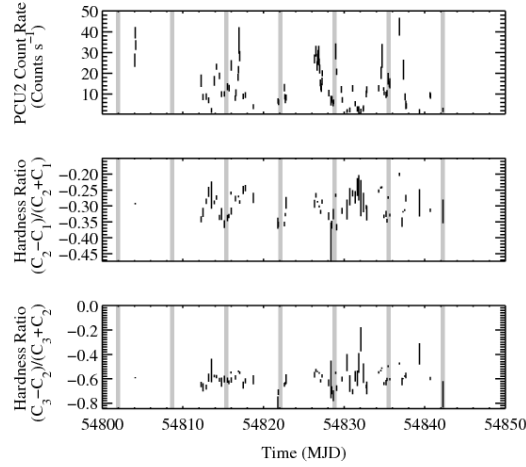


FIG. 3.7. Long-term light curve of 4U1210-64 during the RXTE PCA campaign (top). I calculated the average and standard deviation of the PCU2 count rate for each spacecraft orbit. Also indicated (shaded regions) are the eclipse intervals due to the companion. Hardness ratios of the PCA light curves (middle and bottom), using bin sizes of 0.2 d., where the energy bands for  $C_1$ ,  $C_2$  and  $C_3$  are 2.5–6 keV, 6–10 keV and 10–20 keV, respectively.

the amount of low-frequency red noise present in the power spectrum (Vaughan, 2005). A quadratic fit was found to give a reasonable approximation to the continuum noise level. I subtracted the quadratic fit from the logarithm of the power spectrum along with a constant value of 0.25068 to account for the bias due to the  $\chi^2$  distribution of the power spectrum (Vaughan, 2005). The only statistically significant feature in the power spectrum is an artifact caused by a group of peaks around 15 cycles per day near the spacecraft orbital period (see Figure 3.9).

I created light curves binned to 10 ms for each GoodXenon event mode file, covering no more than a single spacecraft orbit. The estimated low-frequency red noise was

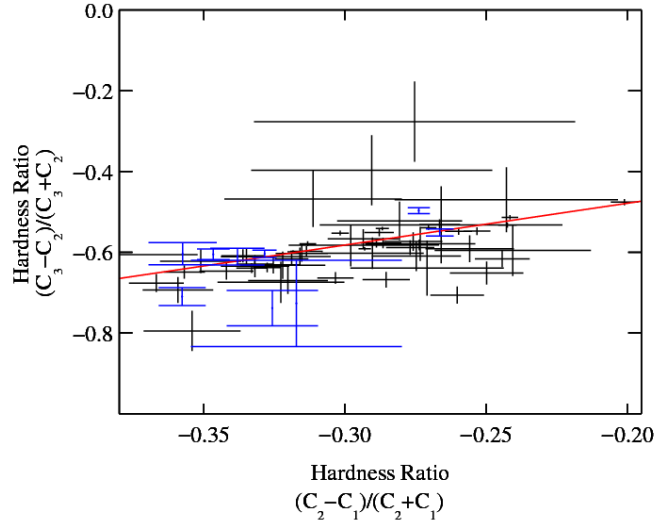


FIG. 3.8. PCA color-color diagram comparing soft color vs. hard color as defined in Figure 3.7. The red line indicates the best linear fit to the points outside the eclipse. The blue points indicate the data collected during eclipse.

removed using the procedures in Vaughan (2005), similar to what is described above. A function that is quadratic for frequencies below  $\sim 10^{-2}$  Hz and constant above this was found to give a reasonable approximation to the continuum noise level found in the log-log plot between power and frequency. The highest peak in the resulting power spectra (see Figure 3.10) was often found at the lowest frequency ( $< 0.01$  mHz), presumably resulting from both source and background variability on  $> 100$  s time scales. In 5 cases, additional higher frequency ( $> 10$  Hz), apparently significant (FAP less than 0.1%) peaks were also found. However, these turned out to be related to the low frequency peak: the removal of the low frequency sinusoid also removed these peaks. I conclude that these were artifacts, created by some (unknown) combination of the sampling pattern, the precise characteristics of the low frequency variability, and possibly also the numerical limitations of the particular implementation of Scargle's algorithm that I used (Scargle, 1982). Other than these, the strongest high frequency peaks had FAP between 1% and

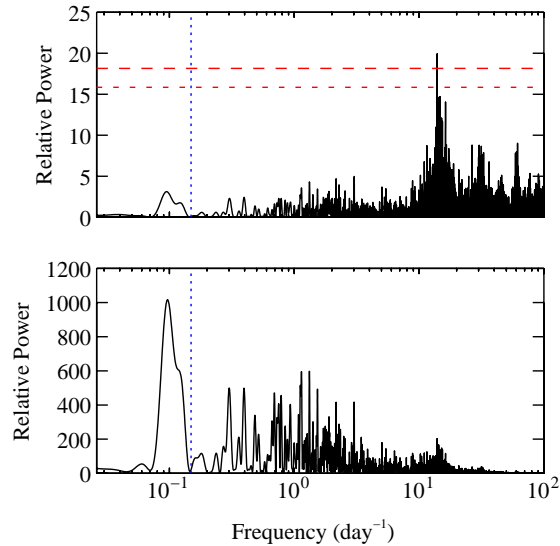


FIG. 3.9. Scargle’s power spectrum of the PCA data up to a frequency of 100 cycles per day with the estimated continuum noise component removed (top). The uncorrected power spectrum (bottom) is dominated by strong low frequency variability. The orbital period (see Sections 3.4.1.1 and 3.4.1.2) is indicated by the blue dashed line. The red short dashed line is the power corresponding to 1% FAP, and the long dashed line 0.1% FAP.

0.1% (note that the number of trials for each Fourier transform is taken into account, but not the fact that I analyzed 84 independent light curves), and none of these candidate frequencies repeated in multiple observations. I conclude that I did not detect the spin period of the compact object in 4U 1210-64. Scaling from the amplitudes of the highest peaks, it can be estimated that a sinusoidal modulation with an amplitude of 8% of the mean flux would have been detectable at 99.9% significance.

### 3.4.4 Spectral Analysis

The X-ray spectral data from the *Suzaku* and PCA observations of 4U 1210-64 were analyzed using the package XSPEC v12.8.0. I made use of the XSPEC convolution model `cflux` to calculate the fluxes and associated errors of 4U 1210-64.

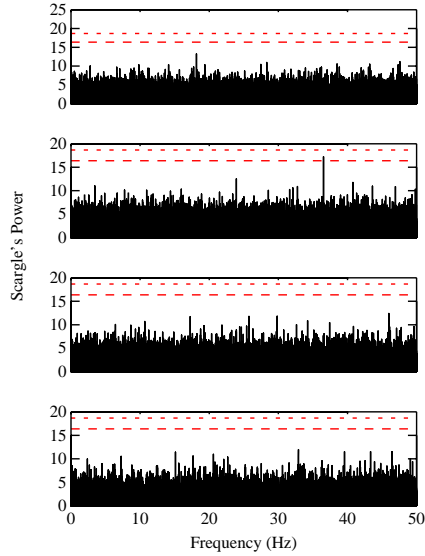


FIG. 3.10. Typical PCA power spectra for Obs ID 99009-01-01-17 (top), Obs ID 99009-01-01-22 (second from top), Obs ID 99009-01-23-00 (third panel) and Obs ID 99009-01-03-02 (bottom). The frequency range is from  $5.73 \times 10^{-4}$ –50 Hz. The long dashed line is the power corresponding to 1% FAP, and the short dashed line the 0.1% FAP. The highest peak in the Obs ID 99009-01-01-22 power spectrum is found to be between the 99% and 99.9% confidence intervals (second from top).

**3.4.4.1 Suzaku Spectral Analysis** To fit the *Suzaku* spectra, I used several models: a power law, thermal bremsstrahlung, a power law modified with a high energy cutoff (see Figure 3.11), and emission due to collisionally-ionized diffuse gas (APEC in XSPEC, Foster et al., 2012). All models were modified by a partially covering absorber in addition to an absorber that fully covers the source using the Balucinska-Church & McCammon (1992) cross sections and Wilms et al. (2000) abundances.

The model that provides a good fit to the data is a power law modified by a high-energy cutoff (reported in Table 3.3). I find that the neutral hydrogen column densities for fully covered and partially covering absorption are  $N_{\text{H}}=0.70 \pm 0.01 \times 10^{22}$  and

$N_{\text{H}}=6.7_{-0.4}^{+0.3}\times 10^{22}$  atoms  $\text{cm}^{-2}$  respectively with a partial covering fraction of  $0.36\pm 0.03$ . The measured values of the fully covered absorber are comparable to the Galactic H I values reported by the Leiden/Argentine/Bonn survey (Kalberla et al., 2005) and in the review by Dickey & Lockman (1990), which are  $8.16\times 10^{21}$  and  $9.37\times 10^{21}$  atoms  $\text{cm}^{-2}$ , respectively. Therefore, I assume that the fully covered absorber is interstellar in origin unless otherwise noted (see Section 3.5.4 for treatment in eclipse). A good fit does not require an additional blackbody to the power law component, even though such a soft excess was seen in the *INTEGRAL* data by Masetti et al. (2010). Furthermore, I do not detect any cyclotron lines in the Suzaku spectra.

Emission features in the Fe  $K\alpha$  region were detected at 6.4 keV, 6.7 keV and 6.97 keV; which were modeled using a Gaussian centered on the peak of the lines (see Figure 3.12). These features are interpreted as Fe  $K\alpha$ , Fe XXV  $K\alpha$  and Fe XXVI  $K\alpha$  respectively (see Figure 3.12). In addition, an emission line was observed at 2.6 keV, which is interpreted as S XVI  $K\alpha$  (see Figure 3.12).

I investigated temporal dependence of the spectral parameters, comparing the parameters during eclipse to those out-of-eclipse. The out-of-eclipse region was subdivided into several 10 ks intervals to further investigate the temporal variability of the spectral parameters. Since 4U 1210-64 is not easily detectable in the HXD-PIN for much of the observation, I only considered the XIS spectra for the analysis of time dependent changes in spectral parameters. A good fit to the spectra does not require a high-energy cutoff although it is needed for the time-averaged out-of-eclipse spectrum for which I analyzed the well-exposed HXD-PIN spectrum along with the XIS data. I chose to model the spectra using a power law with a high-energy cutoff frozen at the values of the time-averaged

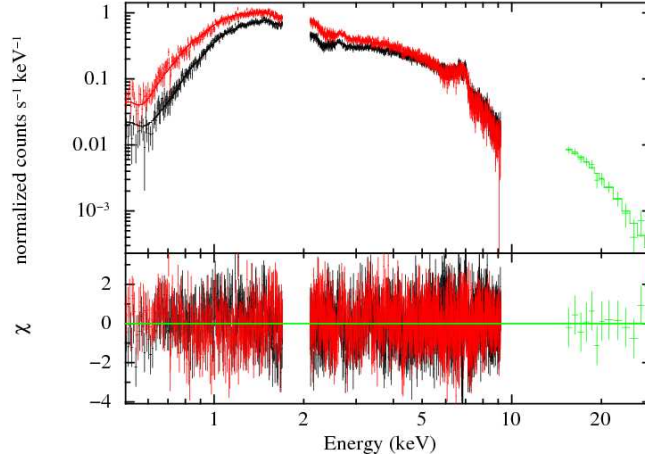


FIG. 3.11. One of the best fit models for 4U 1210-64 where XIS0+3, XIS1 and HXD/PIN are indicated by the black, red and green data/models, respectively. This consists of a continuum comprised of a power law with a high energy cutoff and four emission lines composed of S XVI  $K\alpha$ , Fe  $K\alpha$ , Fe XXV  $K\alpha$  and Fe XXVI  $K\alpha$ . The continuum is absorbed by partial covering absorption and fully covering absorption.

spectra (see Table 3.4). The Fe I line was not detected during eclipse (see Table 3.3). I therefore derived an upper limit for the strength of the line.

In order to place constraints on the origin of the Fe  $K\alpha$  lines, I compared the flux of the Fe  $K\alpha$  lines with the unabsorbed continuum flux in the 7.1–9.0 keV band (see Figure 3.13). The flux of the Fe I line is found to decrease by a factor of  $\sim 15$  during eclipse (see Table 3.4). Additionally, I found that the flux of Fe XXV and Fe XXVI decreases by a factor of approximately 3 during the eclipse phase (see Table 3.4). Within measurement errors, the flux of the Fe  $K\alpha$  lines observed out-of-eclipse was found to follow the flux of the continuum. The correlation coefficients,  $r$ , are as follows:  $r=0.82$ ,  $r=0.81$  and  $r=0.87$  for the Fe I, Fe XXV and Fe XXVI lines, respectively. Using a logarithmic parameter space, I measured the slope of the Fe  $K\alpha$  line flux observed out-of-eclipse versus continuum flux— $m=1.0\pm 0.1$ ,  $m=0.6\pm 0.1$  and  $m=0.7\pm 0.1$  for the Fe I, Fe XXV and Fe XXVI lines, respectively.

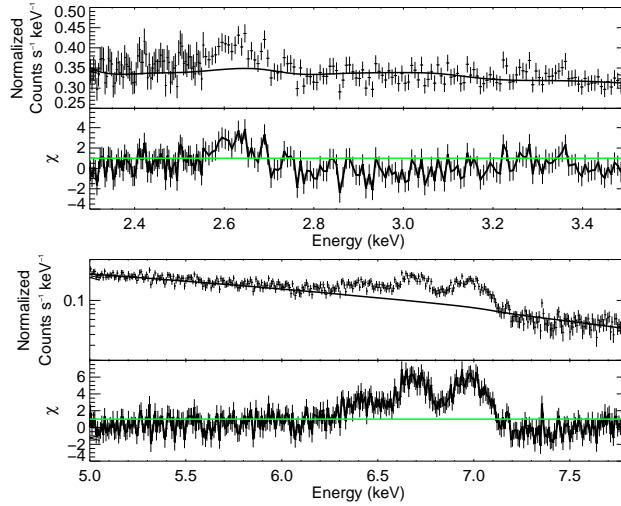


FIG. 3.12. The XIS-0+3 spectrum of 4U 1210-64 in the 2.3–3.5 keV (top) and 5.0–7.8 keV bands (third panel) to illustrate the S XVI and Fe  $K\alpha$  emission lines along with the best fit model. The normalization of the lines was set to 0 in the model. Residuals are plotted in the second from top and bottom panels.

To constrain the state of the plasma, I calculated the flux ratio between the Fe XXV and Fe XXVI emission features. I defined the flux ratio as the flux of the Fe XXV line divided by the flux of the Fe XXVI line. No change was found in the flux ratio between the Fe XXV and Fe XXVI emission features and the continuum flux in the 7.1–9.0 keV band (see Table 3.4).

In contrast to the Fe  $K\alpha$  lines, the S XVI  $K\alpha$  line was not consistently detected throughout the duration of the *Suzaku* observation (see Table 3.4). During the time intervals specified in Table 3.4, I calculated an upper limit of the EQW and flux of the S XVI line at the 90% confidence interval. I also searched for correlations between the continuum spectral parameters (the power law with the high energy cutoff modified with fully covered and partial covering absorption) with respect to the 7.1–9.0 keV continuum flux (see Table 3.4). No clear correlation between the parameter values and flux was found.

In addition, I found that a bremsstrahlung model with a temperature of  $7.2 \pm 0.2$  keV

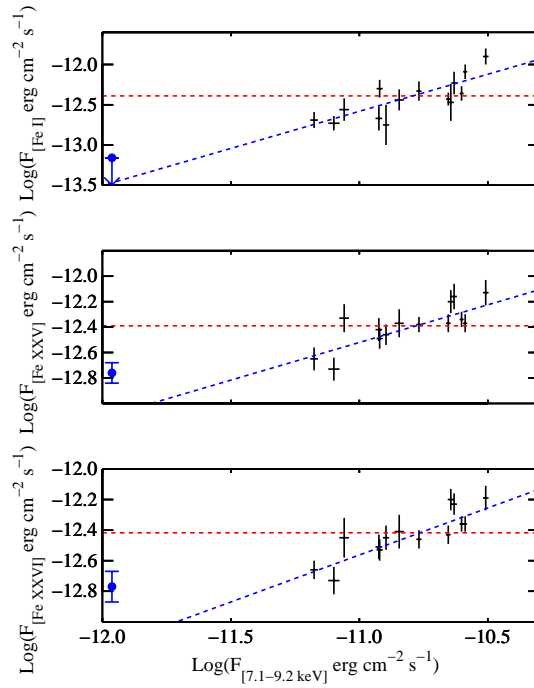


FIG. 3.13. Flux of the Fe I (top), Fe XXV (middle) and Fe XXVI (bottom) lines vs. the unabsorbed continuum flux in the 7.1–9.0 keV band in logarithmic units. An upper limit at the 90% confidence interval is shown for the Fe I line during eclipse. The red and blue lines indicate the best fit for constant and power law models respectively. The correlation coefficients,  $r$ , are as follows:  $r=0.82$ ,  $r=0.81$  and  $r=0.87$  for the Fe I, Fe XXV and Fe XXVI lines, respectively. Using a logarithmic parameter space, I measured the slope of the Fe  $K\alpha$  line flux versus continuum flux— $m=1.0\pm 0.1$ ,  $m=0.6\pm 0.1$  and  $m=0.7\pm 0.1$  for the Fe I, Fe XXV and Fe XXVI lines, respectively. The blue points indicate the data collected during eclipse.

also fits the *Suzaku* data reasonably well. However, this model is found to provide unsatisfactory fits to the PCA spectra where  $\chi^2_\nu$  was found to exceed 2 (see Section 3.4.4.2). Therefore, the power law with the high energy cutoff model is the preferred description of 4U 1210-64.

**3.4.4.2 PCA Spectral Analysis** I analyzed the PCA spectral data of 4U 1210-64 from MJD 54804–54842, using the models described in Section 3.4.4.1. The best-fit

model is a power law with a high energy cutoff (see Figure 3.14, top and middle). Due to the lack of low energy response (see Section A.3.1.2), the absorption that is observed in the *Suzaku* spectra cannot be accurately measured using the PCA (see Section 3.4.4.1). Therefore, I froze  $N_{\text{H}}$  to the out-of-eclipse value determined with *Suzaku*.

The power law index,  $\Gamma$ , and cutoff energies found with the PCA are consistent with those determined with the *Suzaku* analysis. However, I note that the folding energy obtained with the PCA differs somewhat from that obtained with *Suzaku*. I also note that the folding energy was found to be variable among different time segments of PCA data.

Due to the  $\sim 10$  times lower spectral resolution of the PCA compared with *Suzaku* (see Sections A.3.1.2 and 3.3.4.1, respectively), I detected only a broad emission feature between energies 6.4–6.7 keV in the Fe  $K\alpha$  region, which was modeled using a single Gaussian (see Figure 3.14, bottom). Furthermore, the S XVI  $K\alpha$  feature was not detected in the PCA spectra, which is expected due to the low sensitivity of the PCA at 2.62 keV.

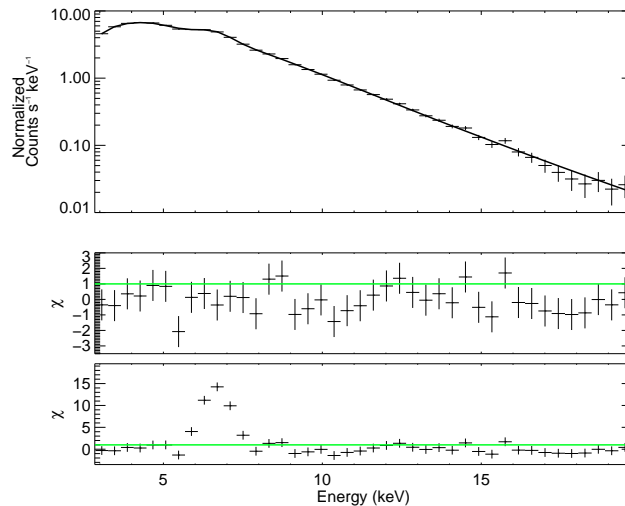


FIG. 3.14. A typical PCA spectrum (MJD 54804) and best fit model (top panel). This consists of a continuum comprised of a power law with a high-energy cutoff and a broad Fe  $K\alpha$  emission line. Residuals of the best fit model are plotted in the middle panel. To illustrate the Fe  $K\alpha$  emission lines along with the best fit model, the normalization of the line was set to 0. Residuals are plotted in the bottom panel.

The temporal dependence of the spectral parameters was investigated (see Table 3.5). I searched for correlations between the continuum spectral parameters (folding energy, the high energy cutoff and the power law index) with respect to the 2.5–20 keV continuum flux (see Figure 3.15). While no clear correlation between the folding energy and flux was found, the high-energy cutoff and power-law index are anti-correlated in respect to the continuum flux. The correlation coefficients ( $r$ ) are: -0.69 and -0.81 for the high energy cutoff and power law index, respectively.

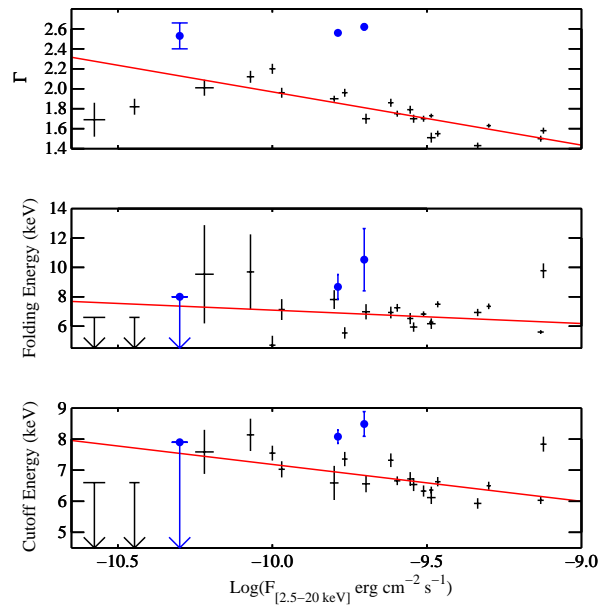


FIG. 3.15. Power Law Index (top), Folding Energy (middle) and High Energy Cutoff Energy (bottom) for the PCA spectra vs. the continuum flux in the 2.5–20 keV band in logarithmic units. The red lines indicate the best fit for the power law model. The correlation coefficients ( $r$ ) are: -0.72 and -0.80 for the high energy cutoff and power law index, respectively. The blue points indicate the data collected during eclipse.

### 3.5 Discussion

In this analysis of 4U 1210-64, I found the presence of an eclipse, long and short-term variability, and an Fe  $K\alpha$  emission complex. Below, I discuss constraints on the mass donor based on the eclipse half-angle, the nature of the compact object, the variability found in the system, and the mechanism responsible for the Fe  $K\alpha$  emission seen in 4U 1210-64.

Similar to what was found in IGR J16393-4643 (see Section 2.5.2), the source emission does not reach 0 counts  $s^{-1}$  in the folded light curves (see Section 3.4.2). Residual emission was also found in the *Suzaku* and PCA observations (see Tables 3.3–3.5). While residual emission has been attributed to a dust-scattering halo in some other HMXBs (Cen X-3; Vela X-1; OAO 1657-415, Day & Tennant, 1991; Woo et al., 1994; Audley et al., 2006), the residual emission found in 4U 1210-64 is seen at much higher levels compared to the out-of-eclipse emission, and is found in both MAXI (2–20 keV) and PCA (2.5–20 keV). A dust-scattering halo is predominantly a soft X-ray phenomenon: given the interstellar  $N_H$  (see Table 3.3) I infer perhaps 10-20% of the out-of-eclipse flux at 1 keV may be in a dust-scattering halo (Predehl & Schmitt, 1995), but a much smaller fraction in the MAXI and the PCA bands. Since the Fe XXV and Fe XXVI lines are detected in eclipse, indicating the presence of an extended region of ionized gas, it is plausible that Compton scattering and reprocessing can account for the residual flux in eclipse (Watanabe et al., 2006).

### 3.5.1 Constraints on the Mass-Donor

My analysis of the ASM, MAXI and BAT folded light curves reveals the presence of a sharp dip, which is suggestive of an eclipse (see Section 3.4.2).

**3.5.1.1 Eclipse Half-Angle Constraints** As discussed in Section 2.3.2, X-ray Binaries that are eclipsing have an eclipse duration that is dependent on the radius of the mass donor, inclination angle of the system and the sum of the donor star and compact object masses. In these calculations, I first assume a  $1.4 M_{\odot}$  compact object, which may be appropriate for an accreting neutron star (Chandrasekhar, 1931). The region allowed by the measured eclipse half-angle for 4U 1210-64 in the Mass-Radius plot is shown in Figure 3.16 (shaded region). An intriguing result is that the duration of the observed eclipse is inconsistent with the proposed B5 V spectral type (see Figure 3.17). A B5 V star has a mass of  $5.9 M_{\odot}$  according to Carroll & Ostlie (2006) and Allen (2000). For a donor star of  $5.9 M_{\odot}$  to satisfy the eclipse half-angle constraint, I calculated the radius must exceed  $5.37 R_{\odot}$ . This is clearly larger than the radii reported in Carroll & Ostlie (2006) and Allen (2000), which are  $4.1 R_{\odot}$  and  $3.9 R_{\odot}$ , respectively (see Table 3.6). Therefore, the radius of a B5 V star is too small to satisfy the observed eclipse duration (see Figure 3.16).

The eclipse half-angle was calculated as a function of inclination angle for other B-type stars—B0 V, B5 III, B0 III, B5 I and B0 I (see Figure 3.17). The eclipse half-angle was found to be consistent with a main-sequence star of spectral class B0 V only at high inclination angles (see Table 3.6). I also consider intermediate and late spectral types in this analysis (see Figures 3.16 and 3.17). These will be discussed in Section 3.5.1.3.

I also calculated the eclipse half-angle as a function of the inclination angle for these stars under the assumption of more massive compact objects. The results are presented in Figures 3.16 and 3.17 for the scenario of a  $1.9 M_{\odot}$  neutron star, which is one of the highest known masses for neutron stars in XRBs (Lattimer, 2012). My results remained the same for more substantial mass donors. However, the results require slightly higher inclination angles for intermediate and late spectral types (see Figure 3.16).

The spectral type of the mass donor places an additional constraint on the distance of 4U 1210-64. Under the assumption that the R-band magnitude ( $m_R$ ) and extinction in the V-band ( $A_V$ ) are magnitudes 13.9 and 3.3 for a B5 V classification (Masetti et al., 2009), the distance and average X-ray luminosity of the source are found to be  $\sim 2.8$  kpc and  $1.79 \pm 0.02 \times 10^{35}$  erg s $^{-1}$ , respectively (see Table 3.6). I calculated the extinction in the V-band ( $A_V$ ) using Equation 1 in Güver & Oumlzel (2009) and the measured neutral hydrogen column densities for the fully covered absorber (see Table 3.4).  $A_V$  was found to be  $3.2 \pm 0.1$  for the power law with high energy cutoff model.

The distance and average X-ray luminosity of 4U 1210-64 assuming the aforementioned spectral types are reported in Table 3.6 using the values for  $M_V$  and  $A_R$  obtained from Carroll & Ostlie (2006). A B0 V star places the system at an estimated distance of  $\sim 9.5$  kpc away from the Sun, indicating that 4U 1210-64 could be located in the Carina arm (approximately 10 kpc). A supergiant classification places 4U 1210-64 at a galactocentric distance exceeding  $\sim 26$  kpc, which is outside the Galaxy. Therefore, the possibility of a supergiant must be excluded. Since Masetti et al. (2009)'s previous classification must also be excluded due to the observed eclipse duration, it is possible that the mass donor could be an early B-type giant or an early F-type giant (see Section 3.5.1.3). Main-

sequence stars with the exception of very early types and very high inclination angles are also excluded.

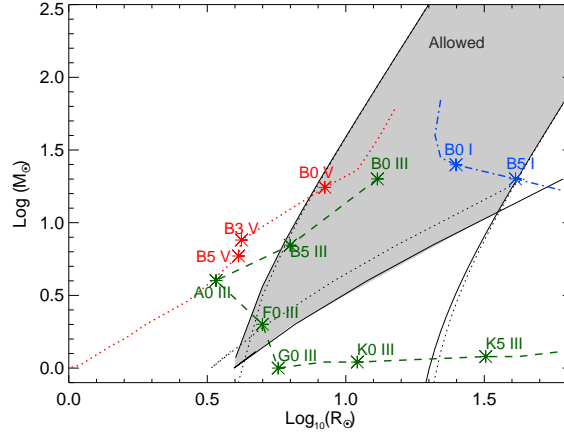


FIG. 3.16. Log-log plot of stellar masses as a function of stellar radii. The shaded region, derived using Equation E.4 in Chakrabarty (1996) for all possible inclination angles, indicates the allowed spectral types that satisfy the eclipse observed in the BAT, MAXI, and ASM folded light curves provided that the compact object is  $1.4 M_{\odot}$  (see Figures 3.3 and 3.4, respectively). The black dotted lines show the allowed spectral types that satisfy the eclipse for a compact object of  $1.9 M_{\odot}$  (see Section 3.5.1). Stellar masses and radii are given in Table 3.6.

**3.5.1.2 Does the Proposed Mass Donor Spectral Type Agree with the Optical Spectrum Reported in Masetti et al. (2009)?** The duration of the eclipse along with the constraint that the mass donor must underfill the Roche lobe allows for the possibility of several different spectral types (see Sections 3.5.1 and 3.5.1.3). I compared the expected optical spectra for each proposed mass donor with the optical spectrum reported in Masetti et al. (2009) (the top-right panel in Figure 4) to place an additional constraint on the nature of the mass donor. Since the  $4000\text{-}5000\text{\AA}$  region is compressed in the broadband spectrum reported in Masetti et al. (2009), there are possible caveats in the identification of spectral features to correctly classify the mass donor.

The features observed in the optical spectrum reported in Masetti et al. (2009) in-

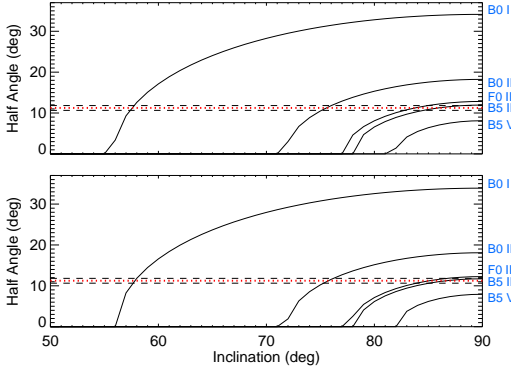


FIG. 3.17. The black curves show predicted eclipse half angle as a function of inclination for stars with the indicated spectral types. The red and black dashed lines indicate the half angle and its estimated error as measured by ASM and MAXI (see Section 3.5.1). I assume a neutron star mass of  $1.4 M_{\odot}$  (top) and of mass  $1.9 M_{\odot}$  (bottom) and typical masses and radii for the assumed companion spectral type (see Table 3.6).

clude absorbed Balmer series lines and the emission of neutral helium, singly ionized helium and a blend of doubly ionized nitrogen and carbon. The optical spectra of B-type stars are expected to show the absorption of neutral helium and  $H\alpha$  lines (Carroll & Ostlie, 2006, and references therein). Singly ionized calcium features at  $\sim 3900\text{\AA}$  become dominant in F-type stars (Carroll & Ostlie, 2006, and references therein), which would be difficult to detect in the broadband optical spectrum. The stellar luminosity type can also in principle be determined using spectral lines, which could lead to distinguishing a B III or B V type. For B5 stars, the ratio of Si II to Si III as well as the Al III and Fe III lines can be used to determine luminosity type (Gray & Corbally, 2009). Unfortunately, the existing optical spectra are not suitable in detecting these effects.

The observed value of the  $B - R$  color of  $1.5^7$  was compared with the intrinsic  $(B - R)_0$  for the proposed mass donors (see Table 3.6). Calculating the difference between the observed  $B - R$  and the intrinsic  $(B - R)_0$ , I found the reddening values  $E(B - R)$  for

<sup>7</sup><http://www.iasfbo.inaf.it/~masetti/IGR/main.html>

each proposed spectral type for the mass donor (see Table 3.6). I calculated the reddening in the  $B - V$  band,  $E(B - V)$ , using Equation 1 in Güver & Oumlzel (2009) and the measured neutral hydrogen column densities for fully covered absorber (see Table 3.4). I converted  $E(B - V)$  to  $E(B - R)$  using Table 3 in Rieke & Lebofsky (1985). I found  $E(B - R)$  to be  $1.82 \pm 0.08$  for the power law with high energy cutoff model, where the reddening was found to be consistent with main-sequence and giant B-type stars but was inconsistent with F-types. Since a B5 V classification does not satisfy the eclipse half-angle, the optical features might indicate that the mass donor is a B-type giant. I note the optical spectra of B-type giants would be difficult to distinguish from those of main-sequence B-type stars because of the low-resolution of the broadband optical spectrum. F-type giants cannot be completely excluded due to systematic effects which prevent a definite determination. For example, I assumed that the fully covered  $N_{\text{H}}$  is entirely interstellar in origin (see Section 3.4.4.1). While this is the simplest interpretation of the data, the possibility that the fully covered  $N_{\text{H}}$  is due to a combination of intrinsic and interstellar absorbers cannot be excluded. According to this calculation, if  $\sim 40\%$  of the measured fully covered  $N_{\text{H}}$  is intrinsic to the source and the rest interstellar, then the inferred  $E(B - R)$  would be consistent with an F-type mass donor.

Finally, I considered the possibility that the apparent spectral type is affected by heating by the radiation of the X-ray source. I first calculated the flux of 4U 1210-64 using both *Suzaku* and the PCA. Out-of-eclipse, the flux of 4U 1210-64 was found to be  $\sim 2 \times 10^{-10} \text{ erg cm}^{-2} \text{ s}^{-1}$  for the power-law model with a high-energy cutoff model in the *Suzaku* data. The flux in the PCA is reported in Table 3.5 ranging from  $0.29 \pm 0.03 \times 10^{-10}$  to  $8.9 \pm 0.4 \times 10^{-10} \text{ erg cm}^{-2} \text{ s}^{-1}$ . I converted the apparent magnitude in the R band

(Masetti et al., 2009) into an optical flux using Bessell (1979). The flux in the R band was found to be 0.08 Jy, which can be converted to  $\sim 2 \times 10^{-7}$  erg cm<sup>-2</sup> s<sup>-1</sup>. The flux ratio  $F_X/F_{opt}$  was found to be  $\sim 10^{-4}$ , which is much smaller than what is observed in systems where irradiation is important (e.g.  $F_X/F_{opt}$  was found to be  $\sim 10^2$  in Her X-1; Bradt & McClintock, 1983). I conclude that irradiation effects are negligible in 4U 1210-64.

**3.5.1.3 Is 4U 1210-64 an Intermediate-Mass X-ray Binary?** In addition to the possibility that the donor star is a B-type giant, the duration of the eclipse suggests that an Intermediate-Mass classification cannot be ruled out. I found the eclipse half angle is consistent with F0 and G0 giants at inclination angles exceeding 79° and 70°, respectively (see Table 3.6). Using the values for  $M_V$  and  $A_R$  published in Carroll & Ostlie (2006) and Masetti et al. (2009), the distance of 4U 1210-64 was found to be  $\sim 0.9$  kpc and  $\sim 1.3$  kpc for a mass donor of spectral type F0 III and G0 III, respectively, which places 4U 1210-64 at a luminosity of  $\sim 10^{34}$  erg s<sup>-1</sup> (see Table 3.6). Other intermediate XRBs that host F-type stars include Cyg X-2 and Her X-1 (e.g. Seward & Charles, 1995), which have considerably higher luminosities on the order of  $\sim 10^{37}$  erg s<sup>-1</sup>. The luminosities calculated for the F0 III and G0 III spectral types still exceed that of cataclysmic variables (see Section 4.5.3).

The possibility that the mass donor in 4U 1210-64 is an intermediate or late-type star hints at the presence of an accretion disk. XRBs that host intermediate- and low-mass stars accrete matter through Roche-lobe overflow (see Equation 2, Eggleton, 1983). The Roche lobe places an additional constraint on the spectral type of the mass donor in 4U

1210-64. While a spectral type of G0 III satisfies the observed eclipse half-angle, the Roche lobe would be significantly overfilled (see Table 3.6).

Finally, I discuss caveats in the hypothesis that the mass donor is an Intermediate-Mass star. No strong disk component was found, which is expected in the X-ray spectra of Intermediate-Mass X-ray Binaries (e.g. Seward & Charles, 1995). I note that the reddening,  $E(B - R)$ , was found to be consistent with main-sequence and giant B-type stars but was inconsistent with F-type and G-type stars (see Section 3.5.1.2). While  $E(B - R)$  is apparently inconsistent with F-type stars, the possibility of systematic effects prevents excluding F-type stars as the possible mass donor (see Section 3.5.1.2). However, I can confidently exclude G-type stars due to the additional constraint that the Roche lobe is not significantly overfilled.

### **3.5.2 What is the Nature of the Compact Object?**

The nature of the compact object present in 4U 1210-64 remains ambiguous. An analysis of the ASM, MAXI and PCA power spectra shows that no pulsation period could be identified. A pulsation period would provide a clear indication that the compact object is a neutron star. The PCA power spectra, which cover the range of 860 s–38 d (see Figure 3.9) and 10 ms–14 minutes (see Figure 3.10), are dominated by red noise, which could compromise the search for the pulsation period. While the low-frequency noise from the power spectra was removed (see Section 3.4.3.2), the PCA power spectrum covering the range of 860 s–38 d was still compromised due to the orbital period of *RXTE* (see Figure 3.9). Spectral results so far have also been inconclusive. Cyclotron lines, which would have proved a neutron star explanation for the compact object, are absent in the *Suzaku*

spectra. Additionally, the *Suzaku* and PCA data suggest the continuum can be modeled using an absorbed cutoff power law where the high-energy cutoff is  $5.5 \pm 0.2$  keV. Since a firm identification of the nature of the compact object in 4U 1210-64 has so far proven elusive, I compare my findings to systems where the compact object is known.

I first discuss the possible scenario that the compact object present in 4U 1210-64 is a black hole. Observations show that the exponential cut-off energy in HMXBs that host black holes exceeds 60 keV (Tomsick et al., 2009), sharply contrasting with the  $5.5 \pm 0.2$  keV cut-off observed in the *Suzaku* spectra. Additionally, *INTEGRAL* observations reveal the presence of a soft excess in 4U 1210-64 (Masetti et al., 2010), which is characteristic of HMXBs that host neutron stars (Hickox et al., 2004). The low cutoff energy suggests that a black hole explanation of the compact object is unlikely.

I also consider the possibility that the compact object could be an accreting white dwarf. The luminosities observed in cataclysmic variables depend on the magnetic nature of the white dwarf, which affects the mode of accretion. The most luminous sub-type of CV, the intermediate polars, were found to be on the order of  $10^{31} - 4 \times 10^{33}$  erg s<sup>-1</sup> (Brunschweiler et al., 2009). In comparison, the luminosities calculated for 4U 1210-64 exceed the above result by at least 1–2 orders of magnitude (see Table 3.6). Assuming a bremsstrahlung fit, Brunschweiler et al. (2009) found the temperatures ( $kT_{\text{brems}}$ ) of intermediate polars are on the order of 10–40 keV, which differs from the value observed in 4U 1210-64 (see Section 3.4.4.1). Since a bremsstrahlung model was found to be an unsatisfactory fit to the PCA data, I conclude that the CV explanation is unlikely.

Finally, I discuss the possibility that 4U 1210-64 contains a neutron star. Several geometries have been proposed to describe the apparent lack of a signal corresponding to

the pulsation period. One possibility is a co-alignment of the magnetic and spin axes of the neutron star (e.g. Bodaghee et al., 2010). A second explanation suggests that throughout the rotation the accretion beam points along the line of sight (e.g. Bodaghee et al., 2010). The absence of a well defined pulsation period could also be explained by a weak magnetic field. Another possibility is that the compact object in 4U 1210-64 is a slowly rotating neutron star (e.g. 2S 0114+650, Farrell et al., 2008, and references therein).

### **3.5.3 What is the physical process responsible for the low state observed in the ASM data?**

The ASM data reveal the presence of three distinct system states as previously noted by Corbet & Mukai (2008). These are two active states and one low state I interpret as quiescence (see Section 3.4.1.1). This long-term variability is suggestive of a variable accretion rate.

I first discuss the possibility that 4U 1210-64 is powered by the Be mechanism. In BeXBs the compact object accretes material from the circumstellar disc of a rapidly rotating main-sequence or giant B-type star. If the system is a BeXB, changes in the circumstellar disc around the Be star could also explain the period of low activity. Observations indicate that bright and faint states might correspond to the formation and dissipation of the circumstellar disc (Reig et al., 2010). The timescale for the development and disappearance of a circumstellar disc is typically on the order of 3–7 years, which is consistent with the ASM data. One notable BeXB is SAX J2103.5+4545, which consists of a neutron star in a 12.7 day orbit around a B0Ve star (Reig et al., 2010). The timescale for the development and disappearance of the circumstellar disc is 1–2 years,

possibly due to the short orbital period (Reig et al., 2010). While a BeXB explanation supports the presence of high and low states observed in the ASM data, the presence of an eclipse of the compact object is inconsistent with most main-sequence B-type stars, where main-sequence stars later than a B0 do not satisfy the observed eclipse half angle (see Figures 3.16– 3.17). This is not surprising due to the smaller radius of the mass donors observed in most BeXBs. I note, however, that B-type giants would satisfy the observed eclipse duration at high inclination angles (see Section 3.5.1). Additionally, the Balmer lines, particularly the  $H\alpha$  line, were found to be in absorption during the optical campaign of 4U 1210-64 (MJD 54529.3) reported in Masetti et al. (2009). Since this occurred during a high state of the system (see Table 3.1 and Section 3.4.1.1), it would be expected for  $H\alpha$  to be in emission (Silaj et al., 2010).

I also consider the possibility that the state transitions originate due to a mechanism similar to what is observed in Black Hole Candidates (BHCs). Multiple states are observed in BHCs, which are defined as soft/high, intermediate and hard/low (Cygnus X-1; GX 339-4, Grinberg et al., 2013; Nowak, 2006; Dunn et al., 2010). The high-energy cut-off in BHCs exceeds 60 keV (Tomsick et al., 2009), which is in variance with my results obtained with *Suzaku* and PCA. Additionally, a disk blackbody is required to model the low-energy spectra of BHCs in the soft/high state (Shakura & Sunyaev, 1973; Nowak, 2006), which is not seen in the *Suzaku* and PCA analysis of 4U 1210-64.

Finally, I discuss the possibility that the mode of accretion in 4U 1210-64 is Roche-lobe overflow, which primarily occurs in both Intermediate- and Low-Mass X-ray Binaries. I compare the long-term behavior of 4U 1210-64 to that seen in soft X-ray transients, NS-LMXBs that host at least two different states (e.g. Aql X-1; Sakurai et al., 2014). In

soft X-ray transients, the physical mechanism that could lead to a reduction of intensity is changes in the accretion rate,  $\dot{M}$  (Sakurai et al., 2014). The luminosity is significantly reduced when the accretion rate is low. Since the magnetic field of the majority of NS-LMXBs is weak, the propeller effect becomes important when the accretion rate,  $\dot{M}$ , is low (Sakurai et al., 2014). The long-term behavior of 4U 1210-64 differs from soft X-ray transients. While there are extended low states (Matsuoka & Asai, 2013; Sakurai et al., 2014), the high states are shorter and brighter than what is observed in 4U 1210-64 (Coti Zelati et al., 2014).

No mechanism described above appears to be consistent with 4U 1210-64. While there are uncertainties in the spectral classification, I note that the behavior of Intermediate-Mass X-ray Binaries is not well known. Therefore, if 4U 1210-64 is a member of this class, unusual variability may be possible.

### **3.5.4 What is the origin of the variability in the high-state?**

My analysis of the *Suzaku* and PCA data reveals the presence of strong variability in the light curves (see Figures 3.5 and 3.7). In the *Suzaku* data, “flares” were observed to reach nearly 1.4 times the mean count rate (i.e. a modulation depth of 140%). The variability is even stronger in the PCA data, where the modulation depth was found to be 330%. A reduced count rate was found in the PCA light curve between  $\sim$ MJD 54830–54833, which is outside the eclipse (see Figure 3.7). The unabsorbed flux of 4U 1210-64 was found to vary by a factor of  $\sim$ 25 over the course of both the *Suzaku* and PCA observations (see Sections 3.4.4.1 and 3.4.4.2).

The large variability in the Suzaku and PCA light curves could be attributed to several different physical processes, all resulting in changes in the accretion rate,  $\dot{M}$ . A positive correlation between the *Suzaku* hardness ratio and continuum flux was found (see Figure 3.6), which provides evidence against a strong wind. This is further strengthened by a decrease in the *Suzaku* hardness ratio during the egress phase of the observation. Since the system is eclipsing, a strong wind should lead to an increase in absorption and thus the X-ray hardness ratio during the ingress and egress phases of the orbit (Clark et al., 1988; Doroshenko et al., 2013; Suchy et al., 2008). The folded MAXI and ASM light curves (see Figure 3.18, top and bottom) provide additional evidence against it. The increase in the folded MAXI hardness ratio is modest (Figure 3.18, top), indicating the possible presence of a tenuous wind but not of a typical HMXB wind (e.g. Vela X-1; Cen X-3, Doroshenko et al., 2013; Suchy et al., 2008). Such behavior is not seen in the folded hardness ratio produced by the ASM, which is possibly due to the low count rate (see Figure 3.18, bottom). The observed  $N_{\text{H}}$  could possibly originate in an accretion stream (e.g. Cygnus X-1, Hanke et al., 2009, and references therein).

Magnetic and centrifugal barriers have been proposed to inhibit the accretion process in XRBs on hourly timescales (Bozzo et al., 2008), where the timescale is consistent with the variability in the light curve. This could explain the reduced count rate in the PCA lightcurve (see Figure 3.7, top). Another mechanism that could lead to such a reduction is the formation and dissipation of an unstable accretion disk (e.g. Bodaghee et al., 2011, and references therein).

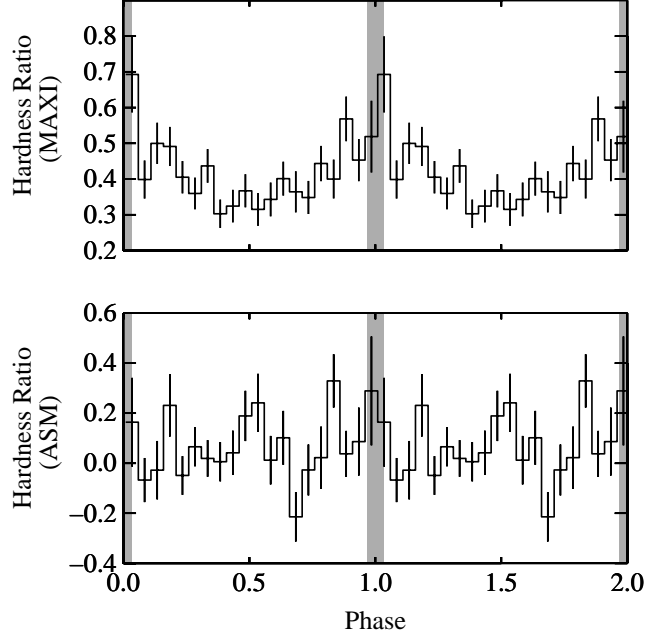


FIG. 3.18. Hardness ratios of the folded MAXI (top) and ASM (bottom) light curves. The hardness ratio is defined as  $C_{\text{hard}} - C_{\text{soft}} / C_{\text{hard}} + C_{\text{soft}}$ , where the soft and hard energy bands are defined as 2–4 keV and 4–10 keV and 1.5–5 keV and 5–12 keV for the MAXI and ASM light curves, respectively. The eclipse is indicated by the shaded regions.

### 3.5.5 Emission Lines

The analysis of spectral data produced by *Suzaku* reveals the presence of emission lines at energies 2.6 keV, 6.4 keV, 6.7 keV and 6.97 keV. I interpret the emission lines as S XVI  $K\alpha$ , Fe  $K\alpha$ , Fe XXV  $K\alpha$  and Fe XXVI  $K\alpha$ , respectively. Below I discuss the mechanisms that are proposed to explain the emission lines seen in 4U 1210-64.

**3.5.5.1 Fe  $K\alpha$  Emission** A 6.4 keV emission line has been shown to be present in many XRBs (e.g. Vela X-1, 4U 1700-377, Cen X-3 and 4U 1822-37; Schulz et al., 2002; van der Meer et al., 2005; Naik et al., 2011; Sasano et al., 2014). The origin of the

6.4 keV emission line is due to neutral Fe or Fe in a low ionization state. Unless otherwise stated, I assume that Fe I emission is responsible for the 6.4 keV emission line.

My analysis of the Fe I line indicates that the line flux tracks the flux in the continuum in the 7.1–9.0 keV band when 4U 1210-64 is out-of-eclipse and is not detected in eclipse (see Section 3.4.4.1). This is suggestive that the region responsible for the Fe I emission is close to the compact object. The accretion mechanism in 4U 1210-64 differs from the X-ray excited wind observed in the HMXB Cen X-3 (Day & Stevens, 1993), but the Fe  $K\alpha$  emission region is similar in both objects. For instance, the Fe I emission line in Cen X-3 was observed to be weakest during the eclipse phase (Ebisawa et al., 1996; Naik & Paul, 2012). Because of these similarities, I compare 4U 1210-64 with Cen X-3 to understand the Fe  $K\alpha$  emission feature.

Possible mechanisms that have been suggested to cause the fluorescence of cold material include a plasma layer at the surface of the Alfvén shell and an optically thick accretion disc (Basko, 1980; Ebisawa et al., 1996). The flux of Fe I was found to decrease by more than an order of magnitude during eclipse, which is comparable to the change of flux observed in the continuum. This is further indication that the origin of the Fe I emission is close to the compact object. The slope of the Fe I flux versus the continuum flux is near unity, which shows that the Fe I emission is in agreement with fluorescence (Nespoli et al., 2012; Reig & Nespoli, 2013).

I also consider the mechanism responsible for the Fe XXV and Fe XXVI emission features. A possible correlation between the flux of both the Fe XXV and Fe XXVI emission features with respect to the continuum flux in the 7.1–9.0 keV band was found, which shows that the presence of Fe XXV and Fe XXVI increases as the continuum flux

increases (see Section 3.4). I note that the slope between the continuum flux and the flux of the lines is significantly less than 1, which can be interpreted as a possible sign that an increasing part of the medium might be completely ionized.

To place constraints on the state of the plasma, I analyzed the flux ratio between the Fe XXV and Fe XXVI emission features and the continuum flux in the 7.1–9.0 keV band. No change was found in the flux ratio between the Fe XXV and Fe XXVI emission features and the continuum flux in the 7.1–9.0 keV band (see Table 3.4), which indicates that the Fe XXV and Fe XXVI features possibly originate in the same region of a structured medium, where the ionization state can be independent of luminosity (Ebisawa et al., 1996), which is in agreement with my result of a constant flux ratio as a function of luminosity.

Fe XXV and Fe XXVI are likely due to photoionization. Recombination followed by electron cascade transitions is present in systems such as SMC X-1 (Vrtilek et al., 2001), Cen X-3 (Nespoli et al., 2012; Reig & Nespoli, 2013), Vela X-1 (Goldstein et al., 2004), 4U 1700-37 (Liedahl & Paerels, 1996) and 4U 1822-37 (Sasano et al., 2014). Emission features are more prominent during eclipse since direct emission from the compact object irradiating the accretion stream is no longer visible. The photoionization mechanism must originate in regions of low density since the range of luminosities I inferred in 4U 1210-64 (see Table 3.6) is significantly lower than what is observed in systems such as Cen X-3 and SMC X-1 ( $\sim 10^{37}$  erg s<sup>-1</sup>, Naik & Paul, 2012; Vrtilek et al., 2001).

The very large EQWs of the Fe XXV and Fe XXVI emission features in eclipse (see Section 3.4) are consistent with an origin due to the reprocessing of photons in the

accretion stream. In comparison, the EQW of the Fe XXV and Fe XXVI emission features observed in the HMXB Cen X-3 is largest during eclipse and tends to decrease as the continuum flux increases (Naik & Paul, 2012). Naik & Paul (2012) show that the region responsible for the Fe XXV and Fe XXVI emission observed in Cen X-3 is extended and is comparable to the size of the mass donor in the system, which is likely what is observed in 4U 1210-64.

**3.5.5.2 The presence of S XVI in 4U 1210-64** Different ionization species of low to mid-Z elements such as S are present in eclipsing XRBs (e.g. Vela X-1, 4U 1700-377 and LMC X-4, Schulz et al., 2002; van der Meer et al., 2005; Hung et al., 2010). While near neutral fluorescent lines in addition to highly ionized species of emission lines were observed in SGXBs such as Vela X-1 (Schulz et al., 2002), the *Suzaku* spectra of 4U 1210-64 reveal only the highly ionized species of S XVI.

It has been shown that photoionization and radiative recombination are responsible for the presence of hydrogen-like species of S in absorbed XRBs (Iaria et al., 2004). The S XVI  $K\alpha$  emission features only appeared during part of the *Suzaku* observation (see Table 3.4). As a result, the temporal variability of the EQW or fluxes of S XVI could not be measured.

## 3.6 Conclusion

4U 1210-64, for which an orbital period of  $6.7101 \pm 0.0005$  days was determined, is a unique XRB. The companion star was previously proposed to have a spectral type of B5 V. I found that a B5 V classification does not satisfy the eclipse half-angle, compelling

evidence against a B5 V classification. 4U 1210-64's spectral features seem to indicate that the mass donor could be a B0 V or B0-5 III star. A Be-type accretion mechanism, with most BeXBs hosting primaries of spectral type late O to B2 (Negueruela, 1998), is unlikely, since these systems usually have longer periods and are transients. A supergiant classification must be excluded since the implied distance would put the object outside the Galaxy. F-type giants also satisfy the constraints imposed by the eclipse half-angle and Lagrange point, L1, where Roche-lobe transfer would be expected to occur. To further constrain the spectral type of the mass donor, the reddening values  $E(B - R)$  were calculated for the possible spectral types. The reddening was found to be consistent with main sequence and giant B-type stars but was inconsistent with F-types. Due to the uncertainties in the conversion between  $N_{\text{H}}$  and  $E(B - R)$ , an F-type mass donor cannot be completely excluded.

4U 1210-64 hosts a compact object that remains ambiguous in nature. No signs of pulsations or cyclotron features were found in this analysis of 4U 1210-64, which would prove that the compact object is a neutron star. The spectral properties of the continuum strongly contrast with those typically seen in black hole candidates (BHC) as well as CVs. In particular, a disk blackbody is required to model the low energy spectra of BHCs in the soft/high state while CVs are typically fit with a bremsstrahlung model. While the nature of the compact object has proven elusive, a neutron star with a weak magnetic field possibly aligned with the spin axis is consistent with the lack of pulsations and cyclotron features.

Emission lines at 2.62 keV, 6.41 keV, 6.7 keV and 6.97 keV were all clearly detected in the *Suzaku* spectra, which can be interpreted as S XVI  $K\alpha$ , Fe  $K\alpha$ , Fe XXV  $K\alpha$  and

Fe XXVI  $K\alpha$ , respectively. The flux of the Fe  $K\alpha$  lines closely tracks the flux of the unabsorbed continuum. I found a linear relationship between the flux of Fe I vs. the continuum, which shows that the most probable origin of the Fe I line is fluorescence of cold and dense material close to the compact object. An origin close to the compact object is further supported by the fact that Fe I is not clearly detected during eclipse. The slopes of the relationship between the logarithm of the Fe XXV and Fe XXVI flux versus the logarithm continuum possibly show that an increasing part of the medium might be completely ionized as the flux increases.

Strong variability was found in the *Suzaku* and PCA observations. The out-of-eclipse flux was found to be  $1.73_{-0.05}^{+0.06} \times 10^{-10} \text{ erg cm}^{-2} \text{ s}^{-1}$ , which implies a luminosity  $\sim 10^{34} - 10^{36} \text{ erg s}^{-1}$ . The variability was found to be a factor of 25 in both the *Suzaku* and PCA observations. A positive correlation was seen in both the *Suzaku* hardness-intensity diagram and the PCA color-color diagram, which provides evidence against a strong wind. In eclipsing X-ray binaries, a strong wind should lead to an increase in absorption and thus the X-ray hardness ratio during the ingress and egress phases of the orbit. Additional evidence from the folded MAXI and ASM light curves suggests that the observed  $N_{\text{H}}$  could possibly originate in an accretion stream.

4U 1210-64 appears to be a NS-HMXB but conclusive evidence remains to be found. Additional multi-wavelength observations are required to achieve a full understanding of the source.

Model Parameter	Cutoff power law Out-of-Eclipse	Cutoff power law Eclipse
$\chi^2_\nu$ (dof)	1.08 (2553)	0.81 (382)
Cutoff Energy (keV)	$5.5 \pm 0.1$	
Folding Energy (keV)	$12 \pm 1$	
Phabs $N_{\text{H}}$ ( $\times 10^{22}$ atoms $\text{cm}^{-2}$ )	$0.70 \pm 0.01$	$0.94 \pm 0.08$
Pcfabs $N_{\text{H}}$ ( $\times 10^{22}$ atoms $\text{cm}^{-2}$ )	$6.7^{+0.3}_{-0.4}$	$11^{+2}_{-1}$
Covering Fraction	$0.36 \pm 0.03$	$0.80^{+0.04}_{-0.05}$
$\Gamma$	$1.80^{+0.04}_{-0.05}$	$2.9 \pm 0.2$
Normalization ( $\times 10^{-2}$ )	$2.9 \pm 0.2$	$1.8^{+0.7}_{-0.5}$
S XVI Energy (keV)	$2.62 \pm 0.02$	$2.58 \pm 0.05$
S XVI Width ( $\sigma_{\text{SXVI}}$ )	$0.1^b$	$0.1^b$
Normalization ( $\times 10^{-3}$ photons $\text{cm}^{-2} \text{s}^{-1}$ )	$0.11 \pm 0.02$	$0.11^{+0.06}_{-0.05}$
S XVI EQW (eV)	$20 \pm 3$	$51^{+26}_{-22}$
S XVI Flux ( $\times 10^{-13}$ erg $\text{cm}^{-2} \text{s}^{-1}$ )	$0.54 \pm 0.09$	$0.4 \pm 0.2$
Fe I Energy (keV)	$6.39 \pm 0.01$	$6.4^a$
Fe I Width ( $\sigma_{\text{FeI}}$ )	$0.1^b$	$0.1^b$
Normalization ( $\times 10^{-3}$ photons $\text{cm}^{-2} \text{s}^{-1}$ )	$0.093 \pm 0.007$	$0.009^c$
Fe I EQW (eV)	$77^{+7}_{-5}$	$122^c$
Fe I Flux ( $\times 10^{-13}$ erg $\text{cm}^{-2} \text{s}^{-1}$ )	$1.02 \pm 0.08$	$0.7^c$
Fe XXV Energy (keV)	$6.684 \pm 0.008$	$6.68 \pm 0.04$
Fe XXV Width ( $\sigma_{\text{FeXXV}}$ )	$0.1^b$	$0.1^b$
Normalization ( $\times 10^{-3}$ photons $\text{cm}^{-2} \text{s}^{-1}$ )	$0.185 \pm 0.008$	$0.043 \pm 0.009$
Fe XXV EQW (eV)	$144 \pm 7$	$392^{+160}_{-70}$
Fe XXV Flux ( $\times 10^{-13}$ erg $\text{cm}^{-2} \text{s}^{-1}$ )	$1.25 \pm 0.06$	$1.5 \pm 0.3$
Fe XXVI Energy (keV)	$6.970^{+0.007}_{-0.005}$	$6.98 \pm 0.05$
Fe XXVI Width ( $\sigma_{\text{FeXXVI}}$ )	$0.1^b$	$0.1^b$
Normalization ( $\times 10^{-3}$ photons $\text{cm}^{-2} \text{s}^{-1}$ )	$0.219^{+0.008}_{-0.009}$	$0.035 \pm 0.009$
Fe XXVI EQW (eV)	$199^{+9}_{-8}$	$319^{+160}_{-74}$
Fe XXVI Flux ( $\times 10^{-13}$ erg $\text{cm}^{-2} \text{s}^{-1}$ )	$1.16 \pm 0.05$	$1.5 \pm 0.4$
Absorbed Flux ( $\times 10^{-10}$ erg $\text{cm}^{-2} \text{s}^{-1}$ )	$1.024 \pm 0.003$	$0.108 \pm 0.004$
Unabsorbed Flux ( $\times 10^{-10}$ erg $\text{cm}^{-2} \text{s}^{-1}$ )	$1.73^{+0.06}_{-0.05}$	$0.16 \pm 0.01$

Table 3.3.

<sup>a</sup> The energy is frozen because I could only obtain an upper limit.

<sup>b</sup> The natural width was frozen to 0.1 keV, the resolution of the XIS instruments.

<sup>c</sup> The upper limit for the parameters (90% confidence interval) associated with the Fe I line is reported during eclipse.

Time <sup>b</sup> (ks)	Phabs $N_{\text{H}}$ ( $10^{22}$ cm <sup>-2</sup> )	Pcfabs $N_{\text{H}}$ ( $10^{22}$ cm <sup>-2</sup> )	Cvr	$\Gamma$	EQW S XVI (eV)	EQW Fe I (eV)	EQW Fe XXV (eV)	EQW Fe XXVI (eV)	Flux Ratio <sup>c</sup>	$F_{\text{unabs}}$ ( $10^{-10}$ erg cm <sup>-2</sup> s <sup>-1</sup> )	$\chi^2_{\nu}$ (d.o.f)
0-22.5	0.93±0.08	11 <sup>+2</sup> <sub>-1</sub>	0.80 <sup>+0.04</sup> <sub>-0.05</sub>	2.9±0.2	51 <sup>+26</sup> <sub>-22</sub>	70 <sup>d</sup>	420 <sup>+162</sup> <sub>-76</sub>	364 <sup>+156</sup> <sub>-83</sub>	1.0±0.3	0.53±0.03	0.82(382)
30-40	0.76±0.06	8±2	0.49 <sup>+0.07</sup> <sub>-0.08</sub>	1.9±0.1	48 <sup>e</sup>	118 <sup>+50</sup> <sub>-36</sub>	231 <sup>+53</sup> <sub>-40</sub>	147 <sup>+47</sup> <sub>-37</sub>	1.3 <sup>+0.5</sup> <sub>-0.4</sub>	1.0±0.1	0.92(499)
40-50	0.71 <sup>+0.04</sup> <sub>-0.05</sub>	4±1	0.33±0.05	1.69 <sup>+0.07</sup> <sub>-0.06</sub>	16 <sup>e</sup>	55 <sup>+19</sup> <sub>-20</sub>	100 <sup>+28</sup> <sub>-25</sub>	174 <sup>+39</sup> <sub>-32</sub>	1.2±0.3	2.1±0.1	0.96(1146)
50-60	0.69±0.03	5.7±0.9	0.38±0.04	1.76±0.05	24 <sup>+7</sup> <sub>-8</sub>	67 <sup>+14</sup> <sub>-13</sub>	100 <sup>+18</sup> <sub>-15</sub>	171 <sup>+21</sup> <sub>-19</sub>	1.0±0.2	2.5±0.1	0.97(2030)
60-70	0.75±0.02	6.3±0.7	0.43±0.04	1.94±0.05	18±8	65 <sup>+16</sup> <sub>-13</sub>	121 <sup>+19</sup> <sub>-16</sub>	193 <sup>+23</sup> <sub>-19</sub>	1.0±0.2	3.0 <sup>+0.2</sup> <sub>-0.1</sub>	0.92(2094)
70-80	0.76±0.03	6.6±0.9	0.41±0.04	1.97±0.06	18±9	50 <sup>+17</sup> <sub>-15</sub>	205 <sup>+26</sup> <sub>-21</sub>	206 <sup>+27</sup> <sub>-25</sub>	1.2±0.2	2.1±0.1	0.97(1572)
80-90	0.68 <sup>+0.04</sup> <sub>-0.05</sub>	5±2	0.32±0.07	1.84±0.09	23 <sup>+12</sup> <sub>-13</sub>	59 <sup>+26</sup> <sub>-22</sub>	158 <sup>+33</sup> <sub>-26</sub>	263 <sup>+47</sup> <sub>-39</sub>	1.2±0.3	1.3±0.1	0.96(1103)
90-100	0.72 <sup>f</sup>	6±1	0.35 <sup>+0.08</sup> <sub>-0.09</sub>	1.95 <sup>+0.08</sup> <sub>-0.09</sub>	42 <sup>+16</sup> <sub>-15</sub>	129 <sup>+31</sup> <sub>-29</sub>	203 <sup>+37</sup> <sub>-31</sub>	264 <sup>+46</sup> <sub>-41</sub>	1.0 <sup>+0.3</sup> <sub>-0.2</sub>	0.82 <sup>+0.07</sup> <sub>-0.06</sub>	0.94(809)
100-110	0.67±0.05	12±3	0.3±0.1	1.6±0.1	26 <sup>+17</sup> <sub>-18</sub>	108 <sup>+33</sup> <sub>-27</sub>	207 <sup>+46</sup> <sub>-41</sub>	174 <sup>+45</sup> <sub>-31</sub>	1.1 <sup>+0.4</sup> <sub>-0.3</sub>	1.2±0.1	0.91(631)
110-120	0.70±0.04	9±1	0.42 <sup>+0.06</sup> <sub>-0.07</sub>	1.69±0.08	15 <sup>+12</sup> <sub>-13</sub>	88 <sup>+23</sup> <sub>-20</sub>	110 <sup>+25</sup> <sub>-20</sub>	168 <sup>+32</sup> <sub>-27</sub>	1.2±0.3	2.8±0.2	0.96(1022)
120-130	0.66 <sup>+0.04</sup> <sub>-0.05</sub>	5±2	0.27±0.07	1.73±0.08	20 <sup>+11</sup> <sub>-12</sub>	31 <sup>+21</sup> <sub>-20</sub>	155 <sup>+31</sup> <sub>-25</sub>	215 <sup>+38</sup> <sub>-30</sub>	1.0±0.3	2.1 <sup>+0.2</sup> <sub>-0.1</sub>	0.96(1021)
130-140	0.70±0.03	9±1	0.37±0.07	1.86 <sup>+0.09</sup> <sub>-0.08</sub>	38 <sup>+13</sup> <sub>-12</sub>	26 <sup>+21</sup> <sub>-20</sub>	247 <sup>+37</sup> <sub>-28</sub>	206 <sup>+34</sup> <sub>-25</sub>	1.0 <sup>+0.3</sup> <sub>-0.2</sub>	1.4±0.1	1.07(1036)
140-150	0.66±0.03	7±1	0.30±0.06	1.66±0.06	17 <sup>e</sup>	101 <sup>+18</sup> <sub>-17</sub>	126 <sup>+21</sup> <sub>-16</sub>	190 <sup>+24</sup> <sub>-23</sub>	1.1±0.2	1.9±0.1	0.95(1616)
150-160	0.72±0.03	7±1	0.40 <sup>+0.06</sup> <sub>-0.07</sub>	1.89±0.08	16±12	78 <sup>+23</sup> <sub>-20</sub>	198 <sup>+34</sup> <sub>-25</sub>	231 <sup>+33</sup> <sub>-28</sub>	1.1 <sup>+0.3</sup> <sub>-0.2</sub>	1.4±0.1	0.98(1108)
160-170	0.63 <sup>f</sup>	16 <sup>+13</sup> <sub>-5</sub>	0.23 <sup>+0.08</sup> <sub>-0.09</sub>	1.64 <sup>+0.08</sup> <sub>-0.07</sub>	61±16	161 <sup>+34</sup> <sub>-30</sub>	164 <sup>+32</sup> <sub>-27</sub>	242 <sup>+44</sup> <sub>-36</sub>	1.1±0.3	0.70 <sup>+0.05</sup> <sub>-0.04</sub>	0.99(786)

Table 3.4. The best-fit parameters for the eclipse and out-of-eclipse, which is subdivided into 10 ks time intervals.

<sup>a</sup> The cutoff and folding energies of the high energy cutoff are frozen to the best fit values of the out-of-eclipse spectrum: 5.5 keV and 12.0 keV, respectively.

<sup>b</sup> Time is relative to the start of the *Suzaku* observation MJD 55553.16.

<sup>c</sup> The ratio of the strengths of the Fe XXV line with respect to the Fe XXVI line.

<sup>d</sup> The upper limit for the EQW of the Fe I line at the 90% confidence interval is reported during eclipse.

<sup>e</sup> The upper limit for the EQW of the S XVI line at the 90% confidence interval is reported at the time intervals 30–40 ks, 40–50 ks, and 140–150 ks.

<sup>f</sup> The fully covered absorber is frozen to the value that was extracted using the power-law model.

Time (MJD)	Phabs $N_{\text{H}}$ ( $10^{22}$ cm $^{-2}$ )	Pcfabs $N_{\text{H}}$ ( $10^{22}$ cm $^{-2}$ )	Cvr	High Energy Cutoff (keV)	Folding Energy (keV)	Power Law $\Gamma$	Power Law Normalization ( $10^{-2}$ )	Fe K $\alpha$ Energy (keV)	EQW Fe K $\alpha$ (eV)	$F_{\text{unabs}}$ ( $10^{-10}$ erg cm $^{-2}$ s $^{-1}$ )	$\chi^2_{\nu}$ (d.o.f)
54804	0.70 <sup>a</sup>	6.74 <sup>a</sup>	0.36 <sup>a</sup>	6.0±0.1	5.6±0.1	1.50±0.03	7.8±0.3	6.66 <sup>+0.01</sup> <sub>-0.02</sub>	228 <sup>+26</sup> <sub>-18</sub>	7.4±0.2	0.82(35)
54812	0.70 <sup>a</sup>	6.74 <sup>a</sup>	0.36 <sup>a</sup>	7.4±0.2	5.5±0.4	1.96±0.04	4.6±0.3	6.65 <sup>+0.01</sup> <sub>-0.07</sub>	414 <sup>+52</sup> <sub>-39</sub>	1.71±0.04	0.49(35)
54813	0.70 <sup>a</sup>	6.74 <sup>a</sup>	0.36 <sup>a</sup>	6.6±0.3	7.0 <sup>+0.5</sup> <sub>-0.4</sub>	1.70±0.05	3.2±0.2	6.59 <sup>+0.08</sup> <sub>-0.02</sub>	306 <sup>+30</sup> <sub>-36</sub>	2.01±0.06	0.71(35)
54814	0.70 <sup>a</sup>	6.74 <sup>a</sup>	0.36 <sup>a</sup>	6.5±0.2	5.9±0.3	1.70±0.04	4.6 <sup>+0.3</sup> <sub>-0.2</sub>	6.66±0.09	159 <sup>+27</sup> <sub>-32</sub>	2.86±0.08	0.35(35)
54815	0.70 <sup>a</sup>	6.74 <sup>a</sup>	0.36 <sup>a</sup>	6.3±0.2	6.8 <sup>+0.2</sup> <sub>-0.3</sub>	1.70±0.03	5.0±0.2	6.662 <sup>+0.004</sup> <sub>-0.085</sub>	250 <sup>+32</sup> <sub>-23</sub>	3.08 <sup>+0.07</sup> <sub>-0.06</sub>	0.74(35)
54816	0.70 <sup>a</sup>	6.74 <sup>a</sup>	0.36 <sup>a</sup>	5.9±0.2	6.9 <sup>+0.3</sup> <sub>-0.2</sub>	1.43±0.03	4.2±0.2	6.61 <sup>+0.03</sup> <sub>-0.04</sub>	297 <sup>+37</sup> <sub>-36</sub>	4.6±0.1	1.00(34)
54817	0.70 <sup>a</sup>	6.74 <sup>a</sup>	0.36 <sup>a</sup>	6.1±0.2	6.2 <sup>+0.4</sup> <sub>-0.3</sub>	1.51±0.05	3.5±0.2	6.56 <sup>+0.04</sup> <sub>-0.05</sub>	318 <sup>+47</sup> <sub>-46</sub>	3.3±0.1	0.51(34)
54818	0.70 <sup>a</sup>	6.74 <sup>a</sup>	0.36 <sup>a</sup>	7.6 <sup>+0.7</sup> <sub>-1.0</sub>	10 <sup>+3</sup> <sub>-2</sub>	2.01 <sup>+0.08</sup> <sub>-0.11</sub>	1.7 <sup>+0.2</sup> <sub>-0.3</sub>	6.486 <sup>+0.002</sup> <sub>-0.085</sub>	909 <sup>+175</sup> <sub>-135</sub>	0.60 <sup>+0.04</sup> <sub>-0.02</sub>	0.55(35)
54821	0.70 <sup>a</sup>	6.74 <sup>a</sup>	0.36 <sup>a</sup>	7.6 <sup>+0.2</sup> <sub>-0.3</sub>	4.7 <sup>+0.6</sup> <sub>-0.5</sub>	2.20±0.05	4.3±0.3	6.669 <sup>+0.089</sup> <sub>-0.001</sub>	502 <sup>+51</sup> <sub>-62</sub>	1.00±0.02	0.70(35)
54822 <sup>b</sup>	0.94	10.73	0.80	8.1±0.2	8.7 <sup>+0.8</sup> <sub>-0.7</sub>	2.56 <sup>+0.02</sup> <sub>-0.03</sub>	13.5±0.5	6.67±0.01	440 <sup>+26</sup> <sub>-39</sub>	1.63±0.01	1.17(35)
54826	0.70 <sup>a</sup>	6.74 <sup>a</sup>	0.36 <sup>a</sup>	6.5±0.1	7.4±0.2	1.63±0.02	7.1 <sup>+0.3</sup> <sub>-0.2</sub>	6.63 <sup>+0.04</sup> <sub>-0.05</sub>	160 <sup>+16</sup> <sub>-14</sub>	5.01±0.08	1.00(35)
54827	0.70 <sup>a</sup>	6.74 <sup>a</sup>	0.36 <sup>a</sup>	6.7±0.2	6.5 <sup>+0.4</sup> <sub>-0.3</sub>	1.79±0.04	5.4±0.3	6.67±0.06	306 <sup>+23</sup> <sub>-34</sub>	2.79 <sup>+0.07</sup> <sub>-0.06</sub>	0.83(35)
54828	0.70 <sup>a</sup>	6.74 <sup>a</sup>	0.36 <sup>a</sup>	7.3±0.2	6.9±0.4	1.86±0.04	5.3±0.3	6.63 <sup>+0.02</sup> <sub>-0.07</sub>	305 <sup>+39</sup> <sub>-27</sub>	2.41±0.05	1.07(35)
54829 <sup>b</sup>	0.94	10.73	0.80	8.5±0.4	11±2	2.62±0.03	18.1±0.9	6.48 <sup>+0.01</sup> <sub>-0.08</sub>	485 <sup>+56</sup> <sub>-45</sub>	1.98±0.02	1.69(35)
54830	0.70 <sup>a</sup>	6.74 <sup>a</sup>	0.36 <sup>a</sup>	6.6 <sup>c</sup>	6.6 <sup>c</sup>	1.82±0.08	0.7±0.1	6.51 <sup>+0.06</sup> <sub>-0.03</sub>	696±105	0.36±0.01	0.87(37)
54831	0.70 <sup>a</sup>	6.74 <sup>a</sup>	0.36 <sup>a</sup>	8.1±0.5	10 <sup>+3</sup> <sub>-2</sub>	2.12±0.06	3.0 <sup>+0.2</sup> <sub>-0.3</sub>	6.59±0.03	1061 <sup>+159</sup> <sub>-131</sub>	0.85±0.02	0.81(34)
54832	0.70 <sup>a</sup>	6.74 <sup>a</sup>	0.36 <sup>a</sup>	7.0±0.3	7.1 <sup>+0.7</sup> <sub>-0.6</sub>	1.96±0.05	2.9±0.2	6.54 <sup>+0.04</sup> <sub>-0.05</sub>	568 <sup>+56</sup> <sub>-39</sub>	1.07±0.02	0.77(35)
54834	0.70 <sup>a</sup>	6.74 <sup>a</sup>	0.36 <sup>a</sup>	6.6±0.2	7.5±0.2	1.55±0.03	4.1±0.2	6.49±0.04	267 <sup>+15</sup> <sub>-20</sub>	3.43±0.07	1.07(35)
54835	0.70 <sup>a</sup>	6.74 <sup>a</sup>	0.36 <sup>a</sup>	6.7 <sup>+0.1</sup> <sub>-0.2</sub>	7.2 <sup>+0.3</sup> <sub>-0.2</sub>	1.75±0.03	4.5±0.2	6.66±0.09	148 <sup>+19</sup> <sub>-16</sub>	2.53±0.06	0.84(35)
54836	0.70 <sup>a</sup>	6.74 <sup>a</sup>	0.36 <sup>a</sup>	7.8 <sup>+0.2</sup> <sub>-0.3</sub>	9.8 <sup>+0.5</sup> <sub>-0.4</sub>	1.58±0.03	9.4 <sup>+0.4</sup> <sub>-0.3</sub>	6.488 <sup>+0.086</sup> <sub>-0.002</sub>	312 <sup>+36</sup> <sub>-41</sub>	7.5±0.2	0.79(35)
54837	0.70 <sup>a</sup>	6.74 <sup>a</sup>	0.36 <sup>a</sup>	6.4±0.1	6.3±0.1	1.73±0.02	5.6±0.2	6.68 <sup>+0.07</sup> <sub>-0.01</sub>	236 <sup>+14</sup> <sub>-17</sub>	3.26±0.05	0.95(35)
54839	0.70 <sup>a</sup>	6.74 <sup>a</sup>	0.36 <sup>a</sup>	6.6 <sup>c</sup>	6.6 <sup>c</sup>	1.7±0.2	0.41 <sup>+0.12</sup> <sub>-0.09</sub>	6.4±0.1	570 <sup>+202</sup> <sub>-182</sub>	0.27±0.02	0.94(37)
54840	0.70 <sup>a</sup>	6.74 <sup>a</sup>	0.36 <sup>a</sup>	6.6 <sup>+0.6</sup> <sub>-0.3</sub>	7.8±0.6	1.90 <sup>+0.03</sup> <sub>-0.04</sub>	3.8 <sup>+0.4</sup> <sub>-0.2</sub>	6.73 <sup>+0.04</sup> <sub>-0.13</sub>	362 <sup>+48</sup> <sub>-47</sub>	1.59±0.05	0.55(35)
54842 <sup>b</sup>	0.94	10.73	0.80	7.9 <sup>d</sup>	8.0 <sup>d</sup>	2.5±0.1	3.3 <sup>+0.8</sup> <sub>-0.6</sub>	6.9±0.2	529 <sup>+217</sup> <sub>-211</sub>	0.50±0.03	0.55(37)

Table 3.5. The best-fit parameters for the PCA spectra.

<sup>a</sup> Out-of-eclipse, the fully covered absorber and partially covered absorber are frozen to the best fit values of the *Suzaku* out-of-eclipse spectrum (see Table 3.3)

<sup>b</sup> Time intervals when 4U 1210-64 is in eclipse.  $N_{\text{H}}$  is frozen to the best fit values of the *Suzaku* eclipse spectrum (see Table 3.3)

<sup>c</sup> The Cutoff Energy and Folding Energy parameters at these time intervals are frozen to the weighted average of the out-of-eclipse spectra.

<sup>d</sup> The Cutoff Energy and Folding Energy parameters at these time intervals are frozen to the weighted average of the eclipse spectra.

Spectral Type	$M/M_{\odot}$	$R/R_{\odot}$	$R_L/R_{\odot}^a$	$M_V$	$(B - R)_0^b$	$E(B - R)^b$	$i_{\min}^{\circ c}$	$d_{\text{odot}}^d$ (kpc)	$d_{\text{gal}}^e$ (kpc)	$L_{\text{xavg}}$ ( $\times 10^{35} \text{ erg s}^{-1}$ )
<i>B5 V<sup>f</sup></i>	<i>5.9</i>	<i>4.1</i>	13.7	-1.2	-0.21	1.71	<sup>g</sup>	~2.8	~7.4	~1.6
<b><i>B5 V<sup>f</sup></i></b>	<b>5.9</b>	<b>3.9</b>	13.7	-1.2	-0.21	1.71	<sup>g</sup>	~2.8	~7.4	~1.6
<i>B0 V</i>	18	8.4	23.1	-4.0	-0.40	1.90	84	~9.8	~9.3	~20.0
<i>B5 III</i>	7.0	6.3	14.9	-2.2	-0.21	1.71	85	~4.1	~7.3	~3.4
<i>B0 III</i>	20	13	24.6	-5.1	-0.34	1.84	75	~15	~13	~44.6
<i>B5 I</i>	20	41	24.6	-6.2	-0.10	1.60	9	~29	~26	~175
<i>B0 I</i>	25	25	27.2	-6.4	-0.36	1.86	57	~31	~28	~197
<i>F0 III</i>	2.0	5.0	7.7	1.5	0.45	1.05	82	~0.9	~7.9	~0.2
<i>G0 III</i>	1.0	5.7 <sup>h</sup>	5.2 <sup>h</sup>	1.0	1.11	0.39	77	~1.3	~7.8	~0.3

Table 3.6. Physical Parameters for Candidate Mass Donors in 4U 1210-64

The values in italics are obtained from Carroll & Ostlie (2006) and Masetti et al. (2009).

The values in both italics and bold are obtained from Allen (2000) in comparison with those in Carroll & Ostlie (2006).

<sup>a</sup> The definition for the Roche lobe,  $R_L$ , as given in Eggleton (1983), assuming  $M_{\text{NS}}$  is  $1.4 M_{\odot}$ .

<sup>b</sup> The value for  $(B - R)_0$  was calculated using  $(B - V)_0$  and  $(R - V)_0$  published in Wegner (1994).  $E(B - R)$  is found by subtracting  $(B - R)_0$  from the observed  $B - R$  (see Section 3.5.1.2)

<sup>c</sup> The minimum inclination angle of the system that is consistent with the measured eclipse half-angle.

<sup>d</sup> The distance the object is from the Sun.

<sup>e</sup> Galactocentric distance of 4U 1210-64.

<sup>f</sup> Masetti et al. (2009)'s proposed spectral type and distance of the object.

<sup>g</sup> A B5 V classification is inconsistent with the observed eclipse half-angle.

<sup>h</sup> A G0 III classification significantly overfills the Roche lobe assuming a  $1.4 M_{\odot}$  compact object.

## Chapter 4

# A MULTI-WAVELENGTH STUDY OF THE GAMMA-RAY BINARY 1FGL J1018.6-5856

### 4.1 Overview

1FGL J1018.6-5856, the first gamma-ray binary discovered by the *Fermi* Large Area Telescope (LAT), consists of an O6 V((f)) star and suspected rapidly spinning pulsar. While 1FGL J1018.6-5856 has been postulated to be powered by the interaction between a relativistic pulsar wind and the stellar wind of the companion, a microquasar scenario where the compact object is a black hole cannot be ruled out. Long-term multi-wavelength studies with the LAT, the *Swift* X-ray Telescope (XRT) and the *Australia Telescope Compact Array (ATCA)* provide temporal and spectral information to investigate changes in the multi-wavelength properties of the  $16.531 \pm 0.006$  day orbital modulation. The epoch of maximum flux in the gamma-ray is also seen in the X-ray bandpass. A secondary maximum at binary orbital phase  $\sim 0.3$  is also seen in the X-ray and radio light curves, which could possibly be attributed to inferior conjunction. The best-fit spectral model of the *Swift* XRT data consists of a featureless power law with index  $\Gamma \sim 1.3-1.7$

modified by an absorber that fully covers the source. I find the radio amplitude modulation to decline with increasing frequency, which is a possible indication of the presence of free-free absorption. The radio spectral index closely tracks the flux density, further supporting intrinsic free-free absorption.

## 4.2 Introduction

Persistent emission in the GeV and/or TeV energy bandpasses is observed in gamma-ray binaries, which are often thought to be in an early stage in the evolutionary history of a High-Mass X-ray Binary (HMXB; Meurs & van den Heuvel, 1989; Dubus, 2006). Consisting of a compact object and a high mass optical companion, gamma-ray binaries are characterized by GeV and/or TeV emission modulated on their orbital period. Additionally, radio and X-ray emission are seen in gamma-ray binaries. While hundreds of HMXBs have been found (Chaty, 2011, and references therein), there is a significant paucity of interacting binaries that emit at gamma-ray energies. This apparent rarity can be attributed to a “short” lifetime of these sources and that most of the emission is in the gamma-ray regime, which is less accessible for study than optical or X-ray emission. While five gamma-ray binaries have been identified as *Fermi* sources, 1FGL J1018.6-5856 stands alone as the only gamma-ray binary discovered by the *Fermi* LAT.

1FGL J1018.6-5856 is a luminous gamma-ray binary that was first discovered by the *Fermi* LAT in 2011 (Corbet et al., 2011). 1FGL J1018.6-5856 was identified by Ackermann et al. (2012) to be one of the brighter LAT sources with a mean flux of  $2.9 \times 10^{-8}$  photons  $\text{cm}^{-2} \text{s}^{-1}$  in the 1–100 GeV band. Observations in the X-ray in-

clude the *Swift* XRT and *XMM-Newton* surveys (An et al., 2013) at fluxes between  $\sim 0.7\text{--}2.5 \times 10^{-12} \text{ erg cm}^{-2} \text{ s}^{-1}$  and  $\sim 1.6 \times 10^{-12} \text{ erg cm}^{-2} \text{ s}^{-1}$  in the 0.5–10 keV band, respectively. Recently An et al. (2015) found 1FGL J1018.6-5856 to be at flux levels in the 3–10 keV band  $\sim 0.5\text{--}1.1 \times 10^{-12} \text{ erg cm}^{-2} \text{ s}^{-1}$ ,  $\sim 0.3\text{--}1.2 \times 10^{-12} \text{ erg cm}^{-2} \text{ s}^{-1}$  and  $\sim 0.6\text{--}1.1 \times 10^{-12} \text{ erg cm}^{-2} \text{ s}^{-1}$  using *XMM-Newton*, *Swift* XRT and *NuSTAR*, respectively. Under the assumption that the spectrum of 1FGL J1018.6-5856 is similar to that of LS 5039, Li et al. (2011) derived the flux in the 18–40 keV band to be  $0.75 \times 10^{-12} \text{ erg cm}^{-2} \text{ s}^{-1}$  using *INTEGRAL/IBIS* (Ubertini et al., 2003). Using the *High Energy Stereoscopic System (H.E.S.S.)*, the (H. E. S. S. Collaboration et al., 2015) found the flux to be  $\sim 1 \times 10^{-12} \text{ photons cm}^{-2} \text{ s}^{-1}$  at  $E > 0.35 \text{ TeV}$  (Ackermann et al., 2012).

Using the *Chandra* X-ray observatory, 1FGL J1018.6-5856 was detected at coordinates (J2000) R.A.= $10^{\text{h}}18^{\text{m}}55^{\text{s}}62$ , Dec= $-58^{\circ}56'46''06$  (An et al., 2013). This was consistent with those found using *Swift* UVOT and the United States Naval Observatory B1.0 catalog: R.A.= $10^{\text{h}}18^{\text{m}}55^{\text{s}}60$ , Dec= $-58^{\circ}56'46''2$  with a position uncertainty of  $0.1''$  (Ackermann et al., 2012). Using *ATCA*, 1FGL J1018.6-5856 was detected with sub-arcsecond accuracy at coordinates R.A.= $10^{\text{h}}18^{\text{m}}55^{\text{s}}58$ , Dec= $-58^{\circ}56'45''5$  ( $\pm 0.1''$ ,  $\pm 0.3''$  respectively).

Ackermann et al. (2012) modeled the gamma-ray spectrum of 1FGL J1018.6-5856 using a continuum consisting of a broken power law where the photon index  $\Gamma$  was found to be  $2.00 \pm 0.04_{\text{stat}} \pm 0.08_{\text{syst}}$  below 1 GeV and  $3.09 \pm 0.06_{\text{stat}} \pm 0.12_{\text{syst}}$  above 1 GeV, respectively. A power law with a high-energy exponential cutoff was also found to fit the data reasonably well, where  $\Gamma = 1.9 \pm 0.1_{\text{stat}}$  and  $E_c = 2.5 \pm 0.3_{\text{stat}} \text{ GeV}$  (Ackermann et al., 2012). The XRT spectra of 1FGL J1018.6-5856 were fit with an absorbed power-law

where the photon index  $\Gamma$  was found to vary between  $\sim 1.3$  and  $\sim 2.0$  (An et al., 2013). At energies  $E > 0.35$  TeV, 1FGL J1018.6-5856 was fit with a power-law where the photon index was found to be  $2.20 \pm 0.14_{\text{stat}} \pm 0.2_{\text{syst}}$  (H. E. S. S. Collaboration et al., 2015).

The optical counterpart of 1FGL J1018.6-5856 was observed using the 1.9 m South African Astronomical Observatory and the 2.5 m telescope at the Las Campanas Observatory (Ackermann et al., 2012). Based on its optical spectrum, the proposed spectral class of the optical counterpart is O6 V((f)), which is comparable to what is found for the gamma-ray binary LS 5039 (McSwain et al., 2004). The features observed in the optical spectrum consist of absorption lines of hydrogen, neutral helium and singly ionized helium (Ackermann et al., 2012). The singly ionized helium line is observed in absorption, which is indicative of a main-sequence spectral type. Additionally, an emission line of doubly ionized nitrogen was found along with an absence of a singly ionized helium emission line. The presence of doubly ionized nitrogen in emission along with the absence of an emission line of singly ionized helium is suggestive of an ((f)) classification. The line ratio between singly ionized helium to neutral helium implies a spectral class of O6. The reddening in the  $B - V$  band,  $E(B - V)$ , was estimated to be 0.9 and 1.6 using features at 4430 and 5780 Å, respectively.

This chapter is structured in the following order: *Fermi* LAT, *Swift* XRT and *ATCA* observations are presented in Section 4.2; Section 4.3 focuses on the results on the observation campaign and Section 4.4 presents a discussion of the results. The conclusions are outlined in Section 4.5. If not stated otherwise, the uncertainties and limits presented in this chapter are at the  $1\sigma$  confidence level.

### 4.3 Observations and Data Analysis

The observations outlined below consist of data collected during long-term observations using *Fermi* LAT, *Swift* XRT and ATCA.

#### 4.3.1 Fermi LAT

The Large Area Telescope (LAT) on board the *Fermi* Gamma-ray Space Telescope is an imaging pair-conversion telescope operating in energies from below 20 MeV to above 300 GeV (Atwood et al., 2009). In this analysis, I use data from 100 MeV to 300 GeV. For more information, see Appendix A.4.3.

I analyzed LAT data obtained between MJD 54682.7–57056.4 (2008 August 4–2015 February 3) using the Version 9, Release 33 of the *Fermi* Science Tools<sup>1</sup>, the Pass 7 Reprocessed “source” class events and P7REP instrument response function (IRF). To maximize the signal-to-noise, the light curves were produced using a weighted photon technique where the probabilities of the photons were summed. I calculated the probability that a photon originated from the source of interest using `gtsrcprob` based on the fluxes and spectral models of the 2FGL and 3FGL catalogs (see Appendix B.2).

Light curves were also produced using the maximum likelihood fitting method (e.g. Ackermann et al., 2012). I used the script `like_lc`<sup>2</sup> made available on the *Fermi* Science Support Center webpage<sup>3</sup>. I binned the data into  $\sim 49.5$  day intervals ( $\sim 3$  orbital periods). All photon events within  $10^\circ$  of the source were analyzed where other sources in the

---

<sup>1</sup><http://fermi.gsfc.nasa.gov/ssc/data/analysis/software/>

<sup>2</sup>[http://fermi.gsfc.nasa.gov/ssc/data/analysis/user/like\\_lc.pl](http://fermi.gsfc.nasa.gov/ssc/data/analysis/user/like_lc.pl)

<sup>3</sup><http://fermi.gsfc.nasa.gov/ssc/data/analysis/user/>

region of interest were frozen to the values assigned in the 2FGL and 3FGL catalogs.

Using the probability based aperture photometry and maximum likelihood fitting methods (Ackermann et al., 2012), I produced light curves of 1FGL J1018.6-5856 to investigate possible variability of the source on long timescales (see Figure 4.1). The data span a period of  $\sim 6.5$  years.

### 4.3.2 Swift XRT

The *Swift* XRT is an autonomous Wolter I X-ray imaging telescope sensitive to X-rays ranging from 0.3 to 10 keV. For more information, see Appendix A.4.2.2.

The *Swift* XRT observations of 1FGL J1018.6-5856 took place from 2011 January 14 to 2013 March 7 (MJD 55575–56358) with different exposures ranging from  $\sim 0.7$  ks to  $\sim 10$  ks. The data collected from the observations were reduced and analyzed using the standard criteria defined in the *Swift* XRT Data Reduction Guide<sup>4</sup>. These procedures are described below.

1FGL J1018.6-5856 was observed in Photon Counting (PC; Hill et al., 2004) mode with a data readout time of 2.5 s adopting the standard grade filtering (0–12 for PC). Data collected using the XRT were reduced and screened using the HEASoft v.6.16 package and calibration files dated 2014 July 30 (Capalbi et al. 2005). The data were reprocessed with the XRTDAS standard data pipeline package `xrtpipeline` using the standard filtering procedure to apply the newest calibration and default screening criteria. Following the procedure reported in An et al. (2013), the source spectra were extracted from a circular region of radius of  $20''$  centered on the source. The backgrounds were extracted from

---

<sup>4</sup>[http://swift.gsfc.nasa.gov/analysis/xrt\\_swguide.v1.2.pdf](http://swift.gsfc.nasa.gov/analysis/xrt_swguide.v1.2.pdf)

an annular region of internal radius of 40'' and external radius 80'' centered on the source. The light curves were binned at 2.51 s.

The ancillary response files, accounting for vignetting, PSF correction and different extraction regions, were generated and corrected for exposure using the FTOOL packages `xrtmkarf` and `xrtexpomap`, respectively. I find the count rates in the observations to be  $\sim 0.5\text{--}3.7 \times 10^{-2}$  counts  $\text{s}^{-1}$ , which is significantly less than the standard count rate of 0.5 counts  $\text{s}^{-1}$  where pileup becomes important (Hill et al., 2004; Burrows et al., 2005). Therefore, pileup was not an issue in the observations and I am justified to extract the source spectra from a circular region.

I note that not all individual spectra were useful for a meaningful analysis, as each spectrum was found to have  $\sim 10\text{--}250$  counts, which was also noted in the analysis reported by An et al. (2013). These were folded using an ephemeris where phase zero was the epoch of maximum gamma-ray flux and 10 phase bins. Data in the spectral files produced by `XSELECT` were further processed using the FTOOL `GRPPHA`. `GRPPHA` is designed to define the binning, quality flags and systematic errors of the spectra and used the bad quality flag to further eliminate bad data from the PHA files. Initially, I grouped the bins to ensure a minimum of 20 counts to fit the spectra using  $\chi^2$  statistics. However, insufficient events were found between binary phases 0.1–0.9. Due to the small number of counts, I used the Cash statistic for the spectral analysis for all bins except at phase 0 (see Table 4.3). Depending on the number of counts, these spectra were grouped to have 1–5 counts per bin.

The spectra were analyzed using the package `XSPEC v.12.8.2k.d`. I made use of the `XSPEC` convolution model `cflux` to calculate the fluxes and associated errors of

1FGL J1018.6-5856. I will discuss the spectral analysis and results in Section 4.4.2.2.

### 4.3.3 ATCA

The *Australia Telescope Compact Array (ATCA)* is a radio interferometer consisting of six telescopes that is a part of the Australia Telescope National Facility (ATNF) located near Narrabri, Australia. For more information see Appendix A.4.4.

The *ATCA* radio observations from 2011 February 7 to 2012 February 27 (MJD 55599–55984) monitor the source through  $\sim 23$  orbital periods. These cover 7 frequency bands from 2.1 GHz to 35.0 GHz. The light curves at 5.5 GHz and 9.0 GHz from 2011 February 7 to 4 May 2011 (MJD 55599–55685). These curves were previously analyzed and reported by Ackermann et al. (2012) where a hint of orbital modulation was found. However, I reanalyzed them for consistency.

## 4.4 Results

### 4.4.1 Temporal Analysis

**4.4.1.1 *Fermi* LAT Analysis** I searched for long-term variability using the maximum likelihood method and fit the spectra using a log parabola model, a broken power law and a power law with a high energy cutoff where the normalizations, fluxes and spectral parameters were allowed to vary. No long-term flux variability was seen over the duration of the *Fermi* gamma-ray light curve (see Figure 4.1). No significant long-term variability was found in the spectra, which was consistent for all three tested spectral models (see Figure 4.1).

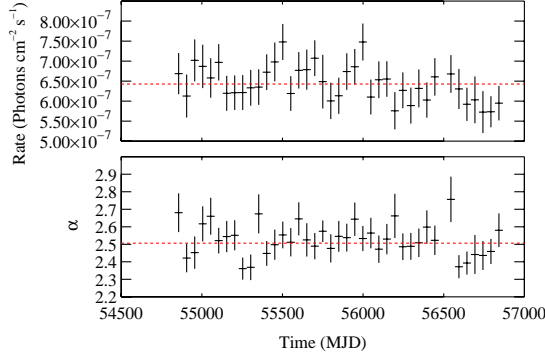


FIG. 4.1. Long-term *Fermi* LAT light curve produced in the 0.1–300 GeV band based on a likelihood analysis (top) spans nearly 6 years (MJD 54832–56867). No major variability is shown over the duration of the light curve. No significant variability is seen in the spectrum (bottom). I illustrate this by plotting the  $\alpha$  parameter of the log-parabola model.

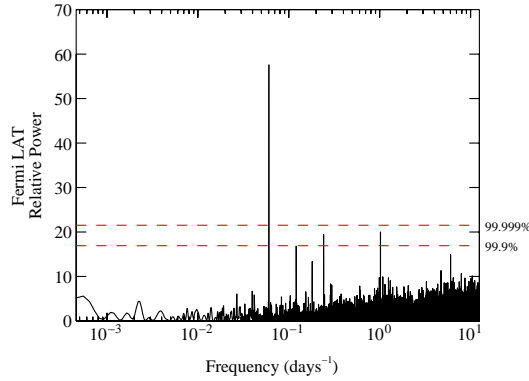


FIG. 4.2. Power spectrum produced from LAT aperture photometry with the 99.9% and 99.999% confidence intervals shown. The power spectrum indicates that the period of the source is  $16.531 \pm 0.006$  d. The probability of this arising by chance is  $\lesssim 10^{-8}$  in the LAT data. Multiple harmonics are also seen in the power spectrum. The peak at 1 d is an artifact.

A power spectrum was used to search for periodicities in the aperture based photometry LAT light curves at a time resolution of 600 s. This shows the presence of a  $16.531 \pm 0.006$  day peak (see Figure 4.2). The false-alarm probability (FAP; Scargle, 1982) in the LAT power spectrum is  $\lesssim 10^{-8}$ . This refines the orbital period of the system, which was previously reported to be  $16.58 \pm 0.02$  d (Ackermann et al., 2012).

Quasi-sinusoidal behavior was found in the aperture photometry *Fermi* LAT folded light curve (see Figure 4.3) where I defined phase zero as the epoch of maximum flux

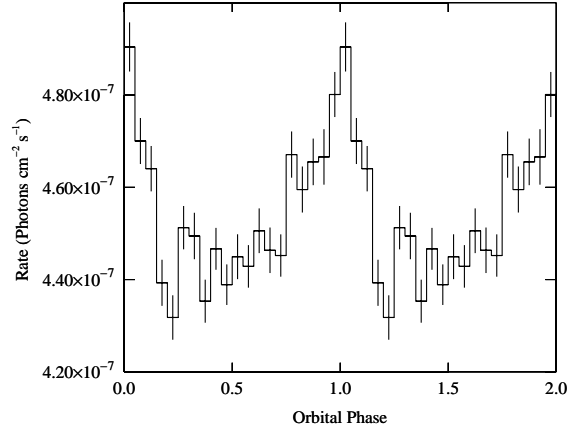


FIG. 4.3. Aperture photometry Fermi LAT light curve folded on the orbital period. Phase 0 is defined as the epoch of maximum flux.

(MJD  $55403.3 \pm 0.4$ ). I confirm this behavior in the folded light curves extracted using the maximum likelihood fitting (see Figure 4.8, top).

**4.4.1.2 *Swift* XRT Analysis** The *Swift* XRT observations monitor the source for more than 47 orbital periods. I binned the light curves to a resolution of 1 d to investigate the X-ray variability of the system, shown in the light curve folded on the *Fermi* ephemeris (see Figure 4.5).

I performed a Fourier transform of all background-subtracted *Swift* XRT data together, which cover the range of 0.2–783 d (see Figure 4.4). No significant peaks (FAP  $\gtrsim 99.9\%$ ) are found in the power spectra; however, a period of  $3.31 \pm 0.002$  d corresponding to the fifth harmonic of a  $16.549 \pm 0.008$  d orbital period is seen with a “blind search” at a FAP of  $\sim 0.08$ . This is consistent with the  $16.544 \pm 0.008$  d period found by An et al. (2015) also using *Swift* XRT.

The folded *Swift* XRT light curve revealed quasi-sinusoidal modulation with a maximum at phase 0 and another maximum at phase  $\sim 0.4$ , which are consistent with previous observations reported in Ackermann et al. (2012) and An et al. (2013, 2015). The sec-

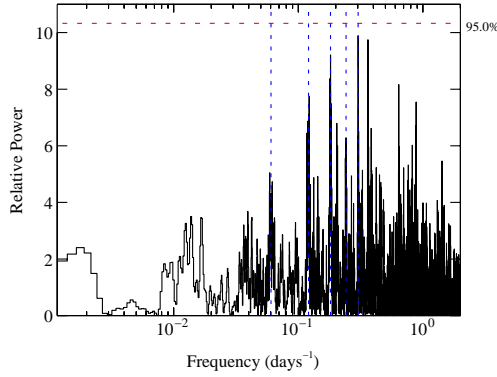


FIG. 4.4. Power spectrum produced by the *Swift* XRT X-ray light curve with the 95.0% confidence interval indicated by the red dashed line. The peak of the power spectrum is at a period of  $3.31 \pm 0.002$  d and has an FAP of 92.3%. While not statistically significant, this is the fifth harmonic of the orbital period. The orbital period and harmonics up to the fifth harmonic are indicated by the blue dashed lines.

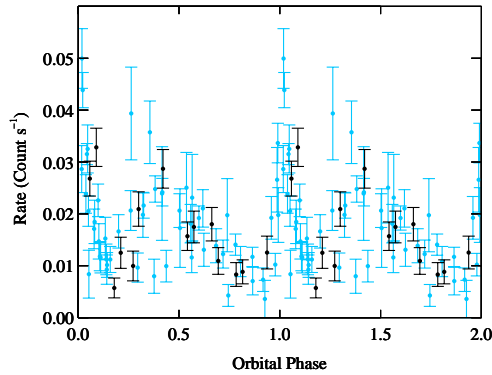


FIG. 4.5. *Swift* XRT X-ray light curves folded on the orbital period. The light blue data is prior to MJD 55984 (An et al., 2013; Ackermann et al., 2012). The black data points after MJD 55984 are unpublished. The modulation appears to be quasi-sinusoidal with a maximum at phase 0 and a secondary maximum at phase  $\sim 0.4$ .

ondary maximum is consistent with that found in the radio bands (see Section 4.4.1.3).

**4.4.1.3 ATCA Analysis** I folded the *ATCA* radio light curves on the orbital period and found clear orbital modulation in the frequency bands 2.1, 5.5, 9.0, 17.0 and 19.0 GHz (see Figure 4.6). The modulation amplitude is found to decrease with increasing frequency. The light curves at 33.0 and 35.0 GHz do not show clear modulation on the orbital period.

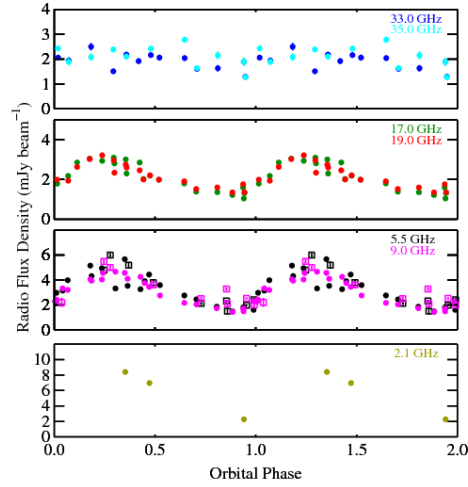


FIG. 4.6. ATCA radio light curves folded on the orbital period. The modulation amplitude decreases with increasing frequency. Light curves at 33.0 and 35.0 GHz do not show clear modulation on the orbital period.

## 4.4.2 Spectral Analysis

**4.4.2.1 *Fermi* LAT Analysis** To fit the *Fermi* gamma-ray spectra, I used several models: a log parabola (see Equation 4.1) that is used to describe radio pulsars and gamma-ray binaries, a broken power law and a power law with a high-energy cutoff.

$$(4.1) \quad \frac{dN}{dE} = N_0 \left( \frac{E}{E_b} \right)^{-(\alpha + \beta \log(E/E_b))}$$

The models that provide a good fit to the data are a log parabola model (see Table 4.1) and a power law with a high-energy cutoff (see Table 4.2). In the case of the power law model with a high-energy cutoff, I find that the scale energy cannot be sufficiently constrained. Therefore, I froze the scale energy to 1 GeV.

I investigated temporal dependence of the gamma-ray spectral parameters, compar-

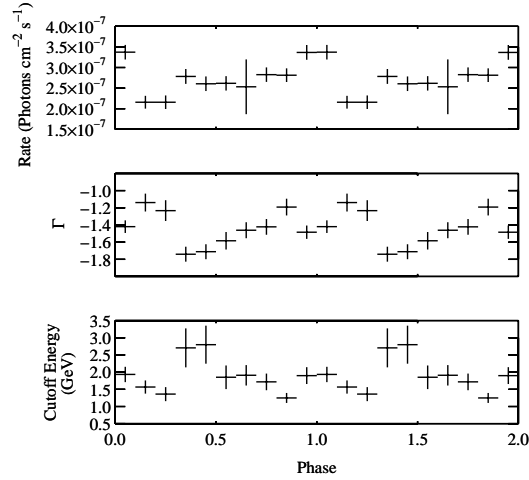


FIG. 4.7. *Fermi* LAT light curve (top) based on a likelihood analysis folded on the orbital period. Phase 0 is defined as the epoch of maximum flux. The photon index and cutoff energies are also folded on the orbital period (see middle and bottom panels).

ing the parameters in different orbital phases. No correlations were found between the continuum spectral parameters with respect to the 0.1–10 MeV continuum flux.

I divided the likelihood light curve into two energy bands where the soft band is defined between energies 0.1–1 GeV, characterized by the count rate  $C_{\text{soft}}$ , and the hard band is between 1–300 GeV, characterized by the count rate  $C_{\text{hard}}$ . Using the definition in Equation 3.2, I produced a hardness ratio folded on the orbital period (see Figure 4.8, bottom), where a soft spectrum is indicated by negative values and a hard spectrum is indicated by positive values. While no apparent correlations were found between the hardness ratio and the count rate in the full energy band (see Figure 4.8, bottom), I find a peak in the hardness ratio at  $\phi \sim 0.1$ .

Phase	Flux ( $10^{-7}$ photons $\text{cm}^{-2}$ $\text{s}^{-1}$ )	Test Statistic	$\alpha$	$\beta$
0.03	$3.6 \pm 0.2$	1318.33	$2.29 \pm 0.04$	$0.25 \pm 0.03$
0.10	$2.4 \pm 0.2$	1104.34	$2.21 \pm 0.05$	$0.36 \pm 0.04$
0.17	$1.8 \pm 0.2$	732.654	$2.13 \pm 0.06$	$0.35 \pm 0.05$
0.23	$1.7 \pm 0.2$	550.041	$2.49 \pm 0.09$	$0.51 \pm 0.07$
0.30	$2.7 \pm 0.2$	620.363	$2.49 \pm 0.07$	$0.31 \pm 0.04$
0.37	$2.4 \pm 0.2$	526.167	$2.40 \pm 0.07$	$0.26 \pm 0.04$
0.43	$2.3 \pm 0.2$	536.274	$2.41 \pm 0.07$	$0.29 \pm 0.04$
0.50	$2.7 \pm 0.2$	588.992	$2.43 \pm 0.08$	$0.24 \pm 0.05$
0.57	$2.4 \pm 0.2$	524.201	$2.48 \pm 0.08$	$0.31 \pm 0.05$
0.63	$2.5 \pm 0.2$	659.285	$2.37 \pm 0.07$	$0.30 \pm 0.04$
0.70	$2.0 \pm 0.2$	606.558	$2.54 \pm 0.09$	$0.48 \pm 0.06$
0.77	$2.8 \pm 0.2$	905.437	$2.42 \pm 0.06$	$0.36 \pm 0.04$
0.83	$2.5 \pm 0.2$	882.396	$2.57 \pm 0.08$	$0.49 \pm 0.05$
0.90	$2.5 \pm 0.2$	902.029	$2.49 \pm 0.09$	$0.45 \pm 0.06$
0.97	$3.1 \pm 0.2$	1536.42	$2.41 \pm 0.05$	$0.33 \pm 0.03$

Table 4.1. The best-fit parameters from a log-parabola model of 1FGL J1018.6-5856, which is subdivided into orbital phase bins of  $\sim 0.067$ .

Phase	Flux ( $10^{-7}$ photons $\text{cm}^{-2}$ $\text{s}^{-1}$ )	Test Statistic	$\Gamma$	Cut-off Energy (GeV)
0.0	$3.4 \pm 0.2$	1831.57	$-1.42 \pm 0.07$	$1.9 \pm 0.2$
0.1	$2.2 \pm 0.2$	1220.85	$-1.1 \pm 0.1$	$1.6 \pm 0.2$
0.2	$2.2 \pm 0.2$	843.258	$-1.2 \pm 0.1$	$1.4 \pm 0.2$
0.3	$2.8 \pm 0.2$	811.767	$-1.74 \pm 0.09$	$2.7 \pm 0.6$
0.4	$2.6 \pm 0.2$	807.537	$-1.71 \pm 0.09$	$2.8 \pm 0.6$
0.5	$2.6 \pm 0.2$	796.908	$-1.6 \pm 0.1$	$1.9 \pm 0.3$
0.6	$2.5 \pm 0.7$	974.152	$-1.46 \pm 0.09$	$1.9 \pm 0.3$
0.7	$2.8 \pm 0.2$	1120.52	$-1.42 \pm 0.09$	$1.7 \pm 0.2$
0.8	$2.8 \pm 0.2$	1331.11	$-1.2 \pm 0.1$	$1.2 \pm 0.1$
0.9	$3.4 \pm 0.2$	1505.73	$-1.48 \pm 0.08$	$1.9 \pm 0.2$

Table 4.2. The best-fit parameters from a power law with high-energy cutoff model of 1FGL J1018.6-5856, which is subdivided into orbital phase bins of  $\sim 0.1$ .

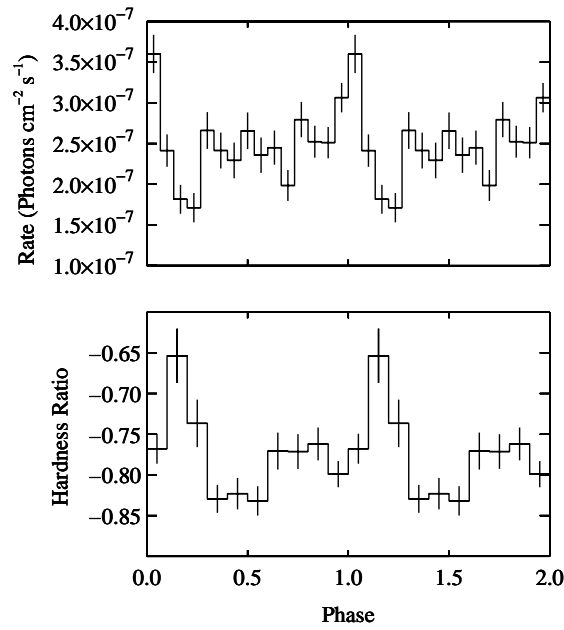


FIG. 4.8. *Fermi* LAT light curve (top) based on a likelihood analysis folded on the orbital period. Phase 0 is defined as the epoch of maximum flux. Hardness ratio (bottom) as produced by a likelihood analysis using *Fermi* LAT. The hardness ratio is defined as  $(C_{\text{hard}} - C_{\text{soft}})/(C_{\text{hard}} + C_{\text{soft}})$ , where the soft and hard energy bands are 0.1–1 GeV and 1–300 GeV, respectively.

**4.4.2.2 *Swift* XRT Analysis** To fit the XRT spectra, I used several models that are used to describe systems that host a neutron star: a power law (see Figure 4.9), a power law with a high-energy cutoff (`highcut×power` in XSPEC), and a cutoff powerlaw (`cutoffpl` in XSPEC). All models were modified by an absorber that fully covers the source using Balucinska-Church & McCammon (1992) cross sections and Wilms et al. (2000) abundances.

The model that provides a good fit to the data is a power law modified by a fully covered absorber (reported in Table 4.3). I find that the neutral hydrogen column density for the fully covered absorption could not be accurately constrained. Therefore, I froze  $N_{\text{H}}$  to  $1.02 \times 10^{22}$  atoms  $\text{cm}^{-2}$ , which was reported in the *XMM-Newton* data by An et al. (2015) assuming Wilms abundances. This value of the fully covered absorber is somewhat less than the Galactic HI values reported by the the Leiden/Argentine/Bonn survey (Kalberla et al., 2005) and in the review by Dickey & Lockman (1990), which are  $1.34 \times 10^{22}$  and  $1.47 \times 10^{22}$  atoms  $\text{cm}^{-2}$ , respectively. This is to be expected if  $N_{\text{H}}$  is overestimated in the LAB and DL surveys. A good fit does not require a high-energy cutoff, which is typically found in accreting pulsars (Coburn et al., 2002; White et al., 1983).

Similar to the gamma-ray analysis reported in Section 4.4.2.1, the temporal dependence of the X-ray spectral parameters was investigated (see Figures 4.10 and 4.11). Since no emission line features were found, which is to be expected if 1FGL J1018.6-5856 is not accreting, I searched for correlations between the continuum spectral parameters (the power-law index) with respect to the 0.3–10 keV continuum flux. The power-law index is found to be anti-correlated with respect to the continuum flux with a correlation coefficient ( $r$ ) of -0.91 (see Figure 4.11). This confirms the result reported in An et al. (2015)

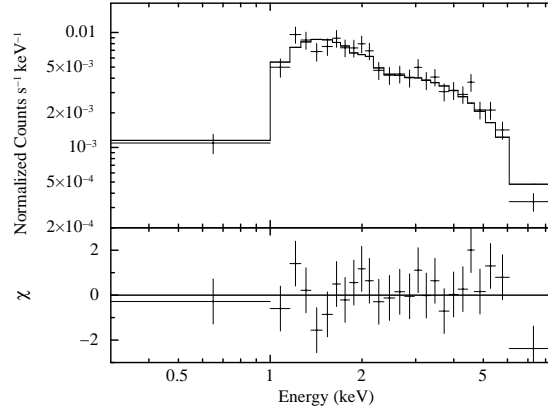


FIG. 4.9. The combined XRT spectrum at phase 0 and best fit model (top panel). This consists of a continuum comprised of an absorbed power law where  $N_{\text{H}}$  is frozen at  $1.02 \times 10^{22}$  atoms  $\text{cm}^{-2}$ . Residuals of the best fit model are plotted in the bottom panel.

where an anti-correlation was found between the power-law index and continuum flux.

**4.4.2.3 ATCA Radio Analysis** The model that provides a good fit to the *ATCA* radio data is a power law (see Figure 4.12). I find the spectral index to be modulated on the orbital period (see Figure 4.13).

Similar to the *Fermi* LAT and *Swift* XRT analyses described above (see Sections 4.4.2.1 and 4.4.2.2), I investigated the temporal dependence of the spectral parameters (see Table 4.4). Since the spectral index is modulated on the  $16.531 \pm 0.006$  day orbital period found with *Fermi* LAT, I searched for correlations between the power law spectral index with respect to flux (see Figure 4.14). A strong correlation was found between the power law spectral index and radio flux density ( $r = 0.89$ ,  $p = 0.056$ ).

Phase	Net Counts <sup>a</sup>	$\Gamma$	Flux ( $10^{-12}$ erg cm <sup>-2</sup> s <sup>-1</sup> )	Method	$\chi^2_\nu$ (d.o.f)
0.0	940	$1.31^{+0.07}_{-0.06}$	$2.8 \pm 0.1$	$\chi^2$	0.88(42)
0.1	263	$1.4 \pm 0.1$	$1.5 \pm 0.1$	cstat	
0.2	154	$1.5 \pm 0.2$	$1.8 \pm 0.2$	cstat	
0.3	274	$1.5 \pm 0.1$	$2.1 \pm 0.2$	cstat	
0.4	171	$1.4 \pm 0.2$	$1.9 \pm 0.2$	cstat	
0.5	208	$1.5 \pm 0.2$	$1.7 \pm 0.1$	cstat	
0.6	200	$1.6 \pm 0.2$	$1.4 \pm 0.1$	cstat	
0.7–0.8	161	$1.7 \pm 0.2$	$1.02^{+0.09}_{-0.08}$	cstat	
0.9	110	$1.6 \pm 0.2$	$1.2 \pm 0.1$	cstat	

Table 4.3. *Swift* XRT spectral parameters of 1FGL J1018.6-5856. Errors are at the  $1\sigma$  level.

<sup>a</sup> Counts are within the extraction regions.

<sup>b</sup>  $N_{\text{H}}$  was frozen to that reported in An et al. (2015) using the *XMM-Newton* data:  $1.02 \times 10^{22}$  atoms cm<sup>-2</sup>

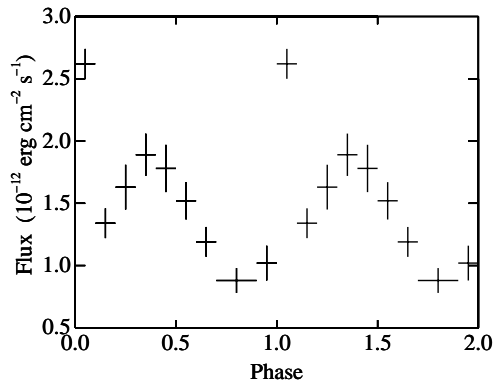


FIG. 4.10. The absorption-corrected X-ray flux of 1FGL J1018.6-5856 folded on the orbital period.

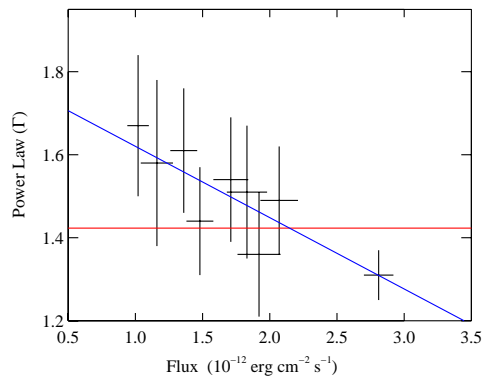


FIG. 4.11. Power-law index for the *Swift* XRT spectra vs. the continuum flux in the 0.3–10 keV band. The red and blue lines indicate the best fit for constant and linear models, respectively. The correlation coefficient ( $r$ ) is: -0.94.

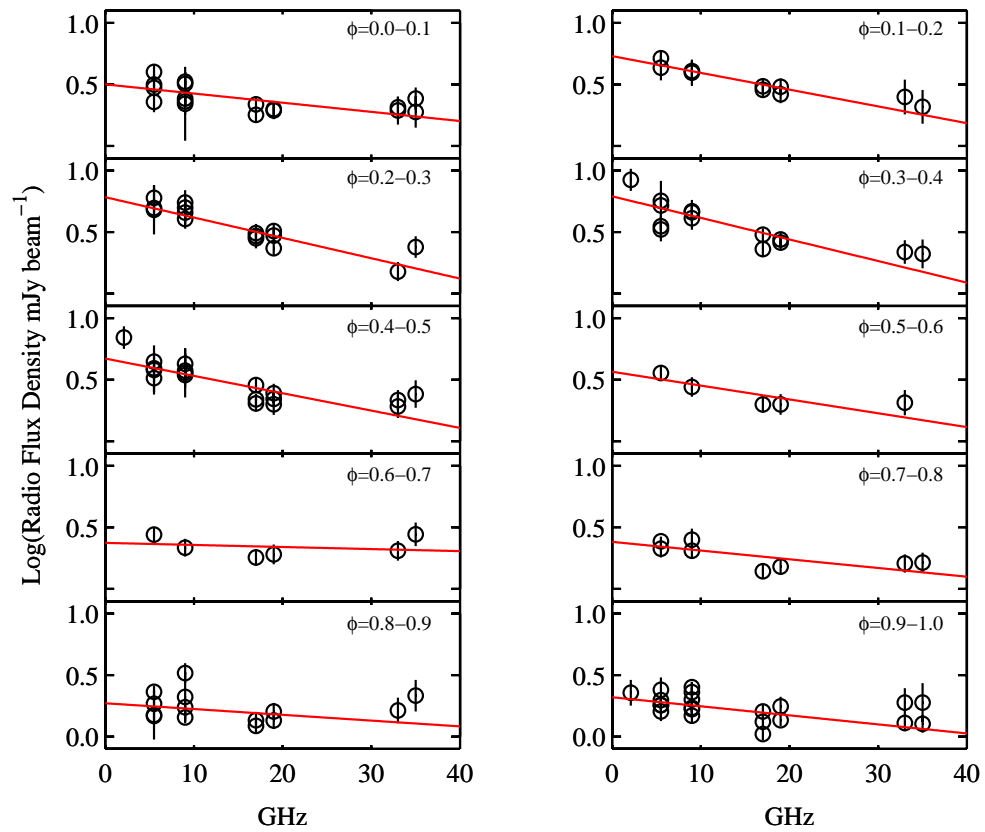


FIG. 4.12. Orbital phase-resolved *ATCA* radio spectra covering frequencies in the 2.1–35.0 GHz band. The red lines indicate the best fit for a power-law model, which is a possible indication of free-free absorption.

Phase	$\alpha$	Radio Flux Density mJy beam <sup>-1</sup>
0.05	0.29±0.06	5.4±0.1
0.15	0.4±0.1	10.5±0.3
0.25	0.58±0.08	13.5±0.3
0.35	0.51±0.06	12.3±0.2
0.45	0.46±0.06	9.7±0.1
0.55	0.4±0.1	7.5±0.4
0.65	0.1±0.1	3.2±0.2
0.75	0.28±0.07	3.9±0.2
0.85	0.18±0.07	2.6±0.1
0.95	0.24±0.05	2.87±0.08

Table 4.4. Spectral parameters of 1FGL J1018.6-5856 from the *ATCA* radio survey. Errors are at the 1  $\sigma$  level.

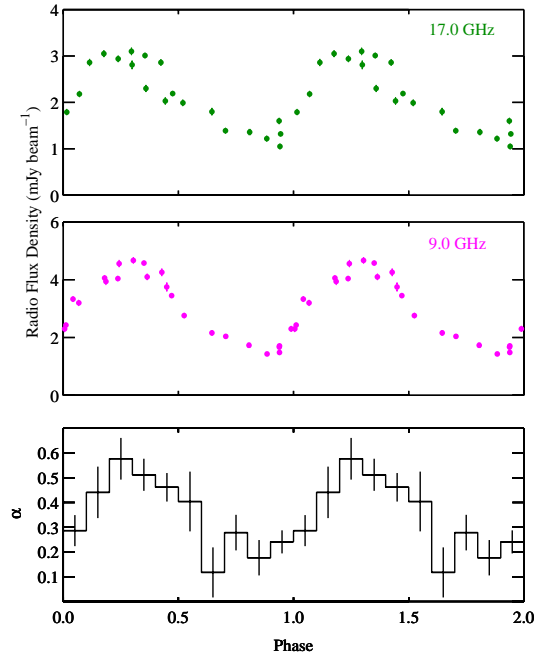


FIG. 4.13. *ATCA* radio light curves at 17.0 GHz (top) and 9.0 GHz (middle) folded on the orbital period. These are used to compare to the power-law frequency index of the *ATCA* radio data folded on the orbital period (bottom).

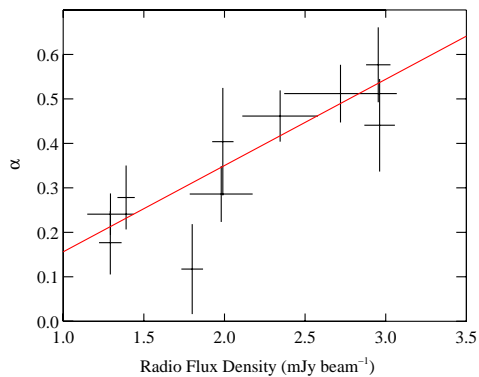


FIG. 4.14. Spectral index for the *ATCA* radio spectra vs. the flux density in the 17.0 GHz frequency band. The data are correlated at the level of  $r = 0.89$ ,  $p = 0.056$ .

## 4.5 Discussion

### 4.5.1 What is the nature of the gamma-ray orbital modulation?

The multiwavelength observations reveal the presence of a complex orbital modulation seen in the folded light curves as previously noted by Ackermann et al. (2012) and An et al. (2013, 2015). The epoch of maximum flux in the gamma-ray band is also seen at X-ray energies (see Section 4.4.1.2). I additionally find a secondary maximum at phases  $\sim 0.3$ – $0.4$  in the X-ray and the radio bands (see Sections 4.4.1.2 and 4.4.1.3).

I first discuss the possibility that the epoch of maximum flux in the gamma-ray bandpass occurs when the compact object is at superior conjunction. In the case where the non-degenerate star is a massive O-type star (e.g. LS 5039 Kishishita et al., 2009), the peak energy where photons are produced is in the ultraviolet according to Wien's Displacement Law. As described in Section 1.8.2, gamma-ray emission could result when UV photons collide with charged particles in the shock due to the pulsar wind and stellar wind and inverse Compton scatter to gamma-ray energies (Mirabel, 2012). Based on this model, it is expected that maximum gamma-ray emission occurs at superior conjunction, where the compact object is on the opposite side of the companion (Mirabel, 2012). The quasi-sinusoidal peak at phase  $\sim 0.4$  seen in the X-ray and radio could arise when the compact object is in front of the companion star along the line of sight (An et al., 2015).

I also consider the possibility that the driving factor in the epoch of maximum flux in the gamma-ray bandpass is due to the varying seed photon density. If the orbit in 1FGL J1018.6-5856 is eccentric, it is possible that the photon density responsible for inverse-Compton emission is orbital phase dependent (Abdo et al., 2009). If this is the case, it is

expected that the maximum gamma-ray emission will occur at periastron, where the compact object is closest to the optical companion. The modulation depth differs from what would be expected for an eccentric orbit. From the definition of modulation depth (see Section 3.4.1.3), I find the modulation depth to be  $\sim 45\%$  using the likelihood light curves and power law with high-energy cutoff model. In comparison, the modulation depth of LS 5039, which has an eccentricity of  $\sim 0.3$ , was found to be  $\sim 60\%$  (e.g. Ackermann et al., 2012). This implies a low inclination and a small to moderate eccentricity as was confirmed by Waisberg & Romani (2015).

#### **4.5.2 What is the nature of the frequency dependent modulation in the ATCA data?**

The *ATCA* radio data reveal the modulation amplitude in the folded light curves to decrease with increasing frequency. There is an absence of clear modulation in the 33.0 and 35.0 GHz bands (see Section 4.4.1.3). This behavior could be suggestive of the presence of free-free absorption. Since bremsstrahlung can be characterized by a power law, I investigated the temporal dependence of the spectral index as a function of orbital phase. The spectral index closely tracks the radio flux density, which is consistent with the presence of intrinsic free-free absorption. This mechanism remains to be further investigated. To further parameterize this, the stellar winds of both the pulsar and main-sequence companion must be taken into account.

### 4.5.3 What is the Nature of the Compact Object?

The nature of the compact object and the gamma-ray emission mechanism in 1FGL J1018.6-5856 remains ambiguous. So far, no neutron star rotation period has been detected in the *Fermi* LAT power spectra. Likewise, no pulsation period in the X-ray has been found. A pulsation period would provide a clear indication that the compact object is a neutron star. However, a possibility remains that the compact object could be powered by a neutron star's rapid rotation. Since a firm identification of the nature of the compact object in 1FGL J1018.6-5856 has proven elusive thus far, I compare my findings to systems where the compact object is known.

I first consider the possible scenario that the compact object present in 1FGL J1018.6-5856 is a black hole and thus the system is powered by the microquasar mechanism. A complex X-ray spectral continuum modeled by a power law with an exponential high energy cutoff is expected in microquasars, which are accretion-powered objects (Coburn et al., 2002; An et al., 2015). This is in sharp contrast to the lack of such features in the *Swift* XRT spectra analyzed here and as recently noted by An et al. (2015). Additionally, emission lines such as the Fe  $K\alpha$  complex are seen in microquasars (e.g. Cygnus X-1, Cygnus X-3 Nowak et al., 2011; Hjalmarsdotter et al., 2009), which are absent in the *Swift* analysis of 1FGL J1018.6-5856. Another marker of an accretion-powered system is fast variability, where properties such as red noise or quasi-periodic oscillations (QPOs) might be expected in the power spectra. So far, these have not been seen in the gamma-ray nor X-ray bandpasses. Finally, a disk blackbody is required to model the soft X-ray spectra of BHCs in the soft/high state (Shakura & Sunyaev, 1973; Nowak, 2006).

This also is not seen in 1FGL J1018.6-5856, suggesting that the emission is unlikely to be powered by the mechanisms seen in microquasars.

I also discuss the possibility that 1FGL J1018.6-5856 contains a neutron star and thus is powered by the pulsar-wind mechanism. I compare the multi-wavelength properties of 1FGL J1018.6-5856 to PSR B1259-63, which so far is the only gamma-ray binary with a confirmed neutron star (Aharonian et al., 2005; Johnston et al., 1994). The neutron star in PSR B1259-63 is a young radio pulsar with a rotation period of 47.8 ms in  $\sim 3.4$  yr orbit around a Be star. Since PSR B1259-63 is likely powered by the shock formed due to the winds of the companion star and pulsar itself, it is postulated that the physical mechanism that could lead to emission in the GeV–TeV energies is inverse-Compton scattering of UV photons. In a multi-wavelength campaign during the 2014 periastron, a power law with a spectral index that ranges from  $1.57 \pm 0.02$  to  $1.94 \pm 0.02$  was found in combined *Swift* XRT and *NuSTAR* spectra. This is comparable to what is found in 1FGL J1018.6-5856 where the photon indices ranges from  $1.31^{+0.07}_{-0.06}$  to  $1.7 \pm 0.2$ . If the same electron population produces the X-ray and TeV emission, some sort of correlation in flux or power-law index might be expected. This can be verified by searching for correlations with the X-ray and the recently discovered TeV emission reported in H. E. S. S. Collaboration et al. (2015).

#### **4.5.4 Comparison and Contrast with LS 5039 and LS I +61° 303**

The emission mechanism responsible for the gamma-ray emission and the nature of the compact object in 1FGL J1018.6-5856 are at present not well understood. To place 1FGL J1018.6-5856 in context with similar gamma-ray binaries, I compare it with LS

5039 and LS I +61° 303.

I first discuss these observations of 1FGL J1018.6-5856 in comparison to the gamma-ray binary LS I +61° 303, which consists of a Be-type optical companion and probably a pulsar in a  $\sim 26.3$  d orbit, also thought to be powered by the pulsar-wind mechanism. In their *Swift* XRT campaign, Esposito et al. (2007) found the spectral continuum to be described by a featureless power law with photon index  $1.78 \pm 0.05$  modified by a fully-covered absorber with  $N_{\text{H}}$  of  $5.7 \pm 0.3 \times 10^{21}$  atoms  $\text{cm}^{-2}$ . No spectral features that are typically attributed to accreting systems were found (Esposito et al., 2007), which is similar to my observations of 1FGL J1018.6-5856. Another similarity between LS I +61° 303 and 1FGL J1018.6-5856 is radio emission that is modulated on the orbital period. A striking difference is the presence of a superorbital modulation in LS I +61° 303, at a period of  $1667 \pm 8$  d (Li et al., 2014). This is seen in the radio (Gregory, 2002), hard X-ray (Li et al., 2014) and gamma-ray bandpasses (Ackermann et al., 2013). The maximum flux in the radio modulation in LS I +61° 303 appears to be modulated on both the orbital and superorbital periods in LS I +61° 303 (Gregory, 2002). No such modulation is seen in 1FGL J1018.6-5856, which is consistent with the lack of a Be star.

I also discuss the gamma-ray binary LS 5039 and how it compares with these observations of 1FGL J1018.6-5856. LS 5039 consists of a O6.5 V((f)) star and suspected rapidly spinning pulsar, which is in an eccentric orbit where the period and eccentricity were found to be  $3.90603 \pm 0.00017$  d and  $0.35 \pm 0.04$ , respectively (Casares et al., 2005). In their X-ray analysis using *ASCA*, *XMM-Newton* and *Chandra*, Kishishita et al. (2009) found the best-fit spectral model to consist of a power law where the index varies from  $\Gamma \sim 1.45$  at apastron to  $\Gamma \sim 1.60$  at periastron. This is similar to my analy-

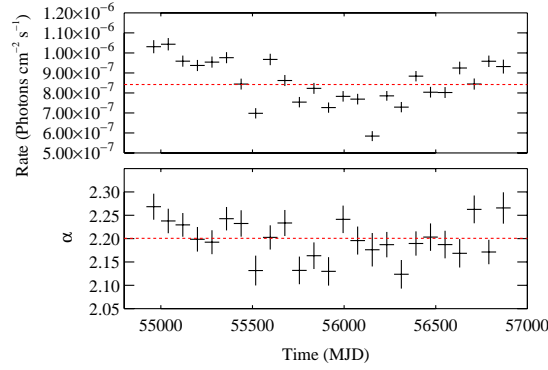


FIG. 4.15. Long-term *Fermi* LAT light curve of the source LS I +61° 303 produced in the 0.1–300 GeV band based on a likelihood analysis (top) spans nearly 6 years (MJD 54961–56869). Long term variability is shown over the duration of the light curve. Significant variability is also seen in the spectrum (bottom). I illustrate this by plotting the  $\alpha$  parameter of the log-parabola model.

sis of 1FGL J1018.6-5856 where I found the power-law index to vary from  $1.31^{+0.07}_{-0.06}$  to  $1.7 \pm 0.2$ . While the power-law index is a minimum at the epoch of maximum gamma-ray flux, the maximum power-law index is not seen at phase 0.3 where the quasi-sinusoidal modulation peaks in the X-ray and radio peaks, which could be attributed to the poor statistics seen in the *Swift* X-ray campaign. No orbital modulation was found at radio frequencies for LS 5039 (Ribó et al., 1999), which is in variance with what is seen in 1FGL J1018.6-5856.

## 4.6 Conclusion

1FGL J1018.6-5856 is thought to be powered by the pulsar-wind mechanism. Modulation on the  $16.531 \pm 0.006$  day orbital period is clearly seen in the gamma-ray, X-ray and radio bandpasses where peaks are found at different binary orbital phases. The epoch of maximum flux in the *Fermi* LAT light curve is also seen in the X-ray bandpass. A

secondary maximum at binary orbital phase  $\sim 0.3$  is also seen in the *Swift* XRT X-ray and *ATCA* radio light curves, which could possibly be attributed to inferior conjunction. I note the possibility that this secondary peak could also originate at apastron, when the seed photon density responsible for inverse Compton emission is at a minimum. No long term variability in the flux nor spectral properties is seen.

The compact object in 1FGL J1018.6-5856 and thus the emission mechanism remains ambiguous in nature. No signs of gamma-ray or X-ray pulsations have been found in 1FGL J1018.6-5856, which would firmly prove the compact object is a neutron star. No spectral features such as high-energy cutoff nor emission lines are seen in the continuum, which is evidence that 1FGL J1018.6-5856 is not powered by accretion and therefore likely not a microquasar.

The emission in the radio as seen with *ATCA* is modulated on the orbital period where the maximum flux occurs around binary orbital phase 0.3, similar to the quasi-sinusoidal peak in the *Swift* XRT light curves. No flux increase at phase  $\sim 0.0$  is seen in the radio bandpass. I find the amplitude modulation to decrease with increasing frequency, which is a possible indication of the presence of free-free absorption. This is further supported by the absence of clear modulation in the 33.0 and 35.0 GHz bands. Since free-free absorption can be described by a power law, I searched for changes in the spectral index as a function of binary orbital phase. The spectral index closely tracks the flux density, which could be consistent with the presence of intrinsic free-free absorption. Since a detailed model that involves the winds of the pulsar and main-sequence companion star remains to be done, I cannot definitively attribute this to bremsstrahlung.

1FGL J1018.6-5856 is likely to be a non-accreting gamma-ray binary powered by

the pulsar wind mechanism but conclusive evidence remains to be found. A detailed model to describe the possibility of free-free absorption seen in the radio and X-ray band-passes is needed, which I plan to develop in the near future. Additionally, I plan to probe the nature of the gamma-ray emission by investigating the long-term orbital variability of 1FGL J1018.6-5856.

## Chapter 5

# CONCLUSION

### 5.1 Overview

This thesis focuses on the study of high-energy emission in the X-ray and gamma-ray bandpasses seen in binary systems containing compact objects. Several wind-fed eclipsing SGXBs, the HMXB 4U 1210-64 that might be powered by the Be mechanism, and the gamma-ray binary 1FGL J1018.6-5856 were studied in this thesis to answer fundamental questions about the properties of the stellar components and probe the variability of these sources at all timescales. All X-ray binaries in the sample are eclipsing sources where the eclipse duration was exploited to constrain the masses and radii of the donor stars. While emission in X-ray binaries is observed due to the conversion of gravitational potential energy to radiation at extreme temperatures, gamma-ray emission could either originate via the microquasar or pulsar-wind mechanisms. While no evidence for the neutron star rotation period was found, it is strongly suggested that the gamma-ray emission in 1FGL J1018.6-5856 is powered by the pulsar-wind mechanism. It should be noted that an origin powered by relativistic jets, the microquasar scenario, cannot be ruled out.

## 5.2 Results on the Systems in this Work

### 5.2.1 Probing the Masses and Radii of Donor Stars in Eclipsing X-ray Binaries

I surveyed the eclipsing XRBs IGR J16393-4643, IGR J16418-4532, IGR J16479-4514, IGR J18027-2016 and XTE 1855-026 using the eclipse duration to determine the mass and radius of the donor star. Using an ‘observed minus calculated’ ( $O - C$ ) analysis, I also refined the orbital periods and improved the error estimate on the orbital period for each XRB by up to an order of magnitude. With the exception of IGR J16393-4643 where the eclipse half-angle was found to be  $\sim 15^\circ$ , the eclipse half-angles were all found to be  $\sim 30^\circ$ . Since the luminosity of each system is less than expected for Roche-lobe overflow (Kaper et al., 2004), I attach the constraint that the mass donor underfills the Roche lobe. IGR J18027-2016 is the only “double-lined binary” in our sample. I assume the mass for the neutron stars in the other systems to be at the white-dwarf Chandrasekhar limit,  $1.4 M_\odot$ .

The process of allowing inclination angles to range from edge-on orbits to those where the Roche lobe was filled made the constraints possible. I found that IGR J16393-4643 is consistent with spectral types B0 V and B0-5 III since they satisfy the constraints imposed by the half-angle and Roche lobe. In IGR J16418-4532 and IGR J16479-4514 the previously proposed mass donors were found to overfill the Roche lobe; however, spectral types O7.5 I and earlier satisfy the constraints of the eclipse half-angle and the Roche lobe.

The mass and radius of the donor star in IGR J18027-2016 were found to be 18.6–

$19.4 M_{\odot}$  and  $17.4\text{--}19.5 R_{\odot}$ , where I constrain mass of the neutron star to be between  $1.37\pm 0.19 M_{\odot}$  and  $1.43\pm 0.20 M_{\odot}$ . I find the mass and radius of the donor star in XTE J1855-026 to lie between  $19.6\text{--}20.2 M_{\odot}$  and  $21.5\text{--}23.0 R_{\odot}$ . The neutron star mass was constrained to be between  $1.77\pm 0.55 M_{\odot}$  and  $1.82 M_{\odot}$ . This method in studying these eclipses has yielded important information in understanding a key dimension of using eclipses to constrain mass. The next logical step would be measuring the radial velocities of both the donor star and compact object to allow key astrophysical parameters to be determined.

### 5.2.2 4U 1210-64

4U 1210-64 is a poorly understood source that has been postulated to be an HMXB powered by the Be mechanism. X-ray observations with the ASM and PCA onboard *RXTE*, *Suzaku*, *Swift* BAT and MAXI provide detailed temporal and spectral information, probing the nature of its variability on all time scales. Long term variability, suggestive of a variable accretion rate, was seen with the ASM (see Chapter 3), which reveals the presence of three distinct system states: two active states and one low state that I interpret as quiescence. While I discuss different mechanisms, the Be-mechanism might explain the  $\sim 2500$  day duration of the quiescent phase. Caveats are seen in the explanation and no mechanism considered in my analysis appears to be consistent with 4U 1210-64. The companion star was previously proposed to have a spectral type of B5 V (Masetti et al., 2009), but it does not satisfy the observed eclipse half-angle, which is compelling evidence against a B5 V classification. Optical and X-ray spectral features of 4U 1210-64 point to a mass donor that could be a B0 V or B0-5 III star. The nature of the compact

object remains ambiguous. No evidence for a pulsation period, which would provide clear indication that the compact object is a neutron star, could be identified in the ASM, MAXI and PCA power spectra. Spectral results that could reveal its nature have also been inconclusive. The properties of the continuum strongly contrast with those typically seen in BHCs as well as CVs. While the nature of the compact object has proven elusive, a neutron star with a weak magnetic field possibly aligned with the spin axis is consistent with the lack of pulsations and cyclotron features.

The best fit spectral model consists of a power law modified by a high-energy cut-off. This is additionally modified by an absorber that fully covers the source as well as partially covering absorption. Emission lines at 2.62 keV, 6.41 keV, 6.7 keV and 6.97 keV were all clearly detected in the *Suzaku* spectra, which I interpret as S XVI  $K\alpha$ , Fe  $K\alpha$ , Fe XXV  $K\alpha$  and Fe XXVI  $K\alpha$ , respectively. I found a linear relationship between the flux of Fe I vs. the continuum, which shows that the most probable origin of the Fe I line is fluorescence of cold and dense material close to the compact object. The slopes of the relationship between the logarithm of the Fe XXV and Fe XXVI flux versus the logarithm continuum flux possibly show that an increasing part of the medium might be completely ionized as the flux increases. A positive correlation was seen in both the *Suzaku* hardness-intensity diagram and the PCA color-color diagram, which provides evidence against a strong wind. Additional evidence from the folded MAXI and ASM light curves suggest that the observed  $N_{\text{H}}$  could possible originate in an accretion stream.

### 5.2.3 1FGL J1018.6-5856

1FGL J1018.6-5856, the first gamma-ray binary discovered by the Fermi Large Area Telescope (LAT), consists of an O6 V((f)) star and suspected rapidly spinning pulsar possibly powered by the interaction between the relativistic pulsar wind and stellar wind of the companion. I refined the orbital period to  $16.531 \pm 0.006$  d using *Fermi*, updating the previously published value of  $16.58 \pm 0.02$  d (Ackermann et al., 2012). Using a likelihood analysis, no long-term flux variability was seen over the duration of the *Fermi* gamma-ray light curve. No significant long-term variability was found in the spectrum, which was modeled using a log-parabola model. Quasi-sinusoidal behavior was found in the aperture photometry Fermi LAT folded light curve where I defined phase zero as the epoch of maximum flux (MJD  $55403.3 \pm 0.4$ ).

I also analyzed the X-ray and radio properties of 1FGL J1018.6-5856 using the *Swift* X-ray Telescope (XRT) and *Australia Telescope Compact Array* (ATCA). While the maximum flux was also seen in the XRT folded light curves at the same phase as the gamma-ray maximum, a secondary peak at phase  $\sim 0.4$  was found. In the radio, there is a single maximum at phase  $\sim 0.4$  (Fig. 4.6). This is consistent with previous observations in the 5.5 and 9.0 GHz bands. The amplitude modulation in the radio was found to decrease with increasing frequency (Fig. 4.6, right), which might be interpreted with a free-free absorption model. The radio light curves at 33.0 and 35.0 GHz do not show clear modulation on the orbital period.

The best fit spectral model to the *Swift* XRT data consists of a power law modified by a fully covered absorber (see Chapter 4). I find that the neutral hydrogen column

density for the fully covered absorption could not be accurately constrained. Therefore, I froze  $N_{\text{H}}$  to  $1.02 \times 10^{22}$  atoms  $\text{cm}^{-2}$ , which was reported in the *XMM-Newton* data by An et al. (2015). A good fit does not require a high-energy cutoff, which is typically found in accreting pulsars (Coburn et al., 2002; White et al., 1983). The *Fermi* LAT data can be best fit with a log-parabola model and a power law with a high-energy cutoff.

### 5.3 Gamma-Ray Binaries

Gamma-ray binaries show gamma-ray emission modulated on the orbital phase and might represent an early stage in the evolutionary lifetime of an HMXB (Ackermann et al., 2012), allowing the history of binary stellar systems to be studied at an even earlier phase. Superorbital variability has been found in the source LS I+61° 303 which hosts a Be-star (Li et al., 2014); however, it has not been found in LS 5039 and 1FGL J1018.6-5856, suggesting that superorbital variability in gamma-ray binaries is not ubiquitous. Gamma-ray binaries are also rare, where only five are known. Exploring 1FGL J1018.6-5856, the most recent gamma-ray binary to be discovered, will help us understand the relative paucity of gamma-ray binaries as well as the mechanisms responsible for their emission.

### 5.4 Outlook

The study of the night sky has come a long way since our ancestors first gazed at the stars. With nearly a half century of multi-wavelength observations, we now have at our fingertips methods to observe the temporal and spectral variability of X-ray and gamma-

ray binaries using both all-sky monitors and pointed observations. The masses and radii of the donor star, masses of neutron stars and orbital evolution can be constrained in eclipsing XRBs, thanks to our ability to express the eclipse duration as a function of stellar radius, inclination angle and the sum of the masses in the binary system. Thanks to nearly 20 years worth of data that monitored long-term changes in the nature of HMXBs and their gamma-ray predecessors, we can constrain physical and geometric properties. This clearly contributes to the understanding of matter accretion in the presence of extreme physical environments for HMXBs. The observations have yielded robust data on astrophysical properties such as variability on orbital and superorbital timescales giving us a powerful means to investigate their underlying mechanisms.

While breakthrough research has unveiled the nature of the magnetic fields of neutron stars, variability on all types of timescales, and accretion physics in extreme environments many unanswered questions remain. To name a few examples that were uncovered in my thesis include the nature of the donor star in 4U 1210-64, the origin of the long-term variability in 4U 1210-64, the mechanism responsible for the disappearance of radio modulation at high frequencies in 1FGL J1018.6-5856 and the neutron star equation of state. The detailed eclipse measurements presented in Chapters 2 and 3 could be used as timing markers to determine the binary orbital evolution of HMXBs. On long timescales, Dynamic Power Spectra could be employed in multiple energy band passes to investigate the evolution of long-term behavior of HMXBs and gamma-ray binaries (Clarkson et al., 2003). Pointed observations with *Nuclear Spectroscopic Telescope Array (NuSTAR)*, the first hard X-ray imaging telescope in orbit, could also be exploited for further study of many of the sources studied in this thesis. Launched on 2012 July 13, *NuSTAR* con-

sists of two co-aligned grazing incidence telescopes sensitive to the energy band 3–79 keV with good energy resolution, extending the focusing sensitivity beyond the  $\sim 10$  keV high-energy cutoff achieved by all previous X-ray imaging satellites (Harrison et al., 2013). I hope that the analysis presented in this thesis contributes to our understanding of these sources and their intriguing behavior.

## Appendix A

# INSTRUMENTATION

### A.1 Overview

Beginning with the discovery of the LMXB Scorpius X-1, the 1960s ushered in the era of X-ray astronomy. These first observations of the X-ray sky were conducted using collimated gas counters onboard balloon and rocket detectors. Over the next few decades, different types of detectors analyzed the temporal and spectral properties of X-ray binaries. These observations each told a different part of the story, which combined with theory allowed us to disentangle the intriguing properties of XRBs as a whole. While all-sky monitors have the capabilities to provide publicly available databases of long-term observations of X-ray sources, the capabilities of modern detectors such as those that implement CCDs allow for observations that disentangle spectral features such as the Fe  $K\alpha$  region and cyclotron resonant scattering features.

A fundamental quantity that measures the performance of an X-ray spectrometer is the spectral energy resolution full-width at half-maximum (FWHM). The energy and FWHM of the energy distribution inferred from the spectrometer are denoted by  $E$  and  $\Delta E$ , respectively. As referenced in Fraser (2009), the FWHM at a specific energy band-

pass for non-dispersive X-ray spectrometers typically follows a power-law function dependent on a proportionality constant and the energy (see Equation A.1).

$$(A.1) \quad \frac{\Delta E}{E} = \frac{K}{E^{1/2}}$$

This chapter is structured in the following order: the physics that makes X-ray collimators, non-dispersive spectrometers and X-ray CCD devices work is outlined in Section 2. Sections 3 and 4 present a discussion of the instrumentation used in this analysis.

## A.2 Detector Physics

### A.2.1 Proportional Counters

With a design similar to that of Geiger counters, proportional counters have been the workhorses of X-ray astronomy from its humble beginnings to the present day. Proportional counters have been used in a variety of different missions and were implemented in all-sky monitors such as the *Rossi X-ray Timing Explorer (RXTE)* ASM and Monitor of All-Sky X-ray Image (MAXI) Gas Slit Camera (GSC) as well as pointed instruments such as the Medium Energy Detector Array (MEDA) onboard the European X-ray Observatory Satellite *EXOSAT*, the Large Area Counter (LAC) onboard the Japanese *Ginga* observatory and the Proportional Counter Array (PCA) onboard *RXTE*. Of interest to this analysis are gas proportional counters, which have provided high temporal and modest spectral resolution observations of X-ray sources.

Gas proportional counters consist of a collimator that absorbs off-axis X-ray photons, a thin window that allows the entrance of X-ray photons, a chamber consisting of a

large volume of gas and an anode maintained at a specific voltage (e.g. Seward & Charles, 1995). The window, which is typically made of a metal such as beryllium, is designed to have a large area to maximize detector sensitivity and a strength to withstand the force due to the gas pressure inside the large chamber. In the case that the window cannot withstand the pressure force, the gas leaks into the vacuum of space and results in the failure of the instrument.

In a gas proportional counter, X-ray photons primarily interact with the gas molecules or atoms via the photoelectric effect (Smith et al. 1984). A photon's energy must be large enough to penetrate the window and ionize the atoms inside the gas chamber, which is typically composed of a noble gas such as argon or xenon. The initial interaction between the X-ray photon and the gas results in the release of the primary photoelectron, which is followed by secondary Auger electrons that form a localized electron-ion cloud (Fraser, 2009). If the contribution to fluorescence is ignored, the number of electrons in the charge cloud is approximately proportional to the energy of the absorbed photon and inversely proportional to the average energy to create a secondary ion pair,  $w$  (see Equation A.2).

$$(A.2) \quad N = \frac{E}{w}$$

Electrons that are removed from the now positively ionized gas rapidly accelerate towards the anode due to the applied electric field. This results in further collisions and ionizations of other atoms referred to as an “avalanche” of electrons (Seward & Charles, 1995). The electron avalanche is finally collected on a central wire, which is maintained

at a voltage where the number of collected electrons is proportional to the energy of the incident X-ray photon. Gas gains, defined as the electron number collected at the anode per electron in the charge cloud, of  $10^3$ – $10^5$  are typical in conventional proportional counters (Fraser, 2009). The energy and position of the X-ray photon can be computed using methods such as the charge-division technique, providing a spectral description of the source and information concerning the X-ray emission mechanism (Levine et al., 1996).

The energy resolution FWHM (see Equation A.1) of a gas proportional counter is dependent on the average energy to create a secondary ion pair, the Fano factor and the relative variance of the gas gain (Equation 2.9, Fraser, 2009). The Fano factor,  $F$ , is a measurement the fluctuation of a electric charge that is obtained in a detector. In noble gases such as argon and xenon, the Fano factor was found to be 0.17 (Fano 1947). For a proportional counter where the primary component of the gas is composed of argon, the proportionality constant in the energy resolution FWHM is  $\sim 0.35$ . For more information, see Fraser (2009, Chapter 2).

Though significant scientific discoveries were made through the use of proportional counters, there are significant limitations to this type of detector. Cosmic rays, particles with energies significantly exceeding those that can be accelerated on Earth, can pass through a spacecraft itself and result in an avalanche of electrons that mimics the signals expected from X-ray photons (Mason & Culhane, 1983). This is referred to as “background” and in the case of a non-imaging proportional counter require several different efficient background rejection techniques. First developed and implemented in the 1960s, rise-time discrimination is one of the primary methods to identify and reject background

particles (Cooke et al., 1967). The rise-time of the pulses produced by background particles typically are slower than those produced by keV X-rays. It should be noted that the efficiency of the rise-time technique decreases as a function of X-ray energy as was found by Harris and Mathieson (1971). At 5.9 keV the background rejection efficiency is typically 97%. A second technique employs independent ‘guard’ and ‘veto’ counters that operate in anti-coincidence within a common gas cell (Fraser, 2009). Background events are rejected when there is a coincident pulse on two different groups, which indicates that the source of ionization is extended. A third method to reject background is energy selection, which is defined as the rejection of events where the energy is outside the desired bandpass. This is dependent on the observed spectrum of the raw background.

Detailed models that account for both cosmic rays and the Cosmic X-ray Background (CXB) are another method to remove background from the desired X-ray emission. The model components are generally time dependent and must be appropriately parameterized for accurate modeling of the temporal and spectral properties of X-ray sources (Jahoda et al., 2006). While proportional counters can operate in the high-energy band, X-ray photons above 20 keV are not detected efficiently. This can be circumvented by the scintillation counter.

### **A.2.2 Scintillation Detectors**

A close relative of the gas proportional counter is the scintillation counter, which is a solid-state detector that makes use of luminescent solids. These nuclear particle detectors were the primary workhorses of balloon-based astronomy and have been used in various types of pointed instruments including the Phoswich Detector System (PDS), the High

Energy X-ray Timing Experiment (HEXTE) and the Hard X-ray Detector (HXD) onboard the *BeppoSAX*, *RXTE* and *Suzaku* observatories, respectively. Of interest to this work is the HXD instrument onboard *Suzaku*, particularly the Positive Intrinsic Negative (PIN) diodes that are sensitive to the  $\sim 13\text{--}70$  keV energy bandpass.

In a scintillation counter, the gas is typically replaced with crystals of sodium iodide (NaI) or cesium iodide (CsI), which can absorb X-ray photons with energies larger than 20 keV much more efficiently than traditional gas proportional counters (Seward & Charles, 1995). It should be noted that xenon-filled gas proportional counters can be sensitive to much higher energies. As an example, the PCA onboard *RXTE* was sensitive to energies up to 60 keV (Jahoda et al., 2006). Scintillation counters also employ photomultiplier tubes, which are sensitive detectors of light, a circuit to measure the pulse height produced by the photomultiplier and a second scintillating material as an anti-coincidence detector. The second scintillating material is specifically chosen where the light pulses have a different rise time than the primary crystal and is used to reject background.

Similar to a gas proportional counter, X-ray photons at large enough energies penetrate a shield/reflector and predominantly interact with the NaI or CsI crystals via the photoelectric effect. The NaI or CsI crystals, which are luminescent in nature, absorb the energy from the X-ray photon and re-emit some of it as a pulse of visible light proportional to the energy of the incident photon (Seward & Charles, 1995). This pulse of light is called a scintillation and passes through a light guide to the photocathode of a photomultiplier tube. Electrons emitted by the photoelectric effect are accelerated through the photomultiplier tube by an applied electric field and are focused to strike the first dynode of the tube. After many subsequent dynode impacts which are held at increasingly higher

electric potentials, the current produced by the initial scintillation is significantly amplified by the time it reaches the anode. The energy of the X-ray photon can be computed using similar techniques to those implemented in gas proportional counters, providing a spectral description of the source and information concerning the X-ray emission mechanism.

With a proportionality constant of 1.67 for the energy resolution FWHM, NaI(Tl) scintillation detectors are severely limited as non-dispersive X-ray spectrometers (Fraser, 2009). Non-imaging scintillation counters are also significantly limited by background where diffuse gamma rays, emission from radioactive nuclei and cosmic rays are the prime contributors. This can be treated by rocking the spacecraft or in detailed models as in the cases of *HEXTE* and *HXD*, respectively. In the latter, the sensitivity is dependent on the sensitivity of the model. Background can also be rejected using a second scintillating material where the risetime is slower than the material used for detection (Seward & Charles, 1995). The *Suzaku* *HXD*, for instance, consists of a well-shape bismuth germanate crystal (BGO), which surrounds a gadolinium silicate crystal (GSO) used for detection. Like gas proportional counters, non-imaging scintillation counters can also be limited by systematics or source confusion. Operating in the hard X-ray bandpass, scintillators are also limited by source fluxes, which could be weaker than the detector background.

### **A.2.3 CCD Detectors**

Many scientific breakthroughs were realized with the introduction of charge-coupled devices (CCDs) to X-ray astronomy, which significantly improved the spectral

energy resolution FWHM (see Equation A.1). First produced at Bell Telephone Laboratories in 1970 (Boyle and Smith, 1970), CCDs have been implemented in many different technological fields including astronomy, where X-ray photons can be positionally resolved. Significant improvements to the temporal and spectral resolution of pointed observatories such as the Solid-state Imaging Spectrometer (SIS) onboard *ASCA*, the X-ray Imaging Spectrometer (XIS) onboard *Suzaku* and X-ray Telescope (XRT) onboard *Swift* were made possible with CCDs (Koyama et al., 2007). Of interest to this work are the observations of 4U 1210-64 and 1FGL J1018.6-5856 with the XIS and XRT instruments, respectively. The constant of proportionality in the energy resolution FWHM of both the XRT and front-illuminated XIS instruments are 0.02 (see Equation A.1). These yield an energy resolution FWHM of  $\sim 130$  eV at 6.0 keV (Burrows et al., 2005; Koyama et al., 2007).

The CCDs typically used for X-ray astronomy are single chips that consist of a three-phase metal-oxide-silicon (MOS) capacitor that operates in frame transfer mode (Koyama et al., 2007). Incident X-ray photons interact with the silicon substrate via photoelectric absorption. Due to their sensitivity to optical and ultraviolet light, X-ray CCDs include optical blocking filters (OBF) that are opaque to photons in the optical and ultraviolet energies. The energy of the incident X-ray photon must be large enough to be transparent to the OBF (Koyama et al., 2007). Once absorbed, the X-ray photon is converted into an electron cloud where the number of electrons is proportional to the energy of the incident photon (Tatum, 2013). Through the application of a time-dependent electric potential, the electron cloud travels across the pixel array to the readout node where the resulting voltage is recorded as a pulse-height amplitude (PHA). Corrections

in temporal and spatial variability in the conversion between PHA and energy are finally stored as PHA invariant (PI).

Due to their pixilated nature, X-ray photons can be positionally resolved through X-ray CCDs combined with mirrors. Additionally, the effects due to background are significantly weaker compared to non-imaging detectors. This is due to their smaller detector volume. Though X-ray CCDs offer a substantial improvement in detector sensitivity compared to non-imaging instruments, there are still limitations to this type of detector. Electrons can be lost to trapping sites in the CCD as they are shifted across the array of pixels to the readout node. This effect, called charge transfer inefficiency (CTI), worsens over time due to degradation while the detector is in orbit. Cosmic rays can further amplify this problem, resulting in radiation damage that increases the likelihood of trapping sites. The *Suzaku* XIS, for instance, mitigates this problem by periodically injecting a sufficient quantity of charge to fill the trapping sites (Koyama et al., 2007; Mitsuda et al., 2007; Tatum, 2013). This method is also used to estimate the variations in the CTI. Another limitation to CCD detectors is pile-up, which is an effect that is particularly problematic in bright sources. Pile-up is the result of when two or more soft photons hit the same or neighboring pixels during a single exposure and cannot be distinguished from a single hard photon (Davis, 2001). This effect is significant in my observations of 4U 1210-64 with *Suzaku* XIS and in the case of *Suzaku* can be mitigated by excising the central pixels of the source. This is described more in detail in Chapter 3.

### A.3 Past Observatories

#### A.3.1 Rossi X-ray Timing Explorer (RXTE)

Built by NASA’s Goddard Space Flight Center (GSFC), the Massachusetts Institute of Technology (MIT) and the University of California, San Diego (UCSD), the *Rossi X-ray Timing Explorer (RXTE)* was launched on a Delta rocket from Cape Canaveral on 1995 December 30 (MJD 50081) and was operational until 2012 January 3 (MJD 55929). Sensitive to energies in the  $\sim 1.5\text{--}250$  keV bandpass, *RXTE* featured unprecedented timing resolution on timescales ranging from  $\sim 1$   $\mu\text{s}$  to years and moderate spectral resolution made possible by the All-Sky Monitor (ASM), the Proportional Counter Array (PCA) and the High Energy X-ray Timing Experiment (HEXTE) instruments. Of interest to this analysis are the ASM and PCA, which are briefly described below.

**A.3.1.1 All-Sky Monitor (ASM)** With a primary objective to monitor the highly variable X-ray sky, the *RXTE* ASM operated in the energy bandpass of 1.5–12 keV from 1996 February 22 to the end of the mission. The light curves are divided into three energy bands: 1.5–3 keV, 3–5 keV and 5–12 keV. ASM scanned approximately 80% of the sky per spacecraft orbit ( $\sim 90$  minutes) with a 90 s time resolution (“dwell”; Remillard & Levine, 1997; Levine et al., 1996). The FOV of the cameras was fixed on the sky for the duration of a “dwell”. The operational duty cycle of the ASM was  $\sim 40\%$  with the remainder lost to high-background regions of the *RXTE* orbit, spacecraft slews, and the rotation of the instrument (Remillard & Levine, 1997). The long-term coverage provided by the ASM allowed for intensive monitoring of X-ray sources on timescales much longer

than previously possible.

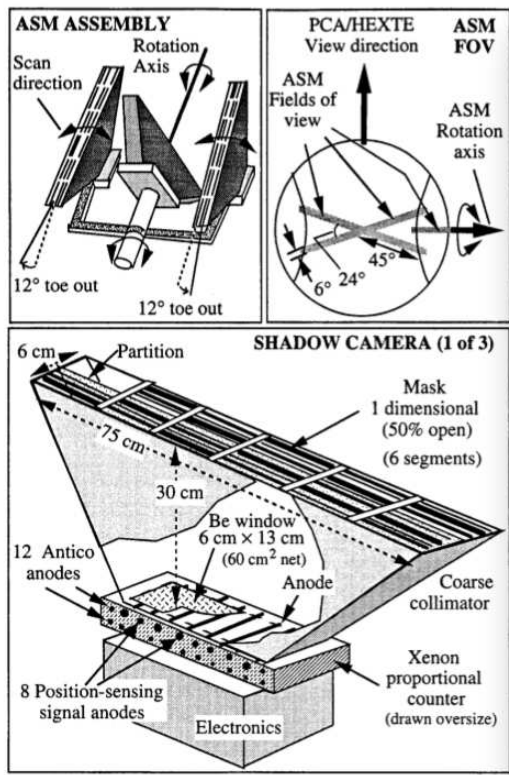


FIG. A.1. Relative orientations of the Scanning Shadow Cameras configured on the ASM (top left). Centers of FOV of SSC 1 and SSC 2 approximately co-aligned perpendicular to ASM rotation axis (top right). For SSC 3, the center of the FOV was pointed parallel to rotation axis. Major components of the SSC in a schematic (bottom, Levine et al., 1996).

The ASM consisted of three coded-aperture Scanning Shadow Cameras (SSCs), each containing a position-sensitive proportional counter (PSPC) that viewed the sky through a slit mask (Levine et al., 1996). Of the three SSCs, SSC3 pointed parallel to the ASM rotation axis, while SSC1 and SSC2 were both perpendicular to the rotation axis with an  $\pm 12^\circ$  angular difference (see Figure A.1). The slit masks were subdivided into twelve  $6 \times 2$  subsections, each containing  $\sim 15$  open and  $\sim 16$  closed slit elements of size 1 by 110 mm. The field of view (FOV) of the PSPCs was  $6^\circ \times 90^\circ$  FWHM (Levine et

al., 1996; Remillard & Levine, 1997).

The systematic noise in the ASM light curves was estimated by observing the Crab Nebula, where the uncertainty was estimated to be 1.9% of the mean flux. Over the entire energy range (1.5–12 keV), the Crab produced approximately  $75.5 \text{ counts s}^{-1}$  (Remillard & Levine, 1997; Levine et al., 1996). “Blank field” observations of regions at high Galactic latitudes, which were used to quantify systematic effects in faint sources, indicate that a systematic uncertainty of  $\sim 0.1 \text{ counts s}^{-1}$  must be taken into account (Levine et al., 1996). In a typical daily exposure, the ASM could reach a systematic and statistical limit of 5 mCrab at  $3\sigma$  significance (Remillard & Levine, 1997).

**A.3.1.2 Proportional Counter Array (PCA)** As one of two co-aligned instruments onboard *RXTE*, the PCA consisted of five co-aligned xenon/methane large-area proportional counter units (PCUs 0–4) each with a net collecting area of  $\sim 1600 \text{ cm}^2$  (Jahoda et al., 2006). Designed to perform observations of bright X-ray sources with high timing and moderate spectral resolution, the PCA monitored the X-ray sky in the energy bandpass of 2–60 keV from 1996 to the end of the mission (see Figure A.2). While two standard data compression modes were commonly used by PCA, the best possible timing resolution was  $\sim 1 \mu\text{s}$  at the expense of energy resolution. At 6.0 keV, the energy resolution FWHM in the PCA was  $\sim 1 \text{ keV}$ .

Each PCA detector consisted of a mechanical collimator with  $\text{FWHM} \sim 1^\circ$ , two Mylar windows, one of which was aluminized, a propane-filled “veto volume” and a xenon-filled main counter (Jahoda et al., 2006). Three layers of xenon cells were divided in half, which was significant for screening of the data and background modeling. It

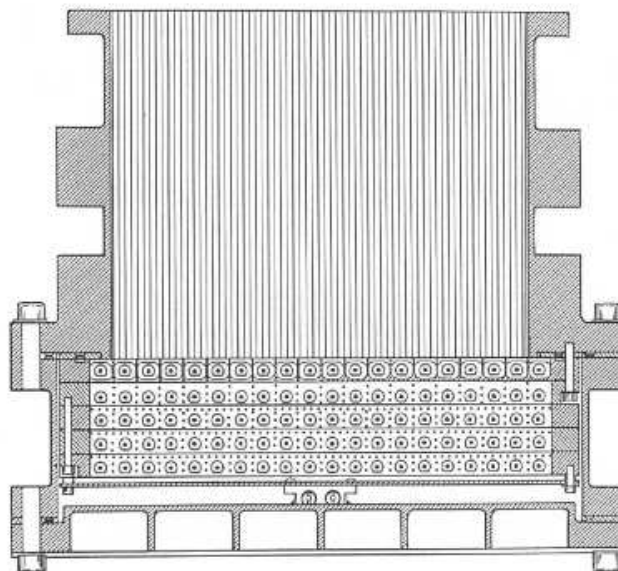


FIG. A.2. Cross section of one PCA detector with FOV defined by the collimator. A Mylar window that is opaque to photons below 2.5 keV was located above and below a propane veto volume. The gas volume was filled with xenon and consisted of three layers of signal anodes and back layer of veto anodes (Jahoda et al., 2006).

should be noted that periodic discharges were found in PCUs 3 and 4 (1996 March) and PCU 1 (1999 March; Jahoda et al., 2006). This issue was circumvented via cycling off and on detectors that broke down by lowering the high voltage of the detector and changing the spacecraft roll angle to increase solar heating of the PCA. In mid-2004, the duty cycles of the five PCUs were as follows: 1.0 (PCU 0), 0.2 (PCU 1), 1.0 (PCU 2), 0.6 (PCU 3) and 0.2 (PCU 4).

As mentioned in Section A.2.1, background subtraction required a detailed model since the PCA was a non-imaging instrument. The components, which included particles from the local environment, radioactivity of the spacecraft and the CXB, were time dependent and were parameterized according to a set of “blank-sky” observations (Jahoda et al., 2006). Two models were used throughout the mission for bright and faint sources,

respectively; where bright was defined to be  $>40 \text{ counts s}^{-1} \text{ PCU}^{-1}$  (Jahoda et al., 2006). In my work on 4U 1210-64, the flux was found to stay mostly below  $40 \text{ counts s}^{-1} \text{ PCU}^{-1}$  (Coley et al., 2014). Therefore, the “faint” model background was generated.

### **A.3.2 *Suzaku***

The *Astro-EII* (*Suzaku*) mission was a joint Japanese-US mission. Launched on 2005 July 10, *Suzaku* was a re-flight of the failed *Astro-E* mission, which was lost on 2000 February 10. Placed in a  $\sim 570 \text{ km}$  near-circular orbit with an inclination angle of  $31^\circ$  and orbital period of 96 minutes, observations were interrupted by the South Atlantic Anomaly (Mitsuda et al., 2007). In the normal mode of operations, *Suzaku* pointed in a single direction for at least 10 ks (1/4 day) with a typical observing efficiency of  $\sim 43\%$ . The Earth further constrains observations, where most targets were occulted for 1/3 of each orbit (Mitsuda et al., 2007), although targets near the poles were observed almost continuously.

Three co-aligned instruments comprised the scientific payload of *Suzaku*. These included the four X-ray imaging telescopes that made the X-ray Imaging Spectrometer (XIS) suite, the collimated Hard X-ray Detector (HXD) and the X-ray Spectrometer (XRS). The XRS, the first orbiting X-ray microcalorimeter, has been inoperable since 2005 August 8 when the liquid helium coolant leaked into space.

**A.3.2.1 X-ray Imaging Spectrometer (XIS)** The *Suzaku* XIS suite (see Figure A.3) consisted of four Wolter-type X-ray imaging telescopes located at the focal plane of a dedicated module of the X-Ray Telescope (XRT). The XIS was each fitted with

a CCD chip covering a region  $17.8 \times 17.8$  (Koyama et al., 2007; Mitsuda et al., 2007; Tatum, 2013). Three of the chips were front-illuminated – XIS-0, XIS-2, and XIS-3. The spectral resolution was moderate where the energy resolution FWHM in the front-illuminated XIS instruments is  $\sim 130$  eV at 6.0 keV. Sensitive to X-rays ranging from 0.6–10 keV, the effective area of the front-illuminated XIS instruments was  $330 \text{ cm}^2$  at 1.5 keV (Mitsuda et al., 2007). XIS-2 failed in late 2006 due to a charge leak. The back-illuminated XIS instrument, XIS-1, was characterized by a greater sensitivity to X-rays in the energy band between 0.2–6 keV. Operating in full window mode, the time resolution of the XIS was 8 s.

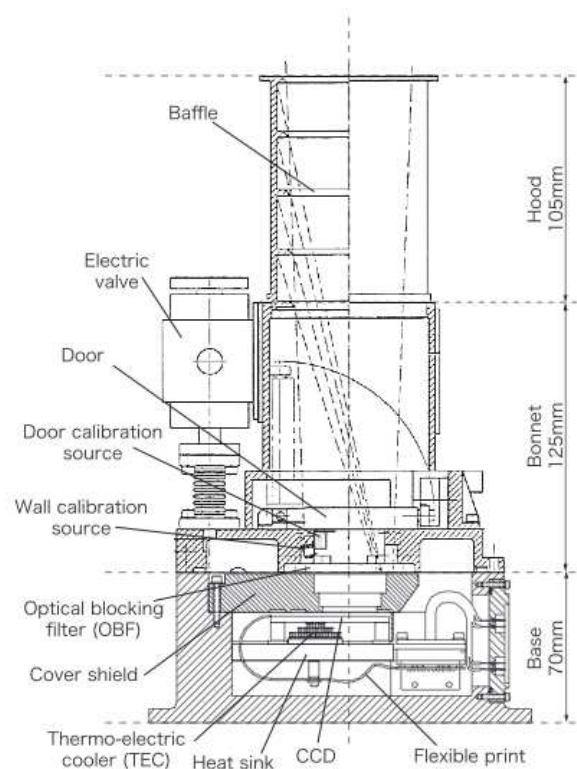


FIG. A.3. This is a cross section of the *Suzaku* XIS, which consists of a CCD and camera body (Koyama et al., 2007).

Each CCD camera used a single CCD chip divided into four segments (segments A, B, C, and D) with an imaging area (IA) of  $1024 \times 1024$  pixels and a shielded frame store area (Koyama et al., 2007; Mitsuda et al., 2007). Since the pixel size was a  $24 \mu\text{m}$  square, the resulting IA is a 25 mm square with a total sky coverage of  $18'$ . The CCDs were sensitive to photons in the optical and ultraviolet energy bands, which were suppressed by optical blocking filters made of polyimide film 20 mm above the IAs (Koyama et al., 2007). Two  $^{55}\text{Fe}$  calibration sources, located on the side walls of the bonnet of the camera, were used for in-flight calibration.

The Non X-ray Background (NXBG) was constructed when the XIS was pointed to the nightside of Earth (Koyama et al., 2007). Since the spacecraft is in low-Earth orbit, the NXBG was fairly low. In the 0.5–10 keV band, the NXBG in the front-illuminated XIS instruments was  $\sim 8 \times 10^{-8}$  counts  $\text{s}^{-1}$   $\text{pix}^{-1}$  (Koyama et al., 2007) and was strongly determined by the geomagnetic cut-off rigidity (COR). Since the background originates from cosmic rays, the COR was measure of the effectiveness of the Earth's geomagnetic field in shield low orbit spacecraft. To achieve an accurate subtraction of the NXBG, the COR distribution of the NXBG had to be the same as that in the source observation (Koyama et al., 2007).

**A.3.2.2 Hard X-ray Detector (HXD)** With a combination of silicon Positive Intrinsic Negative (PIN) diodes and Gadolinium Silicate crystal (GSO) scintillators, the Hard X-ray Detector (HXD) was a collimated, non-imaging instrument that extended the capabilities of the *Suzaku* observatory to energies up to the 600 keV bandpass (Takahashi et al., 2007). Consisting of 16 identical detector units that made up a  $4 \times 4$  matrix, the

HXD was designed to perform observations of X-ray sources with an extremely low in-orbit background and a  $61 \mu\text{s}$  time resolution. The HXD monitored the X-ray sky in the  $\sim 10\text{--}70 \text{ keV}$  bandpass with the PIN diodes and  $\sim 40\text{--}600 \text{ keV}$  with the GSO scintillators. While the field of view and effective area of the HXD was  $34' \times 34'$  and  $\sim 260 \text{ cm}^2$  at energies below  $100 \text{ keV}$ , of interest to this thesis were the PIN diodes, which had an effective area and energy resolution FWHM of  $160 \text{ cm}^2$  and  $3.0 \text{ keV}$ , respectively (Mitsuda et al., 2007; Takahashi et al., 2007). The usable energy range for the PIN diodes was  $\sim 15\text{--}70 \text{ keV}$ .

Each detector unit consisted of 64 PIN diodes that are 2 mm thick, fine collimators made of  $50 \mu\text{m}$  thick phosphor bronze sheets, a photomultiplier, front-end electronics and a phoswich<sup>1</sup> counter made of gadolinium silicate (GSO) and bismuth germanate (BGO) crystals with different rise and decay times of the scintillation light (Takahashi et al., 2007). Collectively these elements made up a well counter unit, where the GSO and BGO crystals were used for detection and shielding, respectively. A novel improvement for HXD is the BGO scintillator was shaped in a well, doubling up as an active collimator and providing efficient shielding for the PIN diodes (Takahashi et al., 2007). Forming a unit of four diodes per phoswich counter, the 64 PIN diodes are placed in front of a GSO crystal and absorb X-rays with energies below  $\sim 70 \text{ keV}$ .

Since the HXD was a scintillation counter, incident X-ray photons were absorbed by scintillation crystals with different rise and decay times of the scintillation light (Takahashi et al., 2007; Kokubun et al., 2007). Not only did a single photomultiplier discriminate between the two types of scintillators, but this particular phoswich combination

---

<sup>1</sup>acronym for PHOSphor sandWICH

provided numerous advantages over those made of NaI/CsI such as a higher stopping power for  $\gamma$ -rays (Takahashi et al., 2007). Fast signal processing was achieved with the fast decay times compared to the conventional NaI/CsI phoswich units (20 ns/1000 ns at 20° C) as well as the number of long-lived  $\gamma$ -rays due to charged particles was smaller than what is seen in other scintillating materials (Takahashi et al., 2007; Kokubun et al., 2007).

In contrast with other scintillation counters such as the *BeppoSAX* PDS and *RXTE* HEXTE instruments, the *Suzaku* HXD did not have rocking capability for on and off source observations and instead required a detailed model to subtract the non-X-ray background (NXB, Kokubun et al., 2007). The NXB primarily consisted of cosmic-ray particles, delayed emission and intrinsic background from radioactive isotopes in the detector itself (Kokubun et al., 2007). The cosmic X-ray background dominated in the  $\sim$ 15–70 keV energy bandpass where the PIN diodes were sensitive and could be reduced with a narrow FOV. Fine collimators inserted in the BGO well-type collimator were used to circumvent the issue. In this work on 4U 1210-64, I modeled the cosmic X-ray background using a simulated CXB spectrum where the parameters were determined by Boldt (1987). This is described in more detail in Chapter 3.

## **A.4 Current Observatories**

### **A.4.1 Monitor of All X-ray Image (MAXI)**

The Monitor of All-sky X-ray Image (MAXI), launched on the Space Shuttle *Endeavour* on 2009 July 16, is the first astronomical payload installed on the Japanese Ex-

periment Module–Exposed Facility (JEM-EF or Kibo-EF; Matsuoka et al., 2009, 2010). MAXI (see Figure A.4), which became operational on 2009 August 3, consists of two types of slit cameras: the Gas Slit Camera (GSC) and the X-ray CCDs onboard the Solid-state Slit Camera (SSC) (Matsuoka et al., 2010). An objective of the MAXI mission pertinent to this work is to monitor the long-term variability of X-ray sources, where the X-ray variability of over 1000 sources is observed over every ISS orbit of approximately 92 minutes (Matsuoka et al., 2010). In this work, I make use of the GSC data that are routinely made available by the MAXI team.

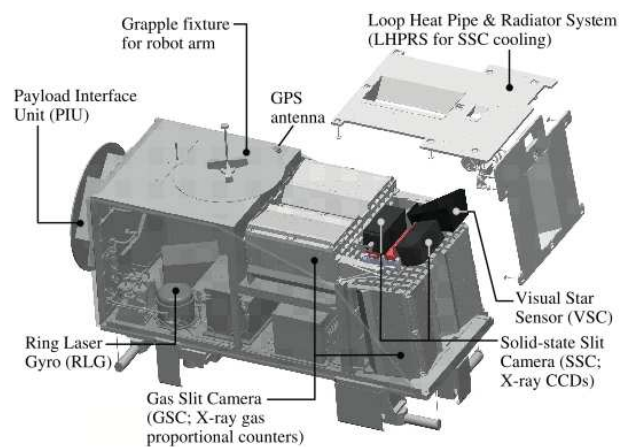


FIG. A.4. Overview of MAXI; major subsystems are indicated (Matsuoka et al., 2009).

Performing as an X-ray ASM where all-sky X-ray images are useful for X-ray variable catalogs, the GSC (see Figure A.4) consists of twelve one-dimensional position sensitive gas proportional counters (PSPC) sensitive to energies in the 0.5–30 keV bandpass with a detection efficiency above 10%. The PSPCs in addition to slit & slat collimators, make six camera units that have a total detection area of 5350 cm<sup>2</sup> (Matsuoka et al., 2009). With a slat collimator response of 3.5° in bottom-to-bottom and slit image corresponding

to  $1.5^\circ$ , the proportional counters are capable of detecting incident X-ray photons from the vertical to the  $\pm 40^\circ$  slant directions. The horizontal and zenith directions are scanned with an overall maximum FOV  $160^\circ \times 3^\circ$ , compensating when the sky is unobservable to one FOV or the other (Matsuoka et al., 2010). Due to the rotation of the ISS, the horizontal GSC is capable of observing the entire sky without Earth occultation (Matsuoka et al., 2009). According to the movement of the ISS, up to 97% of the sky can be scanned every ISS orbit. At the  $5\sigma$  level, the GSC is capable of detecting sources at  $\sim 25$  mCrab for one orbit and  $\sim 8$  mCrab per day (Matsuoka et al., 2010). While the angular resolution FWHM of MAXI is  $1.5^\circ$ , the localization accuracy is up to  $\sim 0.1^\circ$  for bright sources.

#### **A.4.2 *Swift***

Launched 2004 November 20, the *Swift* mission is a low-Earth orbit spacecraft primarily tasked with the study of gamma-ray bursts. *Swift* consists of three instruments: the Burst Alert Telescope (BAT), the X-ray Telescope (XRT) and the Ultraviolet/Optical Telescope (UVOT). In this work, I make use of the BAT and XRT.

**A.4.2.1 Burst Alert Telescope (BAT)** With a broad sky coverage and a large FOV, the *Swift* BAT (see Figure A.5) extends the capabilities of X-ray ASMs into the hard-energy bandpass of 15-150 keV (Barthelmy et al., 2005; Tueller et al., 2010). Operating since 2006 October, the *Swift* BAT observes 80–90% of the sky per day with a sensitivity of 5.3 mCrab per day and a time resolution of 64– $\sim 1000$  s (Krimm et al., 2013). The data produced by BAT have been exploited on different timescales, which make up the BAT hard X-ray survey (Barthelmy et al., 2005; Tueller et al., 2010) made

accessible on the public website<sup>2</sup> and the BAT transient monitor (Krimm et al., 2013), which are available on the NASA website<sup>3</sup>. While the BAT hard X-ray survey is designed for AGN studies combining data covering several years of observation, the BAT transient monitor studies the variability in bright hard X-ray objects in near real time. Of interest to this work are the data from the BAT transient monitor, which covers the 15–50 keV energy band.

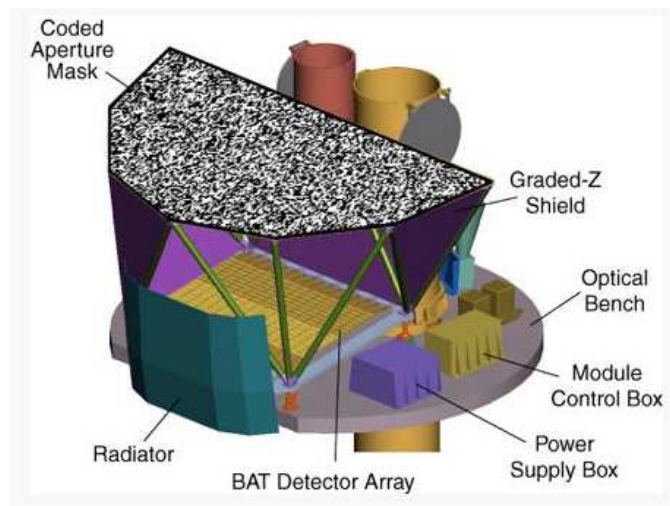


FIG. A.5. BAT cutaway drawing showing the D-shaped coded mask, the CZT array, and the graded-Z shielding. The mask pattern is not to scale (Gehrels et al., 2004)..

The BAT is a coded-mask imager consisting of a detector array of 32,768  $4 \times 4 \times 2$  mm CdZnTe detectors where the detecting area and field of view (FOV) are  $5240 \text{ cm}^2$  and 1.4 sr (half-coded), respectively (Barthelmy et al., 2005). Mounted in a plane 1 m above the detector array, BAT uses a  $2.7 \text{ m}^2$  mask made of 52,000  $5 \times 5 \times 1$  mm lead tiles that do not obscure the detector array over much of the BAT FOV (Barthelmy et al., 2005; Tueller et al., 2010). The partial coding fraction, defined as the fraction of the

<sup>2</sup><http://swift.gsfc.nasa.gov/results/bs70mon/>

<sup>3</sup><http://swift.gsfc.nasa.gov/results/transients/>

array used to make the image in a particular direction, varies across the field of view. The BAT provides an all-sky hard X-ray survey with a sensitivity of  $\sim 1$  mCrab (Tueller et al., 2010). The Crab produces  $\sim 0.045$  counts  $\text{cm}^{-2} \text{s}^{-1}$  over the entire energy band.

The systematic noise in the BAT light curves is estimated using two methods. The first method involves observations of 106 randomly distributed “blank” points in the sky and is used to understand residual systematics in the count distribution from catalog sources (Krimm et al., 2013). Since these “blank points” are chosen to be far from reported X-ray sources (at least 10 arcmin), it is expected that the count rate distribution should follow Gaussian statistics with a mean of zero and a significance histogram width of unity (Krimm et al., 2013). The width of the significance histograms was found to exceed unity with a mean correction of 12.2% for orbital data and 20.5% for daily averages (Krimm et al., 2013). The second source of systematic error was estimated by observing the Crab, where residual scatter was found in the light curves. This was found to have a standard deviation of 3.01% of the Crab trend rate and 1.82% in the trend rate in the daily light curves (Krimm et al., 2013).

**A.4.2.2 X-ray Telescope (XRT)** The X-ray Telescope (XRT) is one of two co-aligned instruments onboard *Swift* (see Figure A.6). Designed to autonomously measure the spectral and temporal variability of gamma-ray bursts (GRBs) and their afterglows with a dynamic range covering seven orders of magnitude of flux (Burrows et al., 2005), the XRT monitors the X-ray sky in the energy bandpass of 0.3–10 keV. The XRT supports four readout modes: the imaging mode, the photodiode (PD) mode, the windowed-timing (WT) mode and photon counting (PC) mode. Of these the WT and PC modes are still

operable, providing a time resolution of 1.8 ms and 2.5 s, respectively. At the time of launch, the energy resolution FWHM in the XRT was  $\sim 140$  eV at 5.9 keV (Burrows et al., 2005).

The *Swift* XRT consists of a grazing Wolter telescope with a focal length of 3.5 m and an effective area of  $110 \text{ cm}^2$  at 1.5 keV, a thermal baffle to prevent thermal gradients that could distort the Point Spread Function (PSF) and a single e2v CCD-22 detector (Gehrels et al., 2004; Burrows et al., 2005). Its primary structural element, the Optical Bench Interface Flange (OBIF), consists of aluminum and provides support for the forward and aft telescope tubes, mirror module, electron deflector and TAM optics and camera (Burrows et al., 2005). The mirror module, built and calibrated for JET-X, has 12 concentric gold-coated electroformed Ni shells with a focal length 3500 mm that are 600 mm long and have diameters ranging from 191–300 mm (Gehrels et al., 2004; Burrows et al., 2005).

Due to the requirements of a rapid response time in the study of gamma-ray bursts, the *Swift* XRT makes autonomous decisions to operate in different readout modes depending on the flux of the source (Hill et al., 2004). The XRT makes use of the windowed timing mode at fluxes below 5000 mCrab, which is a high gain mode used to achieve a temporal resolution of 1.8 ms. This is at the expense of imaging information, which is only preserved in one dimension (Burrows et al., 2005). Pileup is minimal at fluxes below 1000 mCrab. At fluxes below 1 mCrab, the XRT makes use of the photon counting (PC) mode, maintaining full imaging and spectroscopic resolution (Hill et al., 2004; Burrows et al., 2005).

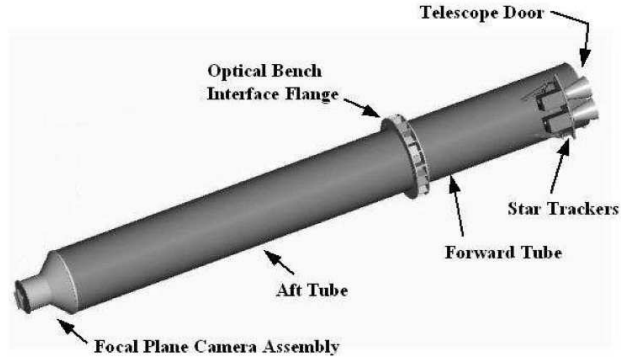


FIG. A.6. XRT design. The telescope focal length is 3.5 m, and the overall instrument length is 4.67 m, with a diameter of 0.51 m.

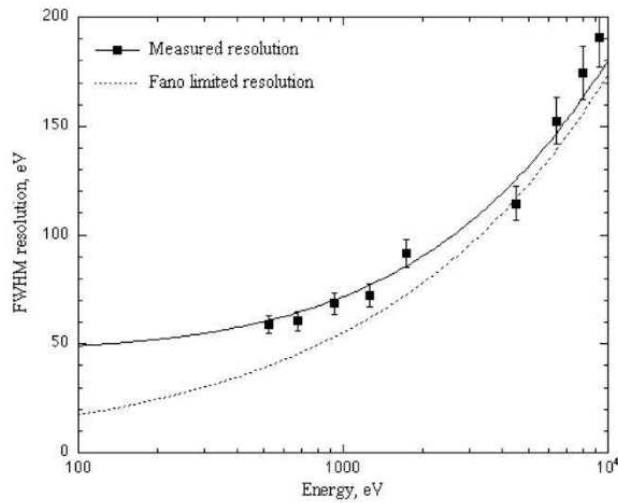


FIG. A.7. CCD-22 energy resolution above 500 eV.

### A.4.3 *Fermi*

The *Fermi Gamma-ray Space Telescope (Fermi)*, formerly known as the *Gamma-ray Large Area Space Telescope (GLAST)*, was launched on 2008 June 11 (MJD 54628) on a Delta II Heavy launch vehicle. Comprising the Large Area Telescope (LAT) and the Gamma-ray Burst Monitor (GBM), *Fermi* has a significant impact on astronomical study particularly in the fields of gamma-ray bursts, AGN, gamma-ray binaries and the search for dark matter. Of interest to this work on gamma-ray binaries is the LAT, which

is sensitive to energies in the 20 MeV–300 GeV bandpass (see Figure A.8).

Extending the capabilities of all-sky monitors to the gamma-ray regime, the *Fermi* LAT builds on the all-sky survey of the Energetic Gamma-Ray Experiment Telescope (EGRET) instrument onboard the *Compton Gamma-Ray Observatory* (Thompson et al., 1993). The *Fermi* LAT primarily operates in a “scanning mode” where its z-axis is pointed in the northern and southern directions every alternate orbit (Atwood et al., 2009). This yields a near uniform sky coverage every 3 hours with a point source sensitivity of  $3 \times 10^{-9}$  photons  $\text{cm}^{-2} \text{s}^{-1}$ . The LAT FOV and effective area at normal incidence are 2.4 sr and 9500  $\text{cm}^2$ , respectively. The on-axis energy resolution at 100 MeV–1 GeV and 1–10 GeV are 9%–15% and 8%–9%, respectively (Atwood et al., 2009).

Since gamma-ray photons cannot be reflected or refracted and instead interact by pair-production, the *Fermi* LAT is a pair-conversion telescope consisting of an  $4 \times 4$  array of 16 modules. The conversion probability is proportional to  $Z^2$ , making tungsten an ideal choice for the thin, high-Z foil. With its precision converter-tracker and calorimeter, *Fermi* LAT monitors the electron-positron pair that results when the photon undergoes pair-production and tracks the trajectory of the resulting particles in the silicon strip detector (SSD, Atwood et al., 2009). The calorimeter modules consists of 96 CsI(Tl) crystals, which have the dual purpose to measure the energy deposition from the electromagnetic particle shower resulting from the  $e^+e^-$  pair and image the shower development profile (Atwood et al., 2009). These are read out by PIN photodiodes, which measure the scintillation light transmitted to each end. The anti-coincidence detector (ACD) is the third LAT subsystem, which is purposed to detect and subsequently reject the charged-particle background (Atwood et al., 2009).

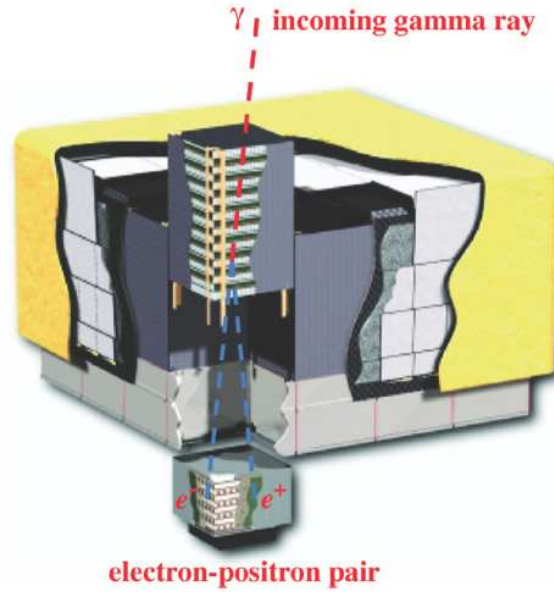


FIG. A.8. Schematic view of the LAT. The telescope's dimensions are  $1.8\text{ m} \times 1.8\text{ m} \times 0.72\text{ m}$ . The power required and the mass are 650 W and 2789 kg, respectively (Atwood et al., 2009)

Compared with the X-ray detectors described above, instrument triggers and down-linked data are initially dominated by background, which must be treated with detailed models (Atwood et al., 2009). These models are based on extensive Monte-Carlo simulations and include gamma-rays originating from the albedo of Earth as well as cosmic rays and other particles that contribute to non-astrophysical signals. Data analysis is made flexible with multiple Instrument Response Functions (IRFs), which are suitable for a variety of different data selection types. The transient class, best suited for transient phenomena such as GRBs, has the largest efficiency but also the highest residual background. Source class provides the best analysis available for localized sources and diffuse gamma-ray emission.

#### A.4.4 *Australia Telescope Compact Array (ATCA)*

The *Australia Telescope Compact Array (ATCA)* is a radio interferometer that is a part of the Australia Telescope National Facility (ATNF) located near Narrabri, Australia; which is 550 km northwest of Sydney (Wilson et al., 2011). Consisting of six identical 22 m dishes, *ATCA* operates in aperture synthesis mode to produce images in the 1.1–3.1 GHz, 4.4–6.7 GHz, 7.5–10.5 GHz, 15–25 GHz, 30–50 GHz and 85–105 GHz bandpasses (see Figure A.9). The Compact Array Broadband Backend (CABB) upgrade improved both the sensitivity and versatility of *ATCA*, where the maximum bandwidth was increased from 128 MHz to 2 GHz. Of interest to this work, I make use of data collected in the 2.1, 5.5, 9.0, 17.0, 19.0, 33.0 and 35.0 GHz bandpasses in the study of 1FGL J1018.6-5856 (see Chapter 4). The extraction and analysis of this data was carried out by Philip Edwards and Jamie Stevens (CSIRO Astronomy and Space Science), I refer the reader to Ackermann et al. (2012) for a more detailed discussion on the instrument.



FIG. A.9. Five of the six identical Cassegrain antennae that comprise the *ATCA* (Wilson et al., 2011).

## Appendix B

# DATA ANALYSIS TECHNIQUES

December 1, 2015

### B.1 Power Spectra Techniques

The Discrete Fourier Transform (DFT) is a discrete superposition of sines and cosines, (see Equation B.1). The DFT is dependent on time stamp,  $t_j$ , and frequency,  $\omega$ .

$$(B.1) \quad X(\omega) = \sum_{j=0}^{N_0} y_j \exp(-i\omega t_j).$$

The square of this quantity at each frequency is a periodogram, also known as a power spectrum. Power spectra are a common tool to search for periodic variability in light curves, which measure the variability of a source over time. The Fourier components, a superposition of sines and cosines, are calculated for each point in the light curve; which in itself is a superposition of a signal and noise. In Fourier space, the dominant term in the power spectra usually corresponds to the frequency of the periodicity (Seward & Charles, 1995). In the case where the error bars are non-uniform, a useful practice

is to weight the data points by their errors. The choice of the appropriate weights is of importance for both the detection and significance levels in periodic variability.

### B.1.1 Semi-Weighted Power Spectra

“Standard weighting” uses a weighting factor of  $y_j/\sigma_j^2$  where each point is weighted according to its contribution to the overall power spectrum (Scargle, 1989; Corbet et al., 2007a,b). This method is advantageous for faint sources and in cases when the scatter in the overall variability is small as was demonstrated in Corbet (2003). It should be noted that when the scatter is large, it is disadvantageous to use the “standard weighting” technique as is described in Corbet et al. (2007b). The data quality could be affected by an artificial periodic or quasi-periodic modulation and spurious signals including the spacecraft precession period could become evident (Corbet, 2003). These complicate the search for periodicity. Two corrections are necessary to circumvent the problem. The first correction requires the variability in the source to be treated as an additional “error”. The estimated variance depends on the difference between the observed variance and the mean square of the error bar sizes (see Equation B.2).

$$(B.2) \quad V_s = \sum_{j=0}^N \frac{\bar{y} - y_j}{(N - 1)} - \sum_{j=0}^N \frac{(f\sigma_j)^2}{N}$$

A second correction factor,  $f$ , involves corrections to the size of the individual error bars, which could be derived from tests where the  $\chi^2$ -value for constant count rate is expected to be unity (Corbet et al., 2007a,b). Sources that can be studied for this test include supernova remnants and galaxy clusters. In the case of early *Swift* BAT, the correction factor is set to 1.2 (Corbet et al., 2007b). This is termed semi-weighting (see

Equation B.3) and is analogous to the semi-weighted mean as outlined in Cochran (1937).

$$(B.3) \quad \frac{y_i - \bar{y}}{(f\sigma_j)^2 + V_s}$$

### B.1.2 Exposure-Weighted Power-Spectra

The choice of the appropriate weights in power spectra is also complicated in the case of *Fermi* LAT. The light curves in my aperture photometry analysis have a bin size of 600 s, which is significantly shorter than the 3 hr survey rocking period of the spacecraft (see Appendix A.4.3 for more information). This is further complicated by a small number of photons in a time bin, which could result in variations in the weighting for bins with the same exposure (Fermi LAT Collaboration et al., 2009). To circumvent the issue, weighting factors based on the relative exposure of the time bins are generally chosen as was demonstrated in Fermi LAT Collaboration et al. (2009). This is based on the mean count rate of all bins and the number of counts expected in each bin,  $N_{\text{pred}}$ , (see Equation B.4).

$$(B.4) \quad \frac{y_i - \bar{y}}{N_{\text{pred}}}$$

## B.2 Probability Based Aperture Photometry

As noted in Section A.4.3, background that could be attributed to a number of Galactic and extragalactic sources dominates *Fermi* LAT, which could possibly obscure periodic emission on different timescales (Atwood et al., 2009). This also affects the point spread function (PSF), which varies by more than two orders of magnitude between 100 MeV and 100 GeV. Background photons at low-energy as a result dominate

those emitted at higher energies, which reduces the signal-to-noise of aperture photometry based on the summation of photons alone (Kerr, 2011). In this work, a weighted photon technique where the probabilities that a photon came from the source of interest are summed is implemented to maximize the signal-to-noise and allow the use of short time bins. I calculated the probability that a photon originated from the source of interest using `gtsrcprob` based on the fluxes and spectral models of the 2FGL and 3FGL catalogs (Ackermann et al., 2012).

## Bibliography

- Abdo, A. A., Ackermann, M., Ajello, M., et al. 2009, *ApJ*, 706, L56
- Ackermann, M., Ajello, M., Ballet, J., et al. 2012, *Science*, 335, 189
- Ackermann, M., Ajello, M., Ballet, J., et al. 2013, *ApJ*, 773, L35
- Adams, W. S. 1914, *PASP*, 26, 198
- Aharonian, F., Akhperjanian, A. G., Aye, K.-M., et al. 2005, *A&A*, 442, 1
- Allen, K. W. 2000, *Astrophysical quantities*, 4th ed., by Allen, K. W. Humanities Press Inc. NJ, ISBN O-485-11150-0
- An, H., Dufour, F., Kaspi, V. M., & Harrison, F. A. 2013, *ApJ*, 775, 135
- An, H., Bellm, E., Bhalerao, V., et al. 2015, *ApJ*, 806, 166
- Araya-Góchez, R. A., & Harding, A. K. 2000, *ApJ*, 544, 1067
- Arons, J., & Lea, S. M. 1980, *ApJ*, 235, 1016
- Arons, J., Klein, R. I., & Lea, S. M. 1987, *ApJ*, 312, 666
- Ash, T. D. C., Reynolds, A. P., Roche, P., et al. 1999, *MNRAS*, 307, 357

- Atwood, W. B., Abdo, A. A., Ackermann, M., et al. 2009, *ApJ*, 697, 1071
- Audley, M. D., Nagase, F., Mitsuda, K., Angelini, L., & Kelley, R. L. 2006, *MNRAS*, 367, 1147
- Augello, G., Iaria, R., Robba, N. R., et al. 2003, *ApJ*, 596, L63
- Baade, W., & Zwicky, F. 1934, *Physical Review*, 46, 76
- Balucinska-Church, M., & McCammon, D. 1992, *ApJ*, 400, 699
- Barlow, E. J., Knigge, C., Bird, A. J., et al. 2006, *MNRAS*, 372, 224
- Barthelmy, S. D., Barbier, L. M., Cummings, J. R., et al. 2005, *Space Sci. Rev.*, 120, 143
- Bartlett, E. S., Coe, M. J., & Ho, W. C. G. 2013, *MNRAS*, 436, 2054
- Basko, M. M., & Sunyaev, R. A. 1976, *MNRAS*, 175, 395
- Basko, M. M. 1980, *A&A*, 87, 330
- Becker, P. A., & Wolff, M. T. 2005, *ApJ*, 621, L45
- Becker, P. A., & Wolff, M. T. 2007, *ApJ*, 654, 435
- Becker, P. A., Klochkov, D., Schönherr, G., et al. 2012, *A&A*, 544, A123
- Bessell, M. S. 1979, *PASP*, 91, 589
- Bevington, P. R., & Robinson, D. K. 2003, *Data reduction and error analysis for the physical sciences*, 3rd ed., by Philip R. Bevington, and Keith D. Robinson. Boston, MA: McGraw-Hill, ISBN 0-07-247227-8, 2003.

- Bird, A. J., Bazzano, A., Bassani, L., et al. 2010, *ApJS*, 186, 1
- Blondin, J. M., Kallman, T. R., Fryxell, B. A., & Taam, R. E. 1990, *ApJ*, 356, 591
- Blondin, J. M., & Owen, M. P. 1997, *IAU Colloq. 163: Accretion Phenomena and Related Outflows*, 121, 361
- Bodaghee, A., Walter, R., Zurita Heras, J. A., et al. 2006, *A&A*, 447, 1027
- Bodaghee, A., Tomsick, J. A., Rodriguez, J., et al. 2010, *ApJ*, 719, 451
- Bodaghee, A., Tomsick, J. A., Rodriguez, J., et al. 2011, *ApJ*, 727, 59
- Bodaghee, A., Rahoui, F., Tomsick, J. A., & Rodriguez, J. 2012, *ApJ*, 751, 113
- Boldt, E. 1987, *Observational Cosmology*, 124, 611
- Bondi, H., & Hoyle, F. 1944, *MNRAS*, 104, 273
- Bowers, R. L., & Deeming, T. 1984, *Astrophysics. Vol. I: Stars*. Jones and Bartlett Publishers, Inc., 20 Park Plaza, Boston, Mass. 02116, USA. Vol. I: 344 pp. ISBN 0-86720-018-9 (Vol. I)
- Boyd, P. T., & Smale, A. P. 2004, *ApJ*, 612, 1006
- Boyle, W. and Smith, G. 1970 *Bell. Sys. Tech. J.* 49, 587
- Bozzo, E., Falanga, M., & Stella, L. 2008, *ApJ*, 683, 1031
- Bozzo, E., Stella, L., Israel, G., Falanga, M., & Campana, S. 2009, in *AIP Conf. Ser.* 1126, *Simbol-X: Focusing on the Hard X-Ray Universe: Proc. of 2nd International Simbol-X Symp*, ed. J. Rodriguez P. Ferrando, 319

- Bradt, H. V. D., & McClintock, J. E. 1983, ARA&A, 21, 13
- Brandt, N., & Podsiadlowski, P. 1995, MNRAS, 274, 461
- Brunschweiler, J., Greiner, J., Ajello, M., & Osborne, J. 2009, A&A, 496, 121
- Burrows, D. N., Hill, J. E., Nousek, J. A., et al. 2005, Space Sci. Rev., 120, 165
- Capalbi, M., Perri, M., Saija, B., Tamburelli, F., & Angelini, L. 2005, The Swift XRT Data Reduction Guide, Technical Report 1.2, [http://swift.gsfc.nasa.gov/analysis/xrt\\_swguide\\_v1\\_2.pdf](http://swift.gsfc.nasa.gov/analysis/xrt_swguide_v1_2.pdf)
- Carroll, B. W., & Ostlie, D. A. 2006; An Introduction to Modern Stellar Astrophysics. Institute for Mathematics and Its Applications; Weber State University, Inc.; Addison-Wesley Publishing Company; Reading, Massachusetts, A17
- Casares, J., Ribó, M., Ribas, I., et al. 2005, MNRAS, 364, 899
- Castor, J. I., Abbott, D. C., & Klein, R. I. 1975, ApJ, 195, 157
- Chakrabarty, D. 1996, Ph.D. Thesis, California Institute of Technology.
- Chandrasekhar, S. 1931, ApJ, 74, 81
- Chaty, S., Rahoui, F., Foellmi, C., et al. 2008, A&A, 484, 783
- Chaty, S. 2011, Evolution of Compact Binaries, eds. L. Schmidtobreick, M. R. Schreiber, C. Tappert, ASP Conf. Ser., 447, 29
- Chaty, S. 2013, Advances in Space Research, 52, 2132

- Clark, G. W., Minato, J. R., & Mi, G. 1988, ApJ, 324, 974
- Clarkson, W. I., Charles, P. A., Coe, M. J., et al. 2003, MNRAS, 339, 447
- Coburn, W., Heindl, W. A., Rothschild, R. E., et al. 2002, ApJ, 580, 394
- Cochran, W. G. 1937, Supplement to the Journal of the Royal Statistical Society, 4, 102
- Coleiro, A., & Chaty, S. 2013, ApJ, 764, 185
- Coleiro, A., Chaty, S., Zurita Heras, J. A., Rahoui, F., & Tomsick, J. A. 2013, A&A, 560, A108
- Coley, J. B., Corbet, R. H. D., Mukai, K., & Pottschmidt, K. 2014, ApJ, 793, 77
- Coley, J. B., Corbet, R. H. D., & Krimm, H. A. 2015, ApJ, 808, 140
- Cooke, B. A., Pounds, K. A., Stewardson, E. A., & Adams, D. J. 1967, ApJ, 150, L189
- Corbet, R. H. D. 1984, A&A, 141, 91
- Corbet, R. H. D. 1986, MNRAS, 220, 1047
- Corbet, R. H. D., Marshall, F. E., Peele, A. G., & Takeshima, T. 1999, ApJ, 517, 956
- Corbet, R. H. D., & Mukai, K. 2002, ApJ, 577, 923
- Corbet, R. H. D. 2003, ApJ, 595, 1086
- Corbet, R., Barbier, L., Barthelmy, S., et al. 2006, The Astronomer's Telegram, 779, 1
- Corbet, R., Markwardt, C., Barbier, L., et al. 2007a, Progress of Theoretical Physics Supplement, 169, 200

- Corbet, R. H. D., Markwardt, C. B., & Tueller, J. 2007b, *ApJ*, 655, 458
- Corbet, R. H. D., Sokoloski, J. L., Mukai, K., Markwardt, C. B., & Tueller, J. 2008, *ApJ*, 675, 1424
- Corbet, R. H. D., & Mukai, K. 2008, *The Astronomer's Telegram*, 1861, 1
- Corbet, R. H. D., Krimm, H. A., Barthelmy, S. D., et al. 2010, *The Astronomer's Telegram*, 2570, 1
- Corbet, R. H. D., Cheung, C. C., Kerr, M., et al. 2011, *The Astronomer's Telegram*, 3221, 1
- Corbet, R. H. D., & Krimm, H. A. 2013, *ApJ*, 778, 45
- Coti Zelati, F., Campana, S., D'Avanzo, P., & Melandri, A. 2014, *MNRAS*, 438, 2634
- Cusumano, G., La Parola, V., Segreto, A., et al. 2010, *A&A*, 510, A48
- Davis, J. E. 2001, *ApJ*, 562, 575
- Day, C. S. R., & Stevens, I. R. 1993, *ApJ*, 403, 322
- Day, C. S. R., & Tennant, A. F. 1991, *MNRAS*, 251, 76
- Demorest, P. B., et al. 2010, *Nature*, 467, 1081
- de Val-Borro, M., Karovska, M., & Sasselov, D. 2009, *ApJ*, 700, 1148
- Dickey, J. M., & Lockman, F. J. 1990, *ARA&A*, 28, 215
- Doroshenko, V., Santangelo, A., Nakahira, S., et al. 2013, *A&A*, 554, A37

- Drave, S. P., Bird, A. J., Sidoli, L., et al. 2013a, MNRAS, 433, 528
- Drave, S. P., Bird, A. J., Goossens, M. E., et al. 2013b, The Astronomer's Telegram, 5131,  
1
- Dubus, G. 2006, A&A, 456, 801
- Dubus, G., Cerutti, B., & Henri, G. 2010b, MNRAS, 404, L55
- Dubus, G. 2013, A&ARv, 21, 64
- Dunn, R. J. H., Fender, R. P., Körding, E. G., Belloni, T., & Cabanac, C. 2010, MNRAS,  
403, 61
- Ebisawa, K., Day, C. S. R., Kallman, T. R., et al. 1996, PASJ, 48, 425
- Eggleton, P. P. 1983, ApJ, 268, 368
- Elvis, M., Plummer, D., Schachter, J., & Fabbiano, G. 1992, ApJS, 80, 257
- Esposito, P., Caraveo, P. A., Pellizzoni, A., et al. 2007, A&A, 474, 575
- Falanga, M., Bozzo, E., Lutovinov, A., et al. 2015, A&A, 577, A130
- Fano, U. 1947, Phys. Rev. 72, 26
- Farrell, S. A., Sood, R. K., O'Neill, P. M., & Dieters, S. 2008, MNRAS, 389, 608
- Feldmeier, A., Anzer, U., Boerner, G., & Nagase, F. 1996, A&A, 311, 793
- Fermi LAT Collaboration, Abdo, A. A., Ackermann, M., et al. 2009, Science, 326, 1512
- Forman, W., Jones, C., Cominsky, L., et al. 1978, ApJS, 38, 357

- Foster, A. R., Ji, L., Smith, R. K., & Brickhouse, N. S. 2012, ApJ, 756, 128
- Fowler, R. H. 1926, MNRAS, 87, 114
- Frank, J., King, A., & Raine, D. 1992, Accretion Power in Astrophysics, Cambridge, UK,  
2nd edition
- Fraser, G. W. 2009, X-ray Detectors in Astronomy, by G. W. Fraser, Cambridge, UK:  
Cambridge University Press, 2009,
- Fürst F., 2011, Ph.D. thesis, Friedrich-Alexander-Universität Erlangen-Nürnberg
- Gaensler, B. M., & Slane, P. O. 2006, AR&A, 44, 17
- Gehrels, N., Chincarini, G., Giommi, P., et al. 2004, ApJ, 611, 1005
- Giacconi, R., Gursky, H., Paolini, F. R., & Rossi, B. B. 1962, Physical Review Letters, 9,  
439
- Goldstein, G., Huenemoerder, D. P., & Blank, D. 2004, AJ, 127, 2310
- González-Galán, A. 2015, arXiv:1503.01087
- Goossens, M. E., Bird, A. J., Drave, S. P., et al. 2013, MNRAS, 434, 2182
- Götz, O., Mereghetti, S., Hurley, K., et al. 2007, ESA Special Publication, 622, 533
- Gray, R. O., & Corbally, C., J. 2009, Stellar Spectral Classification by Richard O. Gray  
and Christopher J. Corbally. Princeton University Press, 2009. ISBN: 978-0-691-  
12511-4

- Gregory, P. C. 2002, *ApJ*, 575, 427
- Griffiths, D. J. 1995, *Introduction to quantum mechanics/ David J. Griffiths*. Englewood Cliffs, N.J.: Prentice Hall, c1995.
- Grinberg, V., Hell, N., Pottschmidt, K., et al. 2013, *A&A*, 554, A88
- Güver, T., Oumlzel, F. 2009, *MNRAS*, 400, 2050
- Hanke, M., Wilms, J., Nowak, M. A., et al. 2009, *ApJ*, 690, 330
- Haberl, F., Eger, P., & Pietsch, W. 2008, *A&A*, 489, 327
- Haensel, P., Potekhin, A. Y., & Yakovlev, D. G. 2007, *Astrophysics and Space Science Library*, 326,
- Halpern, J. P., & Holt, S. S. 1992, *Nature*, 357, 222
- Harris, T.J. & Mathieson, E. 1971, *Nucl. Instr. Meth.* 96, 397
- Harrison, F. A., Craig, W. W., Christensen, F. E., et al. 2013, *ApJ*, 770, 103
- Hertzsprung, E. 1915, *ApJ*, 42, 111
- H. E. S. S. Collaboration, Abramowski, A., Aharonian, F., et al. 2015, *A&A*, 577, A131
- Hewish, A., Bell, S. J., Pilkington, J. D. H., Scott, P. F., & Collins, R. A. 1968, *Nature*, 217, 709
- Hickox, R. C., Narayan, R., & Kallman, T. R. 2004, *ApJ*, 614, 881
- Hill, A. B., Walter, R., Knigge, C., et al. 2005, *A&A*, 439, 255

- Hill, A. B., Dubois, R., Torres, D. F., & Fermi LAT Collaboration 2011, Proceedings of the First Session of the Sant Cugat Forum on Astrophysics, Astrophysics and Space Science Proceedings, ISBN 978-3-642-17250-2. Springer-Verlag Berlin Heidelberg, 2011, p.498
- Hill, J. E., Burrows, D. N., Nousek, J. A., et al. 2004, Proc. SPIE, 5165, 217
- Hjalmarsson, L., Zdziarski, A. A., Szostek, A., & Hannikainen, D. C. 2009, MNRAS, 392, 251
- Horne, J. H., & Baliunas, S. L. 1986, ApJ, 302, 757
- Hung, L.-W., Hickox, R. C., Boroson, B. S., & Vrtilik, S. D. 2010, ApJ, 720, 1202
- Iaria, R., Di Salvo, T., Robba, N. R., et al. 2004, ApJ, 600, 358
- Islam, N., Maitra, C., Pradhan, P., & Paul, B. 2015, MNRAS, 446, 4148
- Islam, N., & Paul, B. 2014, MNRAS, 441, 2539
- Jahoda, K., Markwardt, C. B., Radeva, Y., et al. 2006, ApJS, 163, 401
- Jain, C., Paul, B., & Dutta, A. 2009a, MNRAS, 397, L11
- Jain, C., Paul, B., & Dutta, A. 2009b, Research in Astronomy and Astrophysics, 9, 1303
- Johnston, S., Manchester, R. N., Lyne, A. G., Nicastro, L., & Spyromilio, J. 1994, MNRAS, 268, 430
- Joss, P. C., & Rappaport, S. A. 1984, ARA&A, 22, 537

- Kaastra, J. S., & Mewe, R. 1993, *A&As*, 97, 443
- Kalberla, P. M. W., Burton, W. B., Hartmann, D., et al. 2005, *A&A*, 440, 775
- Kaper, L., van der Meer, A., & Tijani, A. H. 2004, *Revista Mexicana de Astronomia y Astrofisica Conference Series*, 21, 128
- Kaper, L., van der Meer, A., van Kerkwijk, M., & van den Heuvel, E. 2006, *The Messenger*, 126, 27
- Karttunen, H., Krüger, P., Oja, H., Poutanen, M., & Donner, K. J. 2007, *Fundamental Astronomy*, Edited by H. Karttunen, P. Krüger, H. Oja, M. Poutanen, and K.J. Donner. Berlin: Springer, 2007. ISBN: 978-3-540-34143-7
- Kerr, M. 2011, *ApJ*, 732, 38
- Kirkpatrick, J. D. 2005, *ARA&A*, 43, 195
- Kishishita, T., Tanaka, T., Uchiyama, Y., & Takahashi, T. 2009, *ApJ*, 697, L1
- Kokubun, M., Makishima, K., Takahashi, T., et al. 2007, *PASJ*, 59, 53
- Kotze, M. M., & Charles, P. A. 2012, *MNRAS*, 420, 1575
- Kouveliotou, C., Dieters, S., Strohmayer, T., et al. 1998, *Nature*, 393, 235
- Koyama, K., Tsunemi, H., Dotani, T., et al. 2007, *PASJ*, 59, 23
- Kraus, U., Nollert, H.-P., Ruder, H., & Riffert, H. 1995, *ApJ*, 450, 763
- Kraus, U., Zahn, C., Weth, C., & Ruder, H. 2003, *ApJ*, 590, 424

- Krimm, H. A., Holland, S. T., Corbet, R. H. D., et al. 2013, *ApJS*, 209, 14
- Kuranov, A. G., & Postnov, K. A. 2015, *Astronomy Letters*, 41, 114
- Kuulkers, E. 2005, *Interacting Binaries: Accretion, Evolution, and Outcomes*, 797, 402
- Lada, C. J. 2006, *ApJ*, 640, L63
- Lattimer, J. M., & Prakash, M. 2004, *Science*, 304, 536
- Lattimer, J. M. 2012, *Annual Review of Nuclear and Particle Science*, 62, 485
- Lefever, K., Puls, J., & Aerts, C. 2007, *A&A*, 463, 1093
- Levine, A. M., Bradt, H., Cui, W., et al. 1996, *ApJ*, 469, L33
- Levine, A. M., Rappaport, S. A., & Zojcheski, G. 2000, *ApJ*, 541, 194
- Levine, A. M., Bradt, H. V., Chakrabarty, D., Corbet, R. H. D., & Harris, R. J. 2011, *ApJS*, 196, 6
- Li, J., Torres, D. F., Chen, Y., et al. 2011, *ApJ*, 738, LL31
- Li, J., Torres, D. F., & Zhang, S. 2014, *ApJ*, 785, L19
- Li, Z., & Han, Z. 2008, *ApJ*, 685, 225
- Liedahl, D. A., & Paerels, F. 1996, *ApJ*, 468, L33
- Liu, Q. Z., van Paradijs, J., & van den Heuvel, E. P. J. 2000, *A&A*, 147, 25
- Lutovinov, A., Revnivtsev, M., Gilfanov, M., et al. 2005, *A&A*, 444, 821

- Maccarone, T. J., Girard, T. M., & Casetti-Dinescu, D. I. 2014, MNRAS, 440, 1626
- Maitra, C., & Paul, B. 2013, ApJ, 771, 96
- Makishima, K. 2010, The Energetic Cosmos: from Suzaku to ASTRO-H. Proceedings of the 3rd Suzaku Conference, 29 June-2 July, 2009, Otaru, Japan. JAXA Special Publication JAXA-SP-09-008E, ISSN 1349-113X. Edited by K. Makishima, pp.2-5
- Manchester, R. N., Hobbs, G. B., Teoh, A., & Hobbs, M. 2005, AJ, 129, 1993
- Marshall, F. E., Gotthelf, E. V., Zhang, W., Middleditch, J., & Wang, Q. D. 1998, ApJ, 499, L179
- Martins, F., Schaerer, D., & Hillier, D. J. 2005, A&A, 436, 1049
- Martins, F., & Plez, B. 2006, A&A, 457, 637
- Masetti, N., Mason, E., Morelli, L., et al. 2008, A&A, 482, 113
- Masetti, N., Parisi, P., Palazzi, E., et al. 2009, A&A, 495, 121
- Masetti, N., et al. 2010, ApJ, 511, A48
- Mason, A. B., Norton, A. J., Clark, J. S., Negueruela, I., & Roche, P. 2010, A&A, 509, A79
- Mason, A. B., Norton, A. J., Clark, J. S., Negueruela, I., & Roche, P. 2011, A&A, 532, A124
- Mason, I. M., & Culhane, J. L. 1983, IEEE Transactions on Nuclear Science, 30, 485

- Massa, D., Prinja, R. K., & Fullerton, A. W. 1995, *ApJ*, 452, 842
- Matsuoka, M., & Asai, K. 2013, *PASJ*, 65, 26
- Matsuoka, M., Kawasaki, K., Ueno, S., et al. 2009, *PASJ*, 61, 999
- Matsuoka, M., Mihara, T., Sugizaki, M., et al. 2010, *Proc. SPIE*, 7732, 77320Y
- McSwain, M. V., Gies, D. R., Huang, W., et al. 2004, *ApJ*, 600, 927
- Meszáros, P. 1984, *Space Sci. Rev.*, 38, 325
- Meurs, E. J. A., & van den Heuvel, E. P. J. 1989, *A&A*, 226, 88
- Mirabel, I. F. 2012, *Science*, 335, 175
- Mitsuda, K., Bautz, M., Inoue, H., et al. 2007, *PASJ*, 59, 1
- Molkov, S., Mowlavi, N., Goldwurm, A., et al. 2003, *The Astronomer's Telegram*, 176, 1
- Naik, S., Paul, B., & Ali, Z. 2011, *ApJ*, 737, 79
- Naik, S., & Paul, B. 2012, *Bulletin of the Astronomical Society of India*, 40, 503
- Negueruela, I. 1998, *A&A*, 338, 505
- Negueruela, I., Casares, J., Verrecchia, F., et al. 2008, *The Astronomer's Telegram*, 1876,

1

1

- Nespoli, E., Fabregat, J., & Mennickent, R. E. 2008, *A&A*, 486, 911
- Nespoli, E., Reig, P., & Zezas, A. 2012, *A&A*, 547, A103
- Nowak, M. A. 2006, VI Microquasar Workshop: Microquasars and Beyond, ed. B. Tomaso (POS), 1.1
- Nowak, M. A., Hanke, M., Trowbridge, S. N., et al. 2011, *ApJ*, 728, 13
- Ogilvie, G. I., & Dubus, G. 2001, *MNRAS*, 320, 485
- Oppenheimer, J. R., & Volkoff, G. M. 1939, *Physical Review*, 55, 374
- Pacini, F. 1967, *Nature*, 216, 567
- Paczyński, B. 1971, *ARA&A*, 9, 183
- Petterson, J. A. 1977, *ApJ*, 218, 783
- Postnov, K., Shakura, N., Staubert, R., et al. 2013, *MNRAS*, 435, 1147
- Pradhan, A. K., & Nahar, S. N. 2011, *Atomic Astrophysics and Spectroscopy*, Cambridge University Press, Cambridge, UK
- Predehl, P., & Schmitt, J. H. M. M. 1995, *A&A*, 293, 889
- Pringle, J. E. 1996, *MNRAS*, 281, 357
- Rahoui, F., Chaty, S., Lagage, P.-O., & Pantin, E. 2008, *A&A*, 484, 801
- Raichur, H., & Paul, B. 2010, *MNRAS*, 401, 1532
- Rajoelimanana, A. F., Charles, P. A., & Udalski, A. 2011, *MNRAS*, 413, 1600

- Rappaport, S. A., & Joss, P. C. 1983, *Accretion-Driven Stellar X-ray Sources*, eds. W. H. G. Lewin & E. P. J. van den Heuvel, 13
- Ray, P. S., & Chakrabarty, D. 2002, *ApJ*, 581, 1293
- Reifenstein, E. C., Brundage, W. D., & Staelin, D. H. 1969, *Physical Review Letters*, 22, 311
- Reig, P. 2011, *ApSS*, 332, 1
- Reig, P., & Nespoli, E. 2013, *A&A*, 551, A1
- Reig, P., Słowikowska, A., Zezas, A., & Blay, P. 2010, *MNRAS*, 401, 55
- Remillard, R. A., & Levine, A. M. 1997, *All-Sky X-Ray Observations in the Next Decade*, ed. M. Matsuoka N. Kawai (Japan: RIKEN), 29
- Revnivtsev, M., Sunyaev, R., Lutovinov, A., & Sazonov, S. 2007, *The Astronomer's Telegram*, 1253, 1
- Revnivtsev, M., Sazonov, S., Krivonos, R., Ritter, H., & Sunyaev, R. 2008, *A&A*, 489, 1121
- Reynolds, A. P., Parmar, A. N., Hakala, P. J., et al. 1999, *A&As*, 134, 287
- Ribó, M., Paredes, J. M., & Martí, J. 1999, *New Astron. Rev.*, 43, 545
- Rieke, G. H., & Lebofsky, M. J. 1985, *ApJ*, 288, 618
- Romano, P., Mereghetti, S., Sidoli, L., & Evans, P. A. 2008, *The Astronomer's Telegram*, 1875, 1

- Romano, P., Sidoli, L., Cusumano, G., et al. 2009, MNRAS, 399, 2021
- Romano, P., Mangano, V., Ducci, L., et al. 2012, MNRAS, 419, 2695
- Rubin, B. C., Finger, M. H., Harmon, B. A., et al. 1996, ApJ, 459, 259
- Rybicki, G. B., & Lightman, A. P. 1986, Radiative Processes in Astrophysics, by George B. Rybicki, Alan P. Lightman, pp. 400. ISBN 0-471-82759-2. Wiley-VCH
- Sakurai, S., Torii, S., Noda, H., et al. 2014, PASJ, 66, 10
- Sasano, M., Makishima, K., Sakurai, S., Zhang, Z., & Enoto, T. 2014, PASJ, 66, 35
- Scargle, J. D. 1982, ApJ, 263, 835
- Scargle, J. D. 1989, ApJ, 343, 874
- Schönherr, G., Wilms, J., Kretschmar, P., et al. 2007, A&A, 472, 353
- Schuler, S. C., King, J. R., & The, L.-S. 2009, ApJ, 701, 837
- Schulz, N. S., Canizares, C. R., Lee, J. C., & Sako, M. 2002, ApJ, 564, L21
- Seward, F. D., & Charles, P. A. 1995, Exploring the X-Ray Universe, by Frederick D. Seward and Philip A. Charles, pp. 414. ISBN 0521437121. Cambridge, UK: Cambridge University Press, November 1995.
- Shakura, N. I., & Sunyaev, R. A. 1973, A&A, 24, 337
- Shklovskii, I. S. 1967, Astron. Zhur, 44, 930
- Sidoli, L., Esposito, P., Sguera, V., et al. 2013, MNRAS, 429, 2763

- Sidoli, L., Mereghetti, S., Sguera, V., & Pizzolato, F. 2012, MNRAS, 420, 554
- Silaj, J., Jones, C. E., Tycner, C., Sigut, T. A. A., & Smith, A. D. 2010, ApJS, 187, 228
- Smith, G. C. Fischer, J. and Radeka, V. 1984, IEEE Trans. Nucl. Sci., NS-31, 111
- Staubert, R., Klochkov, D., Wilms, J., et al. 2014, A&A, 572, A119
- Suchy, S., Pottschmidt, K., Wilms, J., et al. 2008, ApJ, 675, 1487
- Sugizaki, M., Mitsuda, K., Kaneda, H., et al. 2001, ApJS, 134, 77
- Takahashi, T., Abe, K., Endo, M., et al. 2007, PASJ, 59, 35
- Takahashi, T., Kishishita, T., Uchiyama, Y., et al. 2009, ApJ, 697, 592
- Tatum, M. M. 2013, Ph.D. Thesis, University of Maryland Baltimore County
- Thompson, D. J., Bertsch, D. L., Fichtel, C. E., et al. 1993, ApJS, 86, 629
- Thompson, T. W. J., Tomsick, J. A., Rothschild, R. E., in't Zand, J. J. M., & Walter, R.  
2006, ApJ, 649, 373
- Tomsick, J. A., Lingenfelter, R., Corbel, S., Goldwurm, A., & Kaaret, P. 2004, The Astronomer's Telegram, 224, 1
- Tomsick, J. A., Chaty, S., Rodriguez, J., et al. 2009, ApJ, 694, 344
- Torrejón, J. M., Negueruela, I., Smith, D. M., & Harrison, T. E. 2010, A&A, 510, A61
- Trowbridge, S., Nowak, M. A., & Wilms, J. 2007, ApJ, 670, 624
- Tueller, J., Baumgartner, W. H., Markwardt, C. B., et al. 2010, ApJS, 186, 378

- Ubertini, P., Lebrun, F., Di Cocco, G., et al. 2003, *A&A*, 411, L131
- Val Baker, A. K. F., Norton, A. J., & Quaintrell, H. 2005, *A&A*, 441, 685
- van der Klis, M., & Bonnet-Bidaud, J. M. 1984, *A&A*, 135, 155
- van der Meer, A., Kaper, L., di Salvo, T., et al. 2005, *A&A*, 432, 999
- Vaughan, S. 2005, *A&A*, 431, 391
- Verrecchia, F., Negueruela, I., Covino, S., & Israel, G. 2002, *The Astronomer's Telegram*, 102, 1
- Verrecchia, F., in't Zand, J. J. M., Giommi, P., et al. 2007, *A&A*, 472, 705
- Vrtilek, S. D., Raymond, J. C., Boroson, B., et al. 2001, *ApJ*, 563, L139
- Waisberg, I. R., & Romani, R. W. 2015, *ApJ*, 805, 18
- Walborn, N. R. 1971, *ApJS*, 23, 257
- Walter, R., Zurita Heras, J., Bassani, L., et al. 2006, *A&A*, 453, 133
- Wang, W. 2014, *MNRAS*, 440, 1114
- Watanabe, S., Sako, M., Ishida, M., et al. 2006, *ApJ*, 651, 421
- Wegner, W. 1994, *MNRAS*, 270, 229
- Wegner, W. 2006, *MNRAS*, 371, 185
- White, N. E., Swank, J. H., & Holt, S. S. 1983, *ApJ*, 270, 711

Wilms, J., Allen, A., & McCray, R. 2000, ApJ, 542, 914

Wilson, W. E., Ferris, R. H., Axtens, P., et al. 2011, MNRAS, 416, 832

Woo, J. W., Clark, G. W., Day, C. S. R., Nagase, F., & Takeshima, T. 1994, ApJ, 436, L5

Wosley, S., & Janka, T. 2005, Nature Physics, 1, 147

Zahn, J.-P. 1977, A&A, 57, 383

Zavlin, V. E., & Pavlov, G. G. 2002, Neutron Stars, Pulsars, and Supernova Remnants, Proceedings of the 270. WE-Heraeus Seminar on Neutron Stars, Pulsars, and Supernova Remnants. MPE Report 278. Edited by W. Becker, H. Lesch, and J. Trümper. Garching bei München: Max-Planck-Institut für extraterrestrische Physik, p.263

Zdziarski, A. A., Sikora, M., Dubus, G., et al. 2012, MNRAS, 421, 2956

